UNIVERSITY OF CALIFORNIA

Santa Barbara

Dating Deformation with Titanite

A dissertation submitted in partial satisfaction of the

requirements for the degree Doctor of Philosophy

in Earth Science

by

Amy Catherine Moser

Committee in charge:

Professor Brad Hacker, Chair

Professor John Cottle

Professor Matt Rioux

December 2022

The dissertation of Amy Catherine Moser is approved.

_____
John Cottle

_____
Matt Rioux

_____
Brad Hacker, Committee Chair

November 2022

Dating Deformation with Titanite

ACKNOWLEDGEMENTS

This work would not have been possible without the host of collaborators, mentors, friends, and family who have supported me during my PhD. First, thank you to my advisor, Brad Hacker, for the opportunity to pursue my degree here at UCSB. Thanks as well to both John Cottle and Matt Rioux for agreeing to serve on my committee, and for all their support and feedback over the past five years. Matt has also served as an incredible teaching mentor and resource for me; he was both my faculty mentor when I taught EARTH 2 and agreed to be the faculty name on paper when I mentored a senior thesis student in my final year.

Thank you to all my collaborators. Gareth Seward and Andrew Kylander-Clark provided crucial assistance in the labs. Josh Garber has been easily the most important scientific resource during my PhD, particularly over the last year and a half. George Gehrels, Josh Schwartz, Keith Klepeis, Alex Lusk, and Snir Attia provided field assistance, samples, and additional data that were the foundation of these projects. All these folks are either already co-authors on published manuscripts from my PhD or will be co-authors on manuscripts to be submitted. Thanks as well to both Tarryn Cawood and Will Hoover, whose research I have collaborated on during my PhD.

My fellow UCSB Earth Science graduate students provided fundamental scientific and community support during my time at UCSB. Thanks to my fellow Hack Packers Ryan Stoner and Robert Holder (in addition to the previously mentioned Josh Garber) for everything they taught me about MATLAB, as well as data reduction and interpretation. Hack Pack Lunch and Snack provided a much-needed reprieve and opportunity for South Coast Deli/Super Cucas. Devin Rand assisted with much of my MATLAB coding.

Thank you to my students, without whom my time at UCSB would not have been the same. Whether I worked with you in the classroom, field, lab, or through GEMSS, know that you have been a foundational component of my UCSB experience. I would specifically like to thank Michelle Chambers, who I had the absolute gift of mentoring for her senior thesis. Alaina Rosenthal-Guillot spent hours in the lab processing samples for one of my projects; this project would not have been possible without her.

Several people outside of UCSB provided additional mentorship regarding navigating my academic experience. Alexis Ault and Cailey Condit have been kind, thoughtful, and supportive mentors, and friends, without whom I would not be in the position that I am today. Nils A. Sjöberg has been a steadfast supporter of my work, particularly in the height of the pandemic when I needed encouragement the most.

Finally, I would like to thank my friends and family who have been the greatest support system that I could have possibly asked for during my academic journey. This dissertation is dedicated to Dr. Alex Johnson, whose impact on this department and the broader Earth science community will never be forgotten.

VITA OF AMY CATHERINE MOSER
December 2022

EDUCATION

Bachelor of Arts in Geosciences, Franklin & Marshall College, May 2014 (summa cum laude)
Master of Science in Geology, Utah State University, August 2017
Doctor of Philosophy in Earth Science University of California, Santa Barbara, December 2022 (expected)

PROFESSIONAL APPOINTMENTS

2011–2013: Teaching Assistant, Department of Earth and Environment, Franklin & Marshall College
2015: Internship, Chevron Corporation, Houston, Texas
2016: Teaching Assistant, Utah State University, Department of Geology, Utah State University
2017–2019: Teaching Assistant, Department of Earth Science, University of California, Santa Barbara
2020: Instructor of Record, Department of Earth Science, University of California, Santa Barbara

PUBLICATIONS

Hoover, W.F., Condit, C.B., Lindquist, P.C., Moser, A.C., Guevara, V.E., 2022, Episodic Slow Slip Hosted by Talc-Bearing Metasomatic Rocks: High Strain Rates and Stress Amplification in a Chemically Reacting Shear Zone: Geophysical Research Letters, v. 49, e2022GL101083, doi.org/10.1029/2022GL101083.

Cawood, T.K., Moser, A.C., Borsook, A., and Rooney, A.D., 2022, New Constraints on the Timing and Character of Laramide Deformation, Fluid Flow, and Pegmatite Emplacement in Southeastern California: GSA Bulletin, v. 134, no. 11–12, p. 3221–3241, doi.org/10.1130/B36251.1.

Moser, A.C., Hacker, B.R., Gehrels, G.E., Seward, G.G.E., Kylander-Clark, A.R.C., and Garber, J.M., 2022, Linking Titanite U-Pb Dates to Coupled Deformation and Dissolution–Reprecipitation: Contributions to Mineralogy and Petrology, v. 177, no. 3, p. 1–27, doi.org/10.1007/s00410-022-01906-9.

Moser, A.C., Ault, A.K., Stearns, M.A., Evans, J.P., and Guenthner, W.R., 2021, Late Oligocene–Early Miocene Detachment Faulting in Crystalline Basement, Mecca Hills, CA, Documented with Zircon (U–Th)/He Date-eU-Visual Radiation Damage Patterns: Tectonics, v. 40, no. 9, p. 1–24, doi.org/10.1029/2021TC006809.

Ault, A.K., Guenthner, W.R., Moser, A.C., Miller, G.H., and Refsnider, K.A., 2018, Zircon Grain Selection Reveals (De)coupled Metamictization, Radiation Damage, and He Diffusivity: Chemical Geology, v. 490, p. 1-12, doi:10.1016/j.chemgeo.2018.04.023.

Moser, A.C., Evans, J.P., Ault, A.K., Bradbury, K.K., and Janecke, S.U., 2017, (U–Th)/He Thermochronometry Reveals Pleistocene Punctuated Deformation and Synkinematic Hematite Mineralization in the Mecca Hills, Southernmost San Andreas Fault Zone: Earth and Planetary Science Letters, v. 476, p. 87-99. doi:10.1016/j.epsl.2017.07.039.

AWARDS

NSF-EAR Postdoctoral Fellowship, 2022
UCSB Alex Johnson Memorial Award for Outstanding Student Mentoring, 2022
AGU Outstanding Student Presentation Award, 2021
UCSB G.K. Gilbert Award for Best Colloquium Talk, Department of Earth Science, 2021
UCSB Peggy Dearth Wormington Field Studies Award, 2021
UCSB Earth Science Graduate Opportunity Award, 2020
UCSB Graduate Student Association Excellence in Teaching Award, 2020
UCSB Mucker's Coterie TA of the Year, 2019
Mineralogical Society of America Student Research Grant, 2018
UCSB Chancellor's Doctoral Fellowship, 2017–2022
Geological Society of America Student Research Grant, 2016
American Association of Petroleum Geologists Student Research Grant, 2016
Association for Women Geoscientists Research Scholarship, 2016
Utah State College of Science MSc Student Researcher of the Year, 2016
Utah State Department of Geology Outstanding Graduate Researcher, 2016
GDL Foundation Fellowship, 2015
Franklin & Marshall College Rawnsley Science Prize, 2014
Franklin & Marshall College Geology Award, 2014
Franklin & Marshall College Richard A. Shephard '56 Award in Mineralogy and Petrology, 2014
Franklin & Marshall College Lloyd S. Yeakel Memorial Award in Geology and Sedimentology, 2014
Phi Beta Kappa Academic Honor Society

FIELDS OF STUDY

Major Field: Petrochronology and Tectonics

Studies in Geochronology, Structural Geology, and Metamorphic Petrology with Professor Brad Hacker

ABSTRACT

Dating Deformation with Titanite

by

Amy Catherine Moser

Directly dating deformation is a critical, unresolved challenge in tectonics. The mineral titanite ($CaTiSiO_5$) is one of the best candidates for a "deformation chronometer"—a way to interpret dates in their microstructural context to directly date deformation. The purpose of this dissertation is to assess the utility of dating deformation with titanite ("titanite deformation chronometry"). In the following three chapters, I integrate *in situ* titanite U-Pb geochronology with microstructures, zoning, and trace-element compositions of titanite from three ductile shear zones to (1) develop titanite deformation chronometry by assessing titanite recrystallization mechanisms in the Coast shear zone, British Columbia; (2) apply titanite deformation chronometry to directly date amphibolite-facies deformation in the Anita Shear Zone, New Zealand; and (3) evaluate the applicability of titanite deformation chronometry to constraining the temperature and fluid compositions during ductile deformation using an example from cm-scale, Cretaceous shear zones in the Eastern Transverse Ranges, CA. Work from the Coast shear zone, British Columbia illustrates that interface-coupled dissolution–reprecipitation and lattice bending were coupled grain-scale processes that together variably reset titanite U-Pb dates, demonstrating the feasibility of

titanite deformation chronometry. The application of titanite deformation chronometry to the Anita Shear Zone revealed that amphibolite-facies deformation ended at ~11 Ma, unequivocally linking these fabrics to high-temperature deformation within the Alpine Fault system. The example from the Eastern Transverse Ranges illustrates that titanite deformation chronometry is not only a powerful tool to date events in ductile shear zones, but also to document the degree to which temperature and fluid compositions evolve during ongoing deformation.

TABLE OF CONTENTS

INTRODUCTION

Documenting the timing and rates of high-temperature deformation is an outstanding challenge that is crucial for a complete understanding of numerous tectonic processes (e.g., Huntington and Klepeis, 2018). Ductile deformation has traditionally been dated through indirect methods, including by dating cross-cutting relationships and/or synkinematic intrusions (e.g., Klepeis et al., 1998), linking cooling ages to shear-zone related exhumation (e.g., Jacobson et al., 2007), or by dating synkinematic, neocrystallized minerals (e.g., Papapavlou et al., 2017; Ring et al., 2019). The applicability of these approaches, however, can be limited: cross-cutting relationships may be absent or the range of permissible deformation ages that they permit too broad, the closure temperatures of high-temperature thermochronometers are too low to capture cooling in the deepest lithosphere, and whether minerals crystallized pre- or synkinematically is not always clear. In addition, the conditions of deformation—such as the strain rates, differential stress, temperature, pressure, and fluid compositions—are typically constrained by phases separate from those used to date deformation (e.g. quartz, feldspar; Tullis and Yund, 1987; Hirth and Tullis, 1992). This creates significant ambiguity in relating the timescales to the conditions of deformation. Ideally, dates could be combined with microstructural information from the same crystal in a direct approach to dating deformation.

Examples from the materials science literature illustrate that dislocation glide and climb can alter the trace-element systematics of materials. Dislocations serve as fast diffusion pathways (i.e., pipe diffusion; Hart, 1957; Love, 1964) and sweep point defects through deformed metals (i.e., Cottrell atmospheres; Cottrell and Bilby, 1949), ultimately depositing them in grain boundaries where they are trapped or removed (e.g., Piazolo et al., 2016;

Kirkland et al., 2018). A growing body of atom probe tomography studies demonstrate that these processes are directly applicable to geologic materials (e.g., Piazolo et al., 2016; Peterman et al., 2016; Kirkland et al., 2018; Fougerouse et al., 2021). These studies demonstrate that dislocation glide and climb redistribute trace-elements—including radiogenic Pb—and indicate that crystal-plastic deformation may lead to direct resetting of dates. Radiometric dating thus has the potential to provide direct constraints on the timing of deformation when interpreted in their microstructural context (e.g., Piazolo et al., 2012, 2016; Fougerouse et al., 2021).

The titanite U-Pb system is one of the best candidates for such a "deformation chronometer". It is a common accessory mineral in igneous and metamorphic with diverse bulk compositions (Frost et al., 2000). Titanite has a high Pb closure temperature (>750 °C; e.g., Spencer et al., 2013; Stearns et al., 2016; Holder et al., 2019; Hartnady et al., 2019); titanite dates are therefore more likely to reflect crystallization or recrystallization at all but the most extreme metamorphic temperatures (Holder et al., 2019). Titanite also incorporates many trace-elements into its crystal structure that can be used to document the pressure and temperature conditions of (re)crystallization (Hayden et al., 2008; Garber et al., 2017). Importantly, titanite responds to deformation, being shown to both neocrystallize synkinematically and undergo dislocation creep (e.g., Bonamici et al., 2015; Papapavlou et al., 2017; Gordon et al., 2021). Further, individual titanite crystals are commonly hundreds of microns long (e.g., Spencer et al., 2013; Holder et al., 2019), permitting straightforward comparisons among dates, microstructure, and zoning using *in situ* techniques like laser-ablation ICP-MS.

The purpose of this dissertation is to assess the utility of the titanite U-Pb system in directly dating and constraining the conditions of deformation. Because titanite U-Pb dates may reflect crystallization, recrystallization, cooling, or deformation (e.g., Bonamici et al., 2015; Stearns et al., 2016; Garber et al., 2017; Holder and Hacker, 2019), interpretation of titanite U-Pb dates as deformation ages requires careful consideration of the intragrain relationships among dates and chemical zoning, microstructure, and distance from the grain edge and/or grain size. Chapter 1 develops an approach to assess the extent to which various metamorphic processes reset titanite U-Pb systematics and thus directly link titanite U-Pb dates to the tectonic processes that they reflect—including deformation. In this integrated titanite U-Pb, trace-element, microstructural, and zoning dataset from the Coast shear zone, British Columbia, dates young with increasing lattice misorientation and ~55 Ma dates are spatially correlated with fluid-related zoning. These observations indicate that fluid-driven recrystallization and ductile deformation were coupled processes that together reset U-Pb dates and highlight the multitude of processes that may be recorded by a single chronometer in a single sample. The ~55 Ma deformation and fluid-flow age that is documented by the dataset is consistent with previous constraints on the timing of ductile shearing along the Coast shear zone (Klepeis et al., 1998). This dataset therefore provides the framework to date ductile shear zone processes elsewhere using "titanite deformation chronometry". This chapter is published in the journal *Contributions to Mineralogy and Petrology* and is reproduced here with the required permission of the authors.

With this context, chapter 2 explores the applicability of titanite deformation chronometry to ductile shear zones with complex, polyphase deformation histories. The Anita Shear Zone, South Island, New Zealand, is a km-scale ductile shear zone that

preserves at least four phases of deformation at amphibolite- to greenschist-facies conditions (Klepeis et al., 1999). The tectonic significance of the amphibolite-facies fabrics—including their potential relationship to the Miocene development of the Pacific–Australian plate boundary—hinges almost entirely on when they formed (Hill, 1995a, 1995b; Klepeis et al., 1999; Claypool et al., 2002; Czertowicz et al., 2016a). Relationships among titanite U-Pb dates, lattice bending, deformation twins, grain zoning, and trace-element concentrations from titanite deformed in the Anita Shear Zone are consistent with: (1) initial development of the Anita shear zone at amphibolite-facies conditions during extension and orogenic collapse of the Paleo-Pacific Gondwana margin prior to ~90 Ma and (2) amphibolite-facies transpression within the broader Alpine Fault system that commenced as early as ~25 Ma and ended at ~11 Ma. The Anita Shear Zone titanite deformation chronometry dataset therefore provides a critical and rare constraint on the timing of high-temperature fabric formation along the Pacific–Australian plate boundary that was not captured by other U-Pb geochronometers (e.g., zircon) in the same rocks. These results demonstrate that titanite deformation chronometry is useful for constraining the timing of deformation in polyphase shear zones, that both lattice bending and deformation twins play an important role in resetting dates in deformed titanite, and that complex titanite U-Pb datasets from deformed rocks may require microstructural context to be interpreted. A manuscript that presents this dataset is currently in preparation to be submitted to the *Journal of Metamorphic Geology*.

In addition to dating shear zone processes, titanite trace-element systematics make it an ideal candidate to (1) constrain the temperature and fluid compositions of deformation, and (2) document how those conditions change during ongoing deformation. Such constraints are critical for conceptual and quantitative models of how the mid- to deep lithosphere

deforms. Chapter 3 presents an application of titanite deformation chronometry to cm- and dm-scale, mylonitic ductile shear zones in the Eastern Transverse Ranges, CA that details the evolution of temperature and fluid compositions over <1 Myr timescales within these structures. Titanite in these mylonites preserve two textures (rims and aggregates) with different trace-element signatures; dates from both textures constrain the timing of deformation to ~75 Ma. Rims have elevated F contents and record cooler Zr-in-titanite temperatures than the aggregates; these data are consistent with cooling of the system and the evolution of the fluid that accompanied deformation to a more F-enriched brine as deformation progressed. Bent titanite in these mylonites yield partially- to completely reset dates. The trace-element systematics of these grains indicate that bent lattices provided efficient pathways for fluids to recrystallize grain interiors and that fluid-driven recrystallization may be the ultimate mechanism by which dates are reset in titanite deformed by dislocation creep. Titanite deformation chronometry is thus a powerful approach to not only date ductile shear zones, but also to document the degree to and timescales over which temperatures and fluid compositions evolve throughout a single deformation event.

Data tables and oversized figures referenced in the text are available with the electronic supplementary materials associated with this dissertation.

CHAPTER 1: LINKING TITANITE U-PB DATES TO COUPLED DEFORMATION AND DISSOLUTION–REPRECIPITATION

1. Introduction

Establishing the timing, duration, and rates of deformation and fluid flow in ductile shear zones is essential for understanding a host of tectonic processes such as strain partitioning, feedbacks between shallow and deep-crustal deformation, plate boundary initiation and evolution, and the differentiation of Earth's crust. Despite their significance, directly dating ductile slip and associated fluid flow remains challenging. It is well known that deformation and fluids (re)crystallize mineral assemblages as shear zones evolve, with the resulting microstructures and compositional zoning providing direct links to the processes from which they formed (e.g., Austrheim, 1987; Goncalves et al., 2012; Jamtveit et al., 2016). However, most microstructural studies of rocks deformed at high temperature have focused on minerals that are not datable using high-temperature radioactive isotope geochronology (for example, quartz and feldspar; e.g., Tullis and Yund, 1987; Hirth and Tullis, 1992). The microtextures of dateable accessory minerals that (re)crystallize in ductiley deformed rocks therefore provide a critical, but underexplored, window into the timing and nature of high-temperature deformation.

Of the minerals that incorporate appreciable U and Th into their crystal structures, titanite is a useful petrochronometer to directly date the record of tectonic processes preserved in metamorphic rocks. Many crustal rocks contain titanite (Frost et al., 2000), as it crystallizes in a wide range of bulk compositions and metamorphic conditions, and commonly forms crystals several hundred microns in length (Frost et al., 2000; Spencer et al., 2013; Holder et al., 2019). Titanite also incorporates many trace elements into its crystal

structure that can be used to constrain ambient P-T conditions, either using direct thermometry or by connecting titanite to metamorphic assemblages (Hayden et al., 2008; Spencer et al., 2013; Garber et al., 2017; Kohn, 2017). Contrary to experimental data (Cherniak, 1993), data from natural rocks demonstrate that titanite remains largely unaffected by thermally mediated volume diffusion of Pb at temperatures <750 °C (Rubatto and Hermann, 2001; Kohn and Corrie, 2011; Spencer et al., 2013; Stearns et al., 2016; Kohn, 2017; Marsh and Smye, 2017; Walters and Kohn, 2017; Holder and Hacker, 2019). Titanite may recrystallize via dissolution–reprecipitation in the presence of (typically H_2O-rich) fluids (Garber et al., 2017; Marsh and Smye, 2017; Walters and Kohn, 2017; Holder and Hacker, 2019), undergo crystal-plastic deformation at moderate to high metamorphic temperatures (greenschist- to granulite-facies conditions), and preserve several generations of zoning and microstructures (Bonamici et al., 2015; Papapavlou et al., 2017, 2018; Gordon et al., 2021), providing a rich record of superposed metamorphic processes.

Recent advances in our understanding of titanite Pb closure temperature (Kohn and Corrie, 2011; Spencer et al., 2013; Stearns et al., 2016; Garber et al., 2017; Hartnady et al., 2019; Holder et al., 2019) have cast doubt on many early interpretations of titanite U-Pb dates as cooling ages. In the absence of evidence for thermally mediated volume diffusion, titanite U-Pb dates have been variably interpreted as crystallization or recrystallization ages depending on the relationships among U-Pb dates, microtextures, and trace-element compositions. This study investigates the mechanisms of recrystallization in titanite by integrating U-Pb dates, trace-element concentrations, compositional zoning, and microstructural data from twenty titanite grains from a single calc-silicate gneiss that was metamorphosed and deformed in the Coast shear zone, British Columbia (Ingram and

Hutton, 1994; Klepeis et al., 1998; Rusmore et al., 2001; Andronicos et al., 2003). We demonstrate the range and complexities of processes that are responsible for titanite recrystallization at the scale of a single thin section and present a framework to link titanite U-Pb dates to the timing of deformation and metamorphic fluid flow.

2. Background

2.1. Effects of cooling, crystallization, fluids, and deformation on U-Pb systematics

U-Pb dates from accessory minerals may reflect one or more processes that can be tied to the tectonothermal history of a rock. Given the extensive previous work on U-Pb systematics in titanite and other U-bearing minerals, we first consider expected relationships among textural, microstructural, and elemental/isotopic observations in titanite as a function of the mechanism or process responsible for their formation (summarized in Fig. 1).

U-Pb dates are frequently interpreted as cooling ages, or the time that thermally mediated volume diffusion of Pb ceased as that mineral cooled (Fig. 1A; e.g., Dodson, 1973). Experimental titanite data suggest that the Pb closure temperature for 100 μm diameter titanite subject to a ~10 °C/Myr cooling rate is ~600 °C (Cherniak, 1993). However, the length scales of Pb diffusion in natural rocks indicate a closure temperature >750 °C, compatible with slower Pb diffusion (Kohn and Corrie, 2011; Spencer et al., 2013; Stearns et al., 2016; Garber et al., 2017; Hartnady et al., 2019; Holder et al., 2019). The naturally constrained intracrystalline diffusivity of Pb in titanite is similar to the experimentally measured diffusion of Sr in titanite, which is reasonable given their similar charge and ionic radii (Cherniak, 1995; LaTourrette et al., 1996). Though commonly interpreted as such without detailed, grain-scale data, titanite U-Pb dates cannot confidently

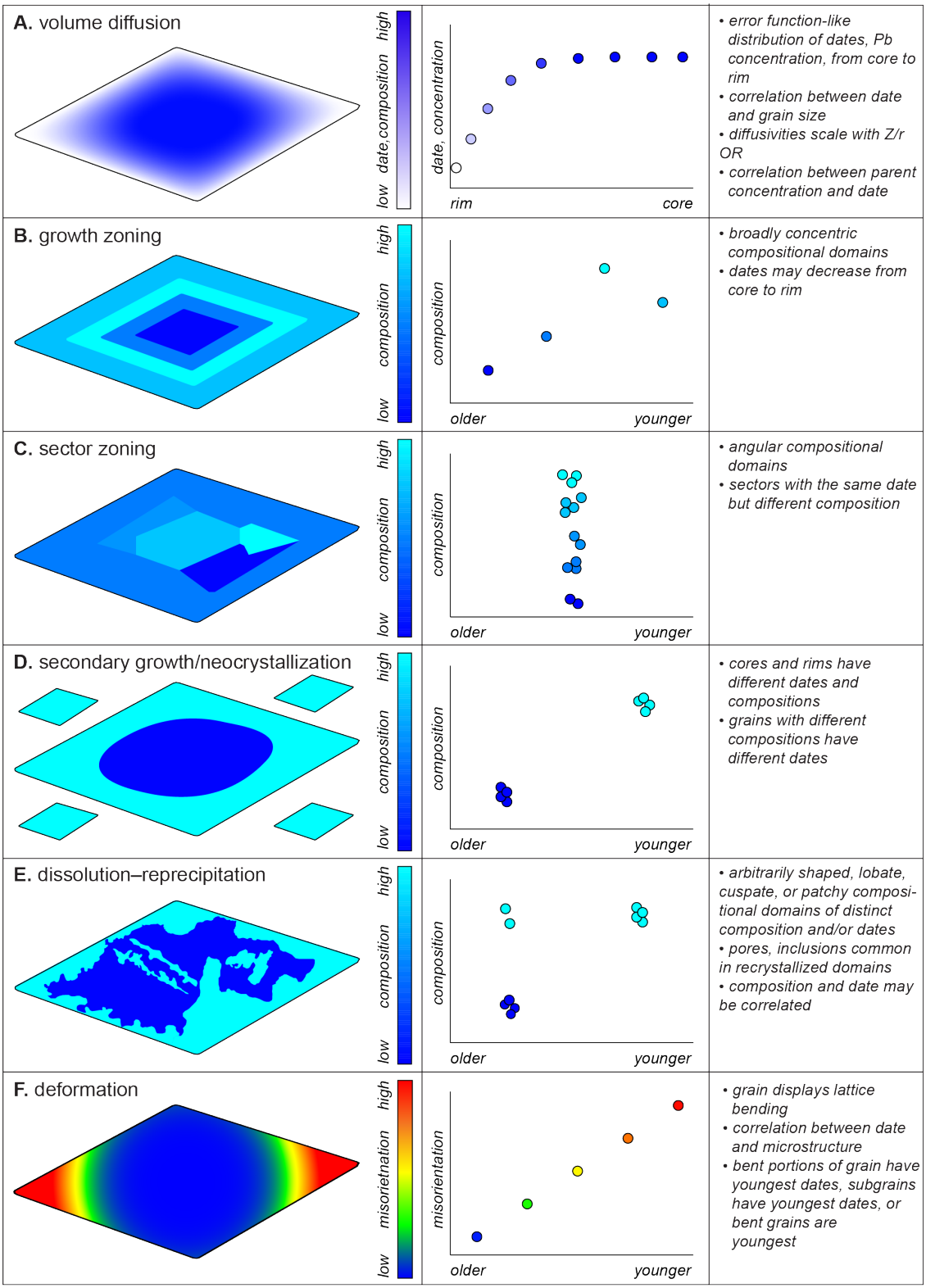

Figure 1. Expected titanite microtextures and relationships between date and distance from the edge of the grain, composition, or intragrain misorientation for various grain-scale processes that may be recorded by titanite U-Pb dates.

be considered “Dodsonian” cooling ages unless there is evidence for volume diffusion in the spatial distribution of Pb and/or U-Pb dates. Such evidence might include variation in dates from grain core to rim, with older dates in the cores asymptotically approaching younger dates in the rims (Fig. 1A; Crank, 1975) or dates that vary systematically with grain size, with larger grains yielding older dates and smaller grains yielding younger dates (Bonamici et al., 2015; Kirkland et al., 2018; Olierook et al., 2019).

Alternatively, U-Pb dates are in the simplest case interpreted as crystallization ages, or the time that a mineral formed below its Pb closure temperature. Growth, sector, or core–rim zoning combined with distinct U-Pb dates from compositional domains provide evidence that dates reflect the timing of crystallization (Fig. 1B–D). Variations in P, T, and/or trace-element partitioning/availability during titanite growth may produce concentric growth zoning, which broadly manifests as progressively outward-stepping compositional domains with sharp or gradational boundaries (Fig. 1B; Lucassen et al., 2011; Bonamici et al., 2015; Garber et al., 2017). In such cases, the U-Pb dates are expected to decrease from core to rim and reflect the duration of titanite growth. Sector zoning may also be produced during crystal growth if partition coefficients vary among different crystal faces and crystal growth outpaces intracrystalline volume diffusion (Fig. 1C; Hollister, 1970; Watson and Liang, 1995); in titanite, trace-element concentrations in different sectors that crystallized simultaneously may vary by a factor of three (Fig. 1C; Paterson et al., 1989; Hayden et al., 2008; Walters and Kohn, 2017). Secondary titanite growth is indicated by core–rim overgrowth textures or multiple generations of compositionally distinct grains, both with clear U-Pb date populations (Fig. 1D; Bonamici et al., 2015; Garber et al., 2017; Olierook et al., 2019).

Titanite dates may also be recrystallization ages. Grains may recrystallize by interface-coupled dissolution–reprecipitation, wherein a fluid-rich interface moves through a crystal, replacing the precursor grain with the same (or similar) phase of different composition and/or date, and typically preserving the original crystal shape (Geisler et al., 2003, 2007; Putnis et al., 2005; Putnis, 2009). Minerals recrystallized by dissolution–reprecipitation may preserve inward-convex, arbitrarily shaped, lobate/cuspate, or patchy compositional domains that penetrate inward from the grain edges, fractures, twin planes, and/or inclusions (Fig. 1E; Geisler et al., 2003, 2007; Putnis et al., 2005; Putnis, 2009). Evidence of dissolution–reprecipitation is common in monazite (Budzyn et al., 2011; Harlov et al., 2011; Williams et al., 2011; Seydoux-Guillaume et al., 2012; Hacker et al., 2015; Weinberg et al., 2020), zircon (Geisler et al., 2003, 2007; Tomaschek et al., 2003; Soman et al., 2010), and increasingly recognized in titanite (Smith et al., 2009; Spencer et al., 2013; Bonamici et al., 2015; Garber et al., 2017; Marsh and Smye, 2017; Holder and Hacker, 2019).

In addition to volume diffusion and (re)crystallization, the presence and movement of line defects through a crystal (i.e., dislocation creep) can redistribute trace elements (Cottrell and Bilby, 1949; Turnbull and Hoffman, 1954; Hoffman, 1956; Hart, 1957; Huang et al., 1989; Larche and Cahn, 1985; Love, 1964; Rabier and Puls, 1989; Ruoff and Balluffi, 1963; Swiatnicki et al., 1986), including radiogenic Pb (Peterman et al., 2016; Piazolo et al., 2016; Fougerouse et al., 2021). Deformation-induced trace-element mobility in minerals has been inferred and directly observed from various microstructural, geochronology, and trace-element datasets (Reddy et al., 2006; Timms et al., 2006, 2011; Macdonald et al., 2013; Piazolo et al., 2016; Kovaleva et al., 2017; Kirkland et al., 2018; Fougerouse et al., 2021). A number of these datasets show correlations between U-Pb date and microstructure in several

dateable minerals; deformed grains, mechanical twins, and low-angle subgrain boundaries have the youngest dates and/or the greatest discordance in the U-Pb system (Moser et al., 2009; Macdonald et al., 2013; Bonamici et al., 2015; Kovaleva et al., 2017; Langone et al., 2017; Papapavlou et al., 2017; Moore et al., 2020; Fougerouse et al., 2021). Transmission electron microscopy and atom probe investigations of geologic materials have revealed the systematic enrichment of trace elements in free dislocations and dislocation loops, and the loss or retention of trace elements along subgrain boundaries (Peterman et al., 2016; Piazolo et al., 2016; Kirkland et al., 2018; Fougerouse et al., 2019, 2021). These data suggest that crystal-plastic deformation may partially or fully reset the U-Pb system in deformed minerals, and it is reasonable to expect that this includes titanite (Bonamici et al., 2015; Papapavlou et al., 2017, 2018; Gordon et al., 2021) even if the precise mechanisms of dislocation-facilitated Pb transport differ among minerals (e.g., Kirkland et al., 2018). U-Pb dates can be interpreted as deformation ages if a grain displays lattice misorientation (hereafter referred to as "bending" or "bent grains"), low-angle boundaries (>1° but <10° of misorientation across a subgrain wall), and/or dynamically recrystallized new grains (>10° with respect to parent grain) and a correlation between U-Pb date and microstructure (Fig. 1F). For example, U-Pb dates may decrease with increased bending, or subgrains and/or bent grains may have the youngest dates (Fig. 1F), although examples from the literature demonstrate these relationships could be more complex if elements are redistributed within and not lost completely lost from the grain during dislocation creep (e.g., Kovaleva et al., 2017).

2.2. Geologic setting

The Coast Mountains Orogen is a ~1700 km-long, ~5–175 km-wide, Jurassic to Eocene calc-alkaline batholith located in westernmost British Columbia and southeasternmost Alaska (Fig. 2A; e.g., Harrison et al., 1979; Crawford and Hollister, 1982; Gehrels et al., 1991). The Coast Mountains host the Coast shear zone, a 5–15 km-wide, >1200 km-long, subvertical, crustal-scale, ductile shear zone along and within the western edge of the Great Tonalite Sill (Fig. 2A; Hollister and Crawford, 1986; Crawford et al., 1987; Gehrels et al., 1991; Ingram and Hutton, 1994; Morozov et al., 1998; Thomas and Sinha, 1999; Rusmore et al., 2001, 2005; Andronicos et al., 2003). The dominant foliation and lineation throughout the Coast shear zone are both steep, with predominantly east-side-up kinematic indicators (e.g., Ingram and Hutton, 1994). Most workers interpret these features to reflect largely dip-slip motion (e.g., McClelland et al., 1992; Klepeis et al., 1998), but some have proposed that the steep fabrics developed during transpression (Fossen and Tikoff, 1998). The timing of deformation in the Coast shear zone is primarily constrained by the crystallization age of the Great Tonalite Sill, a 5–30 km-wide, sheetlike pluton that intruded synkinematically with the Coast shear zone from ~80–55 Ma. Deformation also affected the margins of the metamorphic country rocks to the east and west of the sill (Fig. 2; Ingram and Hutton, 1994; Rusmore and Woodsworth, 1994; Klepeis et al., 1998).

The structural, metamorphic, and tectonic histories of these units in Sitklan Passage (location of the studied sample; Fig. 2B) have been previously studied by Klepeis et al., (1998). Cross-cutting relationships in Sitklan Passage indicate two phases of Coast shear zone deformation: an initial phase of east-side-up deformation from ~65–57 Ma, constrained by the crystallization age of deformed tonalites, followed by ~57–55 Ma east-side-down

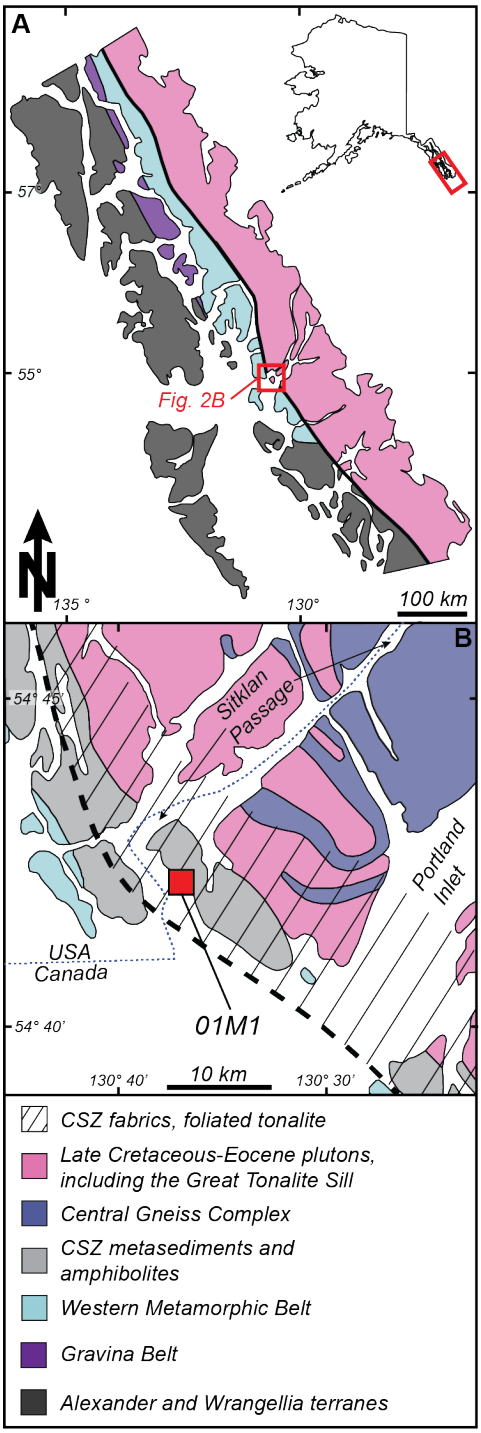

Figure 2. (A) Location and generalized geologic map of the Coast Mountains Orogen and Coast shear zone. Thick black line delineates the main trace of the Coast shear zone. (B) Geology of Wales Island, British Columbia. Red box denotes location of the titanite-bearing calc-silicate gneiss 01M1 analyzed in this study. Thick, dashed black line marks the main trace of the Coast shear zone. After Klepeis et al., (1998).

deformation defined by a suite of deformed pegmatites and undeformed plutons (Klepeis et al., 1998). The latter phase was concentrated in the western portion of the shear zone, hereafter referred to as the "westernmost Coast shear zone." These data suggest ductile deformation along the Coast shear zone in Sitklan Passage ceased around 55 Ma (Klepeis et al., 1998). Early, east-side-up deformation occurred during or after decompression and heating of rocks within the shear zone, as indicated by cordierite coronas on garnet and sillimanite pseudomorphs after kyanite and staurolite in Coast shear zone metapelites (Klepeis et al., 1998). Garnet geochemistry and cordierite coronas indicate that the early deformation phase occurred at 5.6 ± 0.4 kbar and 710 ± 30 °C (Klepeis et al., 1998); there are no prior P-T estimates for the later, east-side-down deformation.

3. Sample description

The studied sample, 01M1, is a metasedimentary calc-silicate gneiss from Wales Island between Portland Inlet and Sitklan Passage (54.741389 N, 130.614345 W; Fig. 2B). The sampled unit comprises metamorphic country rocks intruded by Paleocene–Eocene tonalite sills and pegmatite dikes ("CSZ metasediments and amphibolites," Klepeis et al., 1998; Fig. 2, this study) including the Great Tonalite Sill. The gneiss consists of diopside, potassium feldspar, plagioclase feldspar, Ca-amphibole, titanite, clinozoisite, biotite, quartz, calcite, white mica, chlorite, and trace zircon (Figs. 3, S1). Titanite grains are idioblastic to hypidioblastic and ~50–1,000 μm in maximum length. The bulk rock fabric consists of a foliation defined by compositional layering, with different proportions of diopside and feldspar; the long axes of most titanite grains are aligned with this fabric (Figs. 3, Fig. S1). No lineation was observed. Undulatory extinction is pervasive in feldspar, and additional

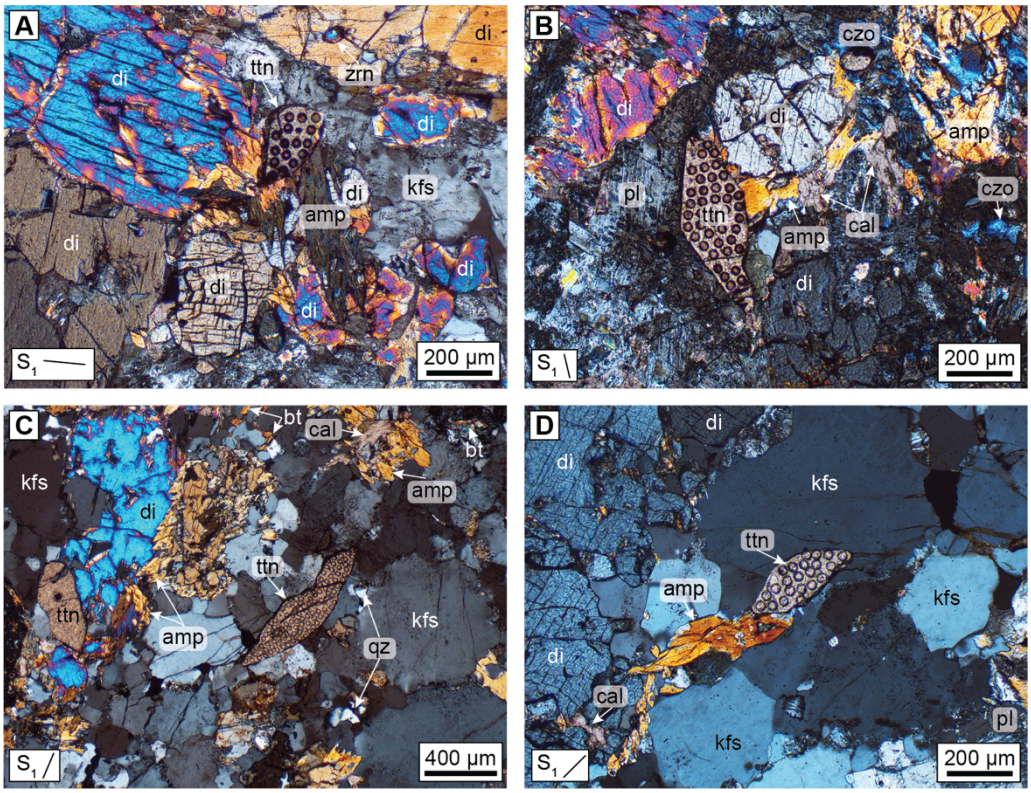

Figure 3. Cross-polarized light images of titanite analyzed from calc-silicate gneiss 01M1. (A) Grain 4, (B) grain 12, (C) grain 19, (D) grain 20. S_1 denotes orientation of foliation (42/028, dip/dip direction) defined by compositional layers of diopside and feldspar. Amp: Ca-amphibole; bt: biotite; cal: calcite; czo: clinozoisite; di: diopside; kfs: K-feldspar; pl: plagioclase feldspar; ttn: titanite; qz: quartz; zrn: zircon.

deformation microstructures are limited to undulatory extinction and low-angle boundaries in a few titanite grains; other phases are mostly unaffected. No shear bands were observed in thin section. The foliation dips moderately (dip–dip direction 42/028) at the studied sample site. Projection along strike places the sample within the westernmost Coast shear zone described above. All analyses were conducted on a single polished thin section that was cut perpendicular to the foliation.

4. Methods

4.1. Electron-backscatter diffraction (EBSD)

Titanite EBSD data were collected on an FEI Quanta 400F field emission source scanning electron microscope coupled with an HKL Technology Nordlys II EBSD camera at the University of California, Santa Barbara. Data were acquired at an accelerating voltage of 20 kV, a 1-5nA beam current, a working distance of ~15 mm, and the sample surface inclined at 70° to the incident electron beam. EBSD pattern maps were acquired and indexed using Oxford/HKL Channel5 Flamenco application. The maps were collected by electron-beam rastering, with sampling on a 2x2 μm grid. EBSD Maps were processed with Oxford/HKL Channel 5 Tango application. Data processing included two steps: removal of single pixels possessing a large misorientation with respect to neighboring pixels, and assignment of an average-orientation to any unindexed pixel with at least 6 neighboring indexed pixels of the same phase. To visualize substructure within individual grains (microstructure), maps of relative misorientation within a grain were calculated; these maps were calculated relative to a point in the approximate center of each grain.

4.2. Electron microprobe (EPMA) X-ray maps

Al, Fe, Zr, Nb, and Ce X-ray maps were collected using a 5-spectrometer Cameca SX100 EPMA at the University of California, Santa Barbara. The data were collected by moving the sample under a stationary 1-2 μm micron defocused beam, with a 150 or 200 ms dwell time, 20kV accelerating voltage, and a 200 nA beam current. ProbeImage and CalcImage (Probe Software Inc.) were used to acquire and process the map data.

4.3. Laser-ablation split-stream inductively coupled plasma mass spectrometry (LASS)

U, Th, and Pb isotopes and trace elements were collected simultaneously from titanite in thin section using the LASS methodology described by Kylander-Clark et al., (2013) and Kylander-Clark (2017). A total of 1,049 laser-ablation spots were analyzed on 20 titanite grains in three separate analytical sessions; all spots within individual grains were collected in the same session. U-Th-Pb isotopes were measured on a Nu Instruments Plasma 3D multi-collector ICP in the first session, and on a Nu Instruments Plasma HR-ES multi-collector ICP in sessions two and three. Trace elements were measured on an Agilent 7700X quadrupole ICP-MS in all sessions. These mass spectrometers were coupled to a Cetac/Photon Machines 193 nm excimer Excite laser with a HelEx cell. Titanite crystals were ablated with a 25 μm spot size and a laser fluence of ~1 J/cm2 at 4 Hz (sessions one and two) and 5 Hz (session three) for 60 shots per analytical spot. To remove surface contamination, two cleaning shots with 15–20 s washout were fired prior to each analysis. Matrix-matched standard MKED1 (1521.02 ± 0.55 Ma $^{206}Pb/^{207}Pb$ isotope dilution thermal ionization mass spectrometry date; Spandler et al., 2016) was run every ~8 unknowns, and was used as the primary standard for the U/Pb, Th/Pb, and Pb/Pb isotopic ratios. Titanite

secondary standards BLR (1047.4 ± 1.4 Ma concordia date, Aleinkoff et al., 2007), Y1710C5 (388.6 ± 0.5 Ma $^{207}Pb/^{206}Pb$-corrected $^{206}Pb/^{238}U$ ID-TIMS date; Spencer et al., 2013) and Fish Canyon (28.4 ± 0.05 ID-TIMS date; Schmitz and Bowring, 2001) along with glass NIST SRM 612 (no date; Pearce et al., 1997) were interspersed in each run to monitor U-Th-Pb ratio accuracies. MKED1 was chosen as the primary standard as it is assumed to be homogeneous and have no common Pb (Spandler et al., 2016). The $^{207}Pb/^{206}Pb$ ratios of the NIST SRM 612 analyses were homogeneous and yielded single populations in-run, suggesting this assumption is valid for the dataset (Table S1E). Lower-intercept, $^{207}Pb/^{206}Pb$-corrected $^{206}Pb/^{238}U$ dates (assuming the contemporaneous Stacey and Kramers, 1975 common-Pb $^{207}Pb/^{206}Pb$ values of 0.91, 0.86, and 0.83, respectively) for the secondary standards across the three analytical sessions were 1042 ± 3 Ma (BLR), 388 ± 3 Ma (Y1710C5), and 28 ± 2 Ma (Fish Canyon Tuff; Table S1), which are within 0.5, 0.0, and 0.0 % of their known values, respectively, where 0.0 % indicates the lower-intercept dates were the same as the known reference value. The U and Pb isotopic data were reduced in IgorPro 6.37 with the Iolite 2.5 plugin using the "U-Pb Geochronology3" reduction scheme (Paton, 2011). The first and last two seconds of each integration were removed prior to the downhole correction; integrations were manually trimmed to include only homogenous portions of the analyses (i.e., to remove inclusions) after the downhole correction was applied.

Two ratio uncertainties are reported for $^{207}Pb/^{235}U$, $^{206}Pb/^{238}U$, $^{207}Pb/^{206}Pb$, and $^{208}Pb/^{232}Th$ for each analysis: in-run uncertainties that should be used to compare dates from the same grain and/or the same session, and uncertainties required to compare dates across the three analytical sessions. In-run uncertainties include analytical uncertainties and an

additional 2% uncertainty propagated in quadrature to each measured ratio, with additional uncertainty added (where required) to make in-run secondary standard BLR a single population within a given run (Table S1). Full dataset uncertainties (~3% for $^{206}Pb/^{238}U$, ~5% for $^{207}Pb/^{206}Pb$) include analytical uncertainties and additional uncertainty required to make secondary standard BLR ratios a single population across the entire dataset. The $^{207}Pb/^{235}U$ uncertainties were recalculated using the propagated uncertainties in $^{206}Pb/^{238}U$ and $^{207}Pb/^{206}Pb$, as ^{235}U was not measured but calculated assuming a $^{238}U/^{235}U$ of 137.88. The analytical precision afforded by the laser-ablation approach is such that using the updated $^{238}U/^{235}U$ value does not change our results. The titanite U-Pb dates were calculated assuming a Stacey and Kramers (1975) common-Pb $^{207}Pb/^{206}Pb$ ratio of 0.83 ± 0.04, which matches the upper Tera-Wasserburg concordia intercept defined by the distribution of U-Pb ratios in the analyzed titanite (Fig. 4). As with the individual U-Th-Pb ratios, in-run and whole dataset uncertainties are also reported for the $^{207}Pb/^{206}Pb$-corrected ^{206}Pb-^{238}U dates. NIST SRM 612 was used as the primary standard for the trace elements (Pearce et al., 1997). The trace-element data were reduced using IgorPro 6.37 with the Iolite 2.5 plugin using the "Trace Elements" data reduction scheme, and assuming 19.2 wt % Ca in the unknown titanite analyses. The trace-element concentrations for secondary trace-element standard MKED1 were within ~10% of the expected values for the reference material, which is typical for use of NIST glasses as a primary reference material for trace elements (Liu et al., 2008).

4.4. U and Pb concentration calculations

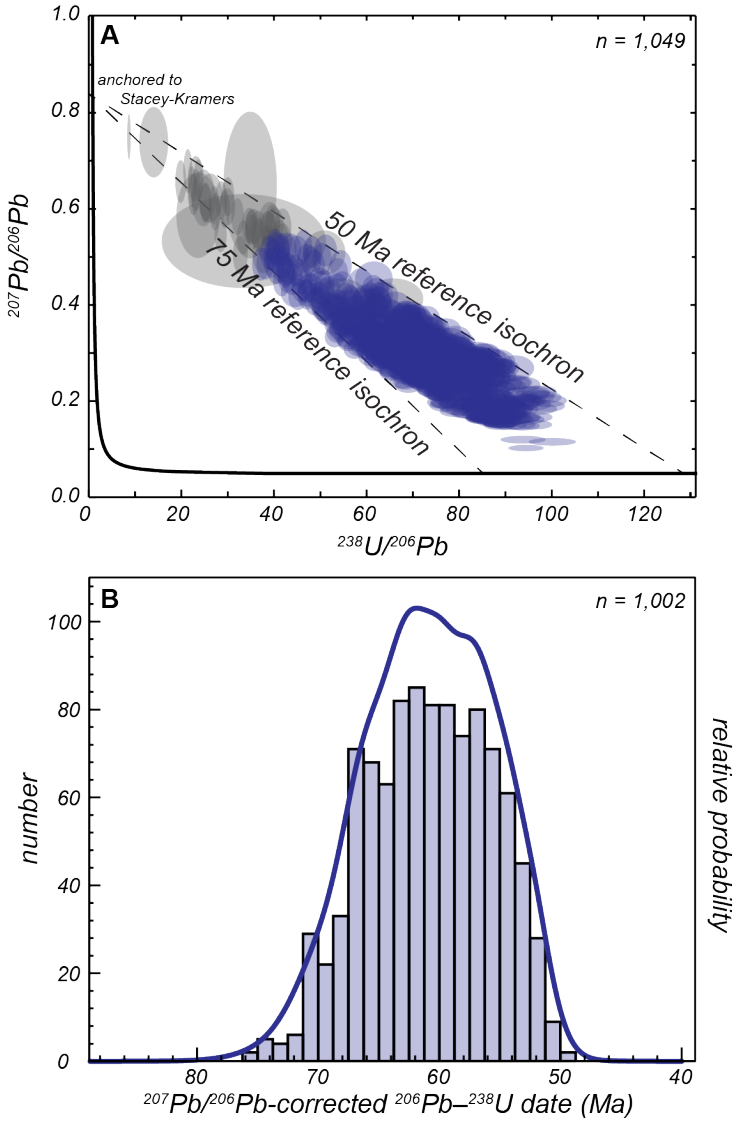

Figure 4. (A) Tera-Wasserburg concordia diagram of all 1,049 titanite laser-ablation analyses from this study. Uncertainties plotted are those required to make secondary standard BLR a single population across all three analytical sessions. Gray ellipses indicate analyses with in-run U-Pb date uncertainties >10% that were removed from the final dataset. Blue ellipses indicate analyses with in-run U-Pb date uncertainties <10%. Isochrons anchored to Stacey and Kramers (1975) common Pb ratios for the oldest (75 Ma) and youngest (50 Ma) date are shown for reference. (B) Histogram and probability density function of 1,002 U-Pb dates with uncertainties <10% used in the final dataset.

Reported titanite U concentrations from the Nu Instruments Plasma 3D multi-collector and Nu Instruments Plasma HR-ES multi-collector ICPs were calculated in Iolite using MKED1 (Spandler et al., 2016) as a primary standard. NIST SRM 612 U concentrations were homogeneous within error within each session, although they are inaccurate by up to ~15% (Table S1). Therefore, even if the reported U concentrations of unknown titanites are inaccurate, the homogeneity of the NIST SRM 612 values suggests that measured U concentrations systematically deviate from their true values by the same amount and are therefore comparable within the same session. Reported U concentration uncertainties include additional uncertainty added in quadrature to make secondary standard NIST SRM 612 a single population in-run (Table S1).

^{206}Pb, ^{207}Pb, and ^{208}Pb concentrations were calculated from U concentrations, using the downhole-corrected ^{206}Pb/^{238}U, ^{207}Pb/^{206}Pb, and ^{208}Pb/^{206}Pb ratios (with MKED1 as the primary standard) and molar masses of ^{238}U and the respective Pb isotopes (see also Garber et al., 2020). ^{204}Pb was calculated from raw ^{204}Pb/^{206}Pb of the unknowns scaled by a factor required to make NIST SRM 612 ^{204}Pb/^{206}Pb ratios the known value for each run. We calculated Pb concentrations in this manner rather than using the values produced in iolite as iolite assumes the isotopic ratios in the reference material and the unknowns are the same (Paton, 2011). Iolite's approach therefore returns incorrect Pb concentrations for minerals with significant radiogenic Pb. The total Pb concentrations for secondary standards BLR (Aleinkoff et al., 2007) and NIST SRM 612 calculated in this manner overlap previously reported values (Table S1). Like the uncertainties in ^{206}Pb/^{238}U and ^{207}Pb/^{206}Pb discussed above, 2% uncertainty was added in quadrature to the ^{208}Pb/^{206}Pb and ^{204}Pb/^{206}Pb ratios; additional uncertainty was added where required to make secondary standards BLR

($^{208}Pb/^{206}Pb$) and NIST SRM 612 ($^{204}Pb/^{206}Pb$) a single population in-run. Only in-run uncertainties are reported for the $^{208}Pb/^{206}Pb$ and $^{204}Pb/^{206}Pb$ ratios as Pb concentrations were only compared within individual sessions. Uncertainties in the concentrations of the Pb isotopes were propagated in quadrature based on the U concentration uncertainties and uncertainties in the U/Pb and/or Pb/Pb ratios used in each individual Pb isotope concentration calculation. The total Pb concentration uncertainty includes the uncertainties of ^{204}Pb, ^{206}Pb, ^{207}Pb, and ^{208}Pb added in quadrature. The fraction of common ^{206}Pb and ^{207}Pb in each analysis was calculated from the measured $^{207}Pb/^{206}Pb$, radiogenic $^{207}Pb/^{206}Pb$ for the $^{207}Pb/^{206}Pb$-corrected $^{206}Pb–^{238}U$ date and assumed Stacey-Kramers (1975) $^{207}Pb/^{206}Pb$ value (0.83) following the approach outlined by Williams, (1998). The fraction of common ^{208}Pb was similarly calculated from the fraction of common ^{206}Pb, Stacey-Kramers (1975) $^{208}Pb/^{206}Pb$ value (2.07) for the $^{207}Pb/^{206}Pb$-corrected $^{206}Pb–^{238}U$ date, and measured $^{208}Pb/^{206}Pb$ (Williams, 1998; Garber et al., 2020). This approach circumvents assumptions about data concordance and the precision and accuracy of using a ^{204}Pb correction. The equations used in the Pb concentration and common Pb fraction calculations can be found in the appendices.

4.5. Erf^{-1} calculations

A normalized concentration gradient that results from volume diffusion is defined by Crank (1975):

$$\left(\frac{C - C_r}{C_c - C_r}\right) = erf\left(\frac{x}{\sqrt{4Dt}}\right)$$

where C is the concentration at a given spot, C_r is the concentration at the rim, C_c is the concentration at the core, x is the distance from the edge of the grain, and D is the diffusivity for a given duration of time (t). For the purposes of treating the concentration data in each grain as a diffusion experiment, we define C_r and C_c as the minimum and maximum concentration within each grain, regardless of whether they occur at the rim or core. Rearranging this equation, the inverse error function of the normalized data that results from volume diffusion is a line:

$$erf^{-1}\left(\frac{C - C_r}{C_c - C_r}\right) = \frac{x}{\sqrt{4Dt}}$$

with slope:

$$m = \frac{1}{\sqrt{4Dt}}$$

Therefore, for single-element data, this approach can be used to calculate the diffusivity of that element if the duration of time at constant temperature is known.

The role of volume diffusion at the grain scale in the analyzed titanite grains was assessed by calculating the inverse error function of the normalized Pb and trace-element concentrations. The linearity of the normalized erf^{-1} as a function of distance from the grain edge was evaluated by calculating the correlation coefficient (Pearson's r) and the r^2 values of linear regressions through these data. The relative uncertainties assigned to the erf^{-1} values were equivalent to the relative uncertainties of the in-run propagated (dates) and raw analytical (trace-element) uncertainties.

4.6. Zr-in-titanite thermobarometry

Zr-in-titanite temperatures were calculated using the calibration of Hayden et al., (2008). A pressure of 5.6 ± 0.4 kbar was assumed based on thermobarometry of a metapelite exposed near the studied sample (Klepeis et al., 1998). The presence of quartz in the studied sample indicates that $a_{SiO2} = 1$. Because rutile is absent, the a_{TiO2} was assumed to be 0.75 ± 0.25, as a_{TiO2} in titanite-bearing rocks is likely ≥0.5 (Chambers and Kohn, 2012; Ghent and Stout, 1984; Kapp et al., 2009). Two Zr-in-titanite temperature uncertainties are quoted herein: the first incorporates the analytical uncertainties on the Zr concentrations and the cited uncertainties on the assumed pressure and a_{TiO2}, whereas the other excludes uncertainties related to pressure and a_{TiO2} (which implicitly assumes pressure and a_{TiO2} were constant during titanite (re)crystallization).

5. Results

A summary of $^{207}Pb/^{206}Pb$-corrected $^{206}Pb–^{238}U$ dates (hereafter simply referred to as "U-Pb dates"), Zr-in-titanite temperatures, microstructures, zoning, and trace-element-date patterns for each of the analyzed grains is reported in Table 1. The complete U-Pb isotopic data, *erf*[1] calculations, Zr-in-titanite temperatures, trace-element data, EBSD texture component maps, and EPMA X-ray maps are contained in the appendices.

5.1. U-Pb dates

U-Pb dates from 1,049 spot analyses across 20 titanite grains from sample 01M1 range from ~75–50 Ma (Fig. 4). Some individual titanite grains preserve almost this entire range in dates (e.g., grains 3, 16; Table 1); other grains yielded a smaller range, sampling various

Grain	Grain length (μm)	Dates (Ma)[a]	Zr-in-ttn (°C)[b]	Date and Zr correlated?[c]	Mis (°)[d]	LABs[e]	Zoning[f]	Interpretation[g]
1	300	68–57	720–762	N	2	N	p	diss–repr
2	275	66–53	689–741	N	8	Y	l-c, p	def ± diss–repr
3	700	76–55	706–754	N	4	Y	l-c, p	def ± diss–repr
4	250	60–51	704–749	N	12	Y	l-c	def ± diss–repr
5	375	75–58	685–763	Y	1	N	l-c	diss–repr
6	550	67–56	704–773	N	3	N	l-c	diss–repr
7	525	69–52	702–785	N	80	Y	c-r, l-c	def ± diss–repr
8	425	72-54	709–756	Y	2	N	l-c, p	diss–repr
9	500	67–50	713–770	Y	2	N	l-c	diss–repr
10	500	69–51	709–769	N	1	N	l-c	diss–repr
11	350	77–59	712–775	Y	1	N	l-c	diss–repr
12	500	70–53	721–776	Y	1	N	c-r, l-c	diss–repr
13	375	59–51	749–780	N	8	Y	l-c	def ± diss–repr
14	250	68–55	706–779	Y	1	N	c-r, p	diss–repr
15	275	65–52	747–779	N	2	N	l-c	diss–repr
16	400	71–53	709–771	Y	2	N	c-r, l-c, p	diss–repr
17	550	59–54	765–783	N	8	Y	l-c	def ± diss–repr
18	1050	68–50	703–743	N	5	N	p	def ± diss–repr
19	900	69–50	714–740	Y	2	N	l-c, p	diss–repr
20	325	67–51	701–743	Y	2	N	l-c, p	diss–repr

[a] $^{207}Pb/^{206}Pb$-corrected ^{206}Pb-^{238}U date using Stacey-Kramers common Pb value of 0.83

[b] calculated using Hayden et al. (2008) Zr-in-ttn calibration, P = 5.6 kbar, $a_{SiO2} = 1$, $a_{TiO2} = 0.75$

[c] Y: Zr-in-titanite temperature and date correlated; N: Zr-in-titanite temperature and date not correlated

[d] maximum intragrain misorientation relative to point in center of grain

[e] misorientation across low-angle grain boundaries (LABs) is <10°

[f] c-r: core-rim, l-c: lobate-cuspate, p: patchy (see main text for explanation)

[g] diss–repr: dissolution–reprecipitation; def: deformation

Table 1. Summary of titanite U-Pb dates, zoning, microstructures, and trace-element signatures.

subsets of the thin section-scale date distribution (e.g., grains 4, 13, 17; Table 1). We excluded 47 spots with uncertainties greater than 10% from the *erf*$^{-1}$ calculations and date, trace-element, and microstructural comparisons, as the large errors preclude meaningful interpretations from these spots (Fig. 4).

5.2. Erf^{-1} *calculations*

Figure 5 presents *erf*$^{-1}$ plots of normalized Pb, Sr, Al, and Ce concentration for grains 3, 7 and 20, as these grains reflect the array of grain sizes observed in the sample. Al (high diffusivity), Sr and Pb (intermediate diffusivity), Ce (low diffusivity) are used to represent the spectrum of elemental diffusivity rates in titanite (Cherniak, 1993; Cherniak, 1995; LaTourrette et al., 1996; Holder et al., 2019). Sr may also be considered a proxy for Pb diffusion, as the two elements have identical charge and similar ionic radii (LaTourrette et al., 1996; Holder et al., 2019). In general, the correlation coefficients and r^2 values of the linear regressions of the *erf*$^{-1}$ calculations (including Pb) for each grain are small, and many of the r^2 values themselves are negative (Figs. 5, S2). This observation still holds when radiogenic and common Pb are considered separately (Fig. S2). Negative correlation coefficients in these plots are a function of the way we have defined C_r and C_c as the minimum and maximum concentrations of the grain rather than the defined rim and core, and thus demonstrate instances where concentrations increase rather than decrease at the grain edges. Negative r^2 values indicate modeled linear regressions that are a poorer fit to the data than a horizontal line. Even those data with high correlation coefficients do not define a line (e.g., total Pb in grain 15, Fig. S2O), which points to the effect of outliers on Pearson's r values. Although these observations indicate that Pearson's r is an imperfect

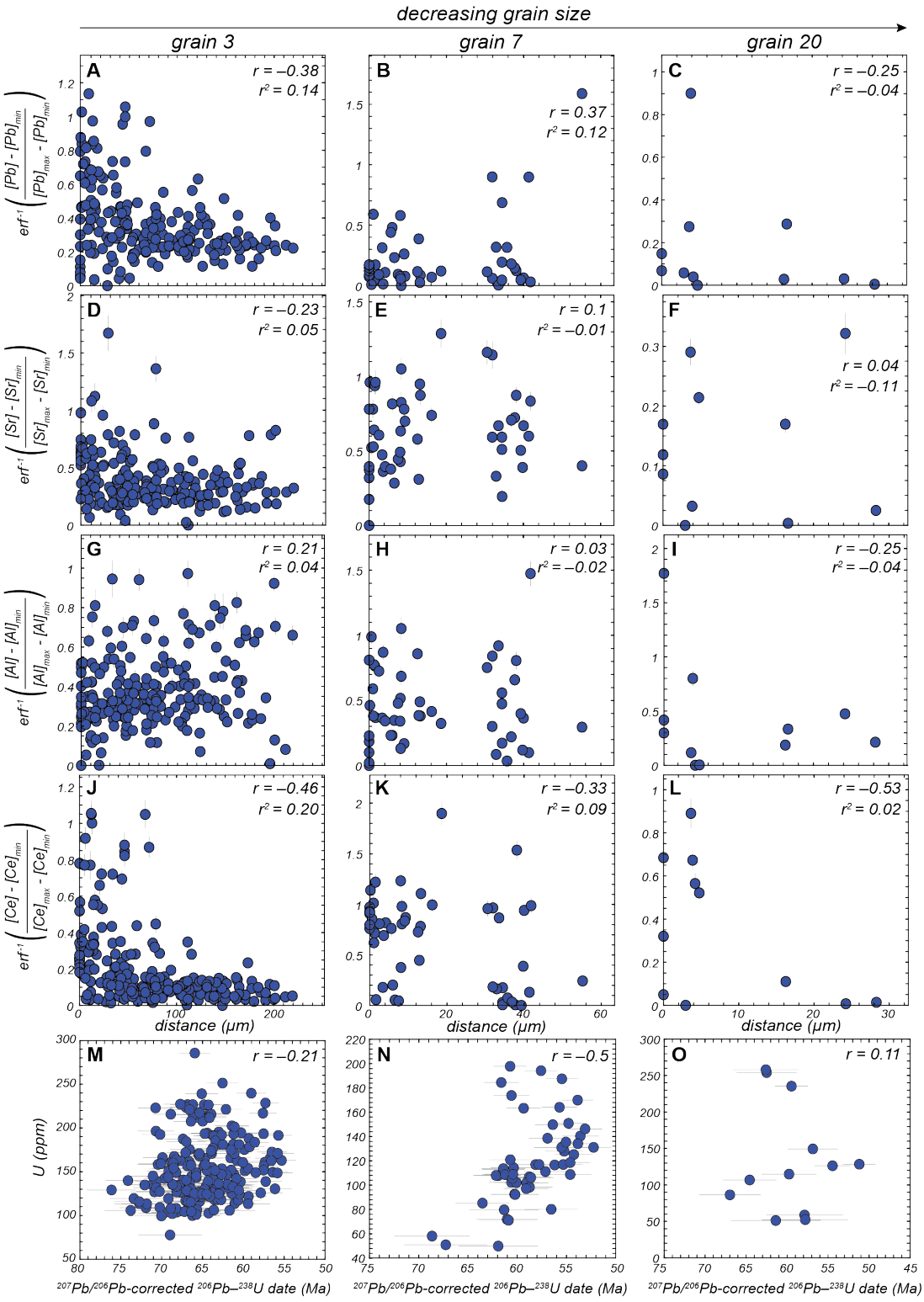

Figure 5. Pb (A–C), Sr (D–F), Al (G–I), and Ce (J–K) erf^{-1}calculations. Distance is the minimum distance of the spot from the nearest grain edge. Each distance measurement has an associated +25 μm uncertainty not shown. (M–N) Date and U concentrations are not strongly negatively correlated at the individual grain scale, indicating that heterogeneous parent concentrations did not drive Pb volume diffusion.

measure of correlation for this reason, it still shows that the erf^{-1} plots reveal no correlation between concentration and spot location within a grain. Correlation coefficients for U concentrations vs. U-Pb date (to assess the role of Pb diffusion driven by U concentration gradients; Paul et al., 2019) range from –0.5 to +0.7, but most values cluster around zero (Figs. 5 M–O, S3).

5.3. Sample-scale Zr-in-titanite temperatures and trace-element concentrations

Calculated Zr-in-titanite temperatures range from ~700–780 °C (Fig. 6A, Table 1). The calculated Zr-in-titanite temperatures from the oldest U-Pb spots overlap published equilibrium thermometry constraints from a nearby Coast shear zone metapelite (~700 °C; Klepeis et al., 1998), suggesting that the Zr-in-titanite temperatures are broadly accurate. U-Pb date and Zr-in-titanite temperature are not correlated at the sample scale (Fig. 6A). It is notable, however, that most Zr-in-titanite temperatures >750 °C are from spots younger than ~65 Ma. With the exception of La_N/Sm_N, which increases with decreasing date, there are no consistent sample-scale trends in date vs. trace-element content (Fig. 6B–D).

5.4. Zoning and individual grain trace-element concentrations

EPMA X-ray maps reveal three types of zoning in the analyzed titanite crystals; the zoning is most evident in the Al and Ce maps (Figs. 7, 8, 9). Seventeen grains have inward-penetrating, lobate–cuspate rims (Figs. 7A, 8A) that are particularly distinctive in the Al maps (Fig. 8A), but also mimicked by the Ce zoning in ten of these grains (e.g., Fig. 7A). Seven titanite grains display Al, Ce, and Nb zoning that is patchy or irregular (Fig. 8A). No porosity or inclusions are associated with the lobate–cuspate rims or areas of patchy zoning,

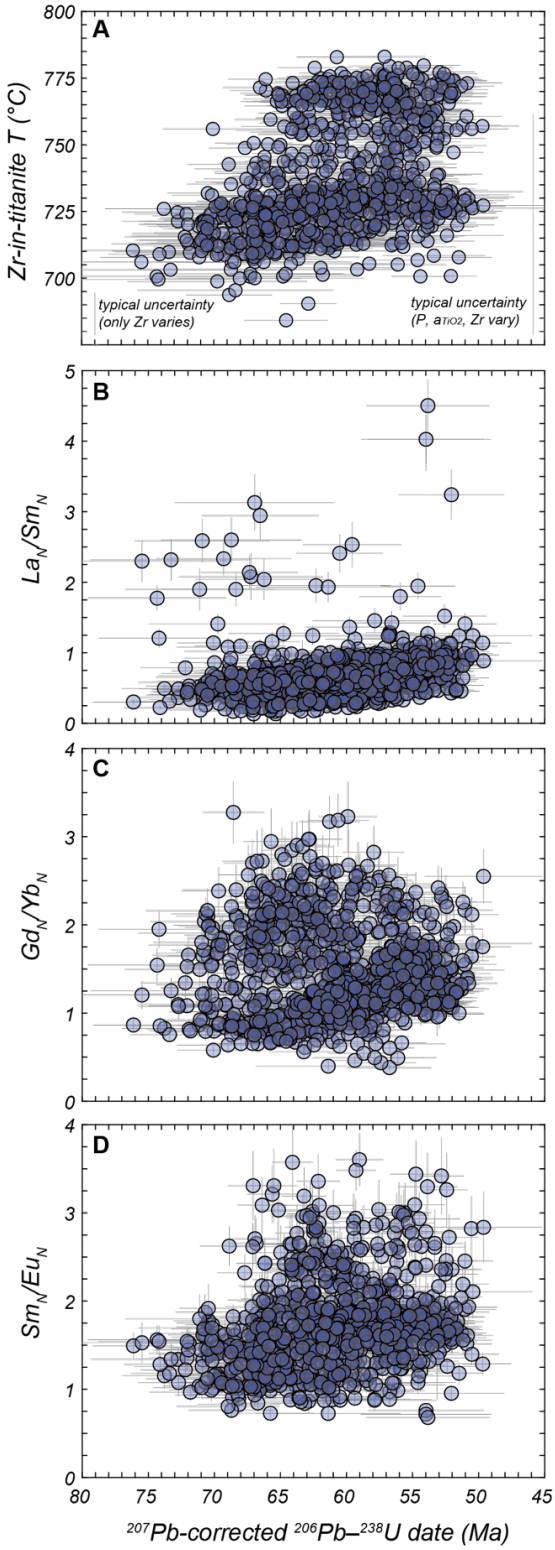

Figure 6. All dates vs. (A) Zr-in-titanite temperature (T, °C), (B) La_N/Sm_N, (C) Gd_N/Yb_N, and (D) Sm_N/Eu_N. Date uncertainties are those required to make secondary standard BLR a single population across all three analytical sessions. REEs are normalized to chondritic meteorite values of McDonough and Sun (1995).

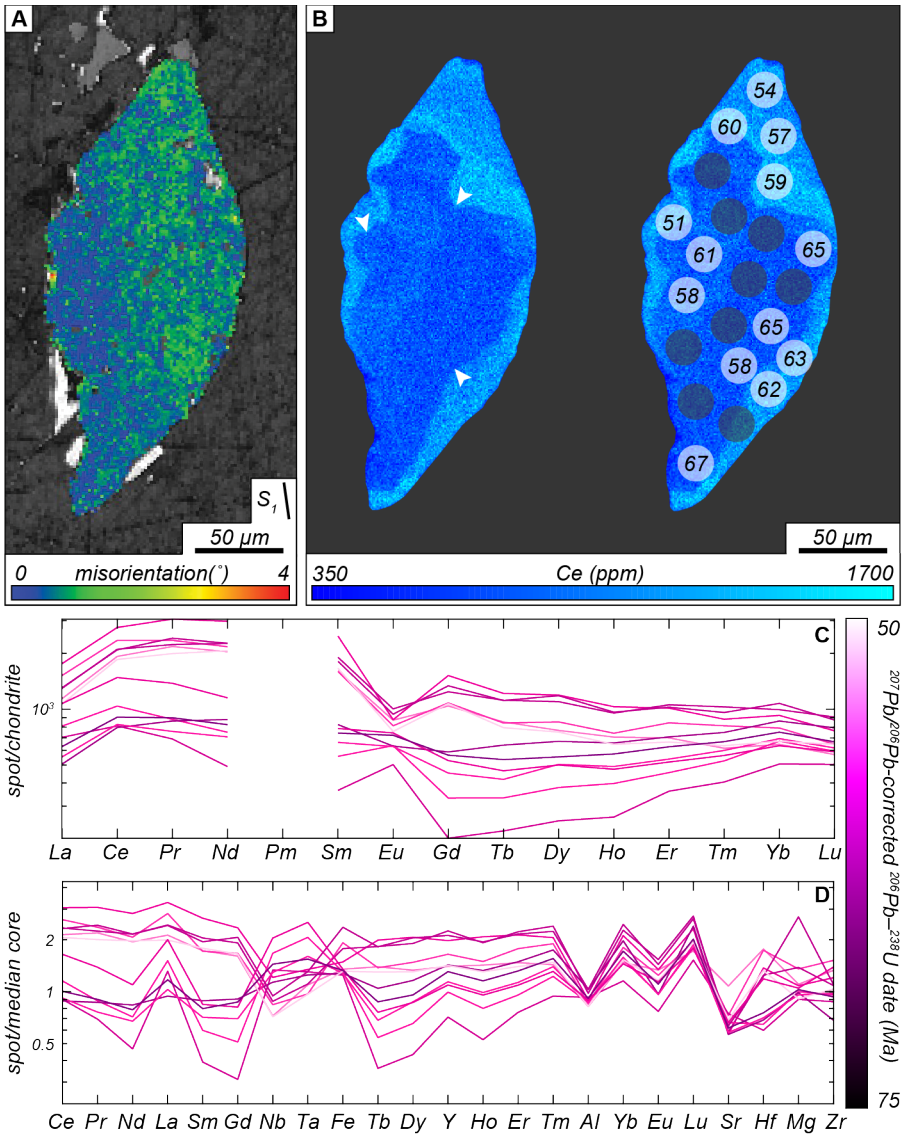

Figure. 7 Undeformed titanite grain (grain 20) displaying lobate–cuspate zoning, one of three zoning patterns observed in the dataset. (A) Misorientation map, (B) Ce X-ray map, (C) chondrite-normalized REEs, and (D) spider diagram of all measured trace elements normalized to the median dataset core values. Maximum and minimum concentrations in (B) were quantified using LASS data. Translucent white spots in (B) indicate the location of LASS analyses and the associated U-Pb dates (Ma). In-run date uncertainties from the dark gray spots are >10% and were removed from the final dataset. In-run, 2σ uncertainties on U-Pb dates for this grain are 2–5 Ma. White arrows in (B) denote lobate–cuspate rim, which is compatible with dissolution–reprecipitation. The elements in this and the other spider diagrams are arranged in compatibility order in titanite (Shannon, 1976). Zr and Hf concentrations increase with younging date in this grain, whereas Al concentrations decrease with younging date (D).

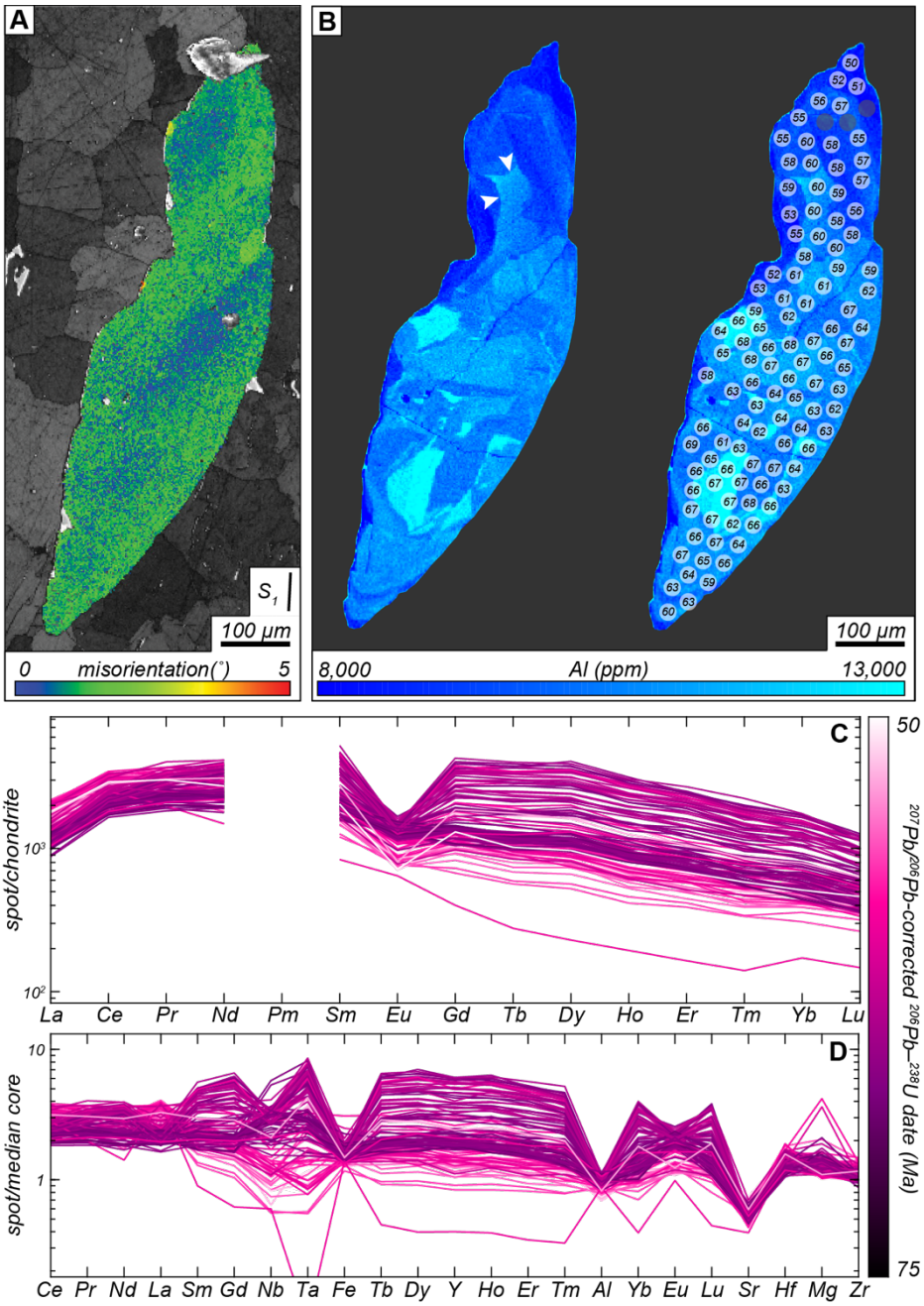

Figure 8. Undeformed titanite grain (grain 19) displaying patchy and lobate-cuspate zoning, two of three zoning patterns observed in the dataset. (A) Misorientation map, (B) Al X-ray map, (C) chondrite-normalized REEs, and (D) spider diagram of all measured trace elements normalized to the median dataset core values. Maximum and minimum concentrations in (B) were quantified using LASS data. Translucent white spots in (B) indicate the location of LASS analyses and the associated U-Pb dates (Ma). In-run date uncertainties from the dark gray spots are >10% and were removed from the final dataset. In-run, 2σ uncertainties on U-Pb dates for this grain are ~2 Ma. White arrows denote lobate–cuspate rim, compatible with dissolution–reprecipitation. Light rare-earth element, Zr, and Hf concentrations increase with younging date in this grain, whereas Al, Nb, and Ta concentrations decrease with younging date (C,D).

as revealed by BSE imaging (Fig. S4). Four grains exhibit core–rim zoning in the Ce X-ray maps, with low-Ce cores and high-Ce rims, but these same grains have lobate–cuspate rims or patchy zoning in the Al maps (Figs. 9A, S5N, S5P).

Correlations among date and some measured trace elements exist in 14 of the grains, but the trace-element–date correlations vary randomly from grain to grain (Figs. 7, 8, 9). For example, young spots in some grains have higher concentrations of nearly every measured trace element (e.g., grain 12; Fig. 9B and C). Other grains have more-complex date–trace-element correlations, with some trace-element concentrations increasing with younging date and others decreasing (e.g., grain 19; Fig. 8B and C), only a few elements correlated with date (grain 20, Fig. 7B and C), or a bimodal distribution of trace-element concentrations that are not correlated with date (e.g., grain 7; Fig. S5G). Six of the analyzed grains yielded no relationship between date and any measured trace element (e.g., grain 3, Fig. S5C).

5.5. Intracrystalline deformation

The degree of intracrystalline deformation is variable among the grains. Thirteen of the analyzed titanite have <3° of misorientation with respect to the center of the grain; these titanite crystals also lack low-angle grain boundaries (1–10° of misorientation; e.g., Figs. 7A, 8A, 9A, Table 1). Six of the remaining titanite grains show ~4–12° of lattice bending, with one grain having up to 80° of misorientation relative to the central reference point (Fig. 10A–D). Six of the seven bent grains also have low-angle boundaries (Fig. 10, Table 1). The bent grains are not oriented differently with respect to the bulk rock fabric compared to the unbent crystals and are not in microstructurally different portions of the rock (e.g., in shear bands) (Fig. S1). This suggests there is no systematic control on whether the titanite lattices

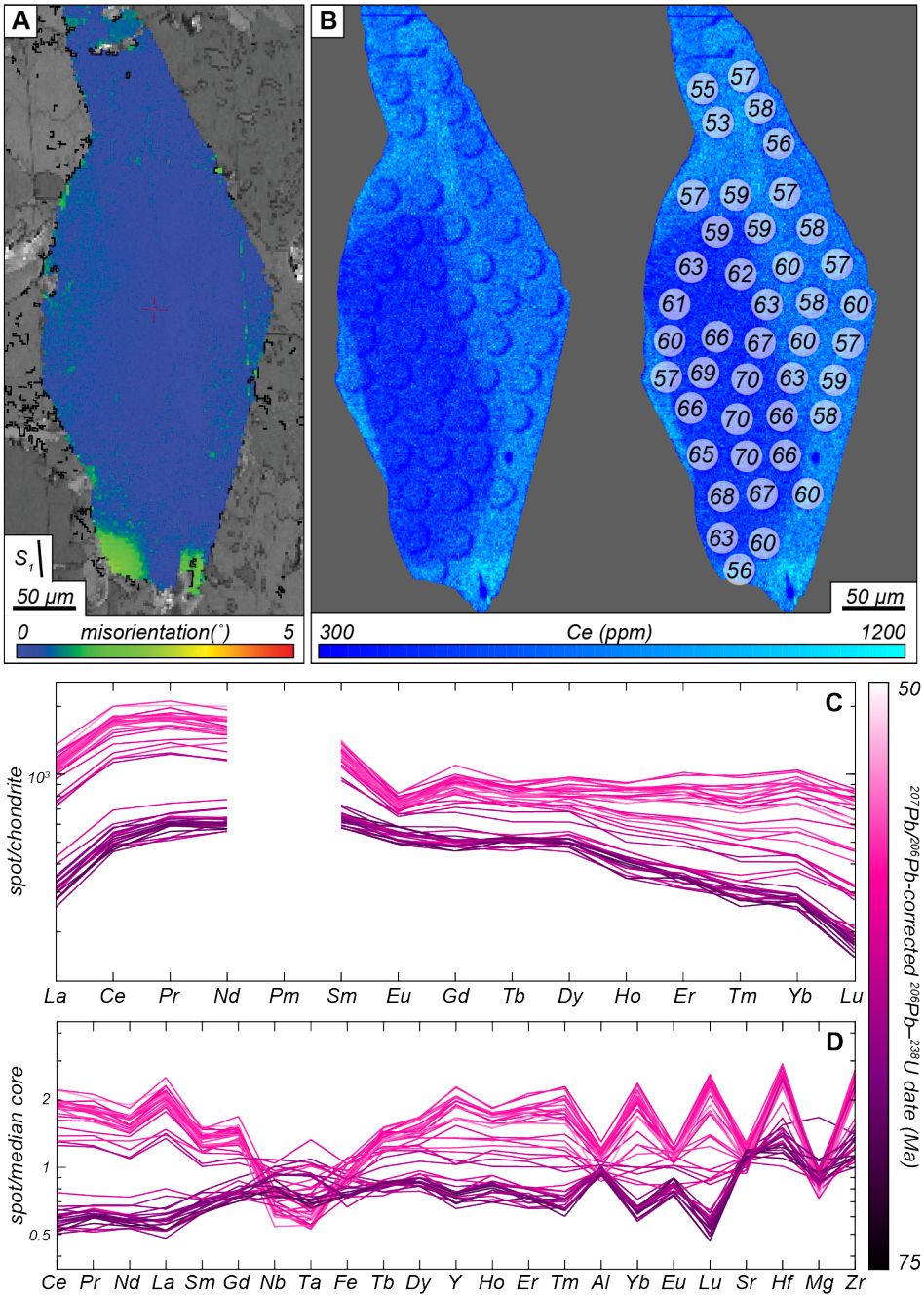

Figure 9. Undeformed titanite grain (grain 12) displaying core–rim zoning, one of three zoning patterns observed in the dataset. (A) Misorientation map, (B) Ce X-ray map, (C) chondrite-normalized REEs, and (D) spider diagram of all measured trace elements normalized to the median dataset core values. Maximum and minimum concentrations in (B) were quantified using LASS data. Translucent white spots in (B) indicate the location of LASS analyses and the associated U-Pb dates (Ma). In-run, 2σ uncertainties on U-Pb dates for this grain are ~2 Ma. Rare-earth element, Y, Fe, Zr, and Hf concentrations increase with younging date in this grain (C, D). The geometrically simple rim revealed by the Ce X-ray map is interpreted to have resulted from dissolution–reprecipitation rather than secondary titanite growth.

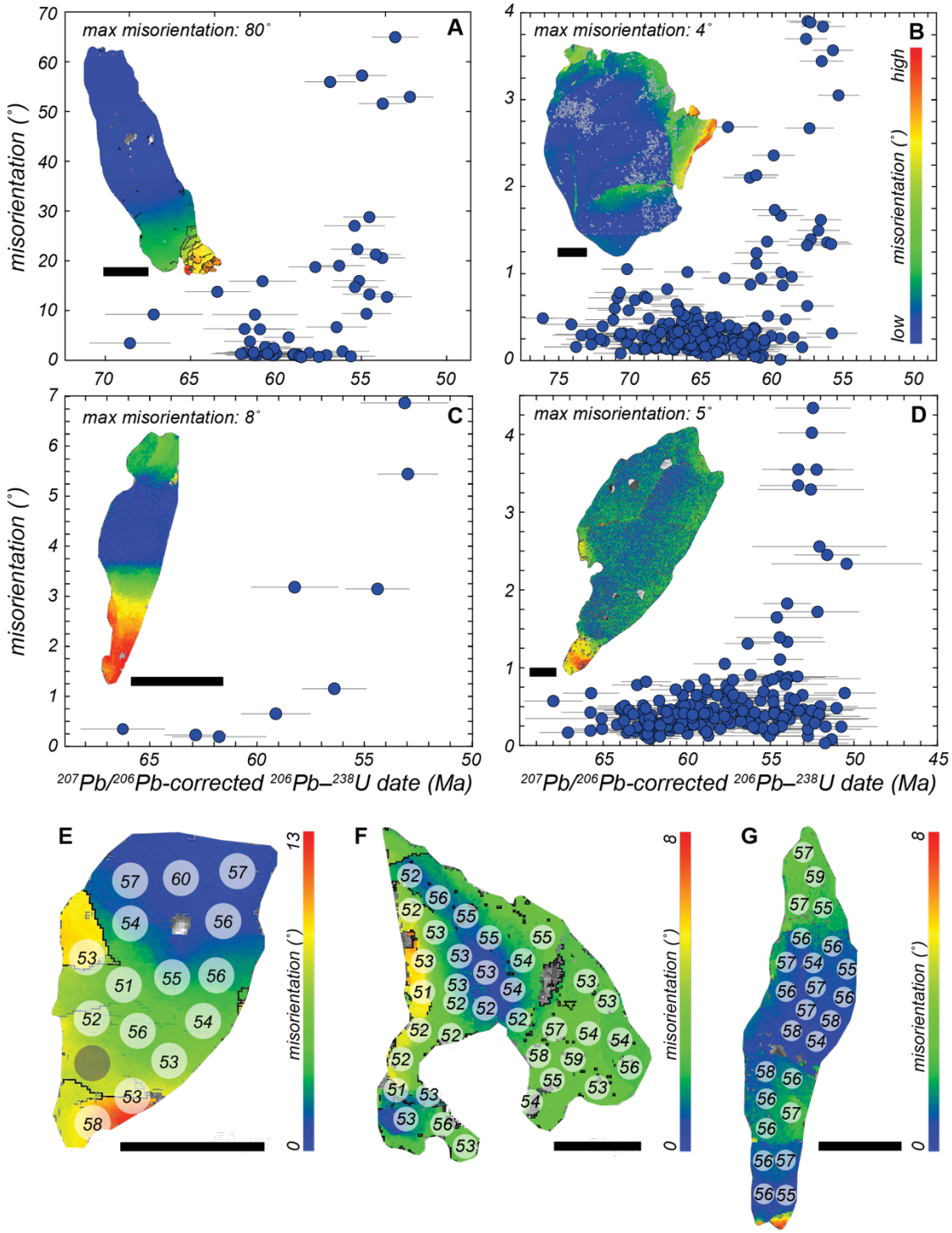

Figure 10. EBSD maps and dates for the seven bent titanite grains. (A–D) Date vs. misorientation plots and EBSD maps for the four bent grains wherein dates young with increasing lattice bending: (A) grain 7, (B) grain 3, (C) grain 2, and (D) grain 18. EBSD scale in (B) applies to all maps in (A–D). (E–F) EBSD maps and dates from the three bent grains that yield dates exclusively younger than 60 Ma. (E) grain 4, (F), grain 13, and (G) grain 17. White circles indicate location of laser ablation analyses with the corresponding date (Ma). Gray spot in (E) yielded a date with >10% in-run uncertainty that was removed from the final dataset. In-run date uncertainties are ~5% for grain 4 (E), ~4% for grain 13 (F), and ~4% for grain 17 (G). Black lines are low-angle subgrain boundaries. All black scale bars in (A–G) are 100 µm.

were bent during deformation. Most low-angle boundaries and bent portions of grains are found at grain tips (Fig. 10). Of the seven grains with subgrains, low-angle grain boundaries, and/or significant lattice bending, four display relationships between date and lattice bending (grains 2, 3, 7, 18; Fig. 10A–D) and three have no dates older than ~60 Ma (grains 4, 13, 17; Fig. 10 E–G).

6. Discussion

6.1. Volume diffusion of Pb and other trace elements

The erf^{-1} calculations suggest that the ~25 Myr spread in titanite U-Pb dates does not reflect a diffusive Pb-loss process at the scale of individual grains (Figs. 5, S2). The erf^{-1} of the normalized Pb concentration and distance from the edge of a grain are not correlated in any of the titanite grains (Figs. 5A–C, S2). The exception is grain 15, which has a correlation coefficient for Pb vs. distance of ~0.76 (Fig. S2O). However, in this grain, distance and Sr concentration are negatively correlated, whereas the opposite relationship is expected from volume diffusion (Fig. S2O). If Pb and Sr behave similarly with respect to intracrystalline diffusion in titanite (LaTourrette et al., 1996; Marsh and Smye, 2017), the contrasting Pb vs. Sr observations make it unlikely that Pb moved via volume diffusion in this grain. Further, none of the measured trace elements yield error function-like correlations between concentration and distance from the grain edge in any of the crystals (Figs. 5, S2). No element, Pb included, appears to have moved via volume diffusion at the grain scale; this requires that the titanite U-Pb dates are not cooling ages, even though the calculated Zr-in-titanite temperatures approached conditions at which Pb diffusion in titanite has been

observed in other rocks (e.g., Garber et al., 2017). We note that our approach precludes assessment of volume diffusion at lengthscales smaller than the analytical spot size (25 μm).

We tested for the effects of U zoning on volume diffusion of Pb by evaluating the relationship between date and U concentration in each titanite grain (Paul et al., 2019). It has been shown elsewhere that heterogeneous U distributions result in Pb concentration gradients that can drive volume diffusion, producing negative correlations between U-Pb date and U concentration (Paul et al., 2019). Except for three grains (grains 5, 7, and 13), U-Pb date and U are not negatively correlated in the Coast shear zone titanites (Figs. 5 M–O, S2), suggesting that U zonation did not obfuscate straightforward core–rim variations in U-Pb date. Rather than volume diffusion, the relationship between date and U concentration in three grains more likely reflects changing fluid composition during interface-coupled dissolution–reprecipitation (see section "Dissolution–reprecipitation" below).

6.2. Dates vs. Zr-in-ttn temperature, trace-element compositions

With the exception of La_N/Sm_N, there is no clear correlation between the titanite U-Pb dates and trace-element compositions or Zr-in-titanite temperature at the scale of the entire dataset (Fig. 6). This implies that the titanite did not simultaneously undergo the same (re)crystallization process, or such a process was variably recorded by individual grains. It is also worth noting that Zr-in-titanite temperatures >750 °C are restricted to dates younger than 65 Ma, and that Zr-in-titanite temperatures younger than 65 Ma are bimodal (~725 or ~770 °C). Although these temperatures cannot be resolved if the uncertainties on pressure, a_{TiO2}, and Zr concentration are all considered, the underlying bimodality in Zr concentrations can be differentiated outside of their analytical uncertainties (Fig. 6A). As such, the sample

effectively records two distinct Zr concentrations within and between different titanite grains that (re)crystallized at the same time. Such bimodality is typically ascribed to sector zoning in titanite (Paterson et al., 1989; Hayden et al., 2008; Walters and Kohn, 2017), yet none of the grains are obviously sector zoned (Fig. S5).

A closer look at the Zr-in-titanite data reveals multiple date vs. temperature patterns (Fig. 11) across individual grains. Date and temperature are correlated in nine grains; in these grains, temperature increases with younging date (Fig. 11A). We suggest the ~700 °C temperatures from spots yielding the oldest dates (~75–60 Ma) reflect the ambient temperature during initial crystallization, as the temperatures overlap prior constraints for the beginning of Coast shear zone deformation (Klepeis et al., 1998). It is expected that the ambient metamorphic temperature increased during intrusion of the Great Tonalite Sill at ~65 Ma; the higher temperatures from the younger (~60–50 Ma) spots likely record peak metamorphic conditions at this time. The correlation between date and temperature in these grains represent instances of dates and Zr contents reset at the same time, most likely by the same process.

The data patterns from the remaining grains are responsible for the bimodality of temperature data at the sample scale. Three grains yield the full sample range in dates, but the Zr-in titanite temperatures are consistently low (~700–730 °C; Fig 11B). An additional subset of grains yields a more restricted range of young dates (≤65 Ma) and the calculated temperatures are largely >750 °C (Fig. 11C). Two grains produce among the youngest dates in the dataset (<60 Ma) with all temperatures >750 °C (Fig. 11D). A single titanite crystal likewise exhibits only young dates (<60 Ma), but with <750 °C temperatures (Fig. 11E). Finally, U-Pb dates and Zr contents of the three remaining grains are uncorrelated and

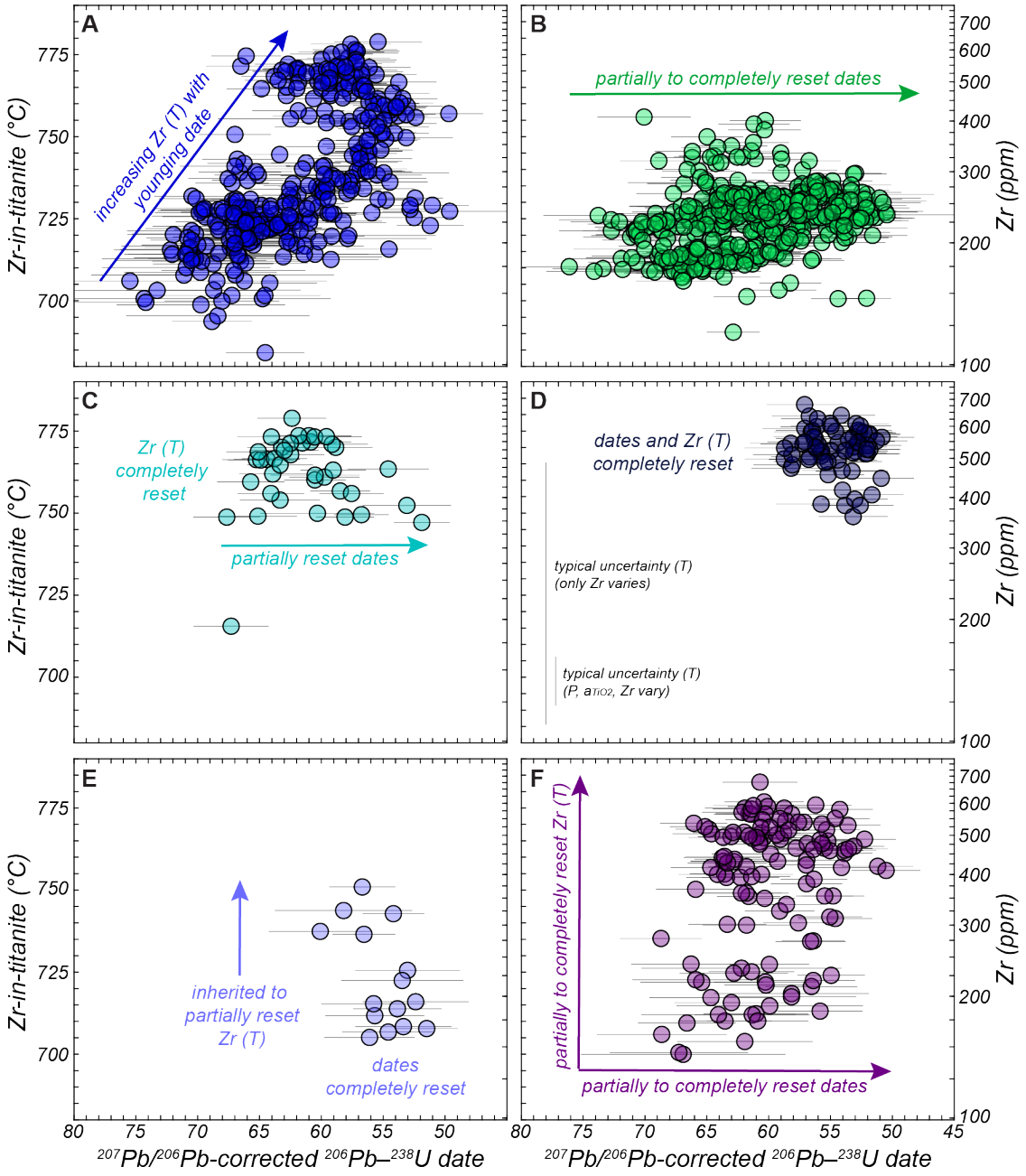

Figure 11. Date vs. Zr-in-titanite temperature for (A) titanite wherein Zr increases with younging date (9 grains), (B) titanite with Zr-in-titanite temperatures ~700–730 °C (3 grains), (C) grains with Zr-in-titanite temperatures ~750–775 °C (three grains), (D) bent titanite grains with <60 Ma dates and ~750–775 °C Zr-in-titanite temperatures (2 grains), (E) a single grain with <60 Ma dates and variable Zr contents, and (F) completely scattered dates and Zr-in-titanite temperatures from three grains. In aggregate, these six patterns have an apparently bimodal Zr-in-titanite temperatures at the scale of the entire dataset. Representative temperature uncertainties indicated in (D) apply to all plots.

encompass the entire date and temperature range of the dataset (Fig. 11F). These data demonstrate that U-Pb and Zr resetting was highly variable at the scale of individual grains. There are no consistencies among the microstructures, compositional zoning, or grain size within the above groupings of titanites (Table 1; Fig. S5), nor are they spatially related within the thin section (Fig. S6). These data imply that localized, grain-scale processes heterogeneously recrystallized the titanite at the scale of a single thin section and within single crystals, leading to the absence of clear sample-scale (or in some cases, even grain-scale) trends. In the following section, we explore these recrystallization processes as revealed by the relationships among dates, zoning, trace-element compositions, Zr-in-titanite temperatures, and microstructures.

6.3. Localized, grain-scale processes recorded by titanite U-Pb dates

6.3.1. Dissolution–reprecipitation

The zoning textures and the relationships between dates and trace-element concentrations suggest fluid-driven recrystallization affected all the titanite grains analyzed in this study. For example, fluid-driven recrystallization textures are ubiquitous in the chemical zoning of the analyzed titanite (Figs. 7–8, S5). Each of the twenty analyzed titanites preserves either lobate–cuspate rims and/or patchy zoning in at least one element (Figs. 7A, 8A, 9A, S5), although several grains have comparatively simple core–rim Ce zoning (e.g., Fig. 9A). The inward-penetrating, lobate–cuspate rims are diagnostic of interface-coupled dissolution–reprecipitation recrystallization, in which a fluid-driven reaction boundary propagates into the crystal along grain rims, cracks, twin planes, or around inclusions (Geissler et al., 2003, 2007; Holder and Hacker, 2019; Putnis et al., 2005; Putnis, 2009; Fig. 1E). However, even

the titanite grains that lack these features may have been affected by fluids. Intragrain interfaces become lobate–cuspate when the migrating interface becomes pinned by impurities such as inclusions (e.g., Ruiz-Agudo and Putnis, 2012); without these impurities, the reaction boundary may be near-planar and produce more geometrically straightforward core–rim relationships. Given that the grains with simple core–rim Ce zoning also have lobate–cuspate or patchy domains in the Al maps (Fig. S5G, L, N, P), we suggest that all the titanite rims record the propagation of dissolution–reprecipitation reactions.

In addition to the chemical zoning textures, the absence of systematic, reproducible variations (Fig. 6) among the dates and trace-element compositions can also be explained by the effects of dissolution–reprecipitation. The precise trace elements that correlate positively or negatively with date differ from grain to grain (Table 1; Figs. 8B and C, 9B and C), and some grains yield few or no clear relationships with any trace elements (Figs. 7B and C, Table 1). For example, dates are roughly correlated with all the REEs in ten of the titanite crystals, with Zr content in nine grains, and with Al content in three grains (Table 1; Figs. 7B and C, 8B and C, 9B and C). During dissolution–reprecipitation, the fluid composition at the reaction front continually evolves as the precursor grain dissolves and reprecipitates, potentially resulting in evolving fluid compositions at the individual grain scale (Lippmann, 1980; Putnis and Mezger, 2004; Putnis et al., 2005; Putnis, 2009). If the local fluid composition controls the composition of the reprecipitated phase(s), and if the local fluid composition evolves as each titanite dissolution–reprecipitation reaction proceeds, the extent to which U-Pb dates and trace-element contents are reset may differ within and among individual grains (Fig. 1E; Geisler, 2007; Hacker et al., 2015; Holder and Hacker, 2019; Putnis and Mezger, 2004; Putnis et al., 2005; Putnis, 2009). Alternatively, multiple fluids of

different composition may have been present at the sample scale if they were sourced from the varying lithologies of the western metamorphic belt and the Great Tonalite Sill (e.g., Klepeis et al., 1998) and remained immiscible during metamorphism (Vard and Williams-jones, 1993; Romer et al., 2005; Heinrich, 2007). Regardless of their scale or precise mechanism of their production, variable fluid compositions could explain the nonsystematic variations among date and trace-element concentrations within the dataset.

The composition of the fluid that drove titanite dissolution–reprecipitation must account for the mobilization of Zr, REEs, and Pb. REEs and high field strength elements (HFSE) like Zr are more soluble in aqueous solutions that contain fluorine (Keppler, 1993; Pan and Fleet, 1996; Hetherington et al., 2010; Rapp et al., 2010; Migdisov et al., 2011). The increasing La_N/Sm_N with younging date (Fig. 6B) and with increasing Zr-in-titanite temperature (Fig. S7) further supports an F-bearing fluid, as LREE-F+ aqueous compounds stabilize with increasing temperature (Migdisov et al., 2009). Carbonate-rich fluids also promote mobilization of the HFSE and REEs (Pouchon et al., 2001; Curti and Hummel, 1999), but the REEs complex more easily with carbonate anions than the HFSE (Chakhmouradian and Williams, 2004), which is contrary to the mobilization of both the REEs and Zr that we observed. Further, high fluid X_{CO2} in calcsilicates stabilizes rutile over titanite (Frost et al., 2000; Chakhmouradian and Williams, 2004) and high Ca contents favor precipitation of fluorite (Salvi et al., 2000), but rutile and fluorite are absent from the studied sample. The absence of fluid inclusions in the analyzed titanite crystals preclude directly constraining the composition of the fluid(s) that recrystallized the grains. Further, to our knowledge, there are no experimental data on the fluid compositions associated with titanite dissolution–reprecipitation. Nevertheless, the data broadly support a metamorphic fluid that

was likely an F-bearing, Ca-poor, H_2O-dominant CO_2-subservient mixture in which the relative proportions of F, H_2O, and CO_2 continually evolved as a result of dissolution–reprecipitation, producing variable relationships between dates and trace-element concentrations within and among grains. Such a mixed H_2O–CO_2 metamorphic fluid is further supported by the presence of hydrous (amphibole, clinozoisite, biotite) and carbonate (calcite) minerals in the studied calcsilicate (Fig. 3).

The reason for the variable Pb removal from the grains is less clear. One potential explanation is that radiogenic Pb did not have a consistent oxidation state during recrystallization. For example, if radiogenic Pb was tetravalent, it would have behaved like a HFSE and have been relatively fluid immobile (Frei et al., 1997; Kramers et al., 2009) except in F-rich fluids (see above, Keppler, 1993; Pan and Fleet, 1996; Jiang et al., 2005; Hetherington et al., 2010; Rapp et al., 2010; Migdisov et al., 2011). On the other hand, if Pb was dominantly 2+, it would have behaved like a large-ion-lithophile element and be more soluble in a range of fluid compositions (Kramers et al., 2009). Direct constraints on the radiogenic Pb oxidation state in titanite, however, suggest that it is uniformly divalent (Syverson et al., 2019), making this explanation less plausible. Alternatively, radiation damage accumulation can promote recrystallization by a diffusion-reaction process (Rizvanova et al., 2000; Davis and Krogh, 2000; Geisler et al., 2007), and variable degrees of radiation damage among the analyzed grains might have driven differential removal of Pb. This hypothesis is permissible if some of the titanite grains are detrital (see discussion below), but if the oldest titanite date reflects the onset of metamorphic titanite crystallization, the temperatures would have been too high to permit significant radiation damage accumulation (c.f., Coyle and Wagner, 1998). Instead, we suggest that the

decoupled dates and trace-element contents may reflect the remobilization but not removal of radiogenic Pb during dissolution–reprecipitation, giving host to "parentless daughter", as has been proposed for some fluid-affected zircon (Hoskin and Black, 2000; Carson et al., 2002; Kusiak et al., 2013; Weinberg et al., 2020). However, why this phenomenon occurred in some grains and not others cannot be resolved with our data, but it may be linked to the likely variable fluid compositions at the thin-section scale as discussed above.

6.3.2. Deformation

Four titanite grains have ~4–80° of lattice misorientation with respect to a central reference point ("bent grains"), low-angle boundaries at grain tips, and U-Pb dates that span the entire ~75–50 Ma range of the dataset (Table 1; Figs. 10A–D). Dates young with increasing lattice bending in these crystals, with the youngest dates (~60–50 Ma) in the rotated grain tips and subgrains (Fig. 10A–D). This relationship suggests that the dates from bent grain tips record the timing of crystal-plastic deformation. Three additional titanite grains display ~8–12 ° of total intragrain misorientation, have low-angle grain boundaries, and yield no U-Pb dates older than ~60 Ma (Table 1; Fig. 10E–G). Further, it is only in bent grains where this more restricted range in dates is observed. This implies that the U-Pb dates from these grains were completely reset as a result of the lattice bending that accommodated deformation.

We note that the evidence for dissolution–reprecipitation makes it difficult to unequivocally interpret that the ~60–50 Ma dates from the bent grains record the timing of lattice bending (deformation) rather than fluid-mediated recrystallization. Two of the bent grains (grains 3 and 18; Fig. 10B, D) have ~60–50 Ma dates in unbent parts of the grain; these young dates likely reflect the timing of interface-coupled dissolution–reprecipitation,

rather than lattice bending. Additionally, U-Pb dates are positively or negatively correlated with some trace-elements in two of the bent grains (grains 2 and 18; Figs. S5B, S5R), consistent with date resetting by interface-coupled dissolution–reprecipitation rather than lattice bending. Nevertheless, there is always a relationship between microstructure and date in bent grains: dates either young with increasing misorientation or all dates are younger than 60 Ma (Fig. 10). Despite the evidence for dissolution–reprecipitation, these consistent patterns between dates and microstructure suggests that lattice bending played a role in resetting the U-Pb dates in the bent grains.

The gradational nature of lattice bending and the low-angle subgrain boundaries (Fig. 10) implies that these deformation microstructures formed from the production and motion of dislocations within the titanite. If these are dislocation-related microstructures, and the development of these microstructures played a role in resetting the U-Pb dates, this suggests that dislocations and low-angle boundaries facilitated Pb loss from the titanite. However, we cannot unequivocally invoke the role of dislocations in resetting U-Pb dates given the analytical scale of the dataset. Further, the only existing nanoscale observations of dislocations in titanite show no change in Pb concentration within or across low-angle grain boundaries (Kirkland et al., 2018), implying that in some instances, dislocation-facilitated diffusion (i.e., pipe diffusion and Cottrell Atmospheres) may not affect Pb. We suggest that deformed titanite whose microstructures yield young dates are promising candidates for future studies aimed at constraining the mechanisms and complexities of dislocation facilitated Pb loss in titanite.

6.3.3. Coupled deformation and dissolution–reprecipitation

As discussed above, the superposition of lattice bending and low-angle boundaries on fluid-related zoning makes it difficult to differentiate the roles that deformation and fluid-mediated recrystallization played in resetting the titanite U-Pb dates. In addition, the trace-element compositions of the three grains whose dates we interpret to have been completely reset by deformation (Fig. 10E–G) overlap the range of compositions from the undeformed, fluid-recrystallized rims (Fig. S8). This suggests that the trace-element signatures of the three deformed, completely reset grains were affected by the same fluids that produced the lobate-cuspate rims in other grains. Further, it is only in the bent grains that the trace-element contents appear to be reset across the entire grain and not just at grain margins. These two observations imply that lattice bending and dissolution–reprecipitation were coupled processes that together worked to reset dates and trace-element signatures in the bent grains. We suggest that microstructures provided fast diffusion pathways that facilitated isotopic and trace-element exchange between the fluid and grain interiors in the bent grains, similar to the role porosity has been suggested to play in dissolution–reprecipitation reactions (Putnis, 2009). The resetting of U-Pb dates by lattice bending, therefore, was likely never independent of fluid alteration in these titanite.

6.4. Timing of deformation and dissolution–reprecipitation

Dates from the bent grain tips, subgrains, and crystals we interpret to have been completely reset from deformation range from ~60–50 Ma (Fig. 12A). The weighted mean of these dates is 55 ± 1 Ma (MSWD = 2.6; Fig. 12A). These data are consistent with either ~10 Myr of continuous deformation or a range of partial to complete resetting of dates during a

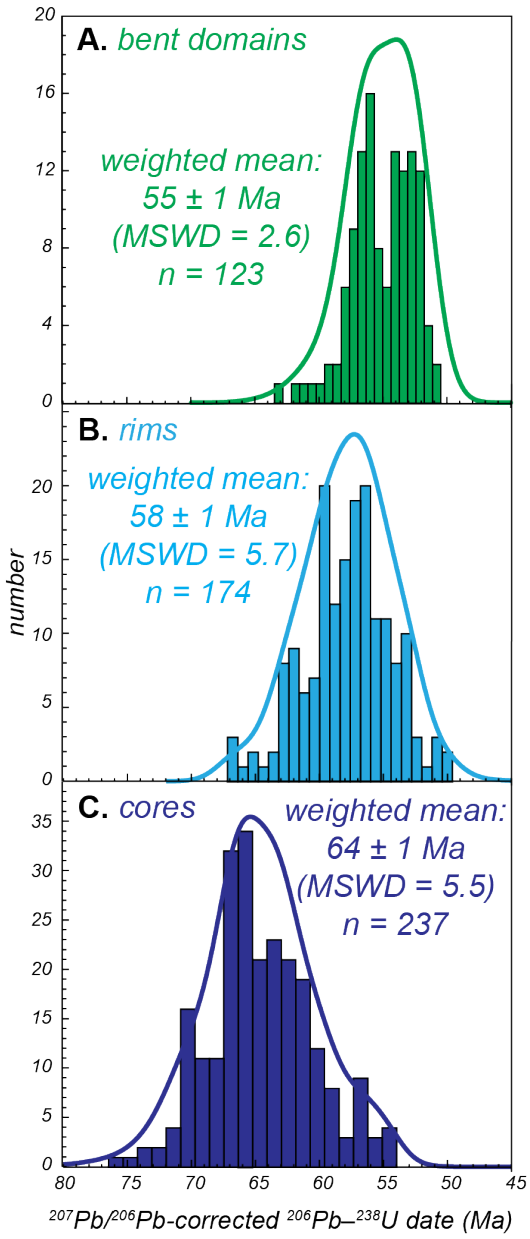

Figure 12. Probability density functions, histograms, and weighted mean values for (A) bent domains, (B) fluid recrystallized rims, and (C) grain cores. Dates included in (A) comprise dates from bent grain tips in grains 2, 3, 7, and 18, as well as all dates from grains 4, 13, and 17 (see Table S2). Dates included in (B) and (C) are rim and core values from the 11 grains that yielded increasing Ce concentration with younging date (see Tables 1 and S2).

discrete deformation event. Ten million years of deformation would be compatible with previous interpretations that the Coast shear zone was active from ~65–55 Ma (Klepeis et al., 1998). However, without more detailed work on the effects of crystal-plastic deformation on elemental mobility in titanite, it is not possible to differentiate between a protracted deformation history or partial to complete resetting of dates during deformation. We therefore suggest that these titanite were almost certainly deforming around 55 Ma, and that deformation may have begun as early as 60 Ma and ended as late as 50 Ma.

We constrain the timing of interface-coupled dissolution–reprecipitation using the dates from the fluid-recrystallized rims wherein dates young with increasing Ce concentration (11 grains, see Table 1). The consistent relationship between dates and Ce concentrations in these grains suggests that these rim dates accurately reflect the timing of fluid mediated recrystallization. Similar to the bent titanite, dates from the fluid recrystallized rims largely range from ~60–50 Ma (Fig. 12B). The weighted mean of dates from the recrystallized rims is 58 ± 1 Ma (MSWD of 5.7; Fig. 12B). The spread in dates and high MSWD imply either ~10 Myr of dissolution–reprecipitation reactions, or partial to complete resetting of the U-Pb system during a discrete event (e.g., Kelly et al., 2012). It is not possible to discriminate between these two interpretations; we conservatively suggest that 60 Ma is the maximum onset of titanite dissolution–reprecipitation, that these reactions were likely ongoing at 58 Ma, and that fluid mediated recrystallization ceased by 50 Ma.

The timing of initial titanite crystallization is constrained by dates from grain cores wherein dates young with increasing Ce concentration (11 grains, see Table 1). The consistent relationships between dates and Ce concentrations in these grains suggest that dates from these cores were least affected by fluid mediated recrystallization and are most

likely to faithfully record the timing of crystallization. Dates in the cores of the fluid-recrystallized titanite range from ~75–60 Ma with a weighted mean of 64 Ma (MSWD = 5.5; Fig. 12C). The spread in dates and large MSWD suggests either 15 Myr of continuous titanite crystallization (e.g., Stearns et al., 2016), partial fluid-mediated resetting of titanite that crystallized at 75 Ma, or detrital cores with crystallization ages significantly older than 75 Ma that were partially reset at ~60–50 Ma. It is not possible to differentiate among these interpretations of the oldest titanite dates given the current data. We therefore suggest that titanite neocrystallization ceased by 60 Ma.

6.5 Implications for titanite petrochronology

The twenty analyzed titanite grains and their associated U-Pb dates, zoning, trace-element composition, and microstructures preserve evidence for simultaneous interface-coupled dissolution–reprecipitation and lattice bending within a single sample. These data highlight the range of processes that can be recorded by titanite grains subjected to the same metamorphic and deformation history at the scale of a single thin section. The workflow presented herein demonstrates the potential complexities in titanite U-Pb dates, and how careful comparison of date with distance from the grain edge, trace-element composition, zoning, and microstructure makes it possible to link those dates to multiple, simultaneous processes affecting titanite chemistry. Our efforts further show that sample-scale date and chemical trends may be misleading: our full titanite dataset shows that there are very few robust sample-scale trends despite the prevalence of clear correlations within individual grains, and indicate chemical heterogeneity on sub-grain, grain, and thin-section scales that might not be evident without detailed, grain-scale analyses.

The highly variable, unsystematic coupling-decoupling of U-Pb dates and trace-element contents observed in the titanite grains in this study, and of titanite and other accessory minerals (zircon, monazite) elsewhere in the literature, is an increasingly recognized phenomenon that apparently results from some combination of fluid alteration, volume diffusion of U and/or Pb, and deformation (Kunz et al., 2018; Garber, Smye, et al., 2020; Weinberg et al., 2020; Gordon et al., 2021). The microtextural evidence of dissolution–reprecipitation presented here implies that U-Pb date and trace-element decoupling in the Coast shear zone titanite was driven by differences in the chemical potentials of trace elements and Pb between the titanite and the metamorphic fluid (Putnis and Mezger, 2004; Putnis, 2005, 2009), and that these controls never achieved equilibrium on the thin-section scale.

Although many advances have been made in the past decade (Moser et al., 2009; MacDonald et al., 2013; Bonamici et al., 2015; Piazolo et al., 2016; Kovaleva et al., 2017; Langone et al., 2017; Papapavlou et al., 2018; Moore et al., 2020; Fougerouse et al., 2021; Gordon et al., 2021), directly dating crystal-plastic deformation, fluid flow, and other processes associated with slip along ductile shear zones remains challenging. Titanite U-Pb dates are correlated with deformation microstructures in our dataset—bent grains, bent grain tips, and subgrains have the youngest dates—but the evidence for dissolution–reprecipitation makes it difficult to specify an unequivocal deformation age. Still, these data contribute to a growing body of work demonstrating that titanite is a promising candidate to directly date crystal-plastic deformation (Bonamici et al., 2015; Papapavlou et al., 2017; Gordon et al., 2021) and fluid flow (Garber et al., 2017; Holder and Hacker, 2019).

Zr-in-titanite data (this study) and prior constraints on metamorphic temperatures of Coast shear zone metapelites (Klepeis et al., 1998) suggest that the analyzed Coast shear zone titanite resided at >700 °C for ~25 Myr, yet the crystals show no conclusive evidence for volume diffusion of Pb at the titanite grain scale. Although we cannot rule out volume diffusion at lengthscales less than 25 μm, our results are nonetheless compatible with the previously published conclusions that Pb volume diffusion in titanite at <750 °C may be negligible (Stearns et al., 2016; Kohn, 2017; Holder et al., 2019). Our data support the notion that titanite U-Pb dates should not be interpreted as cooling ages in the absence of spatial information supporting that contention.

6.6 Implications for the tectonometamorphic history of the Coast shear zone

Coast shear zone titanite U-Pb dates in combination with trace-element concentrations, Zr-in-titanite temperatures, zoning, and microstructures suggest that intrusion of the Great Tonalite Sill caused simultaneous heating, fluid alteration and deformation of the country rocks. The fluid-recrystallized titanite rims with elevated Zr and REE contents and their associated ~60–50 Ma dates in the studied sample (Figs. 7–9, 11A, 12B) likely record heating and igneous or metamorphic fluid influx associated with these intrusions (Hayden et al., 2008), although these data may alternatively reflect the combined effects of exhumation and heating during intrusion of the Great Tonalite Sill (e.g., Wood et al., 1991; Klepeis et al., 1998). The increase in temperature at ~60 Ma may reflect advective fluid pulses or conductive heating from the Sill, but the precise cause is unknown.

Zircon crystallization ages from deformed and undeformed intrusions suggest that the Coast shear zone near Portland Inlet was active from ~65–55 Ma but do not preclude

deformation in the westernmost Coast shear zone, from which the sample analyzed herein is from, after this time (Klepeis et al., 1998). U-Pb dates from the bent titanite grains and grain tips are consistently ~60–50 Ma (Figs. 10, 12), implying that these data record titanite deformation during Coast shear zone slip. If this range reflects 10 Myr of continuous deformation, this suggests that the metasedimentary rocks west of the Great Tonalite Sill (Fig. 2B) deformed as late as ~50 Ma, 5 Myr after the end of Great Tonalite Sill magmatism and 5 Myr later than previously suggested (Klepeis et al., 1998). This interpretation is consistent with the conclusion that the youngest phase of Coast shear zone deformation was concentrated in a ~1–2 km zone west of the Sill (Klepeis et al., 1998). Alternatively, our interpretation that the titanite were likely deforming at ~55 Ma (see section "Timing of deformation and dissolution–reprecipitation" above) is consistent with the notion that ductile deformation along the Coast shear zone ended around this time (Klepeis et al., 1998).

7. Conclusions

Integrated U-Pb, trace-element, zoning, and microstructural data from twenty titanite crystals deformed in the Coast shear zone demonstrate that the grains were modified by two metamorphic processes—interface-coupled dissolution-reprecipitation and lattice bending that accommodated deformation—at the scale of a single thin section. Dates from lobate–cuspate rims, bent grains and grain tips, and subgrains range from ~60–50 Ma, suggesting up to 10 Myr of fluid mediated recrystallization and date resetting via lattice bending. These data are consistent with the onset of concomitant deformation, fluid-flow, and heating and/or exhumation from intrusion of the Great Tonalite Sill and slip along the Coast shear zone by

~60 Ma. Deformation and fluid-flow within the shear zone may have been ongoing as late as ~50 Ma.

Extremely variable correlations between titanite U-Pb dates and trace-elements imply thin section- or even grain-scale differences in the composition of the fluid driving dissolution-reprecipitation. The decoupling of U-Pb dates and trace elements in some of the unbent, fluid-recrystallized titanite further suggests that the relative compatibilities of Pb and trace elements in a mixed H_2O-CO_2 fluid drove differential date–composition decoupling during dissolution–reprecipitation. Deformation microstructures are superimposed on fluid-recrystallized rims, implying that these two processes were coupled at the grain scale and that microstructures may have provided pathways for fluids to reach the reaction front. Although the evidence for fluids and deformation in the same thin section precludes an unambiguous interpretation of the deformation age, titanite remains a promising candidate to directly date both crystal-plastic deformation and fluid flow.

CHAPTER 2: TITANITE DEFORMATION CHRONOMETRY REVEALS MIOCENE AMPHIBOLITE-FACIES DEFORMATION ALONG THE ALPINE FAULT SYSTEM, SOUTH ISLAND, NEW ZEALAND

1. Introduction

Ductile shear zones commonly preserve superimposed fabrics that represent deformation events with different kinematics and/or conditions (i.e., T, P, stress, strain rate, fluid content and composition) of deformation. These spatially coincident fabrics evolve during a single or temporally separate deformation events. Decoding polyphase deformation in ductile shear zones, including dating when the fabrics formed and whether they represent continuous or temporally distinct events, is paramount for elucidating their tectonic significance. Thermochronometers with different temperature sensitivities can be used to constrain the timing of polyphase deformation during cooling (e.g., Jacobson et al., 2007), minerals that define fabrics that formed at different P-T-fluid conditions can be dated to determine the timing of synkinematic growth, or cross-cutting relationships may help define overlapping deformation events. These approaches, however, are less useful where superimposed fabrics formed under similar conditions or where cross-cutting relationships are absent. In these instances, a direct means to date deformation is required.

Deformation chronometry—the interpretation of dates in their grain-scale microstructural context (e.g., Piazolo et al., 2012, 2016; Odlum and Stockli, 2020; Odlum et al., 2022; Gordon et al., 2021; Moser et al., 2022)—is one potential tool to directly constrain the timing of temporally distinct, spatially coincident phases of deformation. Prior work on deformed zircon (Piazolo et al., 2012, 2016), titanite (Gordon et al., 2021; Moser et al., 2022), and apatite (Odlum et al., 2022; Odlum and Stockli, 2020) demonstrates partial to

complete radiogenic Pb loss as a result of lattice bending, subgrain development, and neoblastic grain growth. When minerals are deformed, their U-Pb dates may directly date the timing of deformation when interpreted in their microstructural context (Gordon et al., 2021; Moser et al., 2022; Odlum et al., 2022; Odlum and Stockli, 2020; Piazolo et al., 2012, 2016). Several aspects of titanite make it one of the most-useful high-temperature (i.e., >500 °C) deformation chronometers. It has a relatively high closure temperature (>750 °C; Garber et al., 2017; Hartnady et al., 2019; Holder et al., 2019; Kohn and Corrie, 2011; Moser et al., 2022; Spencer et al., 2013; Stearns et al., 2016), is prevalent in igneous and metamorphic rocks with diverse bulk compositions (e.g., Frost et al., 2000), incorporates a variety of trace elements that reflect ambient metamorphic conditions (Garber et al., 2017; Hayden et al., 2008), and can form grains several hundreds of microns long (e.g., Spencer et al., 2013; Garber et al., 2017; Holder et al., 2019). Previous work that directly links titanite U-Pb dates to the timing of deformation, however, focused on shear zones with a single phase of deformation where the tectonic context is well established (Gordon et al., 2021; Moser et al., 2022). The response of titanite to protracted, polyphase deformation histories has not been studied and is thus unclear.

The Anita Shear Zone (ASZ; Fig. 1) is a polyphase, ductile shear zone that parallels the west coast of northern Fiordland, South Island, New Zealand (Fig. 1; Hill, 1995a, 1995b; Klepeis et al., 1999; Czertowicz et al., 2016a). The ASZ preserves at least three phases of superimposed, amphibolite- to greenschist-facies deformation that have variably been attributed to extensional orogenic collapse of the Fiordland sector of the Median Batholith and/or Cretaceous rifting of Zealandia from Gondwana (Hill, 1995a, 1995b;

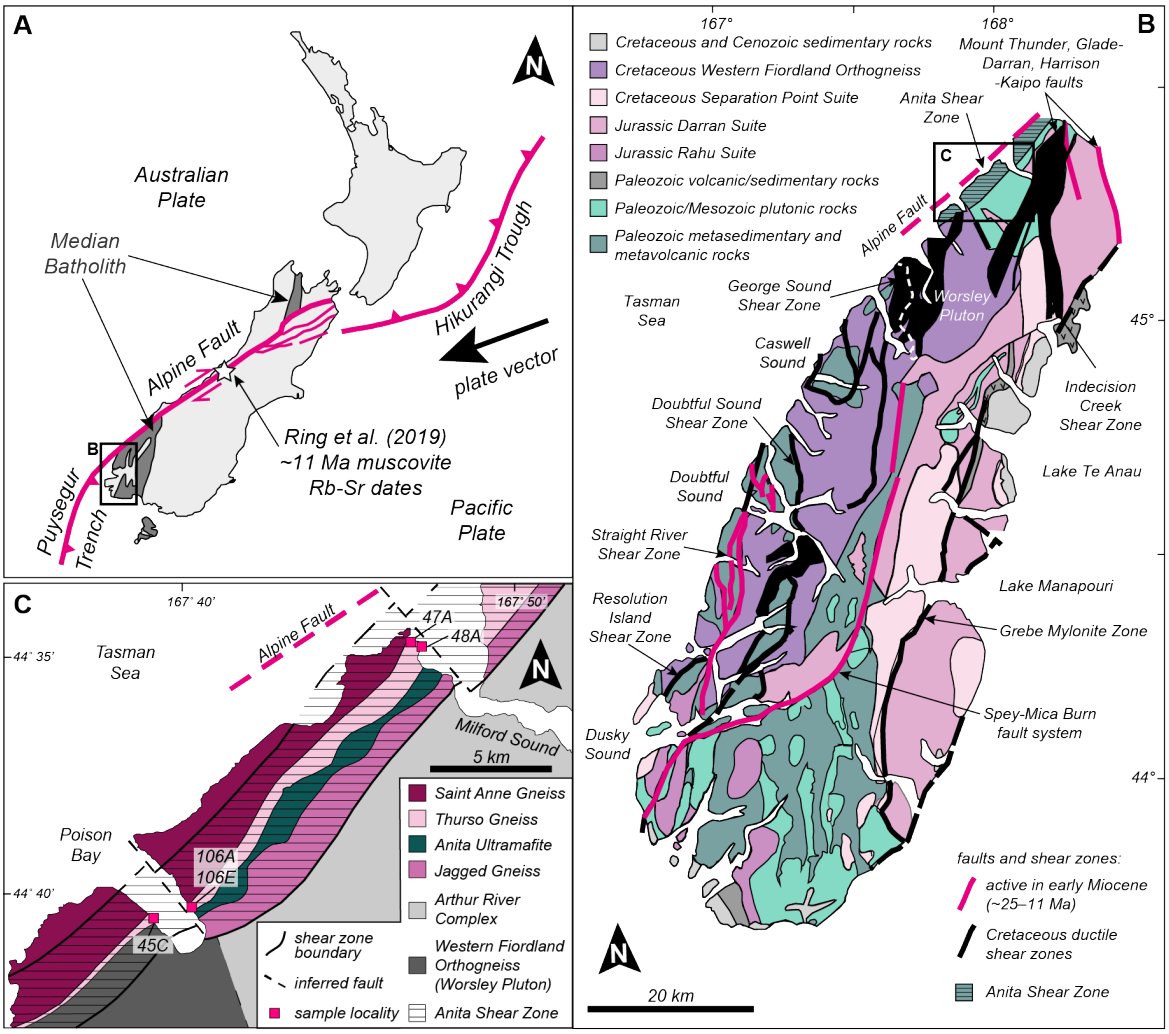

Figure 1. Tectonic context and geologic maps of Fiordland and the Anita Shear Zone. (A) Modern tectonic setting of New Zealand showing location of Median Batholith units and Fiordland (inset B) with respect to the Alpine Fault and the Puysegur Trench. Arrow shows modern motion of the Pacific Plate with respect to the Australian Plate (after DeMets et al., 2010). (B) Geologic map of Fiordland showing major units of the Median Batholith and significant faults and shear zones active in the Cretaceous or Miocene (after Klepeis et al., 2007; Allibone and Tulloch 2008; Schwartz et al., 2017). (C) Geologic map of the Anita Shear Zone (after Hill, 1995a, Klepeis et al., 1999, and Czertowicz et al., 2016b).

Klepeis et al., 1999), Cretaceous transpression during oblique convergence within the Median Batholith (Czertowicz et al., 2016a), a Late Cretaceous precursor to the Alpine Fault zone (Blattner, 1991), transpression as a result of tectonic reorganization and/or oblique microplate convergence in the mid-Cenozoic (Klepeis et al., 1999), and a mid-to deep crustal record of transpression along the broader Alpine Fault system in the Miocene (Claypool et al., 2002; Klepeis et al., 1999). The predominant fabric is an amphibolite-facies, subvertical, NE-striking foliation with a moderately to gently NE/SW plunging lineation interpreted to have formed during dextral transpression (Klepeis et al., 1999). The tectonic significance of the ASZ, including its potential to preserve a mid- to deep-crustal Miocene window into the evolution of the Pacific–Australian Plate boundary, relies on the age of these subvertical, amphibolite-facies fabrics. However, limited existing geochronology only broadly constrains the timing of this transpressive, amphibolite-facies deformation (Claypool et al., 2002; Czertowicz et al., 2016a) to between the Early Cretaceous and mid-Miocene (Klepeis et al., 1999).

This contribution integrates titanite U-Pb dates, microstructures, trace-element compositions, and zoning (i.e., titanite deformation chronometry) to determine the timing of amphibolite-facies deformation along the ASZ. We further relate the newly determined deformation age to the mid- to deep-crustal record of the evolution of the Pacific-Australian Plate boundary from the Cretaceous to the Miocene. The dataset herein demonstrates the applicability of titanite deformation chronometry to shear zones with protracted deformation histories and whose timing of deformation is enigmatic.

2. Geologic background

2.1 Cretaceous–Miocene evolution of Fiordland and the Pacific-Australian Plate boundary

The Median Batholith, New Zealand, comprises ~10,000 km^2 of metaplutonic rocks that represent the Devonian to Early Cretaceous magmatic arc along the paleo-Pacific, east Gondwanan margin (Fig. 1; Mortimer, 1999). Orthogneisses and metamorphic country rock in western Fiordland preserve final emplacement of Median Batholith plutons from ~129–115 Ma, which culminated in crustal thickening, heating, and granulite-facies metamorphism that lasted until ~105 Ma (Buriticá et al., 2019; J. A. Hollis et al., 2003, 2004; Klepeis et al., 2022; Mattinson et al., 1986; Ringwood et al., 2021; Schwartz et al., 2016; Stowell et al., 2014; Tulloch and Kimbrough, 2003). Several mid- to lower-crustal transpressional shear zones were active during these end stages of Median Batholith construction and oblique convergence along the plate boundary, including the George Sound, the Grebe-Indecision Creek, and the Straight River shear zones (Fig. 1; Allibone and Tulloch, 2008; Buriticá et al., 2019; Klepeis and Clarke, 2004; Klepeis et al., 2022; Marcotte et al., 2005; Scott et al., 2011). Subduction-related plutonism ended around ~110 Ma, with extensional collapse of the lower crust initiating at ~108–106 Ma (Schwartz et al., 2016, 2017). Multiple ductile, amphibolite-facies shear zones accommodated extension in the mid- to lower-Fiordland arc crust, including the Doubtful Sound and Resolution Island shear zones (Fig. 1; Allibone et al., 2009; Betka and Klepeis, 2013; Gibson, 1988; Gibson and Ireland, 1995; Klepeis et al., 2007, 2016; Oliver, 1980; Schwartz et al., 2016). Zealandia had rifted from Gondwana by ~83 Ma, when seafloor spreading began along the Tasman Ridge (Gaina et al., 1998). Seafloor spreading in the Tasman sea continued until ~52–47 Ma

(Lawver and Gahagan, 1994) and was followed by the initiation of the modern Pacific–Australian plate boundary at ~45 Ma (Sutherland, 1995).

Fiordland remained a rifted margin until ~25 Ma (Klepeis et al., 2019), when the Pacific Plate motion changed and the Australian/Pacific plate boundary reorganized to accommodate convergence (Jicha et al., 2018; Lebrun et al., 2003; Sutherland et al., 2006). At present, the tectonic setting of the Fiordland sector of the Median Batholith is complex; it lies in the upper plate of the Puysegur subduction zone (e.g., Sutherland et al., 2009; Klepeis et al., 2019) with the southernmost Alpine Fault offshore to the northwest (Fig. 1; Lebrun et al., 2000; Barnes et al., 2005). The modern, oblique convergence of the Pacific and Australian tectonic plates is accommodated by dextral motion along the Alpine Fault zone (Fig. 1A; Norris and Cooper, 2000; Demets et al., 2010) and subduction along the Puysegur trench (Fig. 1A; DeMets et al., 1994; Collot et al., 1995). The age of synkinematic lamprophyre dikes along the SE Alpine Fault (Cooper, 1987) and the presence of a through-going, continental rift system in the Oligocene (Kamp, 1986) indicate that strike-slip motion began on the Alpine Fault at ~25 Ma (Cooper, 1987). Initiation of subduction along the Puysegur trench may have begun as early as ~25 Ma (Klepeis et al., 2019; Lebrun et al., 2003) and was ongoing by ~16–8 Ma (Sutherland et al., 2006).

Potassium feldspar $^{40}Ar/^{39}Ar$ dates from dextral shear zones in central Fiordland indicate that mid- to upper-crustal faults accommodated transpression from ~25–10 Ma, approximately contemporaneous with the initiation of the Alpine Fault zone and subduction along the Puysegur trench (Fig. 1B; Klepeis et al., 2019b). Low-temperature thermochronometers, including zircon and apatite fission track and (U-Th)/He dates reveal a phase of rapid cooling that began in southwest Fiordland at ~25–15 Ma (Sutherland et al.,

2009). The timing of rapid cooling becomes younger towards northern Fiordland, with the onset of cooling at ~10 Ma in the proximity of Milford Sound and the ASZ. This cooling is attributed to northeastward migration of the leading edge of the Australian slab and associated exhumation that resulted from subduction initiation (Sutherland et al., 2009). Convergence rates increased through the Miocene, concomitant with progressive development of the Puysegur trench (Sutherland et al., 2009).

The mid- to deep-crustal record of the Miocene evolution of the Australian–Pacific Plate boundary is limited. Constraints on the evolution of the plate boundary along the southernmost Alpine Fault and the Puysegur Trench come from plate reconstructions (Lebrun et al., 2003), offshore seismic data (Barnes et al., 2005; Lebrun et al., 2000; Sutherland et al., 2006), kinematic data from mid- to upper-crustal brittle faults (Klepeis et al., 2019), and mid- to low-temperature thermochronology (Claypool et al., 2002; Klepeis et al., 2019; Sutherland et al., 2009). Similarly, farther to northeast along the central Alpine Fault, much is understood about the upper-crustal deformation record and the low-temperature cooling and exhumation history of the Southern Alps (Adams, 1981; Batt et al., 2000; Boulton et al., 2012; Kamp et al., 1989; Little et al., 2005; Michailos et al., 2020; Ring and Bernet, 2010; Sutherland et al., 2012; Tippett and Kamp, 1993; Toy et al., 2015), but there are few data that bear on the timing and broader record of high-temperature, mid- to deep-crustal deformation along the plate boundary (e.g., Ring et al., 2019). The mid- to deep-crustal record of Alpine Fault mylonitization is primarily preserved within the Alpine Schist, a metamorphosed accretionary wedge that formed along the paleo-Pacific eastern Gondwana margin in the Mesozoic (Grapes and Watanabe, 1992; Little et al., 2002; Norris and Cooper, 2003). Despite the Alpine Fault-related mylonitization of the Alpine Schist,

most high-temperature mineral assemblages and geochronometers in the Alpine Schist preserve the Cretaceous record of metamorphism that is broadly related to the rifting of Zealandia from east Gondwana (Briggs et al., 2018; Chamberlain et al., 1995; Cooper and Ireland, 2013; Grapes, 1995; Grapes and Watanabe, 1992; Mortimer and Cooper, 2004; Scott et al., 2015; Vry et al., 2004). The exception is a single study by Ring et al., (2019) that combined petrologic modeling and muscovite Rb-Sr geochronology to date the end of amphibolite-facies mylonitization of the Alpine Schist at ~11 Ma along the central Alpine Fault.

2.2 The Anita Shear Zone

The ASZ is a 180 km-long, ~4 km-wide, steeply-dipping, NE–SW-striking ductile shear zone along the west coast of northern Fiordland, South Island, New Zealand (Fig. 1). The shear zone deforms five units from west to east: the Saint Anne Gneiss (which hosts the western margin of the shear zone), Thurso Gneiss, Anita Ultramafite, Jagged Gneiss, and the Western Fiordland Orthogneiss; the latter two of which host the eastern margin of the shear zone (Fig. 1C). The Saint Anne Gneiss and Thurso Gneiss are predominantly metasedimentary units composed of intercalated metapelites, metapsammites, calc-silicates, and marbles, representing the metamorphic country rock of the Median Batholith; minor mafic gneisses are found in both units (Bradshaw, 1990; Czertowicz et al., 2016; Hill, 1995a; Klepeis et al., 1999; Wood, 1972). These metasedimentary rocks are inferred to have Paleozoic depositional ages based on correlation with the Tuhua sequence in central Fiordland (Bradshaw, 1990; Gibson, 1988; Hill, 1995a). The Anita Ultramafite is largely a harzburgite interpreted as a sliver of the sublithospheric mantle that was tectonically

emplaced beneath the Median Batholith (Wood, 1972; Hill, 1995a; Czertowicz et al., 2016a; Czertowicz et al., 2016b). The Jagged Gneiss represents a deformed portion of the Arthur River Complex, a suite of metagabbroic to metadioritic orthogneisses with a Carboniferous crystallization age and an Early Cretaceous (~136–129 Ma) metamorphic overprint (Tulloch et al., 2011). The southernmost portion of the ASZ (near Poison Bay, Fig. 1C) deforms the dioritic to monzodioritic Worsley Pluton of the Western Fiordland Orthogneiss that was emplaced in the structurally deepest portions of the Fiordland arc at ~124–122 Ma (Fig. 1; Gibson, 1988; Ireland and Gibson, 1998; Klepeis et al., 2022; Klepeis et al., 2007, 2016; Mattinson et al., 1986; Muir et al., 1998; Schwartz et al., 2017; Tulloch and Kimbrough, 2003). The fabrics in the ASZ are variably gneissic, schistose, and mylonitic depending on the lithology, with calc-silicates tending to be gneissic and the mafic- to ultramafic assemblages mylonitic (Hill, 1995a).

On the basis of foliation and lineation geometry, mineral assemblage and chemistry, kinematic vorticity, and cross-cutting relationships, Klepeis et al., (1999) recognized four phases of amphibolite- to greenschist-facies fabric formation within the ASZ. The earliest recognizable fabric, which pre-dates ASZ deformation, is a gneissic foliation that is folded and dips moderately east and west with variably oriented down-dip mineral lineations; this fabric is relict bedding in the Thurso Gneiss. This fabric is overprinted by a gently to moderately NE-dipping, amphibolite-facies mylonitic fabric with a gently NNW-SSE plunging lineation (Klepeis et al., 1999). Kinematic indicators and vorticity analyses in these fabrics are consistent with dextral, top-down-to-the SE simple shear on the gently NE-dipping foliation planes (Klepeis et al., 1999). Outcrops that preserve these low-angle fabrics are found predominantly on the north shore of Poison Bay (Czertowicz et al., 2016a).

Thermobarometry of a metapelite from the Thurso Gneiss that preserves these low-angle fabrics suggests that deformation occurred at ~12 kbar and 580 °C (Klepeis et al., 1999). The geometry, kinematics, and PT conditions of this phase of deformation led Klepeis et al., (1999) to suggest that the ASZ initiated as a low-angle, extensional ductile shear zone during mid-Cretaceous crustal thinning and exhumation of the Fiordland arc—though without direct age constraints, the precise tectonic significance of these low-angle, amphibolite-facies fabrics remains unclear.

Superimposed on the low-angle, amphibolite-facies fabric is a subvertical, NE–SW striking foliation with a shallowly NE–SW plunging lineation; this is the prevailing high-temperature fabric within the shear zone (Czertowicz et al., 2016a; Klepeis et al., 1999). Kinematic vorticity analyses revealed that these fabrics resulted from pure shear involving a strong component of horizontal shortening, which together with kinematic indicators is consistent with formation during dextral transpression (Klepeis et al., 1999). The steep, amphibolite-facies foliation transposes and truncates the shallowly dipping fabric (Klepeis et al., 1999). PT estimates from Thurso Gneiss metapelites that preserve the steep, high-temperature fabric suggest that transpressive deformation occurred at ~8–9 kbar and ~590–660 °C (Czertowicz et al., 2016a; Klepeis et al., 1999) and quartz deformation microstructures are consistent with deformation above ~500 °C (Czertowicz et al., 2016a). These PT estimates permit cooling and exhumation between the two amphibolite-facies deformation events, but neither is required when uncertainties on the thermodynamic models and a_{H2O} are taken into account (Czertowicz et al., 2016; Klepeis et al., 1999). Constraints on the age of this phase of deformation are sparse; deformation of the Western Fiordland Orthogneiss at the southern end of the shear zone (Fig. 1; Hill, 1995a, 1995b; Klepeis et al.,

1999) requires that these fabrics postdate emplacement of the 124–122 Ma Worsley Pluton (Gibson, 1988; Ireland and Gibson, 1998; Klepeis et al., 2007, 2016; Mattinson et al., 1986; Muir et al., 1998; Schwartz et al., 2017; Tulloch and Kimbrough, 2003). Metamorphic zircon rims sampled from the subvertical, high-temperature fabrics within the Saint Anne Gneiss are ~103 Ma (Czertowicz et al., 2016a), although this could record metamorphism that preceded dextral transpression at amphibolite-facies conditions. Without direct constraints on their deformation age, the steep, high-temperature fabrics have been variably attributed to extensional orogenic collapse and exhumation of the deepest portions of the Fiordland batholith in the mid-Cretaceous (Czertowicz et al., 2016; Hill, 1995a, 1995b), oblique microplate convergence in the Late Cretaceous related to the establishment of seafloor spreading in the Tasman Sea (Klepeis et al., 1999), tectonic reorganization in response to the cessation of mid-ocean ridge spreading along the Tasman ridge in the early Cenozoic (Klepeis et al., 1999), or the mid- to deep-crustal record of Miocene transpression associated with the development of the broader Alpine Fault system (Claypool et al., 2002; Wood, 1972).

A NNE-striking, subvertical, brittle-ductile, greenschist-facies foliation with subhorizontal slickenlines cuts the steep, amphibolite-facies fabrics (Klepeis et al., 1999). The brittle-ductile fabrics are predominantly developed at the western margin of the ASZ within the Saint Anne Gneiss and along the margins of the Anita Peridotite (Klepeis et al., 1999). These greenschist-facies structures are <10 m wide and distinguished by the predominance of muscovite (Saint Anne Gneiss) and cataclastic textures (Klepeis et al., 1999). K-Ar white mica dates of 30–12 Ma from greenschist-facies brittle-ductile fabrics in the Saint Anne Gneiss at Poison Bay were interpreted to record Miocene neocrystallization

(Claypool et al., 2002). Prior work suggests that the greenschist-faces shear zones represent reactivation of the steep, amphibolite-facies fabrics as brittle splays of the Alpine Fault Zone beginning in mid-Miocene (Claypool et al., 2002; Klepeis et al., 1999).

3 Methods and approach

3.1 Titanite U-Pb deformation chronometry background and approach

Titanite U-Pb dates may reflect the timing of cooling, new mineral growth, recrystallization, and/or deformation depending on the pressure, temperature, fluid-flow, and deformation history of a given sample (Bonamici et al., 2015; Cherniak, 1993; Frost et al., 2000; Garber et al., 2017; Gordon et al., 2021; Hartnady et al., 2019; Holder and Hacker, 2019; Holder et al., 2019; Kohn, 2017; Kohn and Corrie, 2011; Moser et al., 2022; Mottram et al., 2019; Papapavlou et al., 2017; Spencer et al., 2013; Stearns et al., 2016; Walters et al., 2022; Walters and Kohn, 2017). Diffusion experiments suggest that the titanite Pb closure temperature is ~600 °C (Cherniak, 1993), but subsequent empirical studies demonstrate that thermally mediated volume diffusion of Pb is negligible at temperatures <750 °C (Hartnady et al., 2019; Holder et al., 2019; Kohn and Corrie, 2011; Marsh and Smye, 2017; Moser et al., 2022; Smye et al., 2018; Spencer et al., 2013; Stearns et al., 2016). Titanite U-Pb dates are therefore more likely to record the timing of igneous and/or metamorphic crystallization or recrystallization, rather than cooling, at all but granulite-facies conditions. For example, microstructures compatible with recrystallization by interface-coupled dissolution–reprecipitation are common in titanite (Bonamici et al., 2015; Garber et al., 2017; Holder and Hacker, 2019; Moser et al., 2022; Walters et al., 2022); in this process, a fluid-driven recrystallization front propagates through a crystal, variably resets date and trace-element

compositions, and preserves the original grain shape (Geisler et al., 2003, 2007; Putnis and Mezger, 2004; Putnis et al., 2005).

Both the presence of dislocations and motion through crystal lattices via dislocation glide and climb may also result in the loss of trace-elements—including Pb—in minerals (e.g., Lee, 1995; Reddy et al., 2006, 2009, 2016; Timms et al., 2006, 2011; Peterman et al., 2016; Piazolo et al., 2016; Kirkland et al., 2018; Fougerouse et al., 2021). Diffusion is enhanced along the cores of dislocations, a phenomenon known as “pipe diffusion” (Hart, 1957; Love, 1964). Diffusion may similarly be enhanced along the disorganized crystal structure at subgrain boundaries (Hoffman, 1956; Swiatnicki et al., 1986; Turnbull and Hoffman, 1954). Further, the stress field around dislocations affects the chemical potential of interstitial trace elements, trapping point defects and sweeping them towards (sub)grain boundaries (also known as "Cottrell Atmospheres"; Cottrell and Bilby, 1949; Johnston and Gilman, 1959; Rabier and Puls, 1989). The effects of pipe diffusion, subgrain boundary diffusion, and Cottrell Atmospheres are well known in the materials sciences, and a growing body of atom probe tomography studies on geologic materials demonstrates that these processes also affect trace-element concentrations in minerals—including radiogenic Pb—though the exact mechanisms by which line defects affect chemistry and reset dates may differ mineral to mineral (Peterman et al., 2016; Piazolo et al., 2016; Kirkland et al., 2018; Fougerouse et al., 2021). These processes are collectively referred to as “dislocation-assisted diffusion” hereafter.

Thermally mediated volume diffusion, neocrystallization, interface-coupled dissolution–reprecipitation, and dislocation-assisted diffusion generate diagnostic patterns among dates, trace-element zoning, microstructures, and position within an individual titanite grain that

can be used to directly link dates to the process(es) that they record (e.g., Moser et al., 2022). In grains affected by volume diffusion, dates may young towards grain edges (Bonamici et al., 2015) and/or with decreasing grain size (Kirkland et al., 2016; Olierook et al., 2019). Titanite neocrystallization (including secondary crystallization) typically manifests as concentric, sector zoning, and/or core–rim zoning wherein dates vary systematically with trace-element composition (Garber et al., 2017; Walters and Kohn, 2017). Dissolution–reprecipitation produces diagnostic lobate–cuspate or scalloped compositional domains that penetrate inwards from grain boundaries, twins, fractures, and/or inclusions (Garber et al., 2017; Geisler et al., 2003, 2007; Hartnady et al., 2019; Holder and Hacker, 2019; Moser et al., 2022; Putnis and Mezger, 2004; Putnis et al., 2005; Walters et al., 2022). In grains affected by dislocation-assisted diffusion, dates may young with increasing lattice bending (Moser et al., 2022) and/or bent or dynamically recrystallized grains may yield younger dates compared to their undeformed counterparts (Gordon et al., 2021; Moser et al., 2022). Rigorous interpretation of titanite U-Pb dates in terms of grain-scale (re)crystallization process(es) therefore requires comparison of U-Pb dates with trace-element composition, zoning geometry, microstructure (including the development of lattice bending and subgrains), and location with respect to the edge of the grain and/or grain size (c.f. Moser et al., 2022). We integrate electron backscatter diffraction data and wavelength dispersive X-ray spectroscopy maps together with laser-ablation split-stream analyses of titanite U-Pb dates and trace-element concentrations to directly tie U-Pb dates to the process(es) responsible for titanite (re)crystallization within the ASZ.

3.2 Electron backscatter diffraction (EBSD)

Electron backscatter diffraction (EBSD) data were acquired with an FEI Quanta 400F field emission source scanning electron microscope and attached HKL Technology Nordlys II EBSD camera at the University of California, Santa Barbara. The data were collected at a working distance of 15–17 mm using a 20 kV accelerating voltage and 1–5 nA beam current, with the surface of the sample tilted 70° with respect to the electron beam. Oxford/HKL Channel 5 Flamenco software was used to collect and index EBSD patterns. Patterns were acquired using electron-beam rastering with a pixel size of 2–5 μm. Relative misorientation maps were created using Oxford/HKL Channel 5 Tango application. To reduce noise in the misorientation maps, isolated pixels (i.e., pixels with no indexed neighbor pixels, no indexed neighbor pixels of the same phase, or whose orientation differed significantly from all neighbors) were removed and unindexed pixels surrounded by at least six pixels of the same phase were assigned an average orientation based on the neighboring pixels. Points in the approximate center of the grains were used as the reference point and are marked in each misorientation maps.

3.3 Electron probe microanalysis (EPMA) wavelength dispersive X-ray spectroscopy (WDS) maps

Data for Al, Fe, Ca, Nb, and Ce WDS maps were obtained with a five-spectrometer Cameca SX100 EPMA at the University of California, Santa Barbara. Fe Kα and Ce Lα X-rays were analyzed with an LiF crystal, Nb Lα and Ca Kα X-rays with a PET crystal, and Al Kα X-rays with a TAP crystal. Map data were acquired with a 2 μm pixel size, dwell time of 100–200 ms, 15–20 kV accelerating voltage, and 200 nA beam current. X-ray maps were

collected using Probe Software Inc.'s ProbeImage application; maps were processed in Probe Software Inc.'s CalcImage application and Golden Software's Surfer application.

3.4 Laser-ablation split-stream inductively coupled plasma mass spectrometry (LASS)

Isotopes of U, Th, and Pb were acquired simultaneously with trace-element concentrations across eight analytical sessions using the LASS workflow outlined by Kylander-Clark et al., (2013) and Kylander-Clark (2017). ^{238}U, ^{232}Th, ^{208}Pb, ^{207}Pb, ^{206}Pb, ^{204}Pb were measured using a Nu Plasma HR-ES multi-collector ICP-MS in sessions one through five and session eight; a Nu Instruments Plasma 3D multi-collector ICP-MS was used in sessions six and seven. Titanite was ablated with a Cetac/Photon Machines 193 nm excimer Excite laser in a HelEx cell, using a 25 μm or 35 μm laser spot size, and laser fluence of 1 J/cm^2. Spots were ablated for 60 to 70 shots at a repetition rate of 4 or 5 Hz. Prior to analyses, two cleaning shots were applied and permitted to washout for ~15–20 s. Titanite MKED1, with $^{207}Pb/^{206}Pb$ isotope-dilution thermal-ionization mass spectrometry (ID-TIMS) age of 1521.02 ± 0.55 Ma (Spandler et al., 2016) was chosen as the primary reference titanite for U, Th, and Pb isotopes. To assess accuracy and precision, three secondary reference titanites were analyzed for U, Th, and Pb isotopes including BLR (1047.4 ± 1 Ma ID-TIMS concordia date; Aleinikoff et al., 2007), Y1710C5 (388.6 ± 0.5 Ma ^{207}Pb-corrected ^{206}Pb-^{238}U ID-TIMS date; Spencer et al., 2013), and Fish Canyon (28.4 ± 0.05 Ma ^{206}Pb-^{238}U ID-TIMS date; Schmitz and Bowring, 2001).

U, Th, and Pb isotopic data were reduced using the IgorPro software (version 6.37), Iolite plugin (version 2.5), and "U-Pb Geochronology3" data reduction scheme (Paton, 2011). Two seconds were removed from the beginning and end of each integration before a

downhole fractionation correction was applied. After correcting for downhole fractionation, integrations were manually edited to remove heterogeneous portions (i.e., the signal from inclusions). Additional uncertainty was added in quadrature to $^{206}Pb/^{238}U$ (2.2%) and $^{207}Pb/^{206}Pb$ (3.6%) until all analyses of BLR formed a single population (i.e., MSWD ~1) across all eight analytical sessions. Anchored inverse isochron ages (using the contemporaneous Stacey and Kramers, 1975 initial Pb ratios) of the secondary reference materials across all eight analytical sessions were 1046 ± 2 Ma for BLR (MSWD 0.8, initial $^{207}Pb/^{206}Pb$ = 0.91), 389 ± 1 Ma for Y1710C5 (MSWD of 1.1, initial $^{207}Pb/^{206}Pb$ = 0.86), and 27 ± 1 Ma for Fish Canyon (MSWD 0.9, initial $^{207}Pb/^{206}Pb$ = 0.83). The ages for BLR and Y1710C5 overlap the known values within uncertainty; the Fish Canyon age is within 1.4% of the known value. The ^{207}Pb-corrected ^{206}Pb-^{238}U dates for the unknown titanite were calculated using an initial $^{207}Pb/^{206}Pb$ of 0.83 ± 0.5 Ma, which overlaps the $^{207}Pb/^{206}Pb$ intercept in Tera-Wasserburg space of the free-regressed unknown data and accounts for the range of Stacey and Kramers (1975) values for the Cretaceous–Miocene titanite dates.

Concentrations of ^{24}Mg, ^{27}Al, ^{28}Si, ^{31}P, ^{44}Ca, ^{43}Ca, ^{45}Sc, ^{49}Ti, ^{51}V, ^{52}Cr, ^{56}Fe, ^{88}Sr, ^{89}Y, ^{90}Zr, ^{93}Nb, ^{140}Ce, ^{141}Pr, ^{146}Nd, ^{147}Sm, ^{153}Eu, ^{157}Gd, ^{159}Tb, ^{163}Dy, ^{165}Ho, ^{166}Er, ^{169}Tm, ^{172}Yb, ^{175}Lu, ^{178}Hf, ^{181}Ta were measured simultaneously using an Agilent 7700X quadrupole ICP-MS. Glass BHVO2G was analyzed as the primary standard for trace-element concentrations using the December 2009 GEOREM preferred values. MKED1 served as a secondary reference material for the trace-element analyses. Trace-element data reduction was performed using the IgorPro (version 6.37) software, Iolite plugin (version 2.5), and the "Trace Elements" data reduction scheme. Reduced values use an assumed 19.2 wt% Ca in

titanite. No additional external uncertainty was added to the trace-element concentrations. MKED1 yielded trace-element concentrations within ~15% of previously reported values.

4. Results

4.1 Sample descriptions

All five samples in this study are from the Thurso Gneiss, a heterogeneous unit comprising metasedimentary calc-silicate gneisses, metapsammites, metapelites, and mafic gneisses (Fig. 2; Wood, 1972; Hill, 1995a; Klepeis et al., 1999). Samples were collected from the northern and southern ends of the shear zone from exposures along Anita Bay (48A and 47A) and Poison Bay (45C, 106A, and 106E) (Fig. 1C). Sample 48A is a calc-silicate paragneiss consisting of feldspar, amphibole, calcite, titanite, clinozoisite, biotite, apatite, zircon, and opaque minerals (Fig. 2A). The titanite are up to ~1000 μm long and are idioblastic to hypidioblastic (Fig. 2A). The foliation is defined by biotite, long axes of titanite grains, and compositional layers of amphibole and feldspar. Feldspar microstructures in this sample are consistent with bulge recrystallization (Fig. 2B); the orientation of minor fractures in feldspar suggests that these fractures occur along cleavage planes (Fig. S1). Additional deformation microstructures in 48A include undulatory extinction in feldspar and titanite (Fig. S1), as well as deformation twins in titanite. No penetrative brittle fabric was observed in this sample (Figs. 2A, B; S1). Sample 47A is marble comprising calcite, amphibole, white mica, and titanite (Fig. 2C, D). The titanite grains are small (<100 μm in length, commonly <50 μm long), wedge-shaped crystals with long axes aligned with the foliation (Fig. 2C); the titanite are concentrated in an amphibole-rich band (Fig. 2C). In addition to aligned titanite grains, the foliation is defined by the compositional bands of

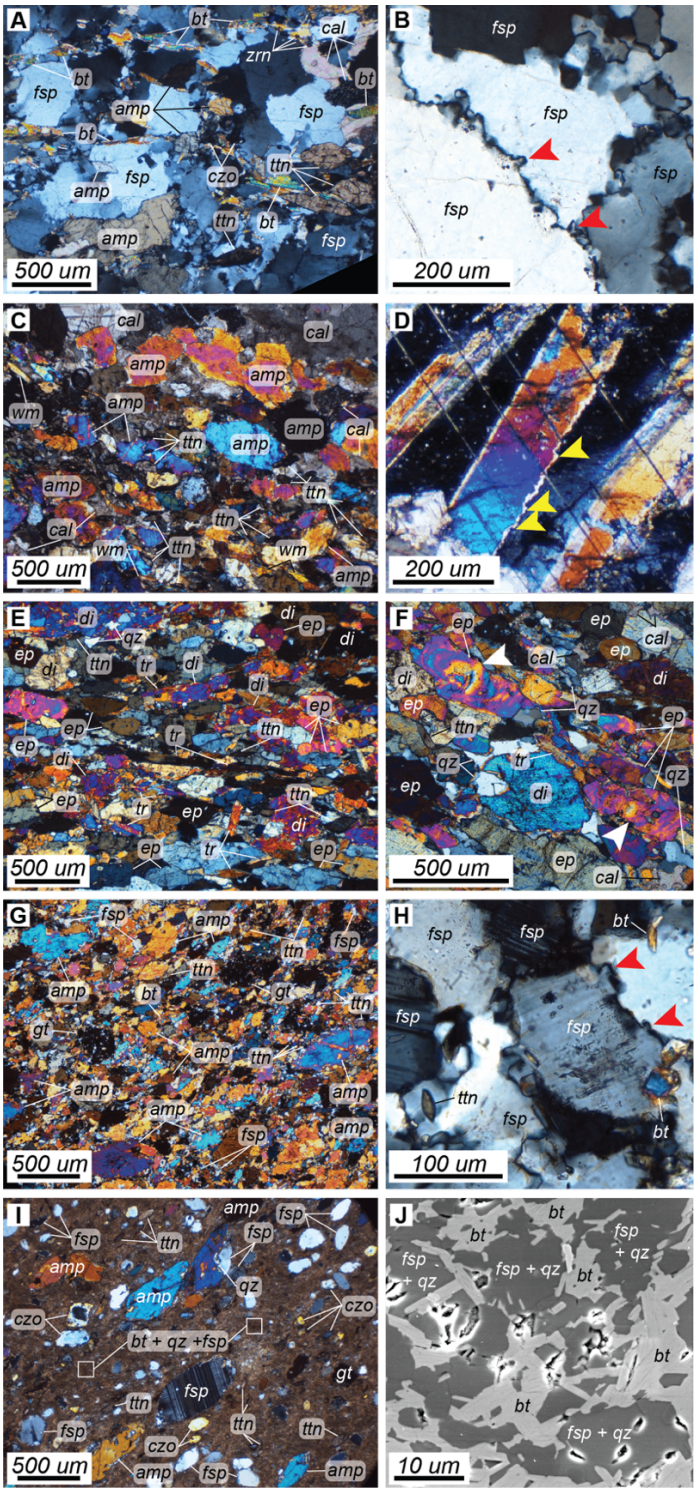

Figure 2. Cross-polarized light, thin section photomicrographs of analyzed in this study. (A and B) Sample 48A; (C and D) sample 47A; (E and F) sample 45C; (G and H) sample 106A; (I and J) sample 106E. Red arrows: feldspar bulge recrystallization microstructures. Yellow: serrated edges of calcite twins. White arrows: truncated zoning in epidote grains. Fsp: feldspar; amp: amphibole; bt: biotite; czo: clinozoisite; ttn: titanite; cal: calcite; zrn: zircon; wm: white mica; ep: epidote; di: diopside; tr: tremolite; qz: quartz; gt: garnet.

calcite and amphibole. Calcite grains are twinned (Figs. 2D, S1); wide twins with serrated boundaries are consistent with type IV calcite twins, though type I and type II twins are also present (Figs. 2D, S1).

Sample 45C from Poison Bay is an epidosite composed of epidote, tremolite, diopside, titanite, calcite, and quartz. (Fig. 2E, F). A ~3 mm thick band of hornblende, feldspar, and opaques within the thin section is consistent with a mafic protolith for the epidosite. Titanite have a maximum length of ~800 μm and are sphenoidal grains that are broadly aligned with the foliation and lineation (Fig. 2E). The foliation in the epidosite is dominated by a shape-preferred orientation of the epidote and tremolite (Fig. 2E, F). Epidote zoning, visible in cross-polarized light, is concentric and truncated at the long axes of grain margins, consistent with their deformation via dissolution–reprecipitation creep (Fig. 2F). Quartz is minor but fine-grained and polygonal (Fig. 2F). Titanite twins and undulatory extinction are uncommon, but subgrains are visible in cross-polarized light. Sample 106A is an amphibolite gneiss consisting of amphibole, plagioclase, garnet, quartz, biotite, titanite, and opaques (Fig. 2G, H). All titanite are <100 μm idioblastic grains, with the majority <50 μm long. Most of the titanite crystals are aligned with the foliation, which is predominantly defined by aligned long axes of amphibole grains (Fig. 2G). Feldspar is generally fine-grained and displays bulge recrystallization (Fig. 2H); few feldspar porphyroclasts are present. Quartz is fine-grained and polygonal. Sample 106E is a calc-silicate gneiss comprising rounded, elongate porphyroclasts of feldspar, amphibole, garnet, titanite, and clinozoisite in a fine-grained matrix of intergrown biotite, feldspar, and quartz (confirmed by EDS; Fig. 2I, J). The foliation is dominated by the long axes of all porphyroclasts, including titanite. Most titanites are <100 μm long, with few ~200 μm grains. The matrix is

coherent and preserves no evidence of fracturing or disaggregation of grains (Fig. 2J). No penetrative brittle fabric is observed in any samples from Poison Bay (Figs. 2E–J).

Titanite LASS analyses were acquired from these five samples; all analyses were completed on standard thickness, microprobe-polished thin sections. Analyses from 48A and 45C were performed on thin sections cut perpendicular to the foliation and oblique to the lineation; additional thin sections were cut perpendicular to the foliation and parallel to the lineation to confirm the orientation of the titanite with respect to the bulk-rock fabric. Samples 48A and 45C were selected for detailed grain-scale analyses (LASS + EBSD + EPMA) as representative samples from the north and south ends of the shear zone, respectively. In the results and discussion, we focus on the grain-scale relationships among dates, trace-element concentrations, zoning, and microstructure from these two samples. The complete results can be found in the appendices.

5.2 Titanite U-Pb dates

Titanite LASS analyses (n=1,241 across all five samples) yielded ^{207}Pb-corrected ^{206}Pb-^{238}U dates (hereafter "U-Pb dates") that predominantly range from ~90 Ma to ~11 Ma (Fig. 3; Table S2). Samples 48A, 45C, 106A, and 106E produced dates that span the full range of the dataset (Figs. 3A, C–E, 4). Sample 45C is the only sample that produced dates older than ~90 Ma, with 6 of 165 dates up to ~120 Ma (Figs. 3C, 4D–F). Several spots from 45C had too little U too calculate a date, but the trace-element concentrations from those spots are reported to assess the possibility of thermally mediated volume diffusion (Table S2). Sample 47A yielded a single population of dates at 11 ± 1 Ma (MSWD = 0.9; Fig. 3B). In sample 48A, some grains preserve the sample-scale or near sample-scale range in dates (Fig. 5; S2),

whereas a subset of grains produced largely Miocene dates with some of these grains producing single populations in Tera-Wasserburg concordia space (e.g., MSWD ~ 1; Figs. 6, 7, S3, S4). Individual grains in sample 45C yielded a range in dates, with most grains producing the sample-scale range in dates (Figs. 8, 9, S5, S6); no individual grains in 45C produced exclusively Miocene dates or single populations.

5.3 Sample-scale trace-element concentrations and Zr-in-titanite temperatures

The relationship between date and trace-element concentration varies from element to element and sample to sample (Figs. 4, S7). In sample 48A, Fe concentrations form a triangle-shaped field in date–composition space; Miocene dates yield Fe concentrations that span the full sample-scale range, whereas analyses with older dates define a progressively more restricted range of high Fe concentration. (Fig. 4A). Ce concentrations produce three distinct trends on a plot of date versus Ce concentration (Fig. 4B). First, a subset of analyses yields the sample-scale range in dates (~90–11 Ma) with Ce concentrations from ~3500–6000 ppm. A second group of data has a similar spread in dates with distinctly low Ce concentrations (~200–1000 ppm). Finally, dates younger than ~20 Ma have Ce concentrations that span sample-scale range (e.g., 200–6000 ppm). Similar patterns are present when dates are compared to LREEs, Th, Hf, and Zr (Figs. 4C, S7A). We do not report Zr-in-titanite temperatures as the total uncertainty on the calculated temperatures are too high to be geologically meaningful. The presence of titanite but absence of rutile, and absence of quartz in some samples indicates that $a_{TiO2} = 0.75$ and $a_{SiO2} < 1$. When combined with the uncertainties in pressure, Zr concentration, and the thermobarometer calibration, the

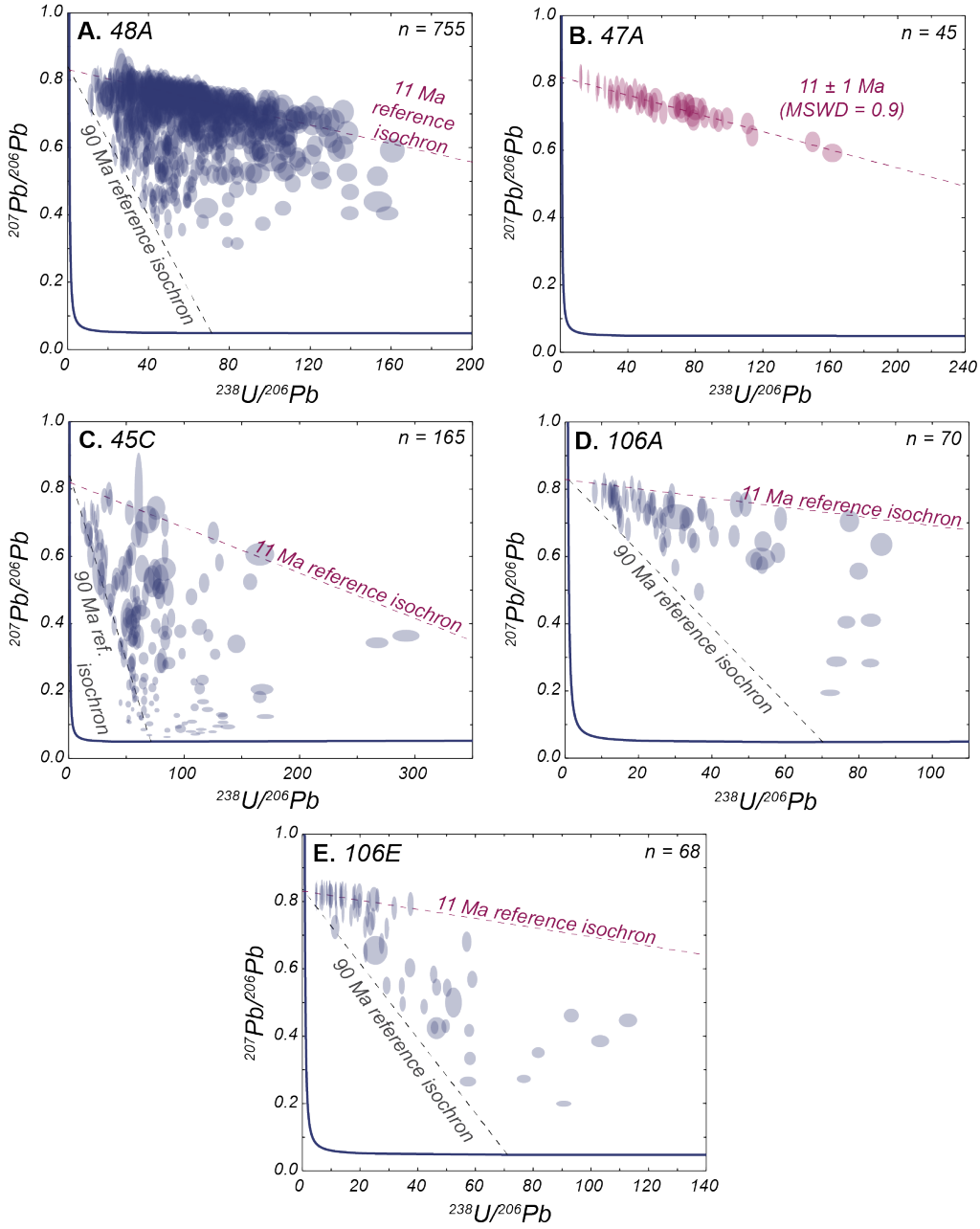

Figure 3. Tera-Wasserburg concordia diagram of titanite LASS analyses from the five studied samples. Reference isochrons in (A,C–E) are anchored to contemporaneous Stacey-Kramers (1975) initial Pb ratios (0.84 for 90 Ma and 0.83 for 11 Ma). Isochron in (B) is an unanchored regression through the data.

total 2σ uncertainty in absolute temperatures is ~180 °C, although observed trends in Zr may still reflect changes in relative (re)crystallization temperatures.

When dates are compared to trace-element concentrations in sample 45C, two general patterns emerge. Sr, Fe, and the REEs + Y show weak trends of decreasing concentration with younging date, with the youngest (e.g., Miocene) dates producing among the lowest concentrations at the sample scale (Figs. 4D, E; S7B). The remaining elements (including Zr) yield no discernable pattern between date and composition (Figs. 4F, S7B). Similar to sample 48A, temperature uncertainties are too high to make meaningful interpretations; we instead focus on the change in Zr concentration.

5.4 EBSD relative misorientation maps

Relative misorientation maps and plots of date vs. misorientation reveal that individual titanite grains preserve gradual, rather than sharp, changes in lattice orientation (hereafter lattice "bending") with respect to a central reference point in both samples 48A and 45C (Figs. 5A, 6A, 7A, 8A, 9A). Intragrain lattice bending commonly ranges from ~10–25° and is typically greatest at grain tips (Figs. 5A, 6A, 7A, 8A, 9A). Subgrain boundaries are common, particularly at grain tips where cumulative misorientation is greatest (Fig. 5A, 6A, 7A, 8A, 9A). Twins are near-ubiquitous in grains from 48A (Figs. 5A, 6A, 7A) and only appear in a single grain from sample 45C (Fig. S6). The vast majority are <5 μm wide and the thickness of individual twins varies along their length (Figs. 5A, 6A, 7A). The predominant misorientation angle-axis relationship that defines twins is 74°/<102> (Fig. S8). The twins are typically bent to the same degree as the host grains (Fig. 5A, 6A, 7A).

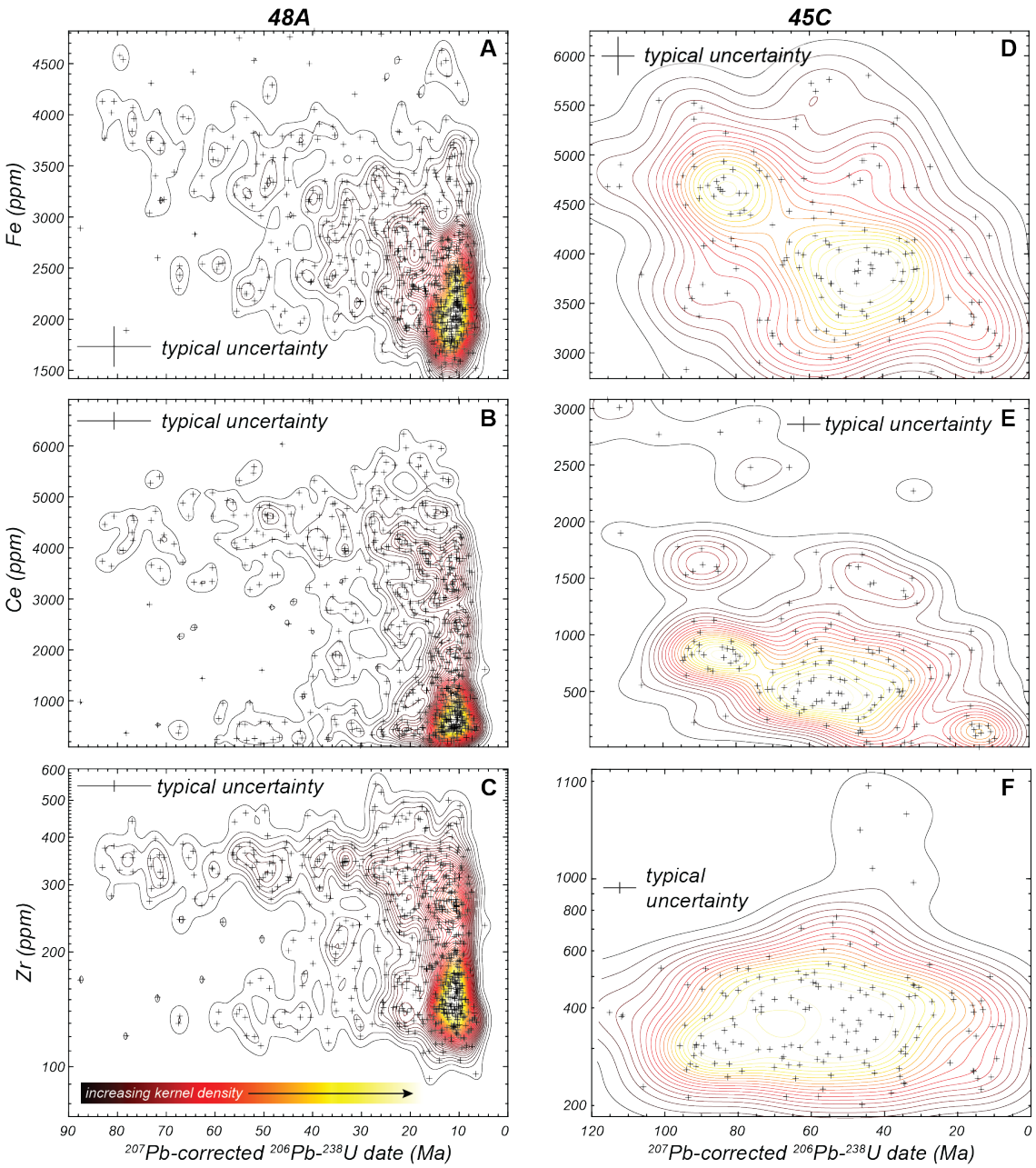

Figure 4 Sample-scale ^{207}Pb-corrected ^{206}Pb-^{238}U date vs. selected trace-element concentrations for samples 48A (A–C) and 45C (D–F) with two-dimensional kernel density contours. Contours were computed in MATLAB using the kernel density estimation of Botev et al., (2010).

5.5 Zoning and grain-scale date vs. trace-element concentrations

Titanite EPMA X-ray maps from sample 48A reveal compositional zoning that is most evident in Fe and Ce (Figs. 5B, C; 6B, C; 7B, C; S2, S3). Most grains in 48A yield core–rim relationships in Fe and Ce, with high Fe and Ce cores and comparatively low Fe and Ce rims (Figs. 5B, C; 6B, C; S2, S3). The contrast in core–rim zoning is sharper in Ce compared to Fe (Figs. 5B, C; 6B, C; S2, S3). The geometry of Fe and Ce rims in 48A ranges from broad scallops (Figs. 6B, C; 7B, C) to lobate–cuspate (Figs. S2, S3). Both Fe and Ce X-ray maps reveal thin, straight domains that transect grains cores; these domains are typically wider in Fe maps when compared to Ce maps (Figs. 5B, C; S2, S3). A subset of grains from sample 48A are near-homogeneous in mapped elements (Figs. 7B, C; S4).

Zoning in sample 45C is clearest in the Fe, Ce, and Al maps (Figs. 8B, C; Figs. 9B, C; S5, S6). Grains in 45C preserve core–rim relationships in Ce, with elevated Ce concentrations in the cores compared to the rims (Figs. 8C, 9C; S5, S6). A subset of grains in sample 45C have similar core–rim zoning in Fe concentrations (Fig. 8B). Though core-rim zoning is typically concentric in these grains (Fig. 8B, C), some Ce rims have irregular, lobate–cuspate geometries (Fig. 9C). Rims of elevated Fe and Al content are common in grains from 45C (Figs. 8B, 9B; S5, S6); these rims are thinner than the low-Ce rims (Figs. 8C; 9C). Thin, linear domains of depleted Ce and Fe content are only present in a single grain from 45C (Fig. S6).

The relationships between dates and trace-element concentrations vary among the individual grains. In sample 48A, grains that preserve the sample-scale range in dates yield correlations between date and trace-element compositions that mirror the sample-scale trends (e.g., Fe, Ce; Fig. 5F, G; cf. Fig 4). Titanite grains with only Miocene dates have

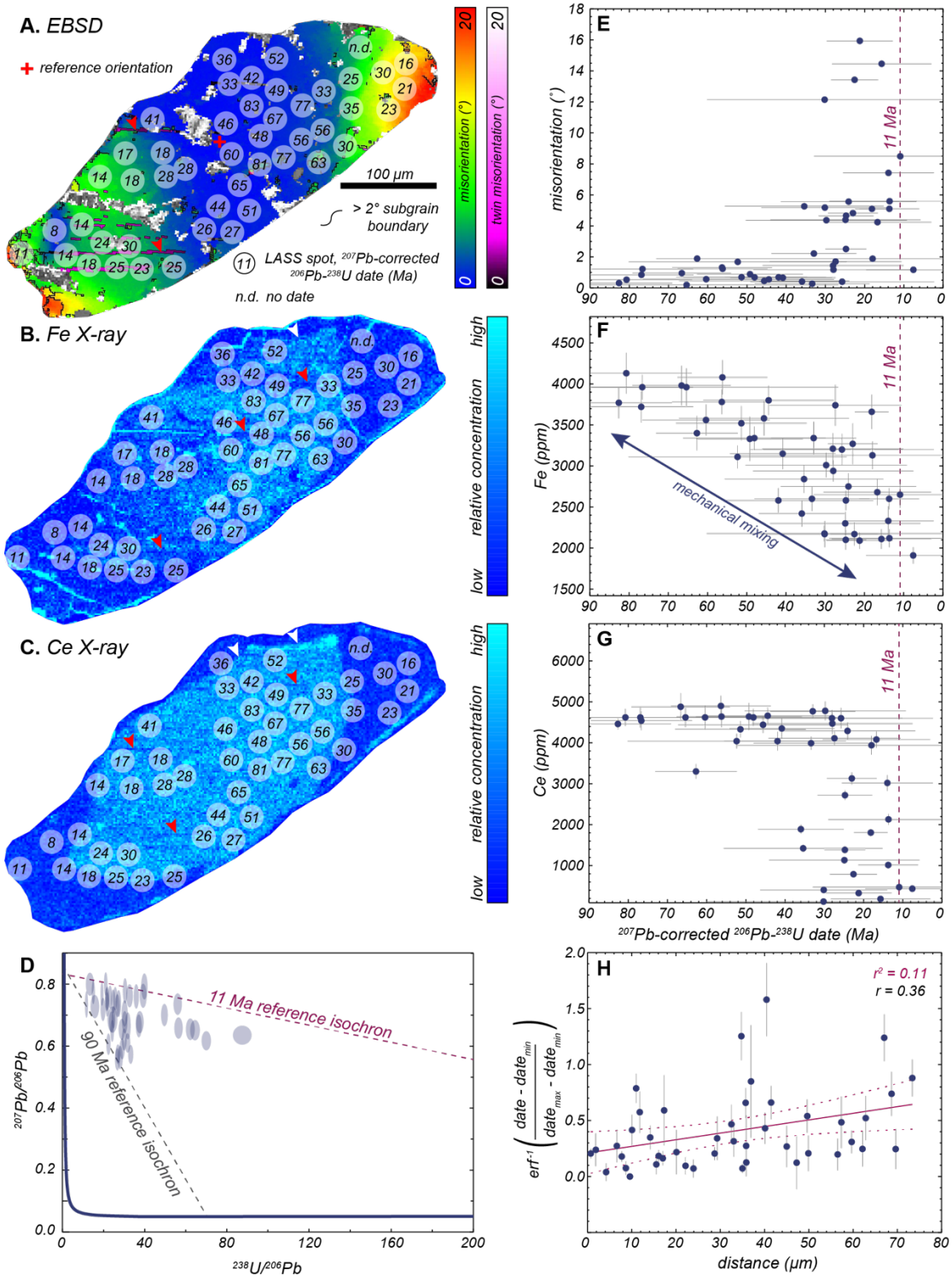

Figure 5 Grain-scale data from representative "Cretaceous–Miocene" grain from sample 48A. Red arrows in (A–C) indicate deformation twins. White arrows in (B) and (C) denote scalloped or lobate–cuspate rims. Reference isochrons in (D) are anchored to contemporaneous Stacey-Kramers (1975) initial Pb ratios. Distance measurements in (H) have a + 25 µm uncertainty removed to avoid cluttering the diagram. In (H), maroon solid line and dashed lines are the linear regression and 95% confidence interval calculated in MATLAB.

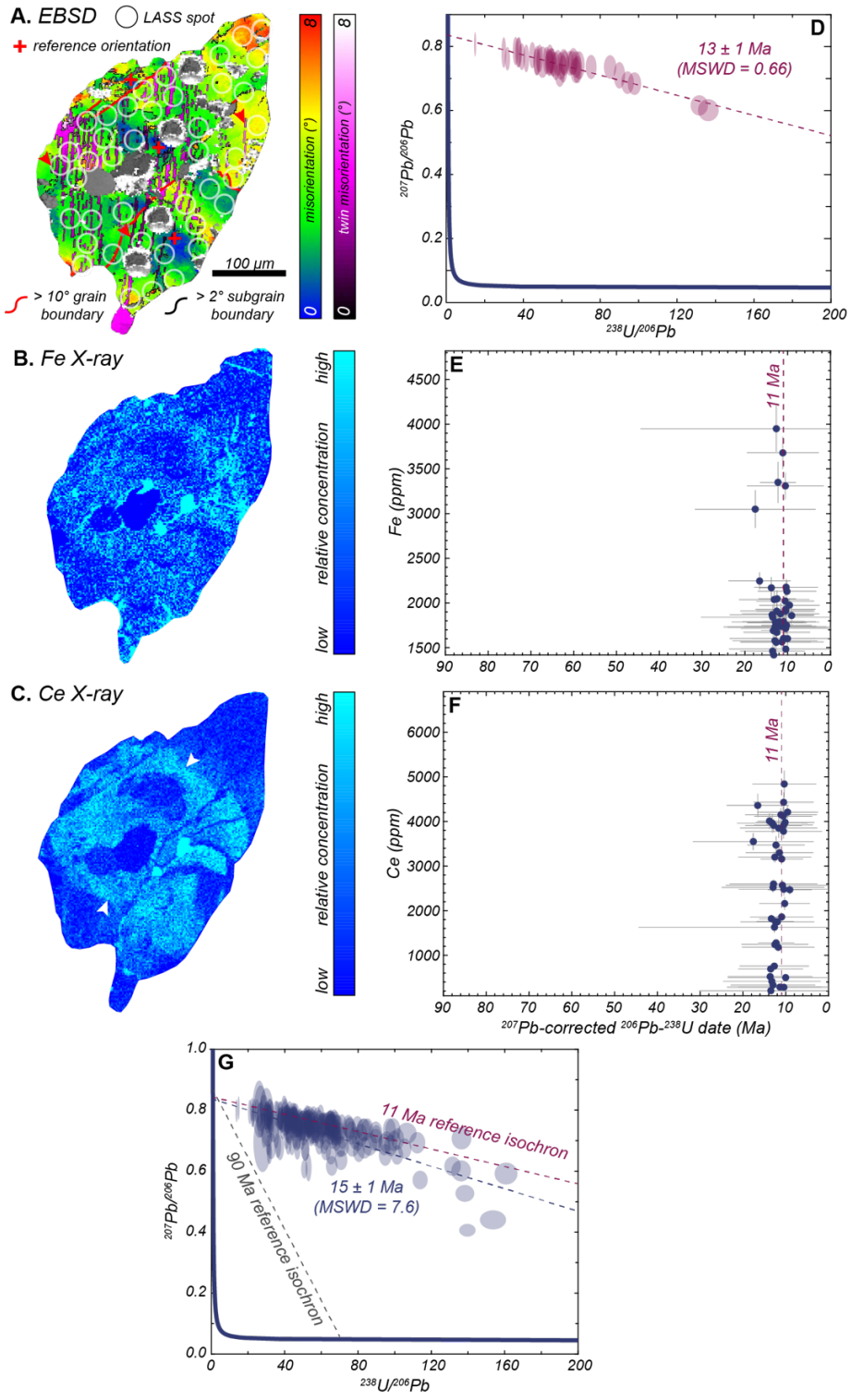

Figure 6. Grain-scale data from a representative "zoned Miocene" grain from sample 48A. Red arrows in (A) indicate deformation twins. White arrows in (B, C) denote scalloped rim geometries. (D) Tera-Wasserburg concordia diagram of U-Pb analyses from analyses from this grain only. (G) Tera-Wasserburg concordia diagram of U-Pb analyses from all sixteen "zoned Miocene" grains in the dataset. Isochrons in (D) and (G) are unanchored regressions unless labeled "reference isochron".

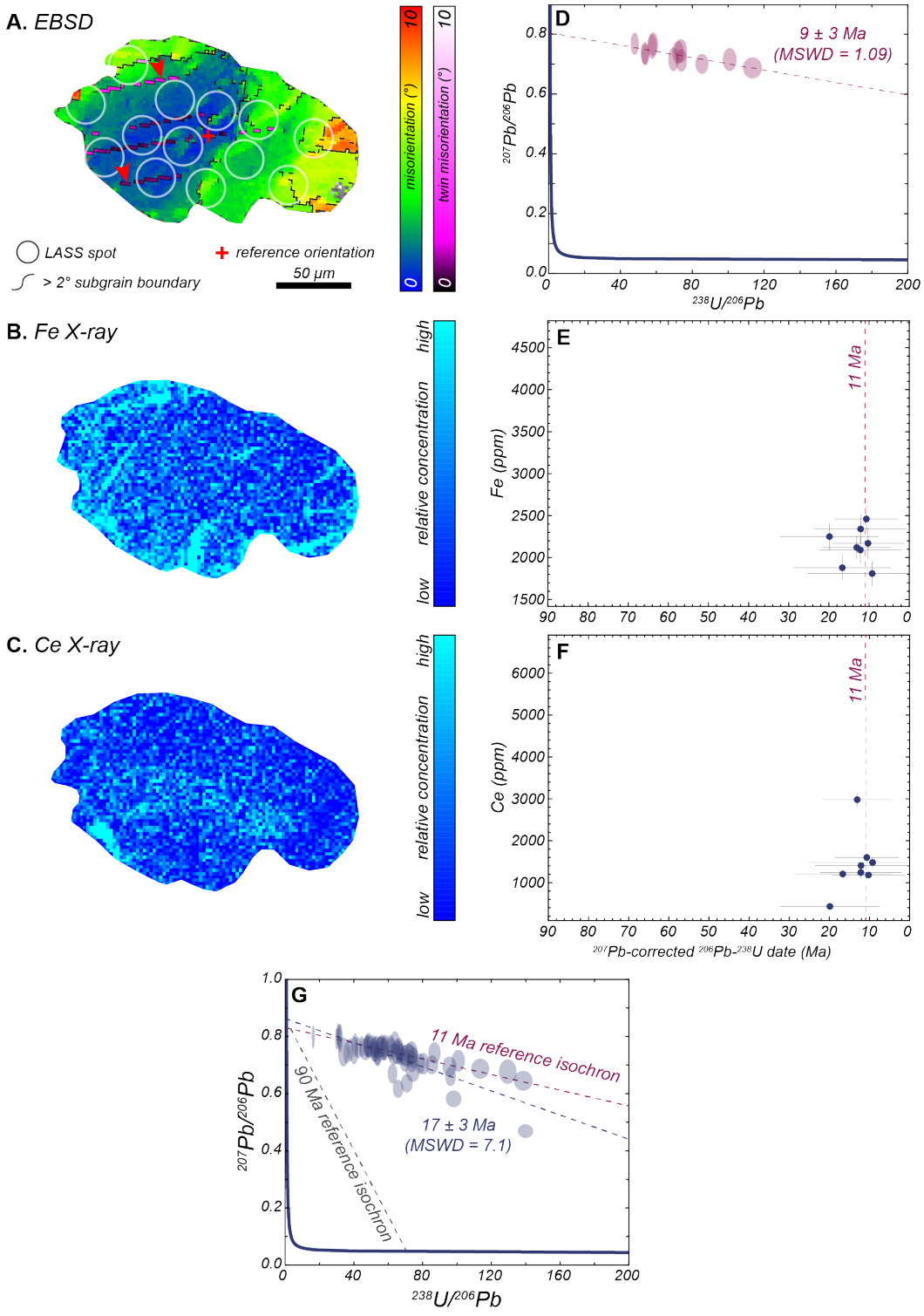

Figure 7 Grain-scale data from a representative "homogeneous Miocene" grain from sample 48A. Red arrows in (A) indicate deformation twins visible in relative misorientation maps. Tera-Wasserburg concordia diagram in (D) includes U-Pb analyses from this grain. (G) Tera-Wasserburg concordia diagram of U-Pb analyses from all seven "zoned Miocene" grains in the dataset. Isochrons in (D) and (G) are unanchored regressions unless labeled "reference isochron".

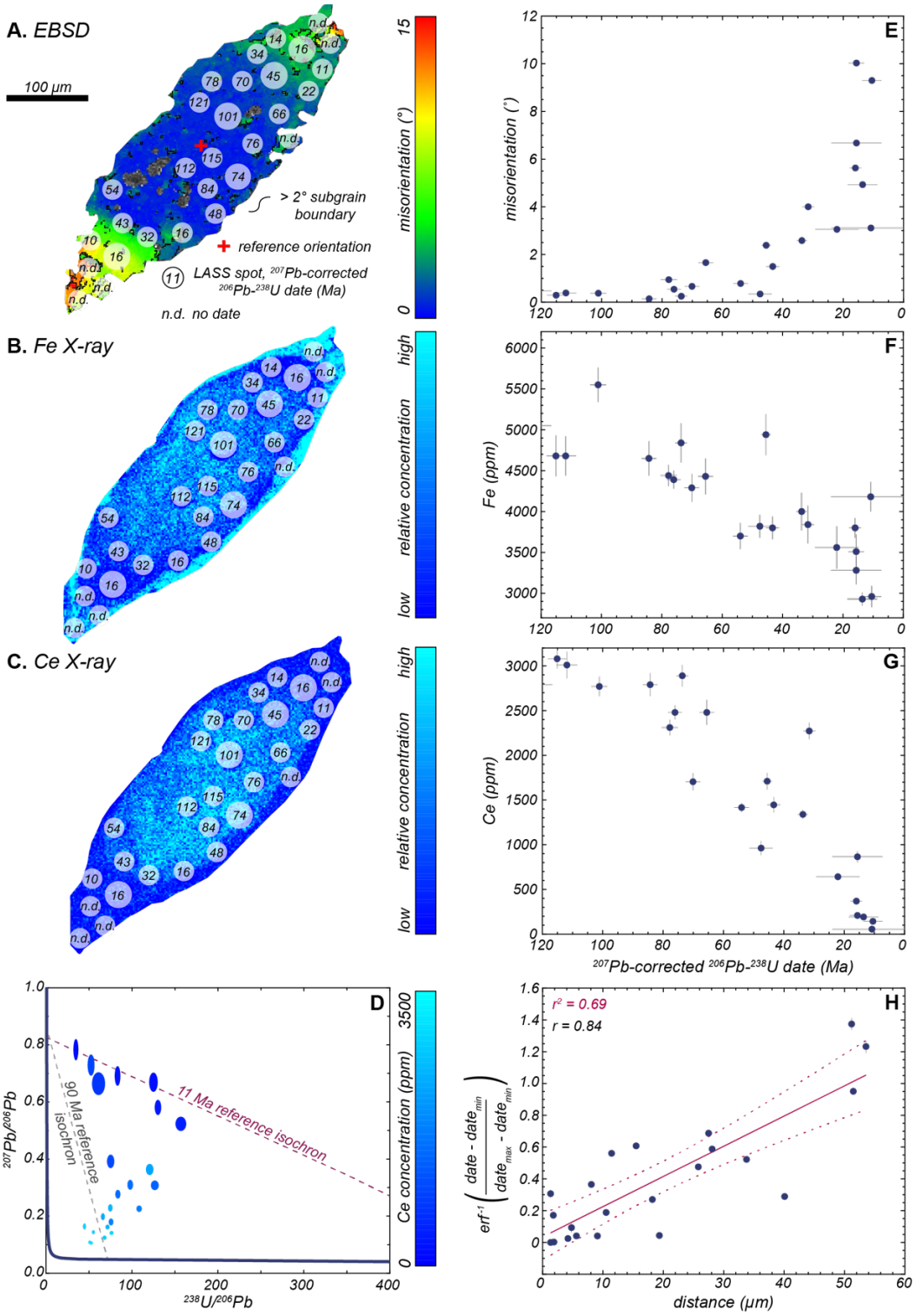

Figure 8 Grain-scale data from a representative titanite grain from sample 45C in which dates and composition are correlated. Reference isochrons in (D) are anchored to contemporaneous Stacey-Kramers (1975) initial Pb ratios. Distance measurements in (H) have a + 25 µm uncertainty removed to avoid cluttering the diagram. In (H), maroon solid line and dashed lines are the linear regression and 95% confidence interval calculated in MATLAB.

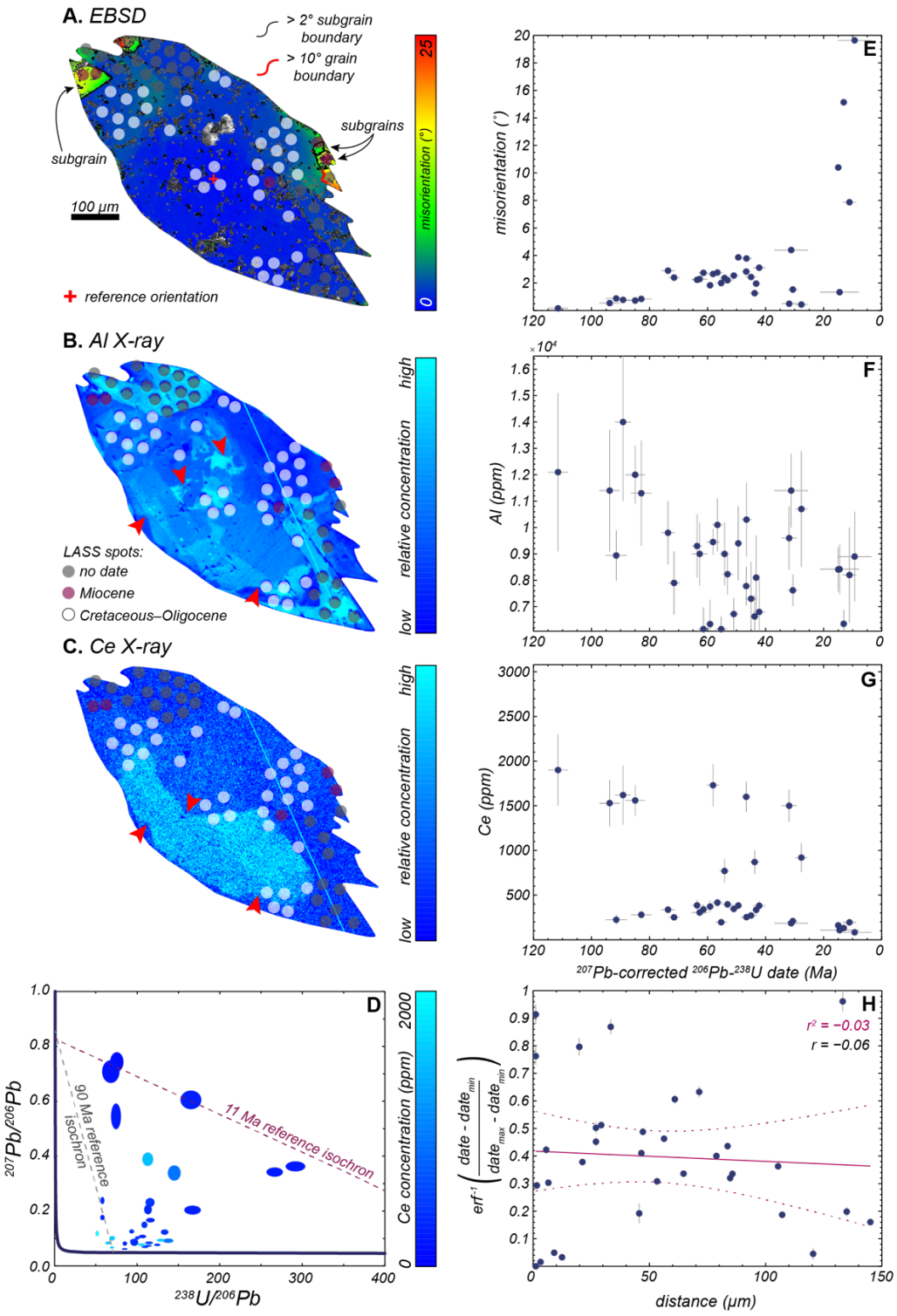

Figure 9 Grain-scale data from a representative titanite grain from sample 45C where dates and composition are not correlated. Red arrows in (B) and (C) indicate patchy and lobate–cuspate zoning. Reference isochrons in (D) are anchored to contemporaneous Stacey-Kramers (1975) initial Pb ratios. Distance measurements in (H) have a + 25 µm uncertainty removed to avoid cluttering the diagram. In (H), maroon solid line and dashed lines are the linear regression and 95% confidence interval calculated in MATLAB.

either a broad range of individual trace-element concentrations comparable to the range observed at the sample scale (Fig. 6E, F; cf. Fig. 4) or yield homogeneously low trace-element concentrations (Fig. 7D–F). In some grains from sample 45C, dates are correlated with composition in a way that mimics the sample-scale patterns (Figs. 8F,G; S5; cf. Fig 4); Sr, Fe, REEs, and Y decrease with younging date whereas the remaining elements produce no discernable relationship with date. Other grains yield no discernible pattern among dates and any trace-element (Figs. 9F, G; S6).

6. Discussion

6.1 Grain-scale relationships among dates, zoning, composition, and microstructure: Sample 48A

6.1.1. "Cretaceous–Miocene" titanite

Most grains in sample 48A preserve core–rim zoning in Ce and a range of Cretaceous to Miocene dates ("Cretaceous–Miocene" titanite; Figs. 5, S2). Dates as old as ~90 Ma in the cores of these grains (Figs. 5, S2) suggest that this is the maximum timing of initial titanite crystallization (Fig. 10A). Many "Cretaceous–Miocene" grains also yield Cretaceous dates in low Ce rims (Fig. S2). Cretaceous dates in grain rims may have resulted from (1) secondary titanite crystallization or interface-coupled dissolution–reprecipitation shortly after titanite core crystallization in the Cretaceous (i.e., at timescales undetectable by the precision of LASS) or (2) incomplete resetting of U-Pb dates during a much later (e.g., Miocene) phase of dissolution–reprecipitation (Moser et al., 2022; Walters et al., 2022). It is not clear from our data which of these interpretations is the most likely. It can only be stated

that the rims developed after ~90 Ma and that a phase of rim development may have occurred prior to deformation in the Miocene (Fig. 10B).

The youngest dates in "Cretaceous–Miocene" titanite may reflect Pb loss by volume diffusion, the timing of secondary titanite growth, interface-coupled dissolution–reprecipitation, dislocation-assisted diffusion, or some combination of these processes. To evaluate the effect that volume diffusion had on the "Cretaceous–Miocene" titanite U-Pb dates at the grain scale, the inverse error function (erf^{-1}) of dates and Pb concentrations (from the LASS trace-element concentrations, normalized to the maximum and minimum values within individual grains) was calculated and compared to the distance between the analysis and edge of the titanite grain. A concentration gradient that results from thermally mediated volume diffusion of a finite source should define an error function (*erf*) with respect to distance from the edge of the grain. The erf^{-1} of such a concentration gradient is a line with intercept zero, whose slope is proportional to the diffusivity of the element (cf. Crank, 1975; Stearns et al., 2016). We assessed whether erf^{-1} distributions of date and Pb concentrations are linear and therefore explicable by thermally mediated volume diffusion at the grain scale using Pearson's r and the r^2 of linear regressions, both calculated in MATLAB (cf. Moser et al., 2022). Of the 18 grains analyzed from sample 48A that preserve a broad range of dates, most did not yield *erf*-like distributions of date, total Pb, radiogenic Pb, or common Pb concentrations (Figs. 4H, S9A). Only two grains in sample 48A yielded a relationship between date and distance from the edge of the grain that are defensibly *erf*-like (Pearson's r's of ~0.8 and r^2 of linear regressions ~0.6; Fig. S9A). Two additional grains from 48A produced erf^{-1}-like distributions of radiogenic Pb (Pearson's r's of 0.5, 0.7; r^2 of linear regressions 0.7 and 0.8; Fig. S9A). However, Sr—to which Pb diffusivity should be

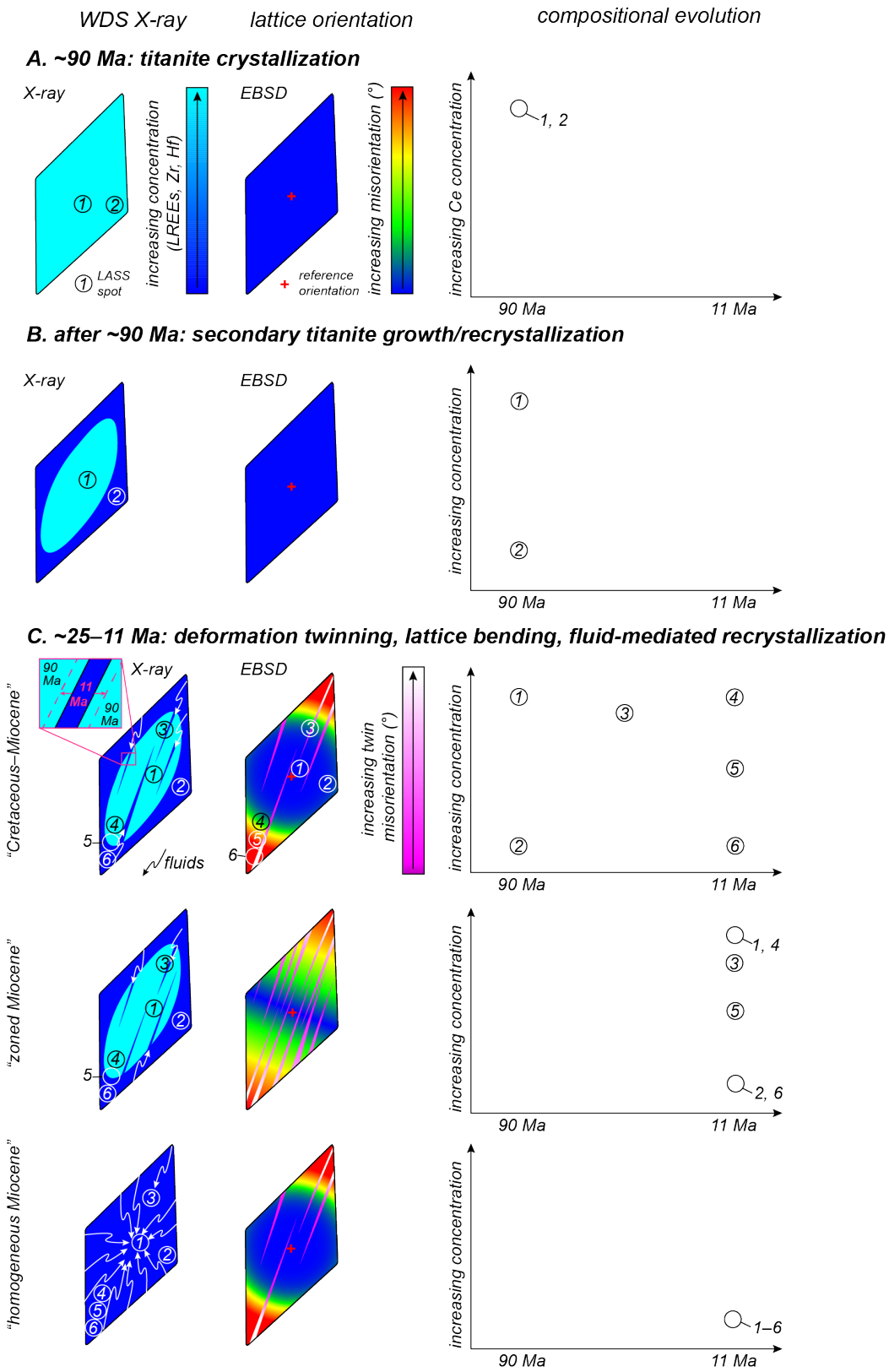

Figure 10 Cartoon schematic showing interpreted textural (left) and date–composition evolution (right) in sample 48A. See text for evolution of titanite textures, dates, and trace-element compositions.

comparable based on the similar charge/radius ratios of the two elements (Cherniak, 1995; LaTourrette et al., 1996)—does not produce an *erf*-like relationship with distance from the grain edge in these grains (Pearson's r = 0.12–0.7; r^2 of linear regressions = –0.12–0.32; Fig. SA9). This suggests that *erf*-like relationships between date and distance from the edge of the grain are not the result of thermally mediated volume diffusion. In addition, there is no consistent correlation between dates and U concentrations as one might expect if heterogeneities in radiogenic Pb concentrations drove volume diffusion that obscured a simple core–rim distribution of dates (Fig. S7A; Paul et al., 2019); these effects, however, could be muted given that common Pb concentrations are higher than radiogenic Pb concentrations in these grains. Overall, the data suggest that the spread in dates in sample 48A is unlikely to reflect volume diffusion of Pb.

Titanite neocrystallization is expected to produce a single age population with a distinct trace-element composition and texture (e.g., grain size, core–rim relationships; Garber et al., 2017; Walters et al., 2022). Neither of these, however, is true for Miocene dates in "Cretaceous–Miocene" titanite. Miocene dates produce the sample-scale range in trace-element concentrations and were found in both cores and rims of "Cretaceous–Miocene" titanite (Figs. 4, 5, S2). In addition, dates from "Cretaceous–Miocene" titanite fill the complete range from Late Cretaceous to mid Miocene, rather than producing two distinct populations. Though it is not possible to rule out that some titanite neocrystallization occurred in the Miocene, it alone is an unsatisfactory explanation for the range of Miocene dates observed in "Cretaceous–Miocene" titanite.

Dates that are reset by dislocation-assisted diffusion that results from crystal lattice reorientation should produce a relationship between dates and dislocation–related

microstructures. For example, dates may young with increasing lattice bending within individual grains (Moser et al., 2022), subgrains and/or dynamically recrystallized grains may yield younger dates (Gordon et al., 2021; Piazolo et al., 2012), or spots that overlap deformation twins may produce younger dates (Bonamici et al., 2015; Fougerouse et al., 2021). The tips of "Cretaceous–Miocene" titanite are typically bent by up to ~25° compared to grain cores (Fig. 5A; S2). The gradual changes in lattice orientation from grain centers to tips is consistent with bending caused by dislocation creep. Dates from bent grain tips are typically among the youngest in the dataset, regardless of whether they are in cores or rims (Fig. 5B, C; S2). For example, the "Cretaceous–Miocene" grain shown in Figure 5 yielded multiple Miocene dates from the high-Ce core that also are within the bent grain tip (Fig. 5A, C). This relationship between lattice bending and dates in "Cretaceous–Miocene" grains suggests that lattice bending contributed to resetting titanite U-Pb dates in the Miocene.

In addition to lattice bending, "Cretaceous–Miocene" titanite preserve thin, tapering twins with a misorientation angle-axis relationship of 74°/<102> with respect to the host grain (Fig. 5A; Fig. S8). This geometry is consistent with the misorientation angle-axis relationship that is specifically produced by titanite deformation twins, rather than growth twins (Borg and Heard, 1972; Papapavlou et al., 2018). Combined with the tapered nature of these grains, these observations imply that that the titanite twins in sample 48A are deformation twins, rather than growth twins. Deformation twins imaged by EBSD correspond to thin (i.e., <5 μm-wide), linear domains of low Fe and Ce concentration in WDS X-ray maps (Fig. 5A–C). Other similarly oriented, linear, low-Fe and low-Ce domains, including those that cut across the cores of some grains, are not revealed by the EBSD data (Fig. 5A–C), but given their similar geometries and similar Fe and Ce response

in WDS maps, these are also likely deformation twins that are thinner than the step size (2–5 μm) of the EBSD data acquisition. This interpretation is supported by grains where EBSD data were acquired with two different step sizes; the data collected with a smaller pixel size (2 μm) revealed additional deformation twins not captured by the data acquired at a larger step size (5 μm; Fig. S10).

The depletion of Fe and Ce in deformation twins indicates that deformation twinning resulted in the loss of at least some trace elements from the ASZ titanite. Removal of trace elements from deformation twins may be a direct or indirect process. For example, the formation of deformation twins in monazite has been suggested to have resulted in complete Pb loss from within deformation twins (Fougerouse et al., 2019); in such cases, dates from deformation twins constrain when the twins formed. Others have suggested that deformation twins promote trace-element loss by thermally mediated volume diffusion by cutting crystals into smaller diffusion domains (Bonamici et al., 2015). Twins may also serve as preferential pathways for fluid-mediated recrystallization. In the titanite from 48A, the lengthscale over which Fe and Ce were lost from within and around deformation twins is clearly different; zones of Fe depletion that surround deformation twins are wider than zones of Ce depletion (cf. Figs 5B and 5C). The spatial variability to which different elements are affected by the deformation twins and the observation that elements were lost not only from within—but also around—twins implies that a process other than twinning itself was at least partially responsible for trace-element loss within and around the deformation twins. Thermally mediated volume diffusion of trace elements from portions of the crystal cut by deformation twins would produce lengthscales of trace-element loss that scale with elemental diffusivity. Iron is expected to diffuse more easily than Ce in titanite (Holder et al., 2019), consistent

with the greater lengthscale of Fe loss. However, even if deformation twins developed when the titanite first crystallized (e.g., ~90 Ma) and remained at T ~ 600 °C for ~80 Myr, the characteristic diffusion lengthscale for Fe is too short (<1 μm; using the diffusivities of Holder et al., 2019) to explain ~10 μm-wide zones of Fe-loss around deformation twins. Alternatively, interface-coupled dissolution–reprecipitation may lead to variable resetting of dates and trace-elements (Holder and Hacker, 2019; Moser et al., 2022; Walters et al., 2022); the varying lengthscales of trace-element loss in domains surrounding deformation twins may simply reflect the lengthscales over which recrystallization reset various trace elements. The recrystallization of titanite along twin planes by fluid is therefore a more plausible explanation for the variable response of trace-elements in domains surrounding the deformation twins. It is not possible, however, to rule out the possibility that the propagation of the deformation twins themselves expelled trace-elements (including radiogenic Pb) from these grains (e.g., Fougerouse et al., 2021).

Deformation twins that transect the cores of "Cretaceous–Miocene" titanite provide an explanation for the range of Miocene–Cretaceous dates in unbent titanite cores (Fig. 5A, 10C). In "Cretaceous–Miocene" titanite, dates are linearly correlated with Fe concentrations (Fig. 5F). This relationship suggests that dates were reset to the same degree as Fe concentrations and is consistent with mechanical mixing between a Cretaceous age domain with high Fe concentrations (untwined portions of cores) and a Miocene domain with low Fe concentrations (deformation twins; Fig 10C). Further, LASS spots from the cores of "Cretaceous–Miocene" that produced a range of Cretaceous to Miocene dates clearly overlap deformation twins (Figs. 5A–C). We suggest that the deformation twins preserve Miocene dates, and that the range of "Cretaceous–Miocene" dates from unbent titanite cores

are geologically meaningless, mixed analyses of Cretaceous cores and Miocene deformation twins (Fig. 10C). This interpretation requires that the fluid event responsible for recrystallization around deformation twins occurred in the Miocene and resulted in complete resetting of dates (Fig. 10C).

The preferential recrystallization of deformation twins may have been syn- or post-deformational. "Zoned Miocene" titanite (see section 6.1.2 below), wherein not all deformation twins have been fluid recrystallized, provide evidence that deformation twinning and lattice bending of titanite were ongoing in the Miocene. Further, titanite from sample 45C record a Miocene phase of dissolution–reprecipitation that did not preferentially recrystallize bent grain tips, subgrains, and deformation twins (see section 6.2 below). This suggests that the exploitation of microstructures as fast diffusion pathways by fluids may be enhanced only if lattice reorientation and interface-coupled dissolution–reprecipitation are concomitant. We therefore prefer the interpretation that fluid-recrystallization, deformation twinning, and lattice bending occurred simultaneously in sample 48A, and that the youngest dates (i.e., ~11 Ma) from "Cretaceous–Miocene" grains provide direct constraints on the timing of plastic deformation of titanite within the ASZ.

6.1.2 "Zoned Miocene" titanite

A subset of grains from sample 48A preserve core–rim zoning in Ce but yield predominantly Miocene dates ("zoned Miocene" grains; Figs. 6, S3). "Zoned Miocene" grains yield similar zoning patterns and range of trace-element concentrations as the "Cretaceous–Miocene" grains; these observations imply that "zoned Miocene" grains experienced the same Cretaceous crystallization and subsequent (re)crystallization history as

the “Cretaceous–Miocene” grains. We therefore suggest that the “Zoned Miocene” grains grew and were recrystallized by fluids in the Cretaceous; this interpretation requires that the U-Pb system in these grains was completely reset in the Miocene by volume diffusion, fluids, or deformation and dislocation-assisted diffusion.

Thermally mediated volume diffusion may produce a relationship between grain size and date, such that smaller grains produce younger dates and larger grains yield older dates (e.g., Kirkland et al., 2016). Though most “zoned Miocene” grains are among the smallest in the dataset (grains ~400 μm long or less), other similar-sized grains retain Cretaceous dates (Fig. S2). Further, as outlined above, the maximum possible duration of heating within the Anita Shear Zone (600 °C for ~80 Myr; based on thermobarometry and thermodynamic modelling by Klepeis et al., 1999 and Czertowicz et al., 2016a) suggests a characteristic diffusion distance of Pb of <1 μm (for naturally determined diffusivities, e.g., Hartnady et al., 2019; Holder et al., 2019) to 13 μm (for experimental diffusivities; Cherniak 1993). Such characteristic diffusion lengthscales are insufficient to explain thermally mediated volume diffusion of Pb in grains as large as ~400 μm. Further, as previously discussed, dates and Pb concentrations do not form erf^{-1}-like relationships in “Cretaceous–Miocene” titanite (Figs. 5H, S9A). Together, these observations indicate that Pb did not move via thermally mediated volume diffusion at the grain-scale in any grain from sample 48A. Miocene dates in “zoned Miocene” grains are therefore not cooling ages.

The primary difference between “zoned Miocene” and “Cretaceous–Miocene” grains is the nature of lattice bending and deformation twinning in the different groups. Although the cumulative lattice bending is similar in “zoned Miocene” and “Cretaceous–Miocene” titanite, lattice bending is more throughgoing or penetrative in “zoned Miocene” compared

to “Cretaceous–Miocene” grains, the latter of which are bent only at the tips (cf. Figs. 5A and 6A; S2 and S3; Fig. 10C). Additionally, many “zoned Miocene” grains have an apparently greater density of deformation twins than “Cretaceous–Miocene” titanite (cf. Figs. 5A and 6A; S2 and S3) although this is difficult to quantity given that not all twins were captured by the EBSD data (see above, Fig. S10). These observations are consistent with the complete resetting of U-Pb dates by lattice bending and deformation twinning in the “zoned Miocene” titanite (Fig. 10C).

The reorientation of crystal lattices in “zoned Miocene” grains may have directly or indirectly reset U-Pb dates; the development of lattice bending and deformation twins may have reset the dates themselves (Fougerouse et al., 2021; Gordon et al., 2021; Odlum et al., 2022; Piazolo et al., 2016) or provided fast pathways for fluids to interact with and recrystallize grain interiors (Moser et al., 2022). A subset of grains in sample 48A yield predominantly Miocene dates and have homogeneous trace-element compositions (Fig. 7; see section 6.1.3 “Homogeneous Miocene” titanite below). We interpret the Miocene dates and homogeneous trace-element compositions as evidence that some grains were completely reset by fluid-mediated recrystallization in the Miocene. However, the core–rim zoning in Ce preserved in the “zoned Miocene” titanite (Fig. 6C) implies that the cores of these grains escaped complete fluid recrystallization in the Miocene. Further, even where revealed by EBSD maps, deformation twins are not always visible in Fe and Ce X-ray maps in “zoned Miocene titanite” (Figs. 6B, C; S3), suggesting that deformation twins were not ubiquitously recrystallized by fluids. Though fluids may have aided in resetting dates in “zoned Miocene” titanite, the relationships among dates, zoning, trace-element concentrations, and microstructures suggest that lattice bending and deformation twinning were the primary

mechanisms of date resetting in "zoned Miocene" grains (Fig. 10C) and that dates from these grains provide a direct constraint on the timing of deformation.

6.1.3 "Homogeneous Miocene" titanite

An additional group of titanite grains from sample 48A yield largely Miocene dates and are broadly homogeneous in all mapped elements ("homogeneous Miocene" titanite; Fig. 7). The homogeneous distributions of elements and Miocene dates suggest that they experienced a different (re)crystallization history than the "Cretaceous–Miocene" titanite and the "zoned Miocene" grains. The trace-element homogeneity and Miocene dates of the "homogeneous Miocene" titanite may reflect thermally mediated volume diffusion of Pb and other trace-elements, titanite neocrystallization in the Miocene, or complete resetting of dates and trace-elements by dislocation-assisted diffusion and/or fluid-mediated recrystallization.

We calculated the erf^{-1} of the normalized concentration gradient for every element measured via LASS in all grains from sample 48A to determine whether any element moved by thermally mediated volume diffusion at the grain scale (Fig. S9A). Of the 40 grains from sample 48A, 17 grains produced *erf*-like relationships between date and at least one element (Pearson's r and r^2 of linear regressions both >0.5; Fig. S9A). However, the specific element (or elements) that define *erf*-like distributions differs grain to grain (Fig. S9A). Further, if trace-element homogenization in "homogeneous Miocene" titanite is a result of volume diffusion, all grains of comparable size (i.e., <500 μm long) should yield homogeneous trace-element compositions. Yet, several <500 μm long grains from sample 48A preserve core-rim zoning in Ce (e.g., "zoned Miocene" grains, Fig. 6). In addition, homogenization of

Ce concentration gradients in even ~50 μm-long titanite would require UHT conditions (>900 °C) for more than 90 Myr (Cherniak, 1995; Holder et al., 2019), which is incompatible with the geology of the Anita Shear Zone and thermodynamic constraints on the deformation temperatures (Czertowicz et al., 2016a; Klepeis et al., 1999). Collectively, these observations indicate that the Miocene dates and homogeneity of trace-element concentrations in "homogeneous Miocene" titanite are incompatible with thermally mediated volume diffusion at the grain scale.

Alternatively, "homogeneous Miocene" titanite may be neocrystallized grains, in which case analyses from these grains should produce a single population of dates with distinct trace-element compositions (e.g., Garber et al., 2017; Walters et al., 2022). Though "homogeneous Miocene" titanite clearly have different trace-element contents compared to "Cretaceous–Miocene" and "zoned Miocene" grains, regression of an inverse isochron through all spots from homogenous titanite reveals that the dates do not define a single population (Fig. 7G). More than ~30 Myr of titanite growth would be required to account for the range in dates in the homogeneous grains, which seems implausible. These observations suggest that "homogeneous Miocene" titanite are unlikely to be neocrystallized titanite.
If dates and trace-element compositions of the "homogeneous Miocene" titanite have been reset by lattice bending and deformation twinning, the degree of lattice bending and/or density of deformation twins should be comparable to "zoned Miocene" titanite. Though some "homogeneous Miocene" titanite have 10° or more of penetrative lattice bending (i.e., more than just the tips of the grain are bent) and have deformation twins (Fig. 7), other grains in this group have only bent tips and/or lack deformation twins (Fig. S4). This indicates that lattice reorientation alone is insufficient to explain the resetting of dates and

trace-element compositions in these grains. Instead, we favor the interpretation that fluids drove recrystallization, U-Pb date resetting, and trace-element homogenization in the Miocene. The similarity between the trace-element composition of "homogeneous Miocene" titanite and the composition of twins from Cretaceous grains, which we suggest were preferentially recrystallized by fluids in the Miocene, supports this interpretation (cf. Figs. 5 and 7). Similar dates between "zoned Miocene" and "homogeneous Miocene" titanite suggest that lattice bending, deformation twinning, and fluid-mediated recrystallization were contemporaneous. Recrystallization in the "homogeneous Miocene" grains may have been promoted by the lattice bending, subgrain boundaries, and twins present in these grains (Moser et al., 2022).

6.1.4 Sample-scale patterns in date vs. trace-element concentrations

These three groups of titanite from sample 48A each yield distinct patterns between dates and trace-element concentrations that combine to produce the date–trace element relationships at the sample scale (cf. Fig. 4A–C and Fig, 10C). In "Cretaceous–Miocene titanite", date–trace element patterns reflect the combination of (1) the varying behavior of dates and trace-element concentrations in domains surrounding deformation twins, resulting in mechanical mixing of domains of varying age but uniform trace-element composition; and (2) portions of the grain wherein dates have been completely reset but the original zoning in the LREEs, Zr, and Hf remains intact (Figs. 5, 10C). The latter domain produces uniformly Miocene dates with the core–rim range in trace-element contents (Fig. 10C). In "zoned Miocene" grains, the complete resetting of dates coupled with the preservation of core–rim zoning results in chiefly Miocene dates that produce the sample scale range of

LREE, Zr, and Hf contents (Figs. 6, 10C). Finally, dates and trace-element concentrations that have both been reset in "homogeneous Miocene" titanite provide Miocene dates with uniform trace-element compositions (Figs 7, 10C).

6.2 Grain-scale relationships among dates, zoning, composition, and microstructure: Sample 45C

Unlike sample 48A, every grain from 45C preserves a broad range of dates (Figs. 8, 9, S5, S6). The range of Cretaceous–Miocene dates in sample 45C may reflect volume diffusion, neocrystallization, interface-coupled dissolution–reprecipitation, dislocation-assisted diffusion, or some combination of these processes. Of the eight grains dated from sample 45C, only two grains have *erf*-like relationships between date and position with the grain (Figs. 8H, 9H, S9B). Neither of these grains yield relationships between Sr concentrations and distance from the edge of the grain, suggesting that *erf*-like distributions of dates are not the result of volume diffusion. Further, there are no consistent correlations between date and U concentrations in grains where *erf*-like distributions of dates are absent, implying that heterogeneities in Pb concentrations did not drive volume diffusion and obscure otherwise straightforward relationships between dates and distance (Fig. S7B; Paul et al., 2019). We note, however, that the effects of heterogeneous parent concentrations could be masked by high common Pb concentrations. Together these observations suggest that the range of dates in sample 45C do not reflect thermally mediated volume diffusion of Pb.

Grains from sample 45C typically preserve core–rim zoning in Ce (Figs. 8C, 9C; S5, S6). In some grains, dates and Ce concentrations are correlated, with dates younging with decreasing Ce concentrations (e.g., Fig. 8G). In grains where dates and Ce concentrations

are correlated, dates are also correlated with other elements that define core–rim zoning, including Fe, P, Sr, Zr, REE, and Y (Figs. 8F, S5). These linear relationships between dates and trace-element concentrations are consistent with analytical mixing of old cores and young rims, each with distinct trace-element compositions. Young rims could have conceivably formed from secondary titanite growth or interface-coupled dissolution–reprecipitation. Straightforward relationships among dates and trace-element concentrations are not present in all grains (Figs. 9, S6) or in all trace elements at the sample scale (Fig. 4D–F) in 45C. For example, the grain in Figure 9 preserves core–rim zoning in Ce concentrations (Fig. 9C), yet there is no correlation between date and Ce concentration (Fig. 9F)—or any other element for that matter (Fig. 9E). Further, some grains in sample 45C preserve patchy Al zoning in grain cores (Fig. 9B) and/or lobate–cuspate rims evident in both Al and Ce WDS X-ray maps (Figs. 9B, C). Such zoning geometries are typically ascribed to interface-coupled dissolution–reprecipitation (Holder and Hacker, 2019; Moser et al., 2022; Walters et al., 2022). Together, these observations suggest that core–rim zoning in sample 45C resulted from interface-coupled dissolution–reprecipitation, and that the resetting of dates and trace-element concentrations was variable both within and among grains (Holder and Hacker, 2019; Moser et al., 2022; Walters et al., 2022). The broad range of dates from both cores and rims in some grains from this sample (Fig. 9) most likely reflects this variable date resetting. The youngest dates (e.g., ~11 Ma) from grains where dates and trace-element concentrations are correlated (i.e., in grains where dates and trace-elements appear to have been reset to the same degree; Fig. 8) suggest that dissolution–reprecipitation of titanite in sample 45C occurred in the Miocene.

The tips of titanite grains from sample 45C are bent up to ~25 °C with respect to the center of grains (Figs. 8A, 9A). Dates consistently young with increasing lattice bending (Figs. 8E, 9E) and subgrains yield among the youngest dates from this sample (Fig. 9A). These relationships between date and lattice bending and/or the presence of subgrains in sample 45C are compatible with the Miocene dates reflecting the timing of deformation (e.g., Moser et al., 2022). Evidence for fluid-driven date resetting in the Miocene, however, makes it impossible to claim that Miocene dates in sample 45C result from lattice bending alone. Note, however, that dates and microstructure are correlated in all but one grain from sample 45C (Figs. 8D, 9D, S5, S6), even in grains that lack straightforward relationships between date and trace-element composition (e.g., Fig. 9). Further, Miocene dates are uncommon in sample 45C, with only 17 of 165 individual spot dates younger than 23 Ma. Of these 17 Miocene dates, 15 come from bent grain tips or subgrains (Figs. 8A, 9A). These aspects of the relationship between dates and lattice bending/subgrains provide compelling evidence that some component of the Miocene dates in this sample resulted from lattice bending and/or subgrain development. Relationships among dates, zoning, trace-element compositions, and microstructure therefore suggest that both dissolution–reprecipitation and lattice bending occurred in the Miocene and that Miocene dates in sample 45C likely reflect a combination of these processes.

Grains from sample 45C also preserve scalloped to lobate–cuspate rims of elevated Fe and Al concentrations and are devoid of U (Figs. 8B, 9B). The geometry of these domains is consistent with their formation via dissolution–reprecipitation. These rims are spatially distinct from and outboard of low Ce and low Fe rims (Figs. 8B, 8C, 9B, 9C), indicating that this fluid event postdated the formation of low Ce and low Fe rims, the latter of which was

contemporaneous with lattice bending and subgrain development. Notably, fluids responsible for Fe- and Al-enriched rims do not appear to have everywhere preferentially recrystallized bent grains tips and subgrains. This is particularly evident in Figure 9, where none of the subgrains have Al contents that match those of these latest-stage rims. Further, in the one grain with deformation twins in this sample, the deformation twins have low Al contents (Fig. S6), indicating that they were not recrystallized by the late-stage fluids. These observations imply that post-deformational fluids do not necessarily exploit microstructures as fast diffusion pathways. Instead, fluid-mediated recrystallization of deformation twins, bent crystal lattices, and subgrains may only be enhanced when these processes are concomitant.

6.3 Conditions and timing of deformation

The titanite and bulk-rock microstructures provide independent constraints on the conditions of deformation of the samples analyzed herein. Feldspars in samples 48A and 106A preserve bulge recrystallization microstructures (Figs. 2B, H; S1) indicating deformation at temperatures >500 °C (Pryer, 1993; Olsen and Kohlstedt, 1985; Tullis and Yund, 1987; Vidal et al., 1980). Though minor brittle fractures are present in feldspar, the orientations of these features are consistent with their occurrence along cleavage planes (Fig. S1), which is typical of plastically deformed feldspar, even at temperatures higher than ~700 °C (Brown and Macaudiére, 1984; Goode, 1978; Kruse and Stünitz, 1999; Kruse et al., 2001; Sodre Borges and White, 1980; Stünitz et al., 2003; Tullis and Yund, 1987). Further, lattice bending and other dislocation-related microstructures have been previously reported in amphibolite-facies titanite (Bonamici et al., 2015; Gordon et al., 2021; Kirkland, et al.,

2018; Moser et al., 2022; Papapavlou et al., 2017). Type IV calcite deformation twins in sample 47A further indicate that deformation occurred at temperatures >250 °C (Fig. 2D; Vernon, 1981; Burkhard, 1993). Finally, none of the analyzed samples preserve a penetrative brittle fabric (Fig. 2), suggesting that deformation of these units was predominantly ductile. The bulk-rock deformation microstructures, including those preserved by titanite, primarily preserve a record of ductile deformation at amphibolite-facies conditions in the ASZ.

All dates from "zoned Miocene" and "homogeneous Miocene" grains in sample 48A were collated to determine the timing of amphibolite-facies deformation. These textural and compositional groupings do not produce single date populations in Tera–Wasserburg space (Fig. 6G, 7G). Probability density functions and associated histograms of all dates from "zoned Miocene" (Fig. 11A) and "homogeneous Miocene" grains (Fig. 10B) yield peaks at ~11 Ma (Fig. 10). These date distributions suggest that titanite ductile deformation, and by inference amphibolite-facies deformation, ended around 11 Ma. An ~11 Ma deformation age is consistent with the youngest dates from bent grain tips in samples 48A and 45C (Figs. 5, 8, 9), the youngest dates in samples 106A and 106E (Fig. 3D, E), and a single titanite date population of 11 ± 1 Ma (MSWD = 0.9, Fig. 3B) in sample 47A.

The range of dates from "zoned Miocene" and "homogeneous Miocene" titanite may reflect protracted titanite deformation, partial resetting of U-Pb dates, or a combination of these processes. The majority of "zoned" and "homogeneous Miocene" titanite preserve single populations of U-Pb dates (i.e., MSWD ~1; Wendt and Carl, 1991; Figs. 6D, 7D, S3, S4). Individual grain single populations range from ~20–7 Ma for "zoned Miocene" (Fig. S3) titanite and ~16–7 Ma for "homogeneous Miocene" titanite (Fig. S4). The range of

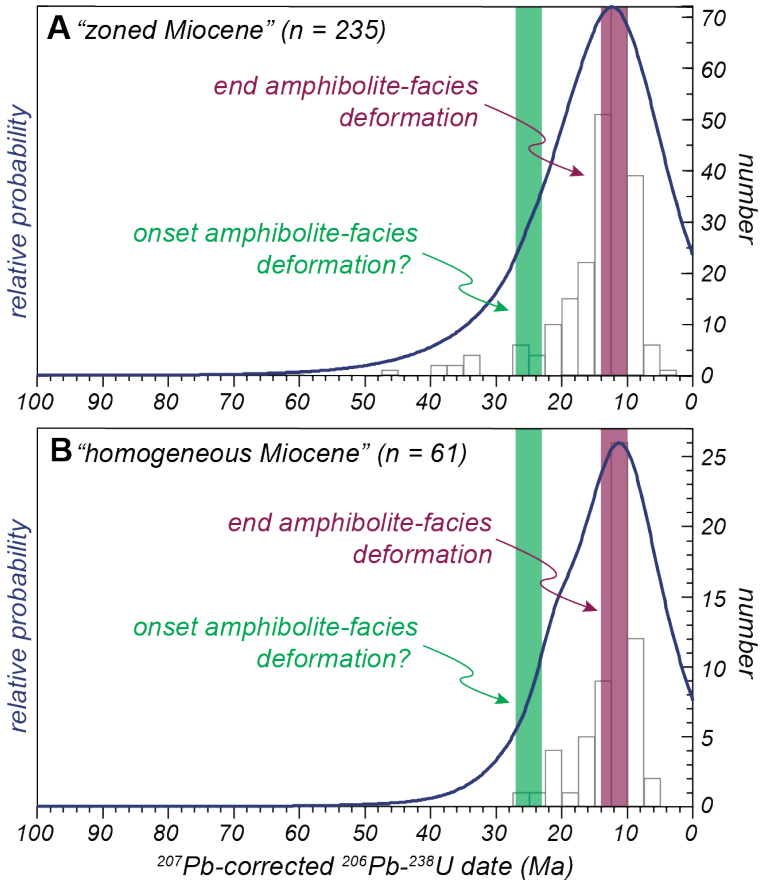

Figure 11. PDFs and histograms of all titanite U-Pb dates from (A) "zoned Miocene" and (B) "homogeneous Miocene" grains from sample 48A. Peaks in these PDFs at ~11 Ma suggest that this is the end of titanite recrystallization during amphibolite-facies deformation.

single populations is distinguishable outside of the associated uncertainties for the "zoned Miocene" grains, but those from the "homogeneous Miocene" titanite overlap within uncertainty. Varying single populations among "zoned Miocene" titanite could reflect the time-progressive resetting of dates among individual grains as conditions became favorable for different grains to deform. The range in single populations among individual "zoned Miocene" grains is consistent with a record of protracted, rather than punctuated, amphibolite-facies deformation. If the range in individual dates from the "zoned" and "homogeneous Miocene" titanite record the duration of this protracted deformation, the spread in dates permits the interpretation that ductile deformation within the ASZ began around ~25 Ma and continued until ~11 Ma (Fig. 10). Deformation beginning at ~25 Ma in the ASZ is compatible with the reorganization of the Pacific–Australian Plate boundary, the onset of transpression, and the development of a throughgoing, strike-slip Alpine Fault system at ~25 Ma (Cooper, 1987; Kamp, 1986). On the other hand, the dispersion in dates in "zoned" and "homogeneous Miocene" titanite could also be explained by a range of partial to complete resetting of dates by dislocation-assisted diffusion and interface-coupled dissolution–reprecipitation. The range of titanite U-Pb dates from the predominantly Miocene titanite are therefore compatible with the onset of ductile deformation at ~25 Ma along the ASZ, but protracted deformation is not required to explain these data.

6.4 Tectonic implications for the Anita Shear Zone

6.4.1 Cretaceous rifting of Zealandia from Gondwana

The ASZ initiated as a low-angle, vertically thinning, extensional shear zone in the lower crust (Klepeis et al., 1999). Comparison with other lower-crustal shear zones in Fiordland

(e.g., Doubtful Sound and Resolution Island shear zones; Fig. 1B; Klepeis et al., 2016; Schwartz et al., 2016) led previous workers to suggest that this early deformation history was most likely related to extensional orogenic collapse of the Zealandia Cordillera (Klepeis et al., 1999). A lack of geochronologic constraints, however, prevented direct testing of this hypothesis. Distributions of titanite U-Pb analyses from samples 48A, 45C, 106A, and 106E indicate that initial titanite crystallization in the ASZ occurred prior to ~90 Ma. We take ~90 Ma to be the youngest possible timing of initial titanite crystallization and formation of the low-angle fabrics in the Anita Shear Zone as it is unclear whether any analysis escaped mixing with Miocene deformed and recrystallized domains (e.g., Fig. 5). The few (i.e., 6 of 165) dates as old as ~120 Ma in sample 45C may reflect titanite growth during regional metamorphism associated with Early Cretaceous plutonism in the adjacent Worsley Pluton (124-122 Ma; Hollis et al., 2003, 2004; Mattinson et al., 1986; Schwartz et al., 2016; Stowell et al., 2014; Tulloch and Kimbrough, 2003).

6.4.2 Miocene deep crustal record of transpression and exhumation

U-Pb dates from "zoned Miocene" and "homogeneous Miocene" titanite are compatible with the onset of transpression along the ASZ at ~25 Ma, coincident with tectonic reorganization of the Pacific–Australian Plate boundary, as a change in Pacific Plate motion caused the Pacific–Australian Plate boundary to become convergent (Jicha et al., 2018; Lebrun et al., 2003; Sutherland et al., 2006). The Alpine Fault also developed as a through-going, strike-slip feature at this time (Cooper, 1987) and subduction along the Puysegur Trench may have initiated as early as ~25 Ma (Klepeis et al., 2019; Lebrun et al., 2003). In addition, feldspar and muscovite $^{40}Ar/^{39}Ar$ dates from structures in central and western

Fiordland indicate that dextral and oblique dextral-reverse slip were active in Fiordland beginning at ~25 Ma (Klepeis et al., 2019). The ASZ is therefore one of several Miocene, dextral transpressive structures that accommodated relative motion between the Pacific and Australian Plates beginning at ~25 Ma, coincident with the initiation of subduction along the Puysegur Trench and the onset of dextral motion on the Alpine Fault. The ASZ, however, is unique in that it provides the mid- to deep-crustal, rather than upper-crustal, record of plate reorganization and the onset of late Oligocene-early Miocene dextral transpression along the Pacific–Australian Plate boundary and broader Alpine Fault system.

Few direct constraints exist on the timing of ductile deformation associated with the onset of transpression along the Pacific-Australian Plate boundary in the Miocene. This presents a rare and much needed constraint on the timing of high-temperature, Miocene transpressive fabrics along the broader Alpine Fault system. Ring et al. (2019) obtained ~11 Ma Rb-Sr muscovite dates from Alpine Schist mylonite proximal to the main trace of the Alpine Fault between the Waikukupa River and Harold Creek (Fig. 1A). Together with PT estimates of mylonitization, these data were interpreted as the end of amphibolite-facies mylonitization of the Alpine Schist (Ring et al., 2019). Our work suggests an identical date for the end of amphibolite-facies along the ASZ. Though these datasets come from only two localities separated by ~300 km along strike of the Alpine Fault, together they suggest a broad synchroneity of the initiation of exhumation of the ductile, deep crustal roots of the broader Alpine Fault system.

The end of amphibolite-facies deformation along the ASZ may reflect a switch in deformation style in Fiordland at ~11 Ma. For example, reverse faults were active in central and northern Fiordland at ~8–7 Ma and have been suggested to have accommodated initial

collision between the leading edge of the Australian slab and the subducted Hikurangi plateau (Klepeis et al., 2019a; Klepeis et al., 2019b). Tectonic reorganization that resulted from this collision may have shut off transpression along the ASZ in favor of more favorably oriented structures in central and northern Fiordland. However, K-Ar white mica dates from greenschist-facies structures at the western margin of the ASZ suggest a switch from amphibolite-facies ductile deformation to greenschist-facies brittle deformation around ~12 Ma (Claypool et al., 2002). Cooling and exhumation to greenschist-facies conditions in the mid-Miocene is compatible with previous low-temperature thermochronology studies that document the initiation of rapid cooling in SW Fiordland around ~25–15 Ma (House et al., 2002; House et al., 2005; Sutherland et al., 2009). Rapid cooling propagated towards the NE through the Miocene, with the onset of cooling reaching northern Fiordland in proximity of the ASZ by ~10 Ma (House et al., 2002, 2005; Sutherland et al., 2009). This cooling signature has previously been attributed to exhumation associated with subduction initiation and the NE propagation of the leading edge of the subducting Australian Plate (House et al., 2002, 2005; Sutherland et al., 2009) and coincides with the timing of reverse motion along the Mount Thunder and Glade-Darran faults in northeast Fiordland (Klepeis et al., 2019). The spatial and temporal overlap of the ~11 Ma titanite deformation age in the ASZ, white mica K-Ar dates in the ASZ, and onset of rapid cooling in NE Fiordland suggests that the end of amphibolite-facies deformation reflects the initiation of cooling and exhumation of the ASZ through the brittle-ductile transition around ~11 Ma, resulting in the localization of strain onto brittle faults along the margins of the shear zone (Claypool et al., 2002; Klepeis et al., 1999). The ASZ therefore provides a window into how the mid to deep crust

responded to this early- to mid-Miocene phase of rapid cooling and exhumation in Fiordland.

6.5 Implications for dating deformation with titanite

This work demonstrates that titanite deformation chronometry provides a means to determine the timing of deformation in polyphase ductile shear zones. Based on correlations to other shear zones, cross-cutting relationships, and limited zircon U-Pb dates, prior work along the ASZ suggested that amphibolite-facies, ductile transpression was Cretaceous (Czertowicz et al., 2016a; Hill, 1995a; Klepeis et al., 1999). The data presented herein indicate that amphibolite-facies transpression also occurred in the Miocene. Titanite deformation chronometry is therefore able to reveal phases of high-temperature deformation that may not be captured by other high-temperature geochronometers (such as zircon U-Pb geochronology) or cross-cutting relationships.

Relationships among dates and microstructure in the ASZ titanite indicate that lattice bending and deformation twins both contributed to U-Pb date resetting. Dates young with increasing lattice bending, spots that overlap deformation twins yield dates in between the inferred Cretaceous crystallization age and the Miocene deformation age, and grains with more penetrative lattice bending and greater densities of deformation twins produce predominantly Miocene dates. Further, titanite in sample 48A are more pervasively deformed than those from sample 45C; grains in 48A have greater degrees of cumulative lattice misorientation, a greater density of deformation twins, and a greater proportion of Miocene dates compared to sample 45C, consistent with the interpretation that lattice reorganization was the dominant mechanism by which dates were reset in the Miocene.

These observations add to a growing body of literature that implies that lattice bending, deformation twinning, and dynamic recrystallization play an important role in resetting U-Pb dates in deformed titanite (Bonamici et al., 2015; Gordon et al., 2021; Moser et al., 2022). However, without observations from a finer spatial scale, such as from atom probe tomography (Piazolo et al., 2016; Kirkland et al., 2018), the precise mechanisms by which these processes reset dates remain unclear.

A major outstanding uncertainty of directly dating deformation with titanite concerns whether lattice reorientation results in direct or indirect resetting of U-Pb dates. In previous studies, the superposition of lattice bending and subgrains on fluid-related zoning has made it difficult to unequivocally state that lattice reorientation was the sole process that affected U-Pb systematics (Gordon et al., 2021; Moser et al., 2022). Instead, workers have postulated that fluids and dislocation-assisted diffusion together reset dates, with the possibility that dislocation-related microstructures only indirectly affect dates by providing efficient pathways for fluids to react with grain interiors (Gordon et al., 2021; Moser et al., 2022). The late-stage, fluid-related rims in sample 45C imply that fluids that post-date deformation do not necessarily preferentially recrystallize bent lattices, subgrains, and deformation twins. Rather, fluid-related recrystallization in bent tips, subgrains, and deformation twins may be enhanced when these two processes occur simultaneously. If true, dates from these features could be taken as the deformation age, even where there is superposed evidence for fluid-driven recrystallization. Further work, however, is required to address this hypothesis.

The ASZ titanite data are inherently complex, with individual grain and sample-scale relationships among dates, composition, and zoning that are difficult to explain by volume diffusion, neocrystallization, or interface-coupled dissolution–reprecipitation alone. It is

only with the additional context provided by the lattice orientation information that these complexities resolve. For example, without the relative misorientation maps, the reason why some grains with core–rim zoning produce Miocene dates ("zoned Miocene" titanite) whereas others yield dates as old as ~90 Ma ("Cretaceous–Miocene titanite") would be unclear. Our study therefore demonstrates that in some instances, lattice orientation information is required to accurately interpret titanite U-Pb dates.

7. Conclusions

Titanite deformation chronometry reveals a previously unknown phase of Miocene, amphibolite-facies, transpressive deformation along the Anita Shear Zone, western Fiordland, New Zealand. Titanite U-Pb dates across four samples predominantly range from ~90–11 Ma, with a single sample yielding a single population of ~11 Ma dates. Detailed grain-scale data (EBSD relative misorientation maps, WDS X-ray maps, LASS U-Pb dates and trace-element concentrations) demonstrate that this range of dates is not readily explained by volume diffusion, neocrystallization, or interface-coupled dissolution–reprecipitation alone. Instead, relationships between dates and lattice bending, as well as dates and deformation twinning, indicate that lattice reorientation as a result of deformation was the primary mechanism by which dates were reset in the Miocene. Lattice reorientation was accompanied by fluid-mediated recrystallization; which variably reset dates and trace-elements concentrations in and around deformation twins. Dynamic recrystallization of feldspar and the lack of a penetrative brittle fabric in the studied samples implies that the bulk of deformation, including plastic deformation of titanite, occurred at amphibolite-facies conditions. Dates from grains interpreted to have been completely reset by lattice bending,

deformation twinning, and fluid-mediated recrystallization are chiefly ~11 Ma, suggesting the end of amphibolite-facies deformation at that time; the range of dates from these grains is compatible with the onset of amphibolite-facies deformation as early as ~25 Ma. These results demonstrate that titanite deformation chronometry is a powerful tool capable of revealing cryptic phases of high-temperature deformation that may not be captured by other high-temperature geochronometers (such as the zircon U-Pb system) or cross-cutting relationships.

The previously unresolved timing of ductile deformation along the ASZ posed major uncertainties for the interpretation of its tectonic significance. The oldest (i.e., ~90 Ma) titanite dates in this study are compatible with initiation of the ASZ in the mid-Cretaceous as a low-angle structure that accommodated lower crustal thinning during the extensional orogenic collapse of the Median Batholith and/or the onset of rifting of Zealandia from Gondwana. The Miocene deformation age for amphibolite-facies transpressive fabrics revealed herein indicate that the ASZ provides a mid- to deep-crustal window into the onset of dextral transpression along the Pacific-Australian Plate boundary, coincident with the development of the Alpine Fault and subduction initiation along the Puysegur Trench. Our dataset represents one of only a few examples that date high-temperature fabrics associated with the onset of transpression along the broader Alpine Fault system. Amphibolite-facies transpression along the ASZ ended at ~11 Ma, and likely reflects exhumation of the shear zone through the brittle-ductile transition, simultaneous with the onset of rapid cooling in northwest Fiordland.

CHAPTER 3: TITANITE PETROCHRONOLOGY DOCUMENTS SECULAR TEMPERATURE AND FLUID EVOLUTION DURING DUCTILE DEFORMATION: AN EXAMPLE FROM CRETACEOUS SHEAR ZONES IN THE EASTERN TRANSVERSE RANGES

1. Introduction

The rheology of the ductile, mid to deep crust plays a fundamental role in the strength of continental lithosphere. Our conceptual and quantitative understanding of how the mid to deep crust deforms, however, is incomplete (e.g., Bürgmann and Dresen, 2008). Many variables influence lithospheric rheology (e.g., mineralogy, temperature, pressure, differential stress, strain rate, fluid abundance and composition), illustrating the inherently complex nature of developing such conceptual and quantitative modelling frameworks (Burlini and Bruhn, 2005; Bürgmann and Dresen, 2008). In addition, the conditions of deformation are not steady state, changing throughout a single phase of deformation. Creating a full picture of how the ductile-plastic portion of the lithosphere deforms requires quantitative constraints on the conditions of ductile deformation and how these conditions vary over the lifetime of individual ductile shear zones. Yet, directly constraining the timescales and conditions of deformation is challenging, and how the conditions of ductile deformation vary throughout a single deformation phase remain poorly understood. This is in part because dating deformation remains difficult, and constraints on the timing vs. the conditions of deformation typically come from separate minerals (e.g., quartz and feldspar (Tullis and Yund, 1987b; Hirth and Tullis, 1992) vs. zircon (Piazolo et al., 2012), monazite (Dumond et al., 2022), titanite (Moser et al., 2022), and apatite (Odlum et al., 2022). There is thus a need for new approaches that combine information on the timing and conditions of

deformation (i.e., temperature, pressure, differential stress, strain rate, fluid abundance and composition) from the same mineral.

The titanite U-Pb system is perhaps one of the best candidates to integrate constraints on the timing and conditions of deformation in ductile shear zones. Titanite is a common accessory mineral in many crustal rocks (Frost et al., 2000) and has a high apparent U-Pb closure temperature (Hartnady et al., 2019; Holder et al., 2019; c.f. Cherniak, 1993), making it more likely to record (re)crystallization than cooling at all but granulite-facies metamorphic conditions. It has a propensity to recrystallize in the presence of metamorphic fluids, which resets U-Pb dates and provide a direct constraint on the timing of fluid infiltration (e.g., Holder and Hacker, 2019). Zr contents in titanite can also be used to document the temperature of (re)crystallization (Hayden et al., 2008). Titanite has been empirically shown to respond to deformation by neocrystallizing synkinematically (Papapavlou et al., 2017) and/or undergoing crystal-plastic deformation (Bonamici et al., 2015; Gordon et al., 2021; Moser et al., 2022), providing a means to link the timing to the temperature and fluid conditions of deformation. However, the full extent to which titanite responds to and records the timing and conditions of ductile deformation remains incompletely understood (Bonamici et al., 2015; Gordon et al., 2021; Moser et al., 2022), limiting its application to structural problems.

This contribution presents an integrated titanite U-Pb, microstructure, zoning, and trace-element dataset from Cretaceous, cm- to dm-scale ductile shear zones hosted in the Jurassic Cottonwood pluton, Eastern Transverse Ranges. These shear zones are ideal for resolving the above problems as their deformation age is (1) independently constrained by aplite dikes and (2) significantly younger than the intrusion age of the host pluton, making it clear which

titanite textures, trace-element compositions, and dates are related to shear-zone deformation. We evaluate the usefulness of titanite petrochronology to delineate not only the timing, temperature, and fluid compositions of deformation, but also how these conditions evolve with ongoing deformation. The dataset further illuminates the diversity of weakening mechanisms that may be concomitant, demonstrating the complex rheological evolution that may occur during a single deformation.

2. Geologic Setting and Field Observations

The Cottonwood Pass area of Joshua Tree National Park is located in the eastern Hexie Mountains of the Eastern Transverse Ranges (Fig. 1). Exposed bedrock comprises Mesozoic Cordilleran arc rocks typical of the Eastern Transverse Ranges and Mojave crustal province basement (Fig. 1; Wooden and Miller, 1990; Powell, 2001; Barth et al., 2008; Needy et al., 2009; Economos et al., 2021). In the field area (Fig. 1B), Proterozoic gneisses (Powell, 2001) were intruded by the granitic to granodioritic Cottonwood pluton at ~155 Ma (Barth et al., 2008) followed by the granitic Smoke Tree Well pluton and granodioritic Porcupine Wash pluton at ~75 Ma (Needy et al., 2009; Fig. 1B). Previous Al-in-hornblende thermobarometry indicates that the Porcupine Wash Pluton was emplaced at ~11 km depth (Needy et al., 2009). There are no emplacement depth estimates for the Cottonwood or Smoke Tree Well plutons. Mesozoic Cordilleran subduction-related arc magmatism ended in the Eastern Transverse Ranges and central Mojave region at ~74 Ma (Economos et al., 2021).

Our observations focus on a series of discrete, cm- to dm-scale mylonitic shear zones that deformed the Jurassic Cottonwood pluton (Fig. 2). These shear zones are anastomosing

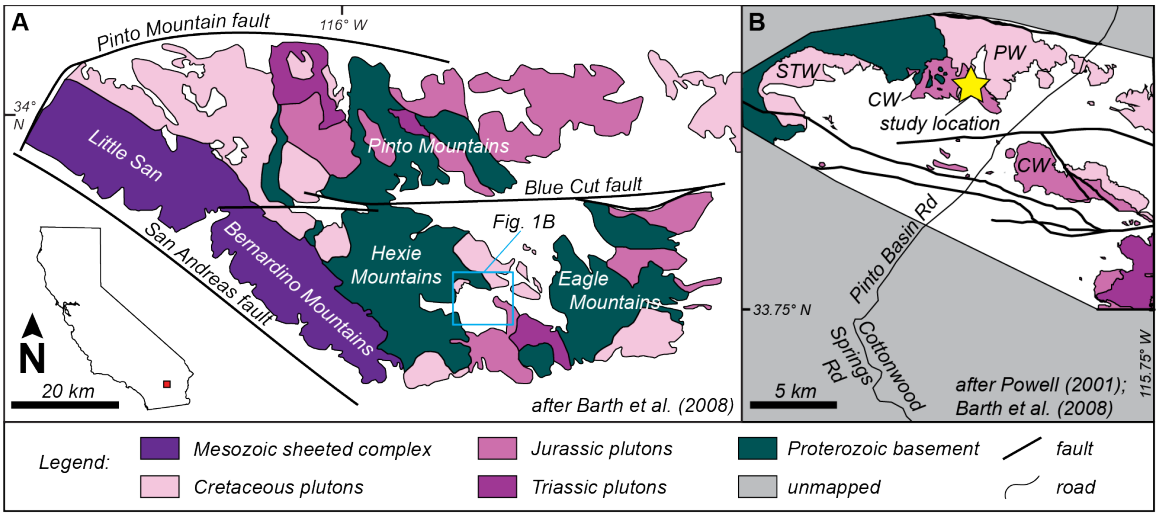

Figure 1. (A) Regional geologic map of the Eastern Transverse Ranges. Inset shows location of Fig. 1B. After Barth et al., (2008). (B) Geologic map of the Cottonwood Pass area of Joshua Tree National Park. Cottonwood pluton (CW); Porcupine Wash pluton (PW); Smoke Tree Well pluton (STW). Yellow star denotes study location. After Powell (2001) and Barth et al., (2008); includes new mapping by the authors.

at the outcrop-scale, bifurcating around relatively undeformed host blocks of the Cottonwood pluton (Fig. 2B). In general, the shear zones are either gently to moderately dipping, broadly NE–SW striking with oblique, normal-sense kinematics, or subvertical, ESE-WNW striking with sinistral kinematics (where shear sense could be determined; Figs. 2C–F; S1). The strike of the gently to moderately dipping shears is highly variable across the field area (Fig. S1). Lineations are gently dipping in both the moderately dipping and subvertical shears (Fig. S1). The shear zones are variably subparallel to and offset aplite dikes (Figs. 2C–F); some offset dikes are continuous for several meters within individual shear zones (Figs. 2E, F). Centimeter-thick quartz veins are common in both the gently to moderately dipping shear zones and are broadly oriented subparallel to the mylonitic foliation; they are never observed cutting the shear zones at a high angle (Figs. 2G, H).

There are few other reports of Late Cretaceous shear zones in the Eastern Transverse Ranges. Recent work describes a km-scale, synmagmatic shear zone with contractional kinematics active at ~76–72 Ma in the Little San Bernardino Mountains (Friesenhahn, 2018). In the central Mojave, km-scale mylonitic shear zones associated with regional extension were active from ~74–68 Ma (Wells et al., 2005; Wells and Hoisch, 2008). Farther south, km-scale ductile thrusts in the Cargo Muchacho Mountains reveal the onset of Laramide contractional tectonics in the southwestern Cordillera around ~65 Ma (Cawood et al., 2022), consistent with recent work that suggests that Laramide orogenesis in this part of the North American Cordillera occurred exclusively after ~74 Ma (Economos et al., 2021). As such, the scale and expression of the Cottonwood shear zones appears to be regionally unique.

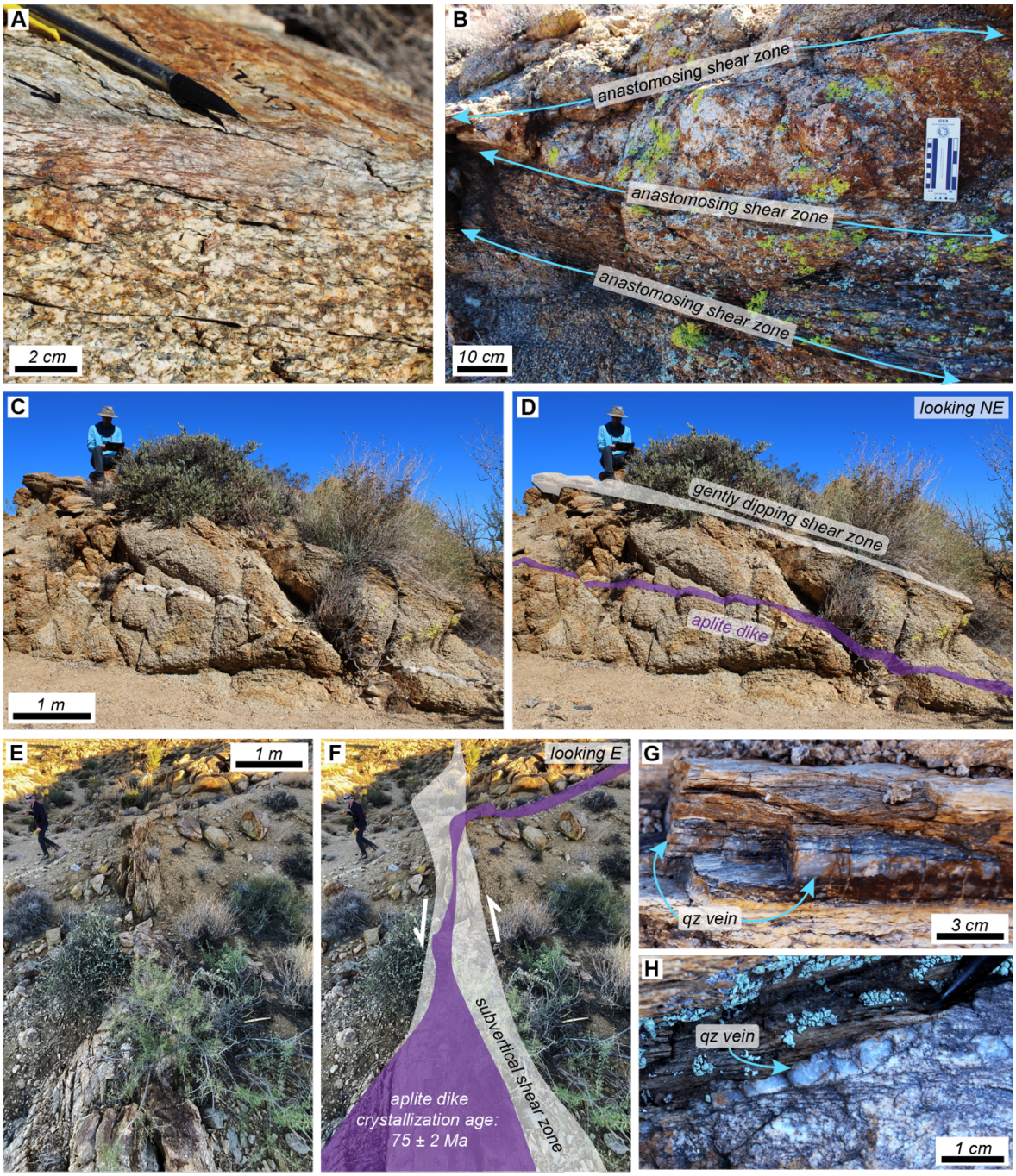

Figure 2. Field photographs of cm- to dm-scale mylonitic shear zones developed in the Cottonwood pluton. (A) Cm-scale shear zone showing strain gradient from relatively undeformed Cottonwood pluton host into core of gently E-dipping shear zone. (B) Shear zones are anastomosing at the outcrop scale, bifurcating around comparatively undeformed blocks of host Cottonwood pluton. (C) Unannotated and (D) annotated photo of gently E-dipping shear zone with subparallel aplite dike. (E) Unannotated and (F) annotated photo of subvertical, ESE-WNW striking shear zone that cuts a ~75 Ma aplite dike. (G, H) Cm-scale quartz veins are common in the shear zones and sub-parallel the mylonitic foliation.

3. Sample descriptions and petrography

We present titanite microtextural, U-Pb, and trace-element data from two Cottonwood pluton mylonites: 5-1A (Fig. 3, S2; 33.807231 N, 115.803005 W) and 18-7A (Fig. 3, S2; 33.807193 N, 115.803447 W). Sample 5-1A is from the shear zone shown in Figure 2B; sample 18-7A is from the shear zone shown in Figures 2E and 2F that offsets an aplite dike. Both samples contain feldspar, quartz, biotite, titanite, ilmenite, magnetite, and minor zircon and apatite (Fig. 3, S2). Feldspar porphyroclasts in sample 5-1A have core-mantle microstructures, with some larger grains displaying irregular or serrated grain boundaries, compatible with subgrain rotation recrystallization (Figs. 3A, C). In sample 18-7A, feldspar is fine-grained and porphyroclasts are absent (Fig. 3B, D). Quartz deformation microstructures in both samples are consistent with recrystallization via subgrain rotation and/or grain-boundary migration (Figs. 3C). Subdomains of larger quartz grains that parallel the foliation are present in both samples (Fig. 3C, D). Titanite grains in the two samples range from euhedral to subhedral, several-hundred μm micron-long grains that typically have their long axes aligned with the foliation (Fig. 3A; S2) to titanite aggregates that are ubiquitously aligned with the foliation, wherein individual grains are ≤50 μm long (Fig. 3B; Fig. S2). The euhedral/subhedral grains are only present in sample 5-1A, whereas titanite aggregates are present in both samples (Fig. S2).

4. Titanite Petrochronology Approach and Methods

Titanite U-Pb dates record a variety of tectonothermal processes depending on the *P-T* and deformation history of a rock. For example, U-Pb dates may reflect one or more phases of igneous and/or metamorphic titanite neocrystallization (i.e., crystallization ages; Spencer et

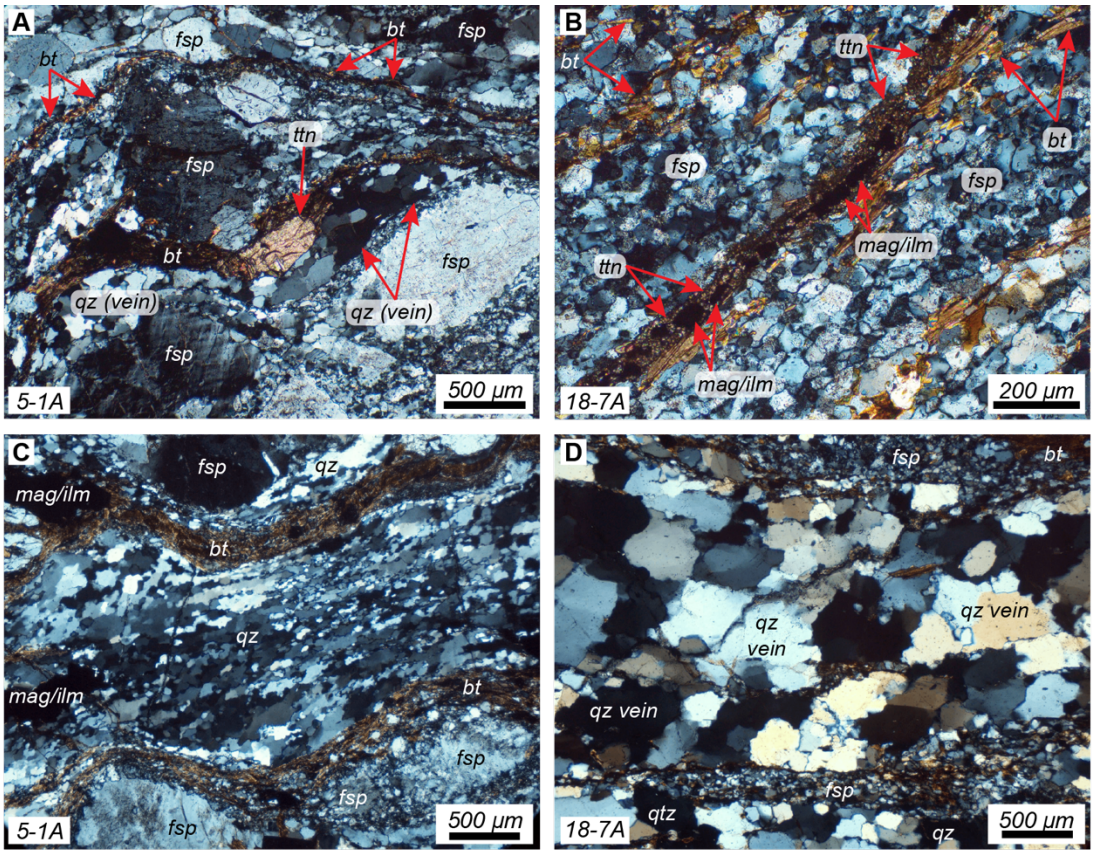

Figure 3. Cross-polarized light photomicrographs showing dominant titanite textures as well as feldspar and quartz microstructures from the Cottonwood mylonites. (A) Sub- to euhedral titanite (sample 5-1A) and (B) titanite aggregates (sample 18-7A). Feldspar microstructures are consistent with subgrain rotation recrystallization of feldspar in sample 5-1A (A, C) and complete recrystallization of feldspar in sample 18-7A (B, D). Quartz deformation microstructures indicate grain-boundary migration (C). The textures of elongate, foliation parallel domains of larger quartz grain size are likely quartz veins (A, D) which are observed in outcrop. Fsp: feldspar; qz: quartz; bt: biotite; ttn: titanite; ilm: ilmenite; mag: magnetite.

al., 2013; Stearns et al., 2016). Thermally mediated volume diffusion of radiogenic Pb produces relationships between date and grain size and/or distance from the edge of a crystal that reflect cooling below the titanite Pb closure temperature (i.e., cooling ages; Dodson, 1973; Cherniak, 1993; Bonamici et al., 2015; Garber et al., 2017). Titanite further recrystallizes via dissolution–reprecipitation recrystallization, wherein a fluid infiltrates a crystal, replaces the original grain with the same or similar phase, alters the trace-element composition, and variably resets the U-Pb dates (i.e., recrystallization ages; Holder and Hacker, 2019; Moser et al., 2022; Walters et al., 2022). The development of crystal-plastic deformation microstructures can also affect U-Pb dates in titanite and other minerals, with dislocations and/or subgrain boundaries variably trapping or serving as fast diffusion pathways for Pb and other trace-elements, or forming efficient conduits for fluids to recrystallize grain interiors (e.g., Reddy et al., 2006; Bonamici et al., 2015; Piazolo et al., 2016; Fougerouse et al., 2021; Gordon et al., 2021; Moser et al., 2022; Odlum et al., 2022).

Each of these processes produces diagnostic intragrain spatial patterns among U-Pb dates, trace-element concentrations, and microstructures that can be used to identify the process responsible for the U-Pb date and trace-element distributions (Cherniak, 1993; Spencer et al., 2013; Bonamici et al., 2015; Stearns et al., 2016; Garber et al., 2017; Walters and Kohn, 2017; Holder et al., 2019; Holder and Hacker, 2019; Moser et al., 2022; Walters et al., 2022). We combine backscattered electron (BSE) imaging, electron backscatter diffraction (EBSD) data, laser-ablation split-stream ICP-MS (LASS) analyses of U-Pb dates and trace-element concentrations, together with electron probe microanalysis (EPMA) measurements of F contents to differentiate among the above processes and relate titanite U-Pb dates to zoning, microstructures, and trace-element compositions. All data were acquired

in standard thickness, microprobe-polished thin sections. A detailed discussion of the effect of volume diffusion on titanite U-Pb dates is included in the supplementary material (Text S1, Fig. S3).

4.1 Scanning electron microscopy (BSE and EBSD)

Scanning electron microscopy (SEM) data were acquired on an FEI Quanta field emission source SEM at the University of California, Santa Barbara. The BSE images were acquired at a 14 mm working distance, 10 kV accelerating voltage, and 1–5 nA beam current. Electron backscatter diffraction (EBSD) data were collected and indexed using an HKL Technology Nordlys II EBSD camera and Oxford/HKL Channel 5 Flamenco software with a 20 kV accelerating voltage, 1–5 nA beam current, and at a ~15 mm working distance. The polished sample surface was tilted 70° with respect to the electron beam. EBSD data were acquired using an electron-beam rastering approach over a 2 × 2 μm grid. The data were processed using Oxford/HKL Channel 5 Tango application; single pixels whose orientations deviated significantly with respect to neighboring pixels were removed, and unindexed pixels were assigned average orientations if at least six of the neighboring pixels were indexed as titanite. Relative misorientation maps were created using Oxford/HKL Channel 5 Tango and titanite pole figures were made using MTEX in MATLAB.

4.2 LASS

Titanite U-Th-Pb isotopes and trace-element concentrations were acquired simultaneously in a single analytical session using the LASS approach outlined by Kylander-Clark et al., (2013, 2017). ^{238}U, ^{232}Th, ^{208}Pb, ^{207}Pb, ^{206}Pb, and ^{204}Pb were analyzed on a Nu Instruments

Plasma HR-ES multicollector ICP-MS. ^{24}Mg, ^{27}Al, ^{28}Si, ^{44}Ca, ^{45}Sc, ^{49}Ti, ^{51}V, ^{52}Cr, ^{55}Mn, ^{56}Fe, ^{88}Sr, ^{89}Y, ^{90}Zr, ^{93}Nb, ^{139}La, ^{140}Ce, ^{141}Pr, ^{146}Nd, ^{147}Sm, ^{153}Eu, ^{157}Gd, ^{159}Tb, ^{163}Dy, ^{165}Ho, ^{166}Er, ^{169}Tm, ^{172}Yb, ^{175}Lu, ^{178}Hf, ^{181}Ta, and ^{182}W were measured on an Agilent 7700X quadrupole ICP-MS. Samples were ablated using a Cetac/Photon Machines 193 nm excimer laser with a HelEx cell, using a 25 μm spot size and ~1 J cm^{-2} laser fluence at 5 Hz for 15 s. Two cleaning shots were fired prior to each analysis and permitted to washout for 20 s.

MKED1 titanite (1521.02 ± 0.55 Ma ^{207}Pb/^{206}Pb ID-TIMS date, Spandler et al., 2016) was selected as the primary standard for U-Th-Pb isotopes and synthetic trace-element glass NIST SRM 612 (Pearce et al., 1997) was the primary trace-element standard. Both primary reference materials were analyzed once for every ~8 unknown analysis. Titanite reference materials BLR (1047.4 ± 1.4 Ma concordia date, Aleinikoff et al., 2007), Y1710C5 (388.6 ± 0.5 Ma common Pb corrected ^{206}Pb-^{238}Pb ID-TIMS date, Spencer et al., 2013), and Fish Canyon (28.4 ± 0.05 Ma, ^{230}Th-disequilibrium corrected ^{206}Pb-^{238}U ID-TIMS date, Schmitz and Bowring, 2001) were analyzed as secondary standards to confirm U-Th-Pb ratio and trace-element concentration accuracies. The ^{207}Pb/^{206}Pb-corrected dates for the secondary titanite reference materials in the analytical sessions presented here were 1046 ± 7 Ma (BLR, MSWD = 1.04; Stacey and Kramers, 1975 common ^{207}Pb/^{206}Pb = 0.91), 394 ± 3 Ma (Y1710C5, MSWD = 0.5; Stacey and Kramers, 1975 common ^{207}Pb/^{206}Pb = 0.86), and 28 ± 1 Ma (Fish Canyon, MSWD = 1.9; Stacey and Kramers, 1975 common ^{207}Pb/^{206}Pb = 0.83), which are all within 1.4% of their known values (Table S1). The trace-element concentrations of the MKED1 analyses are within ~10% of their reported values, which is a typical uncertainty when NIST glass is used as the primary standard (Liu et al., 2008).

The U-Th-Pb and trace-element data were reduced using the Iolite 2.5 plugin for IgorPro 6.37 with the "U-Pb Geochronology3" (for U-Th-Pb isotopes) and "Trace Elements" (for trace-element concentrations, assuming 19.2 wt % Ca in the unknown titanite analyses) data reduction schemes (Paton, 2011). Integrations excluded the first two and last two seconds of each analysis prior to the downhole correction; integrations for unknowns were also trimmed to select only homogeneous date and trace-element portions to remove the effects of inclusions. Reported uncertainties for $^{206}Pb/^{238}U$ and $^{207}Pb/^{206}Pb$ include additional uncertainty propagated in quadrature to make secondary titanite reference material BLR a single population (i.e., MSWD = 1). These additional uncertainties were 2% for $^{207}Pb/^{206}Pb$ and 3.1% for $^{206}Pb/^{238}Pb$. All reported titanite dates are $^{207}Pb/^{206}Pb$-corrected ^{206}Pb-^{238}U dates using a common $^{207}Pb/^{206}Pb$ of 0.86 ± 0.05, as defined by the $^{207}Pb/^{206}Pb$ intercept of an unanchored regression through the youngest population of titanite U-Pb analyses; this value is within uncertainty of the Stacey and Kramers (1976) $^{207}Pb/^{206}Pb$ intercept for the measured dates (0.84).

4.3 Electron probe microanalysis (EPMA)

Quantitative analyses of major and select trace elements in titanite were performed using a Cameca SX100 electron microprobe equipped with five wavelength dispersive spectrometers and Thermo NSS EDS system. The data were acquired with a 15 kV accelerating voltage, 40 nA beam current, and 5 μm beam width. Si K_α, Ca K_α, and Ti K_α X-rays were acquired using EDS. Fe K_α X-rays were analyzed on an LLIF; Mn K_α, Ce L_α, Y L_α, and Nb L_α on an LPET; Al K_α on an LTAP; and F K_α and O K_α on PC0 crystal. Dwell times were 20 s for Y and Nb; 36 s for F and O, 50 s for Mn; 80 s for Ce, Al, and Fe; and

162 s for Si, Ca and Ti. Reference materials included natural and synthetic minerals and glasses. The stoichiometry of each analysis was determined using the workflow outlined in Oberti et al., (1991) with all Fe assumed as ferric.

4.4 Zr-in-titanite thermometry

Zr-in-titanite temperatures were calculated using the Zr concentrations analyzed by LASS and the Hayden et al., (2008) Zr-in-titanite thermometer. We assumed a pressure of 0.3 ± 0.1 GPa for the calculation from previous estimates of the emplacement depth of the Cretaceous Porcupine Wash pluton (~11 km; Needy et al., 2009), which cuts the Cottonwood pluton and was synchronous with aplite dike intrusion and ductile shearing. We further adopted a_{SiO2} = 1 and a_{TiO2} = 0.75 ± 0.25 based on the presence of quartz and titanite, but the absence of rutile (Kapp et al., 2009). We report two uncertainties for each of the temperature estimates: one that includes the uncertainties on the Zr concentrations only (assuming identical pressure and a_{TiO2} among all measured titanite spots), and a second that includes the uncertainties on the pressure and a_{TiO2} estimates.

5. Results

5.1 Titanite petrochronology

5.1.1 U-Pb dates and textures

Titanite LASS analyses (n = 245) were acquired from 14 grains from the two samples (8 sub- to euhedral grains and 4 aggregates from 5-1A, 2 aggregates from 18-7A; Fig. S2, Table S2). The compiled U-Pb data in Tera-Wasserburg concordia space define populations at 151 ± 2 Ma (anchored to initial $^{207}Pb/^{206}Pb$ = 0.86, MSWD = 1.2, 108 analyses; Fig. 4)

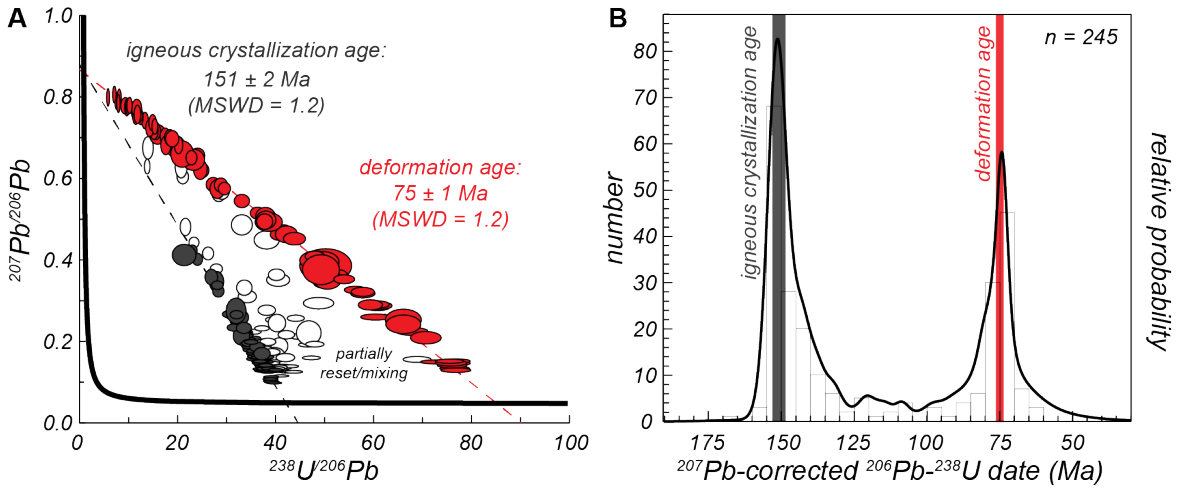

Figure 4. Summary of titanite U-Pb data. (A) Tera-Wasserburg concordia diagram of all 245 titanite LASS analyses from this study. Gray ellipses indicate those used to calculate the oldest population in the dataset, interpreted as the igneous crystallization age of the euhedral titanite. Red ellipses indicate those taken to calculate the youngest population in the dataset, interpreted as the deformation age of the shear zone. White ellipses are those that do not belong to either population and are interpreted to record a combination of partially reset dates and analytical mixing of crystallization and recrystallization ages. (B) Histogram and probability density function of all ^{207}Pb-corrected ^{206}Pb-^{238}U titanite dates illustrating the bimodality of titanite U-Pb dates observed in this study.

and 75 ± 1 Ma (unanchored, MSWD = 1.2, 87 analyses; Fig. 4). A subset of analyses (n = 50; Fig. 4) fall between these populations. Three key relationships among grain morphology, zoning, and microstructure characterize these distinct date populations.

First, all dates from the titanite aggregates belong to the ~75 Ma population (Figs. 5, S4); no age inheritance is observed. BSE images reveal that individual grains within the aggregates are concentrically zoned, have minor lobate–cuspate rims, or are nearly featureless in BSE (Figs. 5A, B, S4). Many individual titanite grains in the aggregates are cored by <10 μm diameter ilmenite inclusions (confirmed by EDS; Fig. 5A, B, S4) and all aggregates are spatially associated with magnetite and ilmenite (confirmed by EDS; Figs. 5A, B; S2, S4). Triple-junction, ~120° grain boundaries are common in the titanite aggregates, though these are more evident (and grain boundaries are straighter) in aggregates from sample 18-7A than in 5-1A (Figs. 5A, B, S4). EBSD data of the aggregates demonstrate that the misorientation between individual grains within the aggregates is >10° (Figs. 5C, D, S4); low-angle boundaries (LABs; 1–10°) are common within individual grains, with aggregates from 5-1A preserving more LABs than those from sample 18-7A (Figs. 5C, D. S4). Pole figures reveal dispersion of the crystallographic axes and poles to crystallographic planes in predominantly great circles; this is particularly evident in the <010> pole figures, in which poles that lie close to the primitive are dispersed along it (Figs. 5E, F, S4). An unanchored Tera-Wasserburg regression of all U-Pb analyses from the aggregate titanite grains from both samples (n = 57) defines a single population at 76 ± 1 Ma (MSWD = 1.2; Fig. 5G).

Second, BSE-dark, lobate-cuspate rims in unbent, sub- to euhedral titanite grains yield dates that predominantly belong to the 75 Ma population (21 of 25 analyses; Fig. 6A, B, S5),

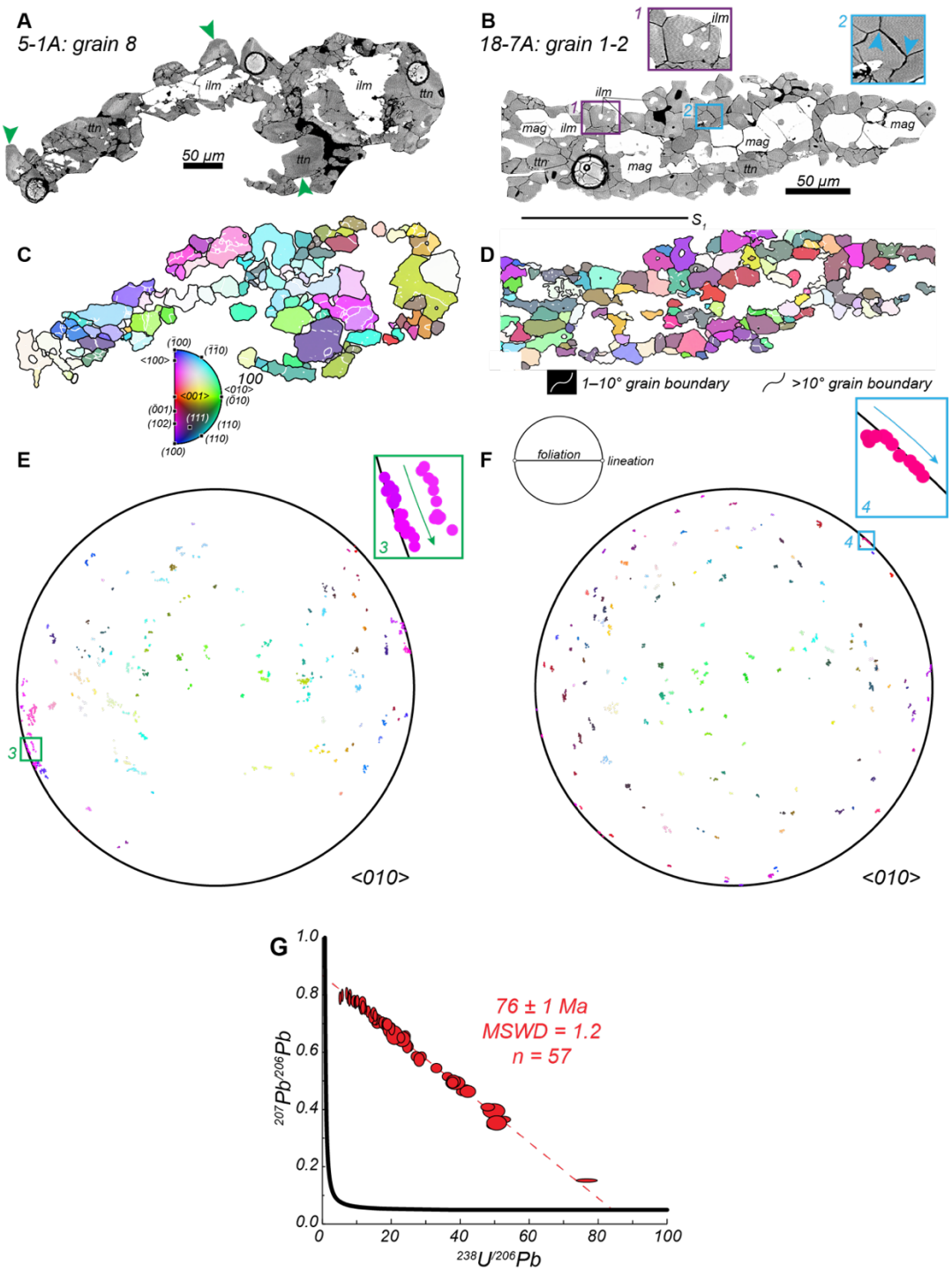

Figure 5. Titanite aggregates from sample 5-1A (left) and 18-7A (right). (A, B) BSE images of aggregate grains. Green arrows in (A) denote lobate–cuspate rims. Inset 1 in (B) shows ilmenite cores. Inset 2 in (B) shows 120° grain boundaries, demarcated by blue arrows. Mineral abbreviations are the same as Figure 3. (C, D) Inverse pole figure (IPF) and grain boundary maps. IPF coloring is shown in legend below (C). (E, F) Pole figures of <010> direction in the grains shown in (A–D). Coloring is the same as IPF. Insets 3 and 4 are enlarged to show detail of dispersion of <010> axes around the primitive. (G) Tera-Wasserburg concordia diagram of all U-Pb analyses (n = 57) from titanite aggregates in the dataset.

with a subset of dates intermediate between the 151 Ma and 75 Ma populations (4 of 25 analyses; Fig. 6A, B, S5). The cores of these grains are characterized by sector and/or oscillatory zoning (Fig. 6A, S5) and largely yield 151 Ma dates (Figs. 6A, S5). EBSD misorientation maps demonstrate that five of the seven sub- to euhedral grains analyzed are effectively unbent (Fig. 6D, S5). The outermost ~20 μm of some of these grain tips are rotated by up to ~6°, but we were unable to sample these domains for LASS analyses due to their small size.

Third, EBSD misorientation maps reveal that two of the analyzed sub- to euhedral grains display up to 10° of continuous intragrain misorientation (Fig. 7A, B). Like the unbent sub- to euhedral grains (e.g., Fig. 6), BSE images demonstrate that these grains contain BSE-dark, lobate–cuspate rims with 75 Ma dates (Fig. 7C, D). Unlike the unbent grains, however, BSE-dark domains cut across the interiors of bent grains, resulting in convoluted and patchy zoning (Fig. 7C, D). Date and misorientation are demonstrably related in these complexly zoned portions (Fig. 7E, F). In one of the bent grains, 15 of 17 analyses from the misoriented grain tip fall between the 151 Ma population and the 75 Ma population (Fig. 7A, E). In the other bent grain, dates young with increasing misorientation and 5 of the 8 analyses that belong to the 75 Ma population lie entirely within lobate-cuspate, BSE-dark domains (Fig. 7D). The majority of dates that fall between the 151 Ma and 75 Ma population when the complete dataset is considered (33 of 50 analyses) come from these two bent grains.

5.1.2 Trace-element chemistry and Zr-in-titanite temperatures

The trace-element compositions and Zr-in-titanite temperatures systematically vary among these date–texture groupings. Aggregates from sample 5-1A are depleted in nearly all REEs

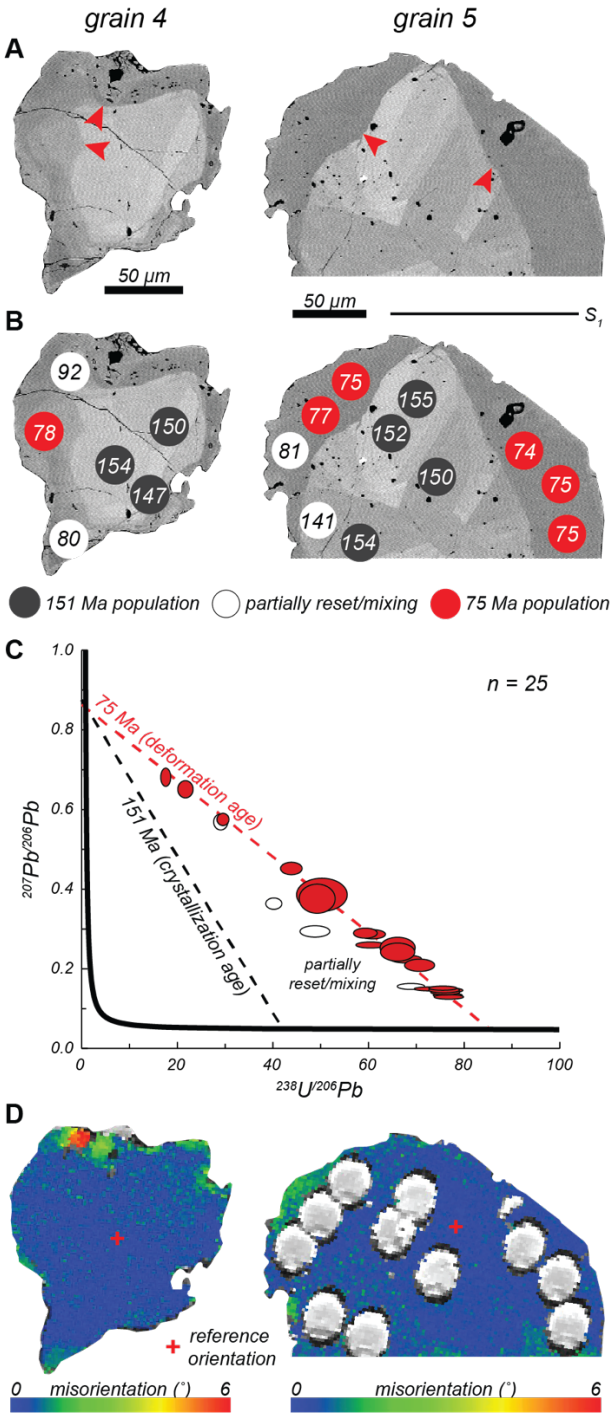

Figure 6. Representative data for unbent, sub- to euhedral titanite in sample 5-1A. (A) BSE images with red arrows indicating lobate–cuspate rims. (B) Same BSE images as (A) with location of LASS analyses. Spots are colored based on the date population to which they belong. Numbers are individual ^{207}Pb-corrected ^{206}Pb-^{238}U dates; the uncertainties on most dates range from ~3–7%. (C) Tera-Wasserburg concordia diagram of all U-Pb analyses (n = 25) from lobate–cuspate rims in the dataset. Ellipses are colored the same as the LASS spots in (B). (D) EBSD relative misorientation maps of the two grains shown in (A) and (B) demonstrating that the lattices of these grains are not bent at scales detectable by the 25 µm laser-ablation spot. Circles in right grain are laser-ablation spots; the EBSD data for this grain were collected subsequent to LASS analyses.

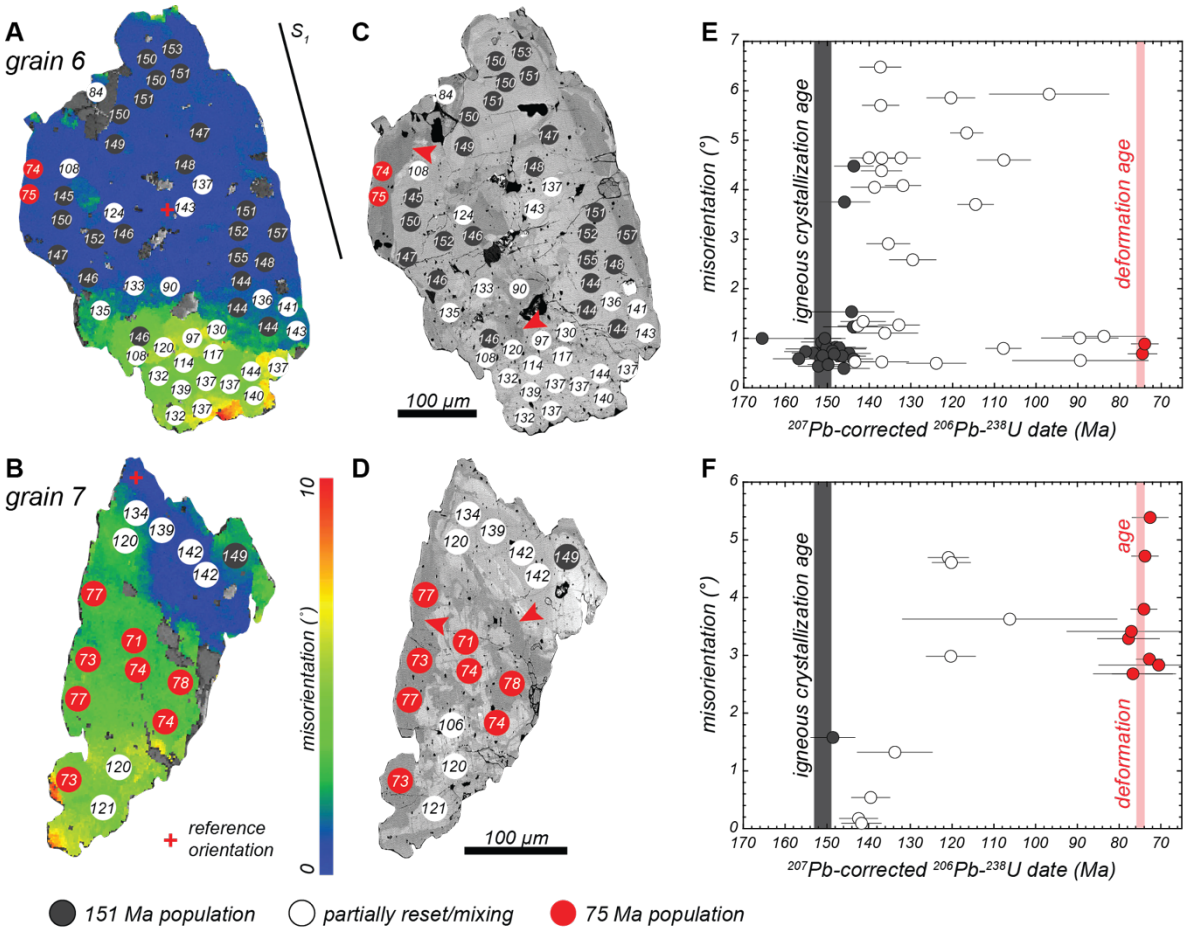

Figure 7. Microstructure, zoning, and relationship between date and lattice bending for the two bent grains from sample 5-1A. (A, B) EBSD relative misorientation maps. Misorientation scale in (B) applies to both grains. (C, D) BSE images of grains shown in (A) and (B). Red arrows indicate lobate–cuspate and patchy textures. Spots in (A–D) are LASS analyses colored by date population. Numbers are individual ^{207}Pb-corrected ^{206}Pb-^{238}U dates for these spots; most date uncertainties are ~3–7%. (E, F) Individual ^{207}Pb-corrected ^{206}Pb-^{238}U date vs. misorientation for the two grains shown in (A–D). Coloring is the same as in (A–D).

(except for Eu), Y, Fe, Zr, Hf, Nb, and Ta when compared to the sector and oscillatory-zoned cores in the same sample (Fig. 8A). The individual trace-element concentrations of the aggregates from the two samples are broadly comparable, though Fe is demonstrably higher, and V and Cr are lower in aggregates from sample 18-7A compared to sample 5-1A (Fig. 8B). BSE-dark rims in sample 5-1A are depleted in the REEs, Y, Sr, Mg, Mn, Fe, Hf, Zr, Nb, and Ta and richer in Cr, Sc, V, and Al compared to their oscillatory and sector-zoned cores (Fig. 8C).

Chondrite-normalized REE profiles of the cores and aggregates from both samples have similarly flat shapes with La depletions (Fig. 9A). The cores yielded a pronounced negative Eu anomaly; Eu anomalies are comparatively minor in the aggregates from both samples, with the aggregates from sample 5-1A yielding a slight negative Eu/Eu* and aggregates from sample 18-7A yielding a slight positive Eu/Eu* (Fig. 9A). M–HREE abundances are similar in the rims from sample 5-1A and the aggregates from both samples; Eu/Eu* is similar in the rims and aggregates from sample 5-1A (Fig. 9A). The LREEs are depleted in the rims in sample 5-1A compared to the cores and aggregates from both samples (Fig. 9A).

Fluorine abundances cluster into two distinct populations: (1) F is generally higher in rims from sample 5-1A compared to oscillatory/sector zoned cores and aggregates from both samples and (2) F contents are similar among aggregates from both samples and the cores from 5-1A (Fig. 9B; Table S3). A subset (3 of 31) of rim F analyses yielded values comparable to cores and aggregates, whereas 4 of 24 F analyses from the aggregates in sample 5-1A are comparable to values from rims (Fig. 9B; Table S3). Rims also have systematically higher $F/(Al+Fe^{3+})$ (Fig. 9B; Table S3). F is positively correlated with Al +

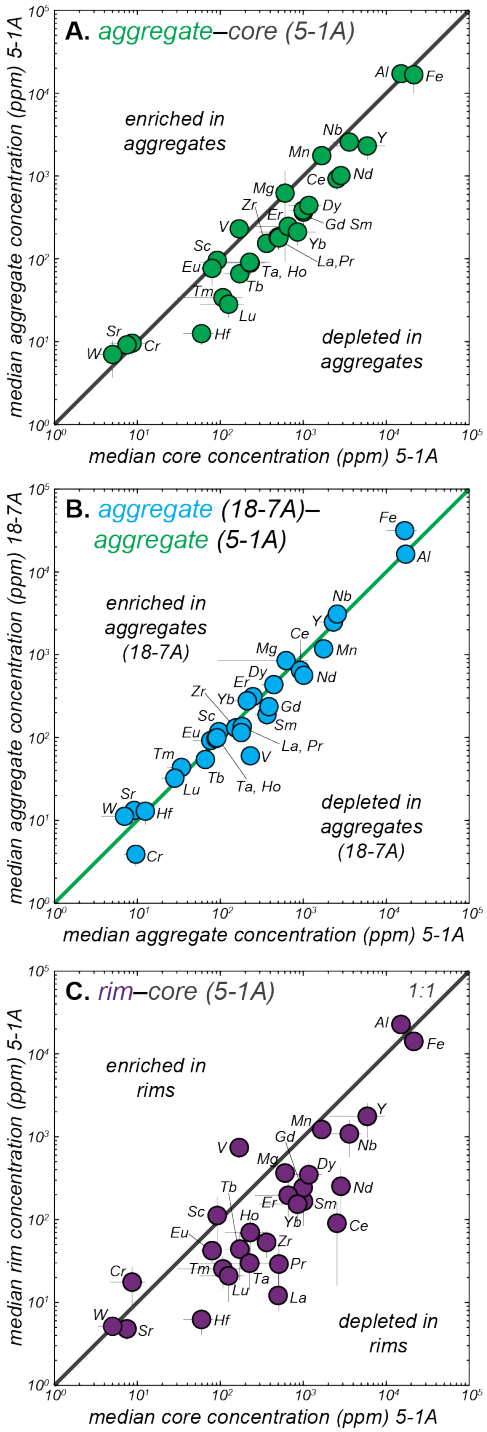

Figure 8. Pseudo isocon diagrams comparing the median trace-element concentrations of the different titanite textures in the two samples. (A) Median aggregate concentrations in sample 5-1A compared to median core concentrations in sample 5-1A. (B) Median aggregate concentrations in sample 18-17A compared to median aggregate concentrations from sample 5-1A. (C) Median rim concentrations in sample 5-1A compared to median core concentrations in sample 5-1A. Only analyses that belong to the 151 Ma population were used to calculate the median trace-element compositions of the cores to capture the unaltered igneous titanite composition.

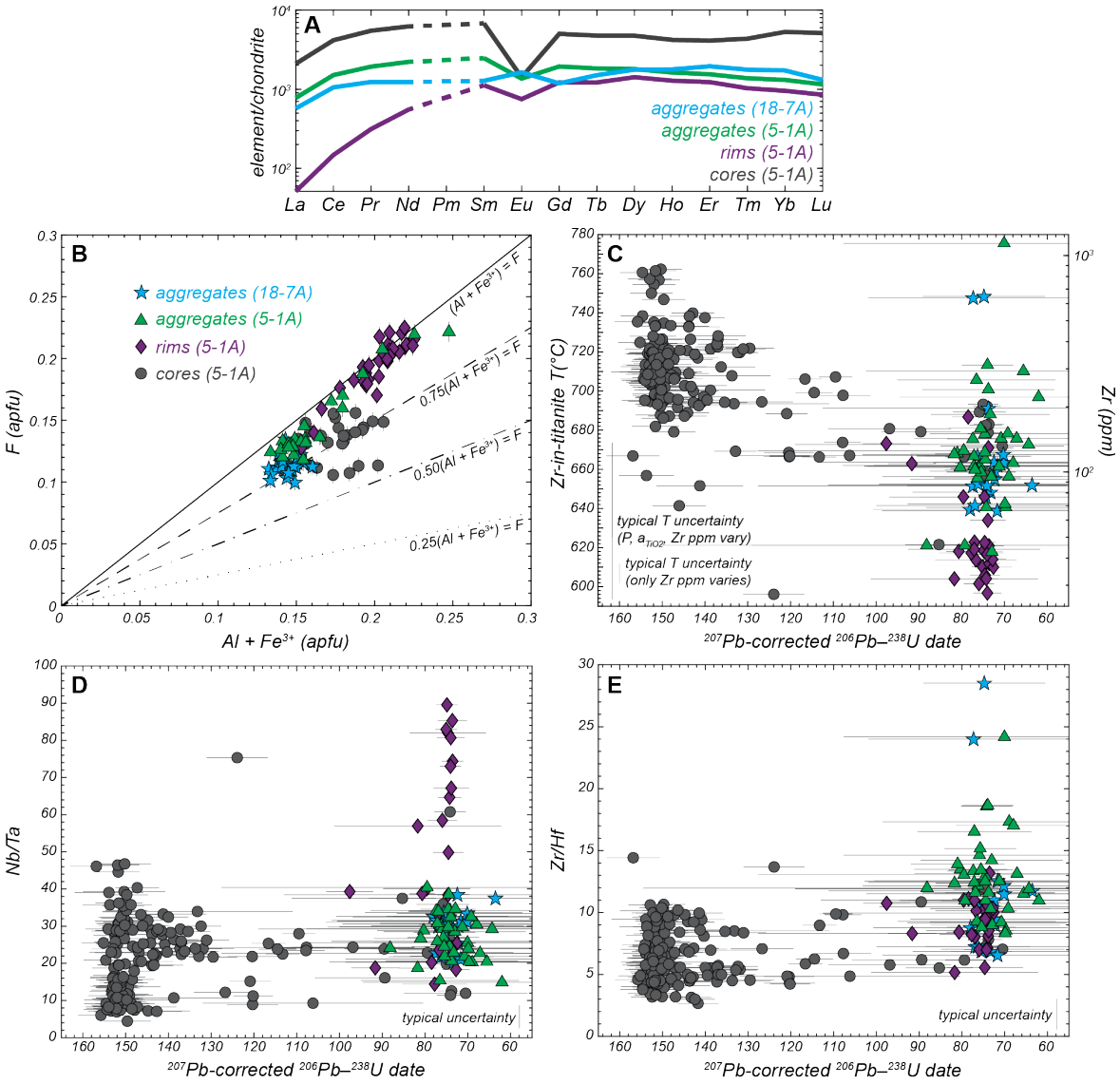

Figure 9. Summary of (A) REE, (B) F contents, (C) Zr-in-titanite temperatures, (D) Nb/Ta, and (E) Zr/Hf among the different titanite textures. REE profiles in (A) are median values for each texture normalized to chondritic meteorite values of Mcdonough and Sun (1995). Only analyses that belong to the 151 Ma population were used to calculate the median core REE values in (A) to capture the composition of the unaltered igneous titanite. Dashed portions of profiles in (A) represent interpolated normalized Pm. Uncertainties not visible in (B) are smaller than the data markers. Representative uncertainties in (C–E) are shown to avoid cluttering the diagrams.

Fe^{3+} (Fig. 9B), consistent with substitution of Al and Fe complexed by volatiles (typically F, OH) in the octahedral Ti site in titanite (Franz and Spear, 1985; Carswell et al., 1996).

Calculated temperatures from the sector- and oscillatory-zoned cores range from ~680–760 °C (Fig. 9C). The temperatures from the aggregates in both samples are predominantly ~640–710 °C (Fig. 9C). The BSE-dark, lobate-cuspate rims record temperatures of ~600–620 °C (Fig. 9C). Although these temperature differences cannot be resolved if the full external uncertainties in pressure and a_{TiO2} are considered, the Zr concentrations of these date-texture populations do differ outside of their 2σ analytical uncertainty (Fig. 9C).

Nb/Ta is similar among the cores and aggregates from both samples (Fig. 9D). In general, Nb/Ta values are higher in the rims than in the cores and the aggregates, though some rim analyses yielded Nb/Ta values that overlap those from cores and aggregates. Rim and aggregate Zr/Hf ratios are similar to but slightly higher than those from cores (Fig. 9E).

5.2 Aplite dike zircon U-Pb data

We acquired zircon U-Pb data from the aplite dike offset by the shear zone in Figure 2E and 2F to independently confirm the timing of deformation along the Cottonwood shear zones (Figure S6, Table S4). The zircon U-Pb data were acquired at the Arizona LaserChron Center; the zircon U-Pb methods and data treatment are presented in the supporting information (text S1). Concordant zircon U-Pb analyses from the aplite dike fall into three groups. Three concordant analyses from oscillatory zoned zircon yield Proterozoic dates between ~1.8 and ~1.6 Ga (Fig. S6). Ten concordant analyses from oscillatory and sector-zoned zircon cores yield a coherent, Jurassic population at 148 ± 3 Ma (MSWD = 2.1; Fig. S6). The youngest, coherent zircon U-Pb date population is defined by five concordant

analyses with a weighted mean ^{206}Pb-^{238}U age of 75 ± 2 Ma (MSWD = 0.9; Fig S6). The analyses that define this 75 Ma population sample sector-zoned cores, oscillatory zoned cores, and oscillatory zoned rims (Fig. S6).

6. Discussion

6.1 Titanite U-Pb date and textural interpretation

6.1.1 Igneous titanite crystallization and shear zone deformation age

The bimodality in titanite U-Pb dates from the two samples (Fig. 4) suggests that these data record the timing of punctuated processes at ~151 and ~75 Ma. Dates that make up the ~151 Ma population are exclusively located within the sector- and oscillatory-zoned cores of the sub- to euhedral grains (Figs. 6, 7, S5). This age also overlaps prior constraints on the intrusion age of the Cottonwood pluton (155 ± 2 Ma, Barth et al., 2008). Together these data suggest that the 151 Ma population represents the igneous crystallization age of the titanite in the Cottonwood pluton (Fig. 10A). The younger, ~75 Ma titanite population is indistinguishable from the youngest coherent population of zircon U-Pb dates from the aplite dike (Fig. S6). Because the analyses that comprise the ~75 Ma zircon population are sampled from sector-zoned cores, oscillatory zoned cores, and oscillatory zoned rims, we take ~75 Ma as the crystallization age of the dike. As the aplite dikes are offset by the shear zones, they provide an independent constraint that deformation must have occurred at or after 75 Ma. Given this context, the ~75 Ma titanite population most likely reflects the timing of deformation along the ductile shear zones. Each of the three titanite textural groupings described in section 4.1.1 can be linked to separate, but related processes active in the ductile shear zones at ~75 Ma.

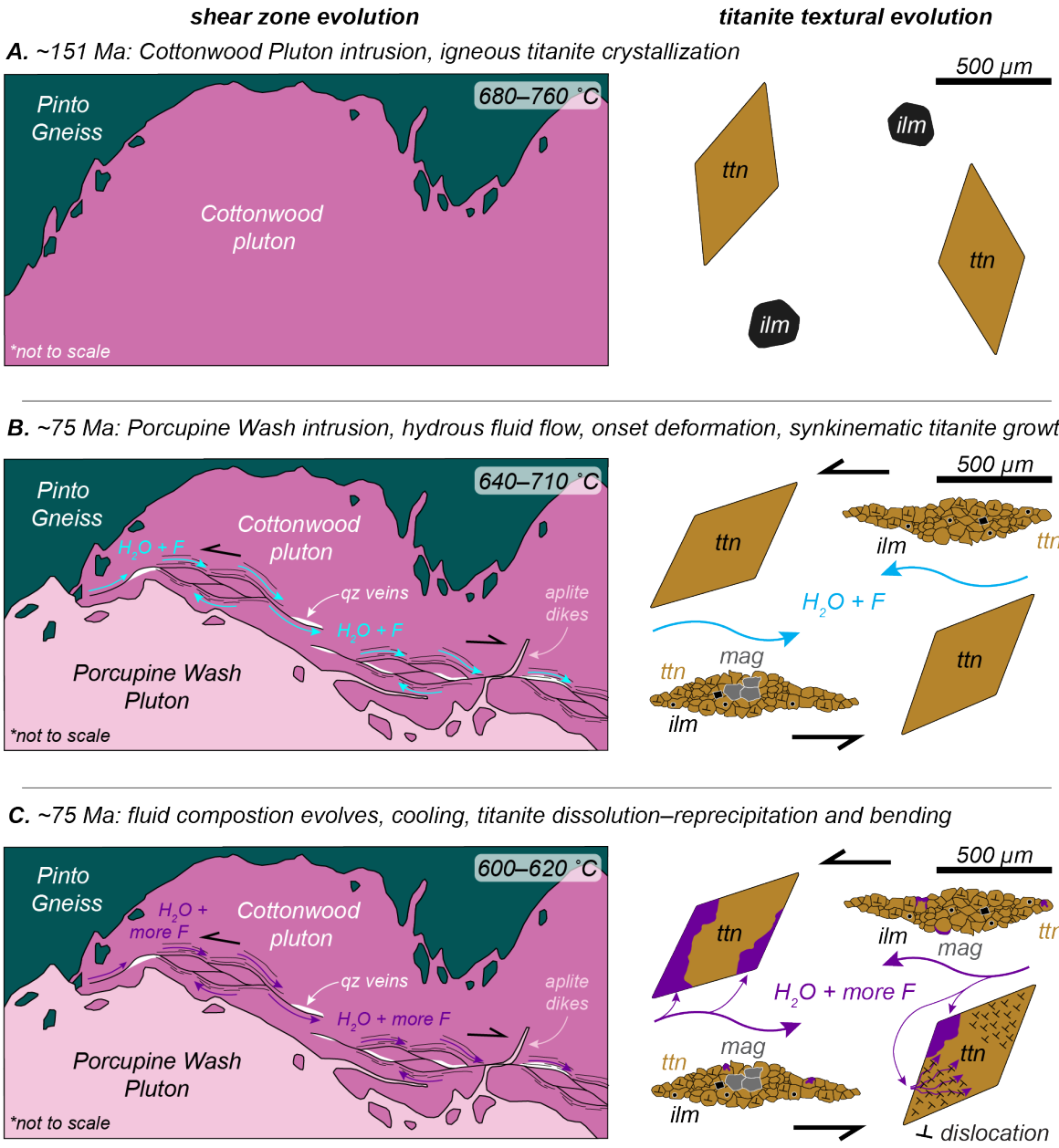

Figure 10. Cartoon summary of Cottonwood shear zone and titanite textural evolution. (A) At ~151 Ma, the Cottonwood pluton intruded the Pinto Gneiss. The sub- to euhedral igneous titanite crystallized in the host pluton, recording temperatures of ~680–760 °C. (B) At ~75 Ma, the Porcupine Wash (and Smoke Tree Well) plutons intruded along with the aplite dikes. Deformation and hydrous, F-bearing fluid flow initiated at ~640–710 °C and was recorded by synkinematic titanite neocrystallization. The synkinematic aggregates deformed via dislocation creep. (C) Less than 1 Myr later, the fluid composition evolved to be more F-enriched and the system cooled to ~600–620 °C, recorded by lobate-cuspate, dissolution–reprecipitation rims on the sub- to euhedral titanite. Fluid-mediated recrystallization of the sub- to euhedral grains was enhanced by lattice bending. Recrystallization of the titanite aggregates by the cooler, F-enriched fluids was less extensive compared to the sub- to euhedral grains. Mineral abbreviations are the same as Figure 3.

6.1.2 Synkinematic titanite growth at 75 Ma

Dates from the titanite aggregates define a single population that is consistent with the maximum deformation age defined by the aplite dikes; there is no trace of an inherited, igneous crystallization age in these titanite (Fig. 5). These aggregates are spatially associated with magnetite and/or ilmenite and some individual grains within the aggregates preserve small ilmenite cores (Figs. 3B, 5A, B, S2, S4). In addition, all aggregates are aligned with the foliation in both samples (Figs. 3B, 5, S2, S4). Together, these data and observations suggest that the aggregate grains formed as a result of synkinematic titanite neocrystallization at 75 Ma, rather than recrystallization of Late Jurassic igneous titanite (Fig. 10B).

The microstructure of the aggregates implies that these titanite grains actively deformed and flowed as they crystallized (Figs. 5, S4). Many individual aggregate grains contain low-angle grain boundaries (Figs. 5C, D, S4); crystallographic axes as well as poles to planes are dispersed along great circles (Figs. 5E, F, S4). These data are consistent with the deformation of these titanite aggregates by dislocation creep, most likely subgrain rotation recrystallization (Lloyd et al., 1997). The polygonal nature of the aggregate grains indicates that temperatures remained high enough after deformation ceased to cause grain boundary area reduction (Bons and Urai, 1992; Gordon et al., 2021).

6.1.3. Titanite dissolution–reprecipitation during deformation

The sub-to euhedral titanite preserve BSE-dark, lobate–cuspate rims that predominantly yield ~75 Ma dates (Figs. 6, S5). Such textures are compatible with recrystallization via dissolution–reprecipitation, a process by which fluids drive recrystallization, changing the

trace-element composition of a grain but preserving the grain shape (Geisler et al., 2007; Putnis, 2009). Strikingly similar textures have been observed in numerous other titanite grains interpreted to have recrystallized via dissolution–reprecipitation (Garber et al., 2017; Holder and Hacker, 2019; Moser et al., 2022; Walters et al., 2022). The dates from the lobate–cuspate rims are identical (within uncertainty) to the timing of deformation recorded by the synkinematic titanite aggregates (Fig. 5). These observations imply that the sub- to euhedral, protolith igneous titanite recrystallized via interface–coupled dissolution-reprecipitation during ductile deformation at ~75 Ma (Fig. 10C). Some rims are nearly continuous around entire titanite grains, and we do not observe any textures indicative of dissolution–reprecipitation creep ("core and beard" structures; Wintsch and Yi, 2002). Therefore, fluid-driven recrystallization was most likely interface-coupled and did not directly cause titanite deformation.

5.1.4. Fluid-driven recrystallization in bent grains

The relationship between dates and microstructure in the two grains with bent crystal lattices suggests that lattice bending played some role in resetting U-Pb dates in some grains (Fig. 7). In one grain, dates from the bent grain tip scatter between the igneous titanite crystallization age and the deformation age of the shear zone (Fig. 7A, C, E). In the other grain, dates young with increasing lattice bending and only 1 out of 17 analytical spots preserves the igneous crystallization age of the grain (Fig. 7B, D, F). These relationships imply that either the development of lattice bending directly facilitated Pb loss via dislocation-assisted diffusion (e.g., Piazolo et al., 2016; Gordon et al., 2021) or that the

microstructures served as efficient pathways for fluids to infiltrate and recrystallize bent domains (e.g., Moser et al., 2022).

The zoning, dates, and trace-element signatures of the titanite microstructures are most consistent with the latter interpretation, i.e., preferential reaction of bent domains with the fluids responsible for dissolution–reprecipitation recrystallization. This is supported by the observation that deformation microstructures (EBSD) correlate with convoluted and/or patchy trace-element zoning (BSE), and it is *only* in bent domains that BSE-dark, fluid-related zoning is observed in grain interiors (cf. Figs. 6 and 7). For example, a BSE-dark compositional domain cuts across the entirety of the smaller of the two deformed grains and is continuous with a BSE-dark lobate–cuspate rim that likely formed by dissolution–reprecipitation recrystallization (Fig. 7D). Further, dates from the bent grains range from the igneous crystallization age to the deformation age (as recorded more robustly by aggregates and fully recrystallized rims). This date span can be explained by either mechanical mixing of fully fluid-reacted and unreacted, igneous domains, or a range of partial to complete resetting of U-Pb dates. Mechanical mixing should produce mixing lines between the ~151 Ma population (i.e., cores) and the ~75 Ma population (i.e., rims) for every measured trace element. The relationship between dates and trace-element concentrations in the bent grains could plausibly be explained by mixing for some elements, but not for every element measured (Fig. S7). For example, Ce concentrations decrease monotonically with younging date in the bent grains (Fig. S7; consistent with mechanical mixing), but V concentrations in areas of convolute zoning retain the composition of unreacted cores (Fig. S7). These data are consistent with the variable resetting of dates and trace-element signatures, as commonly observed in fluid-recrystallized domains (Holder and Hacker, 2019; Moser et al., 2022;

Walters et al., 2022). This indicates that the range of dates in the bent titanite at least partly result from partial resetting by dissolution–reprecipitation, though the small size of some fluid-reacted domains indicates that some mechanical mixing did occur. Together with the observations of convoluted and patchy zoning in the interior of the bent titanite, these data imply that titanite dislocation creep was not wholly sufficient to totally reset the titanite U-Pb and trace-element systematics, and instead facilitated enhanced fluid-related recrystallization in these grains (Fig. 10C).

6.2 Evolution of temperature and fluid composition during deformation

Calculated Zr-in-titanite temperatures from the titanite aggregates from both samples and the lobate–cuspate rims are predominantly ~600–700 °C, with most temperatures from the rims ~30 °C (or ~30 ppm Zr) lower than those from the titanite aggregates (Fig. 9C). This difference may reflect an increase in pressure, a difference in quartz, zircon, or rutile activity, or a true temperature difference between the two titanite populations. Assuming constant temperature, a 30-ppm difference in Zr concentrations would require an increase in pressure of ~0.2 GPa between aggregate and rim (re)crystallization, or about ~7.5 km of burial in timescales undetectable by the precision afforded by LASS for these dates (i.e., ~1–3 Myr). This is geologically unreasonable and can be ruled out as the primary cause. The presence of quartz and zircon indicate that the a_{SiO2} and a_{ZrSiO4} of the system are both 1, and the varying Zr-in-titanite temperatures are not easily explained by under-estimating a_{SiO2} or over-estimating a_{ZrO2}. Underestimating a_{TiO2} by ~0.25 in the rims (i.e., $a_{TiO2} = 1$ instead of 0.75) could explain a ~15 °C difference in calculated Zr-in-titanite temperatures between cores and rims, but this cannot account for the totality of the offset. Varying a_{TiO2} also seems

less plausible given that the two titanite textures occur in the same rock. Alternatively, the lower Zr contents in the rims could reflect ~30 °C of cooling between synkinematic titanite aggregate crystallization and dissolution–reprecipitation recrystallization of the titanite rims. This would imply that the titanite aggregates record early deformation at temperatures >630 °C, with rim recrystallization occurring as the system cooled (Fig. 10B, C). Such an interpretation is supported by the indistinguishable dates between the aggregates and rims. We therefore find it most plausible that the two ~75 Ma titanite textures with varying Zr content faithfully record the temperature evolution of the shear zone as deformation progressed.

The two titanite textures with the same age (aggregates and rims) but different trace-element compositions (Figs. 8, 9) require that two titanite-producing reactions occurred at timescales shorter than LASS uncertainties (i.e., <1–3 Myr). The increase in F compositions and $F/[Al+Fe^{3+}]$ in the rims compared to the aggregates suggests that the two titanite-producing reactions reflect changing fluid compositions as deformation progressed. Elevated F contents alone could be explained by rims enriched in Al (as F incorporation into titanite is complexed with Al and is thus "Al limited"); however, the increased $F/[Al+Fe^{3+}]$ indicates a difference in absolute F contents of the system between aggregate and rim (re)crystallization.

Several aspects of the mineralogy of the mylonites, as well as the geochemistry of the fluid-reacted titanites, are consistent with a predominantly hydrous fluid accompanying deformation. The mylonites lack carbonate minerals that would indicate high CO_2 fluid pressures. In addition, the samples contain other hydrous phases (biotite, apatite) that most likely (re)crystallized during deformation. Further, the presence of titanite over rutile and

ilmenite is consistent with high a_{H2O} (Frost et al., 2000; Kohn, 2017). Finally, the loss of REEs and high field-strength elements in fluid-recrystallized rims is consistent with their recrystallization in the presence of a hydrous, halogen-bearing fluid (Migdisov et al., 2009; Rapp et al., 2010). The titanite chemistry thus records the evolution of the fluid that accompanied deformation from a hotter (640–710 °C), more hydrous fluid (during aggregate crystallization; Fig. 10B) to a cooler (600–620 °C), more halogen-rich brine (during rim recrystallization; Fig. 10C).

The fluid composition evolution could reflect the closed-system partitioning of elements into co-crystallizing mineral phases (such as biotite or apatite) or an open-system change in fluid composition. The rim-forming reaction resulted in the enrichment of F, increased F/[Al+Fe^{3+}], depletion of LREEs, elevated Nb/Ta, and unchanged Zr/Hf compared to the aggregate titanite grains (Figs. 8, 9). Co-crystallization of biotite should result in LREE depletion (Mahood et al., 1983) and similar Zr/Hf ratios between the two textures (Nash and Crecraft, 1985). However, co-crystallizing biotite would not drive titanite enrichment in F (as biotite preferentially incorporates F over OH; Zhang et al., 2022) or elevated titanite Nb/Ta ratios (as D_{Nb}/D_{Ta} is higher for biotite than for titanite; Nash and Crecraft, 1985; Prowatke and Klemme, 2005; Acosta-Vigil et al., 2010; Stepanov and Hermann, 2013). Similarly, co-crystallizing apatite could deplete LREEs (Prowatke and Klemme, 2006), but F contents, Nb/Ta, and Zr/Hf should all *decrease* in titanite that (re)crystallized with apatite (Mathez and Webster, 2005; Prowatke and Klemme, 2006). Alternatively, if the fluids were sourced from the Smoke Tree Well pluton (which intruded at ~75 Ma), then the change in fluid composition could reflect the evolving fluid composition as the pluton crystallized. Fluorine is preferentially incorporated into the residual melt in igneous systems rather than

the exsolved fluid phase; the F-enriched fluids recorded by the titanite rims could represent a transition from pluton-derived fluids to aplite-derived fluids. However, late-stage exsolved fluids typically only evolve to high F contents if systems are significantly F-enriched (e.g., fluorite precipitating; Dolejs and Zajacz, 2018). Regardless of how or why the fluid composition changed, the elevated F contents and increased $F/[Al + Fe^{3+}]$ contents in the titanite rims are consistent with the fluid evolving towards a more F-rich brine as deformation progressed (Fig. 10B, C).

A few analyses from lobate–cuspate BSE dark rims retain trace-element compositions, including F, Zr, and Nb/Ta, that are similar to cores and the aggregate grains (Fig. 9B–D). These data indicate that either some rim development commenced at the same temperature and fluid conditions as synkinematic titanite aggregate neocrystallization, or that trace-element contents were incompletely reset from their core compositions. If these values record "early" rim development (i.e., prior to cooling and evolution of fluid to more F-enriched brine, synchronous with aggregate crystallization) then the analyses with "core/aggregate-like" Zr contents should also retain "core/aggregate-like" Nb/Ta. This, however, is not the case, as several spots with low Nb/Ta (i.e., <40) also yield low Zr contents (i.e., <630 °C or <60 ppm; Fig. S8). Further, the three EPMA analyses from rims with F contents similar to aggregates and cores are located near LASS analyses that yielded incompletely reset U-Pb dates (Fig. S9). These data indicate that these rare rim spots with "core/aggregate-like" trace-element compositions reflect incomplete resetting rather than early rim development.

Conversely, four EPMA analyses from aggregate grains produced F-contents similar to those in rims (Fig. 9B) and three LASS analyses from aggregates yielded Zr contents and

thus temperatures consistent with depleted values observed in rims. These F-enriched and Zr-depleted spots from aggregates are predominantly located within BSE-dark, lobate-cuspate domains at individual grain margins (Fig 5A, Fig. S9). These observations demonstrate that aggregates did experience some interface-coupled dissolution–reprecipitation after they crystallized, although fluid-recrystallization was clearly more extensive in the sub- to euhedral igneous titanite (cf. Figs. 5 and 6). Fluid-mediated recrystallization of the aggregate grains by the F-enrich fluid confirms that such recrystallization post-dated synkinematic titanite neocrystallization. This observation supports the contention that the lower temperatures and higher F-contents of rims record the time-progressive evolution of temperature and fluid composition in these shear zones.

6.3 Tectonic significance of the Cottonwood shear zones

The limited range of Cretaceous titanite U-Pb dates suggest that the Cottonwood shear zones represent a short-lived pulse of Cretaceous crustal weakening; here we consider the possible tectonic drivers of these features. One explanation is that these structures represent a punctuated, mid-crustal response to regional tectonism. However, field observations and structural data demonstrate that the geometries of these shear zones vary at the m and tens of m scale, and their complex kinematics are not readily explained by a prevailing regional tectonic stress field (Fig. S1). Further, though the shear zones are synchronous with the end of Cretaceous magmatism (Economos et al., 2021) and the onset of extension and exhumation in the broader Mojave (Wells and Hoisch, 2008), other regional, Late Cretaceous shear zones in the southwest Cordillera have km-scale mylonite zones (Wells and Hoisch, 2008; Friesenhahn, 2018; Cawood et al., 2022), some of which host evidence

for voluminous fluid flux (Wells and Hoisch, 2008; Cawood et al., 2022). These observations are inconsistent with the formation of the Cottonwood shear zones as regional tectonic structures, which are expected to have consistent kinematics and geometries, as well as a similar age and deformation style, as other Late Cretaceous, regional shear zones in the southwest Cordillera.

Alternatively, the Cottonwood shear zones may have formed in response to local plutonism, such as the intrusion of the ~75 Ma Porcupine Wash and Smoke Tree Well plutons (Fig. 1B; Needy et al., 2009). In this model, the shear zones accommodated the emplacement of the plutons themselves and/or represent weakening of the host rocks from the thermal/fluid pulse associated with plutonism. Such a causal relationship between plutonism and shearing predicts several relationships. First, deformation along the shear zones would be broadly coeval with plutonism. Second, the duration of deformation is expected to mirror the duration of magmatism, which for the Cottonwood area plutons should be ~1 Myr based on the limited age range of the local Late Cretaceous plutons (Fig. 1B; ~75 Ma plutons only, Needy et al., 2009). A causal relationship between plutonism and deformation also predicts a spatial relationship between the plutons and shear zones; shear zone density would likely increase with proximity to the pluton due to the localized stress field and/or the thermal/fluid aureole surrounding the pluton. Evidence for weakening as a result of fluid influx may include the localization of veins and dikes along shear zones and/or evidence for fluid-driven recrystallization within the shear zones.

Our data nominally agree with these predictions and support the notion that these ductile shear zones developed in response to local Cretaceous plutonism. The titanite and zircon U-Pb data reveal that shearing and fluid flow in the Cottonwood shear zones—and intrusion of

the aplite dikes, Porcupine Wash, and Smoke Tree Well plutons—were geologically synchronous and short-lived (i.e., less than a few million years), suggesting that these processes were concomitant. Further, mapping and field observations reveal that the shear zones are broadly clustered within tens of m of the Cottonwood–Porcupine Wash contact, though further work is required to confirm their spatial extent. Finally, quartz veins that subparallel the mylonitic fabric (Figs. 2G, H; 3A, D) testify to high fluid pressures synchronous with shearing, and the ~75 Ma fluid-recrystallized rims in the titanite provide evidence for localized fluid flow that was contemporaneous with deformation. Our data and observations are therefore compatible with the cm- to dm-scale Cottonwood shear zones reflecting a transient phase of deformation, heating, and fluid flow that accompanied the emplacement of the Porcupine Wash and/or Smoke Tree Well plutons, reflecting localized rather than regional crustal weakening. However, additional data, including high precision geochronology from the plutons, dikes, and shear zones, as well as more extensive mapping, are required to further test this hypothesis.

6.4 Implications for dating deformation with titanite

Previous titanite datasets demonstrate that titanite U-Pb petrochronology is potentially a useful tool to constrain the timing of ductile deformation (Bonamici et al., 2015; Papapavlou et al., 2017; Gordon et al., 2021; Moser et al., 2022). Here, dates from deformed, synkinematic titanite aggregates provide an unequivocal deformation age for the studied shear zones. In addition, the trace-element compositions of the titanite aggregates and rims document the temperature at which deformation initiated, cooling of the system as deformation progressed, as well as the evolving volatile contents of the fluid that

accompanied deformation (Fig. 10). Titanite petrochronology is therefore a powerful approach to not only date ductile shear zones, but also document the temperature and fluid compositions of deformation and how these conditions change within a single deformation event.

Further, our integrated titanite petrochronology dataset provides evidence for multiple weakening mechanisms within the Cottonwood shear zones. Ductile deformation accompanied intrusion of the Porcupine Wash and Smoke Tree Well plutons (Fig. 1B), which would have provided a heat source and a mechanism for thermal weakening. Neocrystallized, synkinematic titanite aggregates acted as a weak phase during deformation, deforming via dislocation creep (Fig. 5). The hydrous, F-bearing fluids that accompanied deformation would have been further capable of modifying the strength of the host pluton through the crystallization of new phases (e.g., the synkinematic titanite) and/or hydrolytic weakening (White and Knipe, 1978; Tullis and Yund, 1985; Paterson, 1989; Kronenberg, 1994). This contribution thus highlights the diversity of weakening mechanisms that may be simultaneously active during a single deformation event and that titanite petrochronology captures the complex rheological evolution of ductile shear zones.

Prior work on deformed titanite suggests that in some cases the development of dislocation-related microstructures results in complete resetting of U-Pb dates (Gordon et al., 2021; Moser et al., 2022). In this contribution, two bent titanite yield a range of dates between the crystallization age of the Cottonwood pluton and the deformation age of the shear zones, with one bent grain tip producing dates that predominantly fall between these populations (Fig. 7). These data demonstrate that lattice bending alone is not always sufficient to wholly reset U-Pb dates. The precise reason(s) for the variable effects of the

presence and motion of dislocations on the mobility of Pb in titanite remain unclear and likely relate to several variables beyond the scope of this study. However, we note that the duration of deformation may play a significant role. In other, much larger (i.e., km-scale) mylonitic shear zones, titanite U-Pb dates have been shown to be completely reset as a reset of lattice bending and subgrain development during deformation episodes lasting up to ~10 Myr (Moser et al., 2022). In contrast, the Cottonwood shear zones record only a short (<1 Myr) phase of high-temperature deformation and fluid flow on cm- to dm-scale shear zones. Further work, however, is required to test this hypothesis.

In addition, evidence of fluid-mediated recrystallization that was simultaneous with deformation in previous studies has made it challenging to discriminate between the relative roles of fluids and the direct effects of dislocations on U-Pb dates (Gordon et al., 2021; Moser et al., 2022). In the dataset presented here, the bent grains are the only ones with fluid-related zoning that cuts across grain interiors, rather than only being developed at grain margins (Fig. 7C, D; cf. Fig. 6). These observations illustrate a clear relationship between lattice bending and the extent of fluid-related recrystallization. Though there may be direct effects of lattice bending on U-Pb dates, it is clear that in some cases fluid-related recrystallization is required to ultimately reset U-Pb dates in titanite with bent crystal lattices.

7. Conclusions

Titanite petrochronology documents the timing and evolving temperature and fluid composition of deformation in <m-scale, Cretaceous ductile shear zones in the Jurassic Cottonwood pluton, Eastern Transverse Ranges. Neocrystallized titanite aggregates are

spatially associated with ilmenite and magnetite and yield a single population of U-Pb dates at ~75 Ma. Microstructural evidence of dislocation creep indicates that these grains deformed plastically during synkinematic neocrystallization. Sub- to euhedral titanite preserve oscillatory- and sector-zoned cores with ~151 Ma dates that record the timing of igneous titanite crystallization in the host Cottonwood pluton. Lobate-cuspate rims on these grains yield predominantly ~75 Ma dates that record the age of fluid-mediated recrystallization in the presence of F-rich, hydrous fluids. Titanite with bent crystal lattices yield a range of ~151 to 75 Ma dates, demonstrating that lattice bending enhances fluid-driven recrystallization and that fluids may be the ultimate mechanism by which dates are reset in bent grains. Deformation and fluid flow at ~75 Ma within these shear zones was synchronous with the intrusion of aplite dikes, as well as the Porcupine Wash and Smoke Tree Well plutons. Together with the irregular geometries and kinematics of the shear zones, these data are consistent with a punctuated phase of high-temperature deformation that accompanied the intrusion of plutons in the mid crust.

Titanite aggregates and fluid-recrystallized rims record different Zr-in-titanite temperatures and F contents despite their indistinguishable ages. The aggregates document the initiation of deformation at ~640–710 °C under hydrous, F-depleted fluid conditions, whereas rims formed at ~600–620 °C in the presence of a comparatively F-enriched fluid. These data are consistent with the evolution of the fluid that accompanied deformation to a more halogen-enriched brine as the system cooled during ongoing deformation. Titanite petrochronology is therefore a powerful tool to date deformation, constrain changes in temperature and fluid compositions during ductile shearing, and document the complex rheological evolution of ductile shear zones.

REFERENCES

Acosta-Vigil, A., Buick, I., Hermann, J., Cesare, B., Rubatto, D., London, D., and Morgan VI, G.B., 2010, Mechanisms of crustal anatexis: A geochemical study of partially melted metapelitic enclaves and host dacite, SE Spain: Journal of Petrology, v. 51, p. 785–821, doi: 10.1093/petrology/egp095.

Adams, C. J., 1981, Uplift rates and thermal structure in the Alpine Fault Z o n e and Alpine Schists , Southern Alps , New Zealand: *Geological Society, London, Special Publications*, v. *9*, p. 211–222.

Aleinikoff, J.N., Wintsch, R.P., Tollo, R.P., Unruh, D.M., Fanning, C.M., and Schmitz, M.D., 2007, Ages and origins of rocks in the Killingworth Dome, South-central connecticut: Implications for the tectonic evolution of southern New England: American Journal of Science, v. 307, p. 63–118, doi: 10.2475/01.2007.04.

Allibone, A.H., and Tulloch, A.J., 2008, Early Cretaceous dextral transpressional deformation within the Median Batholith , Stewart Island , New Zealand: New Zealand Journal of Geology and Geophysics, v. 52, p. 115–134, doi: 10.1080/00288300809509854.

Allibone, A. H., Jongens, R., Turnbull, I. M., Milan, L. A., Daczko, N. R., DePaoli, M. C., and Tulloch, A. J., 2009, Plutonic rocks of Western Fiordland, New Zealand: Field relations, geochemistry, correlation, and nomenclature: *New Zealand Journal of Geology and Geophysics*, v. *52*, p. 379–415, https://doi.org/10.1080/00288306.2009.9518465.

Andronicos, C.L., Chardon, D.H., Hollister, L.S., Gehrels, G.E., and Woodsworth, G.J., 2003, Strain partitioning in an obliquely convergent orogen, plutonism, and synorogenic collapse: Coast Mountains Batholith, British Columbia, Canada: Tectonics, v. 22, doi: 10.1029/2001TC001312.

Austrheim, H., 1987, Eclogitization of lower crustal granulites by fluid migration through shear zones: Earth and Planetary Science Letters, v. 81, p. 221–232.

Barnes, P. M., Sutherland, R., and Delteil, J., 2005, Strike-slip structure and sedimentary basins of the southern Alpine Fault, Fiordland, New Zealand: *Bulletin of the Geological Society of America*, v. *117, no.* (3–4), p. 411–435, https://doi.org/10.1130/B25458.1.

Barth, A.P., Wooden, J.L., Howard, K.A., and Richards, J.L., 2008, Late Jurassic plutonism in the southwest U.S. Cordillera: Special Paper of the Geological Society of America, v. 438, p. 379–396, doi: 10.1130/2008.2438(13).

Batt, G. E., Braun, J., Kohn, B. P., and McDougall, I., 2000, Thermochronological analysis of the dynamics of the Southern Alps, New Zealand: *Geological Society of America Bulletin*, v. *112, no.* 2, 250–266.

Betka, P. M. and Klepeis, K. A., 2013, Three-stage evolution of lower crustal gneiss domes at Breaksea Entrance, Fiordland, New Zealand: *Tectonics*, v. *32*, no. 5, p. 1084–1106, https://doi.org/10.1002/tect.20068

Blattner, P, 1991, The north fiordland transcurrent convergence: *New Zealand Journal of Geology and Geophysics*, v. *34, no.* 4, 533–542, https://doi.org/10.1080/00288306.1991.9514488.

Bonamici, C. E., Kozdon, R., Ushikubo, T., and Valley, J. W., 2014, Intragrain oxygen isotope zoning in titanite by SIMS: Cooling rates and fluid infiltration along the Carthage-Colton Mylonite Zone, Adirondack Mountains, NY, USA: *Journal of Metamorphic Geology*, v. *32*, no. 1, 71–92, https://doi.org/10.1111/jmg.12059.

Bonamici, C.E., Fanning, C.M., Kozdon, R., Fournelle, J.H., and Valley, J.W., 2015, Combined oxygen-isotope and U-Pb zoning studies of titanite: New criteria for age preservation: Chemical Geology, v. 398, p. 70–84, doi: 10.1016/j.chemgeo.2015.02.002.

Bons, P.D., and Urai, J.L., 1992, Syndeformational grain growth: microstructures and kinetics: Journal of Structural Geology, v. 14, p. 1101–1109, doi: 10.1016/0191-8141(92)90038-X.

Borg, I. Y., and Heard, H. C., 1972, Mechanical Twinning in Sphene at 8 kbar, 25 to 500 C: Geological Society of America Memoir, v. 132, p. 441–451.

Botev, Z.I., Grotowski, J.F., and Kroese, D.P., 2010, Kernel density estimation via diffusion: Annals of Statistics, v. 38, p. 2916–2957, doi: 10.1214/10-AOS799.

Boulton, C., Carpenter, B. M., Toy, V., and Marone, C., 2012, Physical properties of surface outcrop cataclastic fault rocks, Alpine Fault, New Zealand: *Geochemistry, Geophysics, Geosystems*, v. *13, no.* 1, 1–13. https://doi.org/10.1029/2011GC003872.

Bradshaw, J. Y., 1990, Geology of crystalline rocks of northern Fiordland: Details of the granulite facies Western Fiordland Orthogneiss and associated rock units: *New Zealand Journal of Geology and Geophysics*, v. *33*, no. 3, p. 465–484, https://doi.org/10.1080/00288306.1990.10425702.

Briggs, S. I., Cottle, J. M., and Smit, M. A., 2018, Record of plate boundary metamorphism during Gondwana breakup from Lu–Hf garnet geochronology of the Alpine Schist, New Zealand: *Journal of Metamorphic Geology*, v. *36,* no. 7, 821–841, https://doi.org/10.1111/jmg.12313.

Brown, W. L., and Macaudiére, J., 1984, Microfracturing in relation to atomic structure of plagioclase from a deformed meta-anorthosite: *Journal of Structural Geology*, v. *6*, no. 5, p. 579–586, https://doi.org/10.1016/0191-8141(84)90067-1.

Budzyn, B., Harlov, D.E., Williams, M., and Jercinovic, M.J., 2011, Experimental determination of stability relations between monazite, fluorapatite, allanite, and REE-epidote: American Mineralogist, v. 96, p. 1547–1567, doi: 10.2138/am.2011.3741.

Bürgmann, R., and Dresen, G., 2008, Rheology of the lower crust and upper mantle: Evidence from rock mechanics, geodesy, and field observations: Annual Review of Earth and Planetary Sciences, v. 36, p. 531–567, doi: 10.1146/annurev.earth.36.031207.124326.

Buriticá, L. F., Schwartz, J. J., Klepeis, K. A., Miranda, E. A., Tulloch, A. J., Coble, M. A., and Kylander-Clark, A.R.C., 2019, Temporal and spatial variations in magmatism and transpression in a Cretaceous arc, Median Batholith, Fiordland, New Zealand: *Lithosphere*, v. *11*, no. 5, p. 652–682, https://doi.org/10.1130/L1073.1/4830124/l1073.

Burkhard, M, 1993, Calcite twins, their geometry, appearance and significance as stress-strain markers and indicators of tectonic regime: a review: *Journal of Structural Geology*, v. *15, no.* 3–5, p. 351–368, https://doi.org/10.1016/0191-8141(93)90132-T.

Burlini, L., and Bruhn, D., 2005, High-strain zones: Laboratory perspectives on strain softening during ductile deformation: Geological Society Special Publication, v. 245, p. 1–24, doi: 10.1144/GSL.SP.2005.245.01.01.

Carson, C.J., Ague, J.J., Grove, M., Coath, C.D., and Harrison, T.M., 2002, U-Pb isotopic behaviour of zircon during upper-amphibolite facies fluid infiltration in the Napier Complex, east Antarctica: Earth and Planetary Science Letters, v. 199, p. 287–310.

Carswell, D.A., Wilson, R.N., and Zhai, M., 1996, Ultra-high pressure aluminous titanites in

carbonate-bearing eclogites at Shuanghe in Dabieshan, central China: Mineralogical Magazine, v. 60, p. 461–471, doi: 10.1180/minmag.1996.060.400.07.
Cawood, T.K., Moser, A., Borsook, A., and Rooney, A.D., 2022, New constraints on the timing and character of the Laramide Orogeny and associated gold mineralization in SE California, USA: GSA Bulletin, p. 1–21, doi: 10.1130/b36251.1.
Chakhmouradian, A.R., and Williams, C.T., 2004, Mineralogy of high field strength elements (Ti, Nb, Zr, Ta, Hf) in phoscorite and carbonatitic rocks of the Kola Peninsula, Russia, *in* Wall, F. and Zaitsev, A.N. eds., Phoscorites and Carbonatites from Mantle to Mine: the key example of the Kola Alkaline Province, London, The Mineralogical Society of Great Britain and Ireland, p. 293–340.
Chamberlain, C. P., Zeitler, P. K., and Cooper, A. F., 1995, Geochronologic constraints of the uplift and metamorphism along the Alpine Fault, South Island, New Zealand: *New Zealand Journal of Geology and Geophysics*, v. *38,* no. 4, p. 515–523, https://doi.org/10.1080/00288306.1995.9514678.
Chambers, J.A., and Kohn, M.J., 2012, Titanium in muscovite biotite, and hornblende: Modeling, thermometry, and rutile activities of metapelites and amphibolites: American Mineralogist, v. 97, p. 543–555, doi: http://dx.doi.org/10.2138/am.2012.3890.
Cherniak, D.J., 1993, Lead diffusion in titanite and preliminary results on the effects of radiation damage on Pb transport: Chemical Geology, v. 110, p. 177–194, doi: 10.1016/0009-2541(93)90253-F.
Cherniak, D.J., 1995, Sr and Nd diffusion in titanite: Chemical Geology, v. 125, p. 219–232.
Claypool, A.L., Klepeis, K.A., Dockrill, B., Clarke, G.L., Zwingmann, H., and Tulloch, A., 2002, Structure and kinematics of oblique continental convergence in northern Fiordland , New Zealand: Tectonophysics, v. 359, p. 329–358.
Collot, J. Y., Lamarche, G., Wood, R. A., Delteil, J., Sosson, M., Lebrun, J.F., and Coffin, M., 1995, Morphostructure of an incipient subduction zone along a transform plate boundary: Puysegur Ridge and Trench: *Geology*, v. *23, no.* 6, 519–522, https://doi.org/10.1130/0091-7613(1995)023<0519:MOAISZ>2.3.CO;2.
Cooper, A. F., 1987, Lamprophyre dike intrusion and the age of the Alpine fault , New Zealand: Geology, v. 15, no. 10, p. 941–944.
Cooper, A. F., and Ireland, T. R., 2013, Cretaceous sedimentation and metamorphism of the western Alpine Schist protoliths associated with the Pounamu Ultramafic Belt, Westland, New Zealand: *New Zealand Journal of Geology and Geophysics*, v. *56, no*. 4, 188–199, https://doi.org/10.1080/00288306.2013.809776.
Cottrell, A.H., and Bilby, B.A., 1949, Dislocation Theory of Yielding and Strain Ageing of Iron: Proceedings of the Physical Society, v. 62, p. 49–62.
Coyle, D.A., and Wagner, G.A., 1998, Positioning the titanite fission-track partial annealing zone: Chemical Geology, v. 149, p. 117–125.
Crank, J., 1975, The mathematics of diffusion: Brunel University Press, 414 p.
Crawford, M.L. and Hollister, L.S., 1982, Contrast of metamorphic and structural histories across the Work Channel lineament, Coast Plutonic Complex, British Columbia: Journal of Geophysical Research, v. 87, p. 3849–3860.
Crawford, M.L., Hollister, L.S., and Woodsworth, G.J., 1987, Crustal deformation and regional metamorphism across a terrane boundary, Coast Plutonic Complex, British Columbia: Tectonics, v. 6, p. 343–361, doi: 10.1029/TC006i003p00343.
Curti, E., and Hummel, W., 1999, Modeling the solubility of zirconia in a repository for

high-level radioactive waste: Journal of Nuclear Materials, v. 274, p. 189–196.
Czertowicz, T.A., Scott, J.M., and Piazolo, S., 2016a, Coupled extrusion of sub-arc lithospheric mantle and lower crust during orogen collapse : a case study from Fiordland , New Zealand: Journal of Metamorphic Geology, v. 34, p. 501–524, doi: 10.1111/jmg.12191.
Czertowicz, T.A., Scott, J.M., Waight, T.E., Palin, J.M., Van der Meer, Q.H.A., Le Roux, P., Münker, C., and Piazolo, S., 2016b, The anita peridotite, New Zealand: Ultra-depletion and subtle enrichment in sub-arc mantle: Journal of Petrology, v. 57, p. 717–750, doi: 10.1093/petrology/egw001.
Davis, D.W., and Krogh, T.E., 2000, Preferential dissolution of 234U and radiogenic Pb from a-recoil-damaged lattice sites in zircon: implications for thermal histories and Pb isotopic fractionation in the near surface environment: Chemical Geology, v. 172, p. 41–58.
DeMets, C., Gordon, R. G., Argus, D. F., and Stein, S., 1994, Effect of recent revisions to the geomagnetic reversal time scale on estimates of current plate motions: *Geophysical Research Letters*, v. *21,* no. 20, p. 2191–2194, https://doi.org/10.1029/94GL02118.
DeMets, C., Gordon, R.G., and Argus, D.F., 2010, Geologically current plate motions: Geophysical Journal International, v. 181, p. 1–80, doi: 10.1111/j.1365-246X.2009.04491.x.
Dodson, M.H., 1973, Closure Temperature in Cooling Geochronological and Petrological Systems: Contributions to Mineralogy and Petrology, v. 40, p. 259–274.
Dolejs, D., and Zajacz, D., 2018, Halogens in Silicic Magmas and Their Hydrothermal Systems: Surface, Crust, and Mantle, *in* Harlov, D.E. and Aranovich, L. eds., The Role of Halogens in Terrestrial and Extraterrestrial Geochemical Processes, Cham, Switzerland, Springer International Publishing, p. 431, doi: https://doi.org/10.1007/978-3-319-61667-4.
Dumond, G.D., Mahan, K.H., Goncalves, P., Williams, M.L., and Jercinovic, M.J., 2022, Monazite as a monitor of shear strain in the orogenic crust: Journal of Structural Geology, v. 161, doi: doi.org/10.1016/j.jsg.2022.104672.
Economos, R.C., Barth, A.P., Wooden, J.L., Paterson, S.R., Friesenhahn, B., Wiegand, B.A., Anderson, J.L., Roell, J.L., Palmer, E.F., Ianno, A.J., and Howard, K.A., 2021, Testing models of Laramide orogenic initiation by investigation of Late Cretaceous magmatic-tectonic evolution of the central Mojave sector of the California arc: Geosphere, v. 17, p. 2042–2061, doi: 10.1130/GES02225.1.
Fossen, H., and Tikoff, B., 1998, Extended models of transpression and transtension, and application to tectonic settings: Geological Society, London, Special Publications, v. 135, p. 15–33.
Fougerouse, D., Reddy, S.M., Kirkland, C.L., Erickson, T.M., Saxey, D.W., Rickard, W.D.A., Jacob, D., Leroux, H., and Clark, C., 2021, Mechanical twinning of monazite expels radiogenic lead: Geology, v. 49, p. 417–421, doi: 10.1130/G48400.1.
Fougerouse, D., Reddy, S.M., Kirkland, C.L., Saxey, D.W., Rickard, W.D., and Hough, R.M., 2019, Time-resolved, defect-hosted, trace element mobility in deformed Witwatersrand pyrite: Geoscience Frontiers, v. 10, p. 55–63, doi: 10.1016/j.gsf.2018.03.010.
Franz, G., and Spear, F.S., 1985, Aluminous titanite (sphene) from the Eclogite Zone, south-central Tauern Window, Austria: Chemical Geology, v. 50, p. 33–46, doi:

10.1016/0009-2541(85)90110-X.
Frei, R., Villa, I.., Nagler, T.F., Kramers, J.D., Przybylowicz, W.J., Prozesky, V.M., Hofmann, B.A., and Kamber, B.S., 1997, Single mineral dating by the Pb-Pb step-leaching method: Assessing the mechanisms: Geochimica Et Cosmochimica Acta, v. 61, p. 393–414.
Friesenhahn, B.P., 2018, The Transition from Sevier to Laramide Orogeny Captured in Upper-Plate, Syn-Magmatic Structures, Eastern Transverse Ranges, CA: Southern Methodist University, 50 p.
Frost, B.R., Chamberlain, K.R., and Schumacher, J.C., 2000, Sphene (titanite): phase relations and role as a geochronometer: Chemical Geology, v. 172, p. 131–148, doi: https://doi.org/10.1016/S0009-2541(00)00240-0.
Gaina, C., Muller, D. R., Royer, J., Stock, J., Hardebeck, J., and Symonds, P., 1998, The tectonic history of the Tasman Sea: A puzzle with 13 pieces: *Journal of Geophysical Research*, v. *103,* no. B6, 12413–12433.
Garber, J.M., Hacker, B.R., Kylander-Clark, A.R.C., Stearns, M., and Seward, G., 2017, Controls on trace element uptake in metamorphic titanite: Implications for petrochronology: Journal of Petrology, v. 58, p. 1031–1057, doi: 10.1093/petrology/egx046.
Garber, J.M., Rioux, M., Clark, A.R.C.K., Hacker, B.R., Vervoort, J.D., and Searle, M.P., 2020a, Petrochronology of Wadi Tayin Metamorphic Sole Metasediment, With Implications for the Thermal and Tectonic Evolution of the Samail Ophiolite (Oman/UAE): Tectonics, v. 39, p. 1–28, doi: 10.1029/2020TC006135.
Garber, J.M., Smye, A.J., Feineman, M.D., Kylander, A.R.C., and Simon, C., 2020b, Decoupling of zircon U–Pb and trace-element systematics driven by U diffusion in eclogite-facies zircon (Monviso meta-ophiolite, W. Alps): Contributions to Mineralogy and Petrology, v. 175, p. 1–25, doi: 10.1007/s00410-020-01692-2.
Gehrels, G.E., McClelland, W.C., Samson, S.D., Patchett, P.J., and Brew, D.A., 1991, U-Pb geochronology of late Cretaceous and early Tertiary plutons in the northern Coast Mountains Batholith: Canadian Journal of Earth Sciences, v. 28, doi: 10.1139/e91-082.
Geisler, T., Pidgeon, R.T., Kurtz, R., van Bronswijk, W., and Schleicher, H., 2003, Experimental hydrothermal alteration of partially metamict zircon: American Mineralogist, v. 88, p. 1496–1513.
Geisler, T., Schaltegger, U., and Tomaschek, F., 2007, Re-equilibration of Zircon in Aqueous Fluids and Melts: Elements, v. 3, p. 43–50, doi: https://doi.org/10.2113/gselements.3.1.43.
Ghent, E.D., and Stout, M.Z., 1984, TiO2 activity in metamorphosed pelitic and basic rocks: principles and applications to metamorphism in southeastern Canadian Cordillera: Contributions to Mineralogy and Petrology, v. 86, p. 248–255, doi: https://doi.org/10.1007/BF00373670.
Gibson, G. M., 1988, Age constraints on metamorphism and the development of a metamorphic core complex in Fiordland, southern New Zealand: *Geology*, v. *16*, no. 405–408.
Gibson, G. M., and Ireland, T. R., 1995, Granulite formation during continental extension in Fiordland, New Zealand: *Nature*, v. *375*, no. 6531, p. 479–482, https://doi.org/10.1038/375479a0.
Goncalves, P., Oliot, E., Marquer, D., and Connolly, J.A.D., 2012, Role of chemical

processes on shear zone formation: an example from the Grimsel metagranodiorite (Aar massif, Central Alps): J. Metamorphic Geology, v. 30, p. 703–722, doi: 10.1111/j.1525-1314.2012.00991.x.
Goode, A. D. T., 1978, High temperature, high strain rate deformation in the lower crustal Kalka Intrusion, central Australia: *Contributions to Mineralogy and Petrology*, v. *66*, no. 2, 137–148, https://doi.org/10.1007/BF00372152
Gordon, S.M., Kirkland, C.L., Reddy, S.M., Blatchford, H.J., Whitney, D.L., Teyssier, C., Evans, N.J., and Mcdonald, B.J., 2021, Deformation-enhanced recrystallization of titanite drives decoupling between U-Pb and trace elements: Earth and Planetary Science Letters, v. 560, p. 116810, doi: 10.1016/j.epsl.2021.116810.
Grapes, R. H., 1995, Uplift and exhumation of Alpine Schist, Southern Alps, New Zealand: Thermobarometric constraints: *New Zealand Journal of Geology and Geophysics*, v. *38*, no. 4, p. 525–533, https://doi.org/10.1080/00288306.1995.9514679.
Grapes, R., and Watanabe, T., 1992, Metamorphism and uplift of Alpine schist in the Franz Josef–Fox Glacier area of the Southern Alps, New Zealand: *Journal of Metamorphic Geology*, v. *10,* no. 2, p. 171–180, https://doi.org/10.1111/j.1525-1314.1992.tb00077.x.
Hacker, B.R., Kylander-clark, A.R.C., Holder, R., Andersen, T.B., Peterman, E.M., Walsh, E.O., and Munnikhuis, J.K., 2015, Monazite response to ultrahigh-pressure subduction from U–Pb dating by laser ablation split stream: Chemical Geology, v. 409, p. 28–41, doi: 10.1016/j.chemgeo.2015.05.008.
Harlov, D.E., Wirth, R., and Hetherington, C.J., 2011, Fluid-mediated partial alteration in monazite: The role of coupled dissolution–reprecipitation in element redistribution and mass transfer: Contributions to Mineralogy and Petrology, v. 162, p. 329–348, doi: 10.1007/s00410-010-0599-7.
Harrison, T.M., Armstrong, R.L., Naeser, C.W., and Harakal, J.E., 1979, Geochronology and thermal history of the Coast Plutonic Complex, near Prince Rupert, British Columbia: Canadian Journal of Earth Sciences, v. 16, p. 400–410, doi: 10.1139/e79-038.
Hart, E.W., 1957, On the Role of Dislocations in Bulk Diffusion: Acta Metallurgica, v. 5, p. 597.
Hartnady, M.I., Kirkland, C.L., Clark, C., Spaggiari, C. V, Smithies, R.H., Evans, N.J., and McDonald, B.J., 2019, Titanite dates crystallization: Slow Pb diffusion during super-solidus re-equilibration: Journal of Metamorphic Geology, v. 37, p. 823–838, doi: 10.1111/jmg.12489.
Hayden, L.A., Watson, E.B., and Wark, D.A., 2008, A thermobarometer for sphene (titanite): Contributions to Mineralogy and Petrology, v. 155, p. 529–540, doi: 10.1007/s00410-007-0256-y.
Heinrich, W., 2007, Fluid immiscibility in metamorphic rocks: Reviews in mineralogy and geochemistry, v. 65, p. 389–430.
Hetherington, C.J., Harlov, D.E., and Budzyn, B., 2010, Experimental metasomatism of monazite and xenotime: mineral stability, REE mobility and fluid composition: Mineralogy and Petrology, v. 99, p. 165–184, doi: 10.1007/s00710-010-0110-1.
Hill, J.E., 1995a, A deep crustal shear zone exposed in western Fiordland, New Zealand: Tectonics, v. 14, p. 1172–1181.
Hill, E.J., 1995b, The Anita Shear Zone: A major, middle Cretaceous tectonic boundary in northwestern Fiordland: New Zealand Journal of Geology and Geophysics, v. 38, p.

93–103, doi: 10.1080/00288306.1995.9514641.
Hirth, G., and Tullis, J., 1992, Dislocation creep regimes in quartz aggregates: Journal of Structural Geology, v. 14, p. 145–159, doi: 10.1016/0191-8141(92)90053-Y.
Hoffman, R., 1956, Anisotropy of grain boundary self-diffusion: Acta Metallurgica, v. 4, p. 97–98.
Holder, R.M., and Hacker, B.R., 2019, Fluid-driven resetting of titanite following ultrahigh-temperature metamorphism in southern Madagascar: Chemical Geology, v. 504, p. 38–52, doi: 10.1016/j.chemgeo.2018.11.017.
Holder, R.M., Hacker, B.R., Seward, G.G.E., and Kylander, A.R.C., 2019, Interpreting titanite U–Pb dates and Zr thermobarometry in high-grade rocks: empirical constraints on elemental diffusivities of Pb, Al, Fe, Zr, Nb, and Ce: Contributions to Mineralogy and Petrology, v. 174, p. 1–19, doi: 10.1007/s00410-019-1578-2.
Hollis, J. A., Clarke, G. L., Klepeis, K. A., Daczko, N. R., and Ireland, T. R., 2003, Geochronology and geochemistry of high-pressure granulites of the Arthur River Complex, Fiordland, New Zealand: Cretaceous magmatism and metamorphism on the palaeo-Pacific Margin: *Journal of Metamorphic Geology*, v. *21,* no. 3, p. 299–313, https://doi.org/10.1046/j.1525-1314.2003.00443.x.
Hollis, Julia A., Clarke, G. L., Klepeis, K. A., Daczko, N. R., and Ireland, T. R., 2004, The regional significance of Cretaceous magmatism and metamorphism in Fiordland, New Zealand, from U-Pb zircon geochronology: *Journal of Metamorphic Geology*, v. *22,* no. 7, p. 607–627, https://doi.org/10.1111/j.1525-1314.2004.00537.x.
Hollister, L.S., 1970, Origin, Mechanism, and consequences of compositional sector zoning in staurolite: American Mineralogist, v. 55, p. 742–766.
Hollister, L.S., and Crawford, M.L., 1986, Melt-enhanced deformation: a major tectonic process: Geology, v. 14, p. 558–561, doi: 10.1130/0091-7613(1986)14<558:MDAMTP>2.0.CO.
Hoskin, P.W.O., and Black, L.P., 2000, Metamorphic zircon formation by solid-state recrystallization of protolith igneous zircon: J. Metamorphic Geology, v. 18, p. 423–439.
House, M. A., Gurnis, M., Kamp, P. J. J., and Sutherland, R., 2002, Uplift in the Fiordland region, New Zealand: Implications for incipient subduction: *Science*, v. *297, no.* 5589, p. 2038–2041, https://doi.org/10.1126/science.1075328.
House, M. A., Gurnis, M., Sutherland, R., and Kamp, P. J. J., 2005, Patterns of Late Cenozoic exhumation deduced from apatite and zircon U-He ages from Fiordland, New Zealand: *Geochemistry, Geophysics, Geosystems*, v. *6, no.* 9, 1–13, https://doi.org/10.1029/2005GC000968.
Huang, J., Meyer, M., and Pontikis, V., 1989, Is pipe diffusion in metals vancancy controlled? A molecular-dynamics study of an edge dislocation in copper: Physical Review Letters, v. 63, p. 628–631.
Huntington, K.W., and Klepeis, K.A., 2018, Challenges and opportunities for research in tectonics: Understanding deformation and the processes that link Earth systems, from geologic time to human time. A community vision document submitted to the US National Science Foundation:, https://digital.lib.washington.edu/researchworks/handle/1773/40754.
Ingram, G.M., and Hutton, D.H.W., 1994, The Great Tonalite Sill: emplacement into a contractional shear zone and implications for late Cretaceous to early Eocene tectonics

in southeastern Alaska and British Columbia: Geological Society of America Bulletin, v. 106, p. 715–728, doi: 10.1130/0016-7606(1994)106<0715:TGTSEI>2.3.CO;2.
Ireland, T. R., and Gibson, G. M., 1998, SHRIMP monazite and zircon geochronology of high-grade metamorphism in New Zealand: *Journal of Metamorphic Geology*, v. *16*, p. 149–167.
Jacobson, C.E., Pedrick, J.N., and Ebert, K.A., 2007, Exhumation of the Orocopia Schist and associated rocks of southeastern California: Relative roles of erosion, synsubduction tectonic denudation, and middle Cenozoic extension: Geological Society of America Special Paper, v. 419, p. 1–37, doi: 10.1130/2007.2419(01).
Jamtveit, B., Austrheim, H., and Putnis, A., 2016, Disequilibrium metamorphism of stressed lithosphere: Earth Science Reviews, v. 154, p. 1–13, doi: 10.1016/j.earscirev.2015.12.002.
Jiang, S.Y., Wang, R.C., Xu, X.S., and Zhao, K.D., 2005, Mobility of high field strength elements (HFSE) in magmatic-, metamorphic-, and submarine-hydrothermal systems: Physics and Chemistry of the Earth, v. 30, p. 1020–1029, doi: 10.1016/j.pce.2004.11.004.
Jicha, B. R., Garcia, M. O., and Wessel, P., 2018, Mid-cenozoic pacific plate motion change: Implications for the Northwest Hawaiian Ridge and circum-pacific: *Geology*, v. *46,* no. 11, 939–942. https://doi.org/10.1130/G45175.1.
Johnston, W. G., and Gilman, J. J., 1959, Dislocation velocities, dislocation densities, and plastic flow in lithium fluoride crystals: *Journal of Applied Physics*, v. *30,* no. 2, p. 129–144, https://doi.org/10.1063/1.1735121.
Kamp, P. J.J., 1986, The mid- Cenozoic Challenger Rift System of western New Zealand and its implications for the age of Alpine fault inception: *Geological Society of America Bulletin*, v. *97*, no. 3, p. 255–281, https://doi.org/10.1130/0016-7606(1986)97<255:TMCRSO>2.0.CO;2.
Kamp, P. J. J, Green, P. F., and White, S. H., 1989, Fisson Track Analysis Reveals Character of Collisional Tectonics in New Zealand: *Tectonics*, v. *8*, no. 2, 169–195.
Kapp, P., Manning, C.E., and Tropper, P., 2009, Phase-equilibrium constraints on titanite and rutile activities in mafic epidote amphibolites and geobarometry using titanite–rutile equilibria: Journal of Metamorphic Geology, v. 27, p. 509–521, doi: 10.1111/j.1525-1314.2009.00836.x.
Kelly, N.M., Harley, S.L., and Möller, A., 2012, Complexity in the behavior and recrystallization of monazite during high-T metamorphism and fluid in filtration: Chemical Geology, v. 322–323, p. 192–208, doi: 10.1016/j.chemgeo.2012.07.001.
Keppler, H., 1993, Influence of fluorine on the enrichment of high field strength trace elements in granitic rocks: Contributions to Mineralogy and Petrology, v. 114, p. 479–488.
Kirkland, C. L., Spaggiari, C. V, Johnson, T. E., Smithies, R. H., Danišík, M., Evans, N., Wingate, M.T., Clark, C., Spencer, C., Mikuckim, E., and Mcdonald, B. J., 2016, Grain size matters: Implications for element and isotopic mobility in titanite: *Precambrian Research*, v. *278*, p. 283–302. https://doi.org/10.1016/j.precamres.2016.03.002
Kirkland, C.L., Fougerouse, D., Reddy, S.M., Hollis, J., and Saxey, D.W., 2018, Assessing the mechanisms of common Pb incorporation into titanite: Chemical Geology, v. 483, p. 558–566, doi: 10.1016/j.chemgeo.2018.03.026.
Klepeis, K.A., Crawford, M.L., and Gehrels, G., 1998, Structural history of the crustal-scale

Coast shear zone north of Portland Canal, southeast Alaska and British Columbia: Journal of Structural Geology, v. 20, p. 883–904, doi: 10.1016/S0191-8141(98)00020-0.

Klepeis, K.A., Daczko, N.R., and Clarke, G.L., 1999, Kinematic vorticity and tectonic significance of superposed mylonites in a major lower crustal shear zone, northern Fiordland, New Zealand: Journal of Structural Geology, v. 21, p. 1385–1405, doi: 10.1016/S0191-8141(99)00091-7.

Klepeis, Keith A., and Clarke, G. L., 2004, The evolution of an exposed mid-lower crustal attachment zone in Fiordland , New Zealand: *Geological Society, London, Special Publications*, v. *227*, p. 197–229.

Klepeis, K.A., King, D., Paoli, M. De, Clarke, G.L., and Gehrels, G., 2007, Interaction of strong lower and weak middle crust during lithospheric extension in western New Zealand: Tectonics, v. 26, p. 1–27, doi: 10.1029/2006TC002003.

Klepeis, Keith A, Schwartz, J., Stowell, H., and Tulloch, A., 2016, Gneiss domes, vertical and horizontal mass transfer, and the initiation of extension in the hot lower-crustal root of a continental arc, Fiordland, New Zealand: *Lithosphere*, v. *8,* no. 3, p. 116–140, https://doi.org/10.1130/L490.1.

Klepeis, K., Webb, L., Blatchford, H., Schwartz, J., Jongens, R., Turnbull, R., and Stowell, H., 2019a, Deep slab collision during Miocene subduction causes uplift along crustal-scale reverse faults in Fiordland, New Zealand: *GSA Today*, v. *29,* no. 9, p. 4–10, https://doi.org/10.1130/GSATG399A.1

Klepeis, K. A., Webb, L. E., Blatchford, H. J., Jongens, R., Turnbull, R. E., and Schwartz, J. J., 2019b, The Age and Origin of Miocene-Pliocene Fault Reactivations in the Upper Plate of an Incipient Subduction Zone, Puysegur Margin, New Zealand: *Tectonics*, v. *38,* no. 8, p. 3237–3260, https://doi.org/10.1029/2019TC005674.

Klepeis, Keith A., Schwartz, J. J., Miranda, E., Lindquist, P., Jongens, R., Turnbull, R., and Stowell, H., 2022, The Initiation and Growth of Transpressional Shear Zones Through Continental Arc Lithosphere, Southwest New Zealand: *Tectonics*, v. *41,* no. 9, p 1–40, https://doi.org/10.1029/2021tc007097.

Kohn, M.J., 2017, Titanite Petrochronology: Reviews in Mineralogy and Geochemistry, v. 83, p. 419–441, doi: 10.2138/rmg.2017.83.13.

Kohn, M.J., and Corrie, S.L., 2011, Preserved Zr-temperatures and U–Pb ages in high-grade metamorphic titanite: Evidence for a static hot channel in the Himalayan orogen: Earth and Planetary Science Letters, v. 311, p. 136–143, doi: 10.1016/j.epsl.2011.09.008.

Kovaleva, E., Klötzli, U., Habler, G., Huet, B., Guan, Y., and Rhede, D., 2017, The effect of crystal-plastic deformation on isotope and trace element distribution in zircon: Combined BSE, CL, EBSD, FEG-EMPA and NanoSIMS study: Chemical Geology, v. 450, p. 183–198, doi: 10.1016/j.chemgeo.2016.12.030.

Kramers, J., Frei, R., Newville, M., Kober, B., and Villa, I., 2009, On the valency state of radiogenic lead in zircon and its consequences: Chemical Geology, v. 261, p. 4–11, doi: 10.1016/j.chemgeo.2008.09.010.

Kronenberg, A.K., 1994, Hydrogen Speciation and Chemical Weakening of Quartz, *in* Heaney, P.J., Prewitt, C.T., and Gibbs, G.V. eds., Silica: Physical Behaviour, Geochemistry, and Materials Applications; Mineralogical Society of America, Reviews of Mineralogy, p. 123–176, doi: 10.1515/9781501509698-009.

Kruse, R., and Stünitz, H, 1999, Deformation mechanisms and phase distribution in mafic

high-temperature mylonites from the Jotun Nappe, southern Norway: *Tectonophysics*, v. *303, no.* 1–4, p. 223–249, https://doi.org/10.1016/S0040-1951(98)00255-8.
Kruse, R., Stünitz, H., and Kunze, K., 2001, Dynamic recrystallization processes in plagioclase porphyroclasts: *Journal of Structural Geology*, v. *23,* no. 11, p. 1781–1802. https://doi.org/10.1016/S0191-8141(01)00030-X
Kunz, B.E., Regis, D., and Engi, M., 2018, Zircon ages in granulite facies rocks: decoupling from geochemistry above 850 °C? Contributions to Mineralogy and Petrology, v. 173, p. 1–21, doi: 10.1007/s00410-018-1454-5.
Kusiak, M.A., Whitehouse, M.J., Wilde, S.A., Nemchin, A.A., and Clark, C., 2013, Mobilization of radiogenic Pb in zircon revealed by ion imaging: Implications for early Earth geochronology: Geology, v. 41, p. 291–294, doi: 10.1130/G33920.1.
Kylander-clark, A.R.C., 2017, Laser-Ablation Inductively Coupled Plasma: Reviews in mineralogy and geochemistry, v. 83, p. 183–196.
Kylander-Clark, A.R.C., Hacker, B.R., and Cottle, J.M., 2013, Laser-ablation split-stream ICP petrochronology: Chemical Geology, v. 345, p. 99–112, doi: 10.1016/j.chemgeo.2013.02.019.
Langone, A., Padrón-Navarta José, A., Ji, W.Q., Zanetti, A., Mazzucchelli, M., Tiepolo, M., Giovanardi, T., and Bonazzi, M., 2017, Ductile–brittle deformation effects on crystal-chemistry and U–Pb ages of magmatic and metasomatic zircons from a dyke of the Finero Mafic Complex (Ivrea–Verbano Zone, Italian Alps): Lithos, v. 284–285, p. 493–511, doi: 10.1016/j.lithos.2017.04.020.
Larche, F.C., and Cahn, J.W., 1985, The interactions of composition and stress in crystalline solids: Acta Metallurgica, v. 33, p. 331–357.
LaTourrette, T., Wasserburg, G.J., and Fahey, A.J., 1996, Self diffusion of Mg, Ca, Ba, Nd, Yb, Ti, Zr, and U in haplobasaltic melt: Geochimica et Cosmochimica Acta, v. 60, p. 1329–1340.
Lawver, L. A., and Gahagan, L. M., 1994, Constraints on the timing of extension in the Ross Sea region: *Terra Antarctica*, v. *1, no.* 3, p. 545–552.
Lebrun, J.F., Lamarche, G., and Collot, J.Y., 2003, Subduction initiation at a strike-slip plate boundary: The Cenozoic Pacific-Australian plate boundary, south of New Zealand: *Journal of Geophysical Research: Solid Earth*, v. *108, no.* B9, https://doi.org/10.1029/2002jb002041.
Lebrun, J. F., Lamarche, G., Collot, J. Y., and Delteil, J., 2000, Abrupt strike-slip fault to subduction transition: The Alpine Fault-Puysegur Trench connection, New Zealand: *Tectonics*, v. *19,* no. 4, p. 688–706, https://doi.org/10.1029/2000TC900008.
Lee, J. K. W., 1995, Multipath diffusion in geochronology: *Contributions to Mineralogy and Petrology*, v. *120, no*. 1, p. 60–82. https://doi.org/10.1007/BF00311008.
Lippmann, F., 1980, Phase diagrams depicting aqueous solubility of binary mineral systems: N.Jb.Miner.Abh., v. 139, p. 1–25.
Little, T. A., Holcombe, R. J., and Ilg, B. R., 2002, Ductile fabrics in the zone of active oblique convergence near the Alpine Fault, New Zealand: Identifying the neotectonic overprint: *Journal of Structural Geology*, v. *24,* no. 1, p. 193–217, https://doi.org/10.1016/S0191-8141(01)00059-1.
Little, Timothy A, Cox, S., Vry, J. K., and Batt, G., 2005, Variations in exhumation level and uplift rate along the oblique-slip Alpine faul , central Southern Alps, New Zealand: *Geological Society of America Bulletin*, v. *117. no.* 5/6, p. 707–723,

https://doi.org/10.1130/B25500.1.
Liu, Y., Hu, Z., Gao, S., Günther, D., Xu, J., Gao, C., and Chen, H., 2008, In situ analysis of major and trace elements of anhydrous minerals by LA-ICP-MS without applying an internal standard: Chemical Geology, v. 257, p. 34–43, doi: 10.1016/j.chemgeo.2008.08.004.
Lloyd, G.E., Farmer, A.B., and Mainprice, D., 1997, Misorientation analysis and the formation and orientation of subgrain and grain boundaries: Tectonophysics, v. 279, p. 55–78, doi: 10.1016/S0040-1951(97)00115-7.
Love, G.R., 1964, Dislocation pipe diffusion: Acta Metallurgica, v. 12, p. 731–737.
Lucassen, F., Franz, G., Dulski, P., Romer, R.L., and Rhede, D., 2011, Lithos Element and Sr isotope signatures of titanite as indicator of variable fluid composition in hydrated eclogite: Lithos, v. 121, p. 12–24, doi: 10.1016/j.lithos.2010.09.018.
Macdonald, J.M., Wheeler, J., and Harley, S.L., 2013, Lattice distortion in a zircon population and its effects on trace element mobility and U–Th–Pb isotope systematics: examples from the Lewisian Gneiss Complex, northwest Scotland: Contributions to Mineralogy and Petrology, v. 166, p. 21–41, doi: 10.1007/s00410-013-0863-8.
Mahood, G., Hildreth, W., 1983, Large partition coefficients For trace elements in high-silica rhyolites: Geochimica et Cosmochimica Acta, v. 47, p. 11–30.
Marcotte, S. B., Klepeis, K. A., Clarke, G. L., Gehrels, G., and Hollis, J. A., 2005, Intra-arc transpression in the lower crust and its relationship to magmatism in a Mesozoic magmatic arc: *Tectonophysics*, v. *407*, p. 135–163, https://doi.org/10.1016/j.tecto.2005.07.007.
Marsh, J.H., and Smye, A.J., 2017, U-Pb systematics and trace element characteristics in titanite from a high-pressure mafic granulite: Chemical Geology, v. 466, p. 403–416, doi: 10.1016/j.chemgeo.2017.06.029.
Mathez, E.A., and Webster, J.D., 2005, Partitioning behavior of chlorine and fluorine in the system apatite-silicate melt-fluid: Geochimica et Cosmochimica Acta, v. 69, p. 1275–1286, doi: 10.1016/j.gca.2004.08.035.
Mattinson, J. M., Kimbrough, D. L., and Bradshaw, J. Y., 1986, Western Fiordland orthogneiss: Early Cretaceous arc magmatism and granulite facies metamorphism, New Zealand: *Contributions to Mineralogy and Petrology*, v. *92*, p. 383–392.
McClelland, W.C., Gehrels, G.E., Samson, S.D., and Patchett, P.J., 1992, Structural and geochronologic relations along the western flank of the coast mountains batholith: Stikine river to Cape Fanshaw, central southeastern Alaska: Journal of Structural Geology, v. 14, p. 475–489, doi: 10.1016/0191-8141(92)90107-8.
Mcdonough, W.F., and Sun, S., 1995, The composition of the Earth: Chemical Geology, v. 120, p. 223–253, doi: https://doi.org/10.1016/0009-2541(94)00140-4.
Michailos, K., Sutherland, R., Townend, J., and Savage, M. K., 2020, Crustal Thermal Structure and Exhumation Rates in the Southern Alps Near the Central Alpine Fault, New Zealand: *Geochemistry, Geophysics, Geosystems*, v. *21,* no. 8, https://doi.org/10.1029/2020GC008972.
Migdisov, A.A., Williams-jones, A.E., Hinsberg, V. Van, and Salvi, S., 2011, An experimental study of the solubility of baddeleyite (ZrO2) in fluoride-bearing solutions at elevated temperature: Geochimica et Cosmochimica Acta, v. 75, p. 7426–7434, doi: 10.1016/j.gca.2011.09.043.
Migdisov, A.A., Williams-jones, A.E., and Wagner, T., 2009, An experimental study of the

solubility and speciation of the Rare Earth Elements (III) in fluoride-and chloride-bearing aqueous solutions at temperatures up to 300 ° C: Geochimica et Cosmochimica Acta, v. 73, p. 7087–7109, doi: 10.1016/j.gca.2009.08.023.
Moore, J., Beinlich, A., Porter, J.K., Talavera, C., Berndt, J., Piazolo, S., Austrheim, H., and Putnis, A., 2020, Microstructurally controlled trace element (Zr, U–Pb) concentrations in metamorphic rutile: An example from the amphibolites of the Bergen Arcs: Journal of Metamorphic Geology, v. 38, p. 103–127, doi: 10.1111/jmg.12514.
Morozov, I.B., Smithson, S.B., Hollister, L.S., and Diebold, J.B., 1998, Wide-angle seismic imaging across accreted terranes, southeastern Alaska and western British Columbia: Tectonophysics, v. 299, p. 281–296, doi: 10.1016/S0040-1951(98)00208-X.
Mortimer, N., and Cooper, A. F., 2004, U-Pb and Sm-Nd ages from the Alpine Schist, New Zealand: *New Zealand Journal of Geology and Geophysics*, v. *47, no.* 1, p. 21–28, https://doi.org/10.1080/00288306.2004.9515034.
Moser, D.E., Davis, W.J., Reddy, S.M., Flemming, R.L., and Hart, R.J., 2009, Zircon U-Pb strain chronometry reveals deep impact-triggered flow: Earth and Planetary Science Letters, v. 277, p. 73–79, doi: 10.1016/j.epsl.2008.09.036.
Moser, A.C., Hacker, B.R., Gehrels, G.E., Seward, G.G.E., Kylander-Clark, A.R.C., and Garber, J.M., 2022, Linking titanite U–Pb dates to coupled deformation and dissolution–reprecipitation: Contributions to Mineralogy and Petrology, v. 177, p. 1–27, doi: 10.1007/s00410-022-01906-9.
Mottram, C. M., Cottle, J. M., and Kylander-Clark, A. R. C., 2019, Campaign-style U-Pb titanite petrochronology: Along-strike variations in timing of metamorphism in the Himalayan metamorphic core, *Geoscience Frontiers*, v. *10*, no. 3, p. 827–847, https://doi.org/10.1016/j.gsf.2018.09.007.
Muir, R. J., Ireland, T. R., Weaver, S. D., Bradshaw, J. D., Evans, J. A., Eby, G. N., and Shelley, D., 1998, Geochronology and geochemistry of a Mesozoic magmatic arc system, Fiordland, New Zealand: *Journal of the Geological Society*, v. *155, no.* 6, p. 1037–1053, https://doi.org/10.1144/gsjgs.155.6.1037.
Nash, W.P., and Crecraft, H.R., 1985, Partition coefficients for trace elements in silicic magmas: Geochimica et Cosmochimica Acta, v. 49, p. 2309–2322, doi: 10.1016/0016-7037(85)90231-5.
Needy, S.K., Anderson, J.L., Wooden, J.L., Fleck, R.J., Barth, A.P., Paterson, S.R., Memeti, V., and Pignotta, G.S., 2009, Mesozoic magmatism in an upper- to middle-crustal section through the Cordilleran continental margin arc, eastern Transverse Ranges, California: Special Paper of the Geological Society of America, v. 456, p. 187–218, doi: 10.1130/2009.2456(07).
Norris, R. J., and Cooper, A. F., 2003, Very high strains recorded in mylonites along the Alpine Fault, New Zealand: Implications for the deep structure of plate boundary faults: *Journal of Structural Geology*, v. *25,* no. 12, 2141–2157, https://doi.org/10.1016/S0191-8141(03)00045-2.
Oberti, R., Smith, D.C., Rossi, G., and Caucia, F., 1991, The crystal-chemistry of high-aluminium titanites: European Journal of Mineralogy, v. 3, p. 777–792, doi: 10.1127/ejm/3/5/0777.
Odlum, M. L., and Stockli, D. F., 2020, Geochronologic constraints on deformation and metasomatism along an exhumed mylonitic shear zone using apatite U-Pb, geochemistry, and microtextural analysis: *Earth and Planetary Science Letters*, v. *538*,

no. 116177, https://doi.org/10.1016/j.epsl.2020.116177.
Odlum, M.L., Levy, D.A., Stockli, D.F., Stockli, L.D., and DesOrmeau, J.W., 2022, Deformation and metasomatism recorded by single-grain apatite petrochronology: Geology, v. XX, p. 1–7, doi: 10.1130/g49809.1.
Olierook, H.K.H., Taylor, R.J.M., Erickson, T.M., Clark, C., Reddy, S.M., Kirkland, C.L., Jahn, I., and Barham, M., 2019, Unravelling complex geologic histories using U–Pb and trace element systematics of titanite: Chemical Geology, v. 504, p. 105–122, doi: 10.1016/j.chemgeo.2018.11.004.
Oliver, G. J. H., 1980, Geology of the granulite and amphibolite facies gneisses of Doubtful Sound, fiordland, New Zealand: *New Zealand Journal of Geology and Geophysics*, v. *23, no*. 1, p. 27–41, https://doi.org/10.1080/00288306.1980.10424190.
Pan, Y., and Fleet, M.E., 1996, Rare earth element mobility during prograde granulite facies metamorphism: significance of fluorine: Contributions to Mineralogy and Petrology, v. 123, p. 251–262.
Papapavlou, K., Darling, J.R., Moser, D.E., Barker, I.R., White, L.F., Lightfoot, P.C., Storey, C.D., and Dunlop, J., 2018, U–Pb isotopic dating of titanite microstructures: potential implications for the chronology and identification of large impact structures: Contributions to Mineralogy and Petrology, v. 173, p. 82, doi: 10.1007/s00410-018-1511-0.
Papapavlou, K., Darling, J.R., Storey, C.D., Lightfoot, P.C., Moser, D.E., and Lasalle, S., 2017, Dating shear zones with plastically deformed titanite: New insights into the orogenic evolution of the Sudbury impact structure (Ontario, Canada): Precambrian Research, v. 291, p. 220–235, doi: 10.1016/j.precamres.2017.01.007.
Paterson, M.S., 1989, The interaction of water with quartz and its influence in dislocation flow, *in* Karato, S. -l. and Toriumi, M. eds., Rheology of soilds and of the Earth, Oxford, Oxford University Press, p. 107–142.
Paterson, B., Stephens, W.E., and Herd, D.A., 1989, Zoning in granitoid accessory minerals as revealed by backscattered electron imagery: Mineralogical Magazine, v. 53, p. 55–61, doi: 10.1180/minmag.1989.053.369.05.
Paton, C., 2011, Iolite: Freeware for the visualization and procession of mass spectrometric data: Journal of Analytical Atomic Spectrometry, v. 26, p. 2508–2518.
Paul, A.N., Spikings, R.A., Chew, D., and Daly, J.S., 2019, The effect of intra-crystal uranium zonation on apatite U-Pb thermochronology: A combined ID-TIMS and LA-MC-ICP-MS study: Geochimica et Cosmochimica Acta, v. 251, p. 15–35, doi: 10.1016/j.gca.2019.02.013.
Pearce, N.J.G., Perkins, W.T., Westgate, J.A., Gorton, M.P., Jackson, S.E., Neal, C.R., and Chenery, S.P., 1997, A Compilation of New and Published Major and Trace Element Data for NIST SRM 610 and NIST SRM 612 Glass Reference Materials: Journal of Geostandards and Geoanalysis, v. 21, p. 1–5, doi: https://doi.org/10.1111/j.1751-908X.1997.tb00538.x.
Peterman, E.M., Reddy, S.M., Saxey, D.W., Rickard, W.D.A., Kylander-Clark, A.R.C., Fougerouse, D., and Snoeyenbos, D.R., 2016, Nanogeochronology of discordant zircon measured by atom probe microscopy of Pb-enriched dislocation loops: Science Advances, v. 2, p. e1601318, doi: 10.1126/sciadv.1601318.
Piazolo, S., Austrheim, K., and Whitehouse, M., 2012, Brittle-ductile microfabrics in naturally deformed zircon : Deformation mechanisms and consequences for U-Pb

dating Brittle-ductile microfabrics in naturally deformed zircon : Deformation mechanisms and consequences for U-Pb dating: American Mineralogist, v. 97, p. 1544–1563, doi: 10.2138/am.2012.3966.
Piazolo, S., La Fontaine, A., Trimby, P., Harley, S., Yang, L., Armstrong, R., and Cairney, J.M., 2016, Deformation-induced trace element redistribution in zircon revealed using atom probe tomography: Nature Communications, v. 7, doi: 10.1038/ncomms10490.
Pouchon, M.A., Curti, E., Degueldre, C., and Tobler, L., 2001, The influence of carbonate complexes on the solubility of zirconia: new experimental data: Progress in Nuclear Energy, v. 38, p. 443–446.
Powell, R.E., 2001, Geologic Map and Digital Databse of the Porcupine Wash 7.5 Minute Quadrangle, Riverside County, California.:
Prowatke, S., and Klemme, S., 2005, Effect of melt composition on the partitioning of trace elements between titanite and silicate melt: Geochimica et Cosmochimica Acta, v. 69, p. 695–709, doi: 10.1016/j.gca.2004.06.037.
Prowatke, S., and Klemme, S., 2006, Trace element partitioning between apatite and silicate melts: Geochimica et Cosmochimica Acta, v. 70, p. 4513–4527, doi: 10.1016/j.gca.2006.06.162.
Pryer, L. L., 1993, Microstructures in feldspars from a major crustal thrust zone: the Grenville Front, Ontario, Canada: *Journal of Structural Geology*, v. *15,* no. 1, p. 21–36.
Putnis, A., 2009, Mineral Replacement Reactions: Reviews in Mineralogy and Geochemistry, v. 70, p. 87–124, doi: 10.2138/rmg.2009.70.3.
Putnis, C.V., and Mezger, K., 2004, A mechanism of mineral replacement: Isotope tracing in the model system KCl-KBr-H2O: Geochimica et Cosmochimica Acta, v. 68, p. 2839–2848, doi: 10.1016/j.gca.2003.12.009.
Putnis, C.V., Tsukamato, K., and Nishimura, Y., 2005, Direct observations of pseudomorphism : compositional and textural evolution at a fluid-solid interface: American Mineralogist, v. 90, p. 1909–1912, doi: 10.2138/am.2005.1990.
Rabier, J., and Puls, M.P., 1989, Atomistic calculations of point-defect interaction and migration energies in the core of an edge dislocation in NaCl: Philosophical Magazine, v. 59, p. 533–546, doi: 10.1080/01418618908229783.
Rapp, J.F., Klemme, S., Butler, I.B., and Harley, S.L., 2010, Extremely high solubility of rutile in chloride and fluoride-bearing metamorphic fluids: An experimental investigation: Geology, v. 38, p. 323–326, doi: 10.1130/G30753.1.
Reddy, S.M., Timms, N.E., Trimby, P., Kinny, P.D., Buchan, C., and Blake, K., 2006, Crystal-plastic deformation of zircon : A defect in the assumption of chemical robustness: Geology, v. 34, p. 257–260, doi: 10.1130/G22110.1.
Reddy, Steven Michael, Timms, N. E., Hamilton, P. J., and Smyth, H. R., 2009, Deformation-related microstructures in magmatic zircon and implications for diffusion: *Contributions to Mineralogy and Petrology*, v. *157*, no. 231–244, https://doi.org/10.1007/s00410-008-0331-z.
Reddy, Steven M, Riessen, A. Van, Saxey, D. W., Johnson, T. E., Rickard, W. D. A., Fougerouse, D., Fischer, S., Prosa, T. J., Rice, K.P., Reinhard, D.A., Chen, Y., and Olson, D, 2016, Mechanisms of deformation-induced trace element migration in zircon resolved by atom probe and correlative microscopy: *Geochimica et Cosmochimica Acta*, v. *195*, no. 158–170, https://doi.org/10.1016/j.gca.2016.09.019.
Ring, U. W. E., and Bernet, M. A., 2010, Fission-track analysis unravels the denudation

history of the Bonar Range in the footwall of the Alpine Fault, South Island, New Zealand: *Geological Magazine*, v. *147,* no. 6, p. 801–813, https://doi.org/10.1017/S0016756810000208.
Ring, U.W.E., Glodny, G., Angiboust, S., Little, T.A., and Lang, K.A., 2019, Middle to Late Miocene Age for the End of Amphibolite - Facies Mylonitization of the Alpine Schist , New Zealand : Implications for Onset of Transpression Across the Alpine Fault: Tectonics, v. 38, p. 4335–4359, doi: 10.1029/2019TC005577.
Ringwood, M. F., Schwartz, J. J., Turnbull, R. E., and Tulloch, A. J., 2021, Phanerozoic record of mantle-dominated arc magmatic surges in the Zealandia Cordillera: *Geology*, v. *49,* no. 10, p. 1230–1234, https://doi.org/10.1130/G48916.1.
Rizvanova, N.G., Levchenkov, O.A., Belous, A.E., Bezmen, N.I., Maslenikov, A.V., Komarov, A.N., Makeev, A.F., and Levskiy, L.K., 2000, Zircon reaction and stability of the U-Pb isotope system during interaction with carbonate fluid: experimental hydrothermal study: Contributions to Mineralogy and Petrology, v. 139, p. 101–114.
Romer, R.L., Heinrich, Æ.W., Schroder-Smeibidl, Meixner, Æ.A., Fischer, C.-O., and Schulz, C., 2005, Elemental dispersion and stable isotope fractionation during reactive fluid-flow and fluid immiscibility in the Bufa del Diente aureole, NE-Mexico: evidence from radiographies and Li, B, Sr, Nd, and Pb isotope systematics: Contributions to Mineralogy and Petrology, p. 400–429, doi: 10.1007/s00410-005-0656-9.
Rubatto, D., and Hermann, J., 2001, Exhumation as fast as subduction? Geology, v. 29, p. 3–6, doi: 10.1130/0091-7613(2001)029<0003:EAFAS>2.0.CO;2.
Ruiz-Agudo, E., and Putnis, C.V.., 2012, Direct observations of mineral–fluid reactions using atomic force microscopy: the specific example of calcite: Mineralogical Magazine, v. 76, p. 227–253, doi: 10.1180/minmag.2012.076.1.227.
Ruoff, A.L., and Balluffi, R.W., 1963, Strain-enhanced diffusion in metals. II. Dislocation and grain-boundary short-circuiting models: Journal of Applied Physics, v. 34, p. 1848–1853.
Rusmore, M.E., and Woodsworth, G.J., 1994, Evolution of the eastern Waddington thrust belt and its relation to the mid-Cretaceous Coast Mountains arc, western British Columbia: Tectonics, v. 13, p. 1052–1067, doi: 10.1029/94TC01316.
Rusmore, M.E., Gehrels, G., and Woodsworth, G.J., 2001, Southern continuation of the Coast shear zone and Paleocene strain partitioning in British Columbia-Southeast Alaska: Bulletin of the Geological Society of America, v. 113, p. 961–975, doi: 10.1130/0016-7606(2001)113<0961:SCOTCS>2.0.CO;2.
Rusmore, M.E., Woodsworth, G.J., and Gehrels, G.E., 2005, Two-stage exhumation of midcrustal arc rocks, Coast Mountains, British Columbia: Tectonics, v. 24, p. 1–25, doi: 10.1029/2004TC001750.
Salvi, S., Fontan, F., Monchoux, P., Williams-Jones, A.E., and Moine, B., 2000, Hydrothermal Mobilization of High Field Strength Elements in Alkaline Igneous Systems: Evidence from the Tamazeght Complex (Morocco): Economic Geology, v. 95, p. 559–576.
Schmitz, M.D., and Bowring, S.A., 2001, U-Pb zircon and titanite systematics of the Fish Canyon Tuff: an assessment of high- precision U-Pb geochronology and its application to young volcanic rocks: Geochimica et Cosmochimica Acta, v. 65, p. 2571–2587, doi: https://doi.org/10.1016/S0016-7037(01)00616-0.
Schwartz, J. J., Stowell, H. H., Klepeis, K. A., Tulloch, A. J., Kylander-clark, A. R. C.,

Hacker, B. R., and Coble, M. A., 2016, Thermochronology of extensional orogenic collapse in the deep crust of Zealandia: *Geosphere*, v. *12,* no. 3, p. 647–677, https://doi.org/10.1130/GES01232.1.

Schwartz, J.J., Klepeis, K.A., Sadorski, J.F., Stowell, H.H., Tulloch, A.J., and Coble, M.A., 2017, The tempo of continental arc construction in the Mesozoic Median Batholith, Fiordland , New Zealand: Lithosphere, v. 9, p. 343–365, doi: 10.1130/L610.1.

Scott, J. M., Auer, A., Muhling, J. R., Czertowicz, T. A., Cooper, A. F., Billia, M. A., and Kennedy, A. K., 2015, New P-T and U-Pb constraints on Alpine Schist metamorphism in south Westland, New Zealand: *New Zealand Journal of Geology and Geophysics*, v. *58, no*. 4, 385–397, https://doi.org/10.1080/00288306.2015.1093005.

Scott, J. M., Cooper, A. F., Tulloch, A. J., and Spell, T. L., 2011, Crustal thickening of the Early Cretaceous paleo-Pacific Gondwana margin: *Gondwana Research*, v. *20, no.* 2–3, p. 380–394, https://doi.org/10.1016/j.gr.2010.10.008.

Seydoux-Guillaume, A.-M., Montel, J., Bingen, B., Bosse, V., Parseval, P. De, Paquette, J., Janots, E., and Wirth, R., 2012, Low-temperature alteration of monazite : Fluid mediated coupled dissolution–precipitation, irradiation damage, and disturbance of the U–Pb and Th–Pb chronometers: Chemical Geology, v. 330–331, p. 140–158, doi: 10.1016/j.chemgeo.2012.07.031.

Shannon R.D., 1976, Revised Effective Ionic Radii and Systematic Studies of Interatomic Distances in Halides and Chaleogenides: Acta Crystallographica v. 32, p. 751–767. https://doi.org/https://doi.org/10.1107/S0567739476001551.

Smith, M.P., Storey, C.D., Jeffries, T.E., and Ryan, C., 2009, In Situ U–Pb and Trace Element Analysis of Accessory Minerals in the Kiruna District, Norrbotten, Sweden: New Constraints on the Timing and Origin of Mineralization: Journal of Petrology, v. 50, p. 2063–2094, doi: 10.1093/petrology/egp069.

Smye, A.J., Marsh, J.H., Vermeesch P., Garber, J.M., and Stockli, D.F., 2018, Applications and limitations of U-Pb thermochronology to middle and lower crustal thermal histories: Chemical Geology, v. 494, p. 1–18, https://doi.org/10.1016/j.chemgeo.2018.07.003.

Sodre Borges, F., and White, S. H., 1980, Microstructural and chemical studies of sheared anorthosites, Roneval, South Harris: *Journal of Structural Geology*, v. *2*, no. 1, p. 273–280.

Soman, A., Geisler, T., Tomaschek, F., Grange, M., and Berndt, J., 2010, Alteration of crystalline zircon solid solutions: a case study on zircon from an alkaline pegmatite from Zomba–Malosa, Malawi: Contributions to Mineralogy and Petrology, v. 160, p. 909–930, doi: 10.1007/s00410-010-0514-2.

Spandler, C., Hammerli, J., Sha, P., Hilbert-Wolf, H., Hu, Y., Roberts, E., and Schmitz, M., 2016, MKED1: A new titanite standard for in situ analysis of Sm-Nd isotopes and U-Pb geochronology: Chemical Geology, v. 425, p. 110–126, doi: 10.1016/j.chemgeo.2016.01.002.

Spencer, K.J., Hacker, B.R., Kylander-Clark, A.R.C., Andersen, T.B., Cottle, J.M., Stearns, M.A., Poletti, J.E., and Seward, G.G.E., 2013, Campaign-style titanite U-Pb dating by laser-ablation ICP: Implications for crustal flow, phase transformations and titanite closure: Chemical Geology, v. 341, p. 84–101, doi: 10.1016/j.chemgeo.2012.11.012.

Stacey, J.S., and Kramers, J.D., 1975, Approximation of terrestrial lead isotope evolution by a two-stage model: Earth and Planetary Science Letters, v. 26, p. 207–221, doi:

10.1016/0012-821X(75)90088-6.
Stearns, M.A., Cottle, J.M., and Hacker, B.R., 2016, Extracting thermal histories from the near-rim zoning in titanite using coupled U–Pb and trace-element depth profiles by single-shot laser-ablation split stream (SS-LASS) ICP-MS: Chemical Geology, v. 422, p. 13–24, doi: 10.1016/j.chemgeo.2015.12.011.
Stepanov, A.S., and Hermann, J., 2013, Fractionation of Nb and Ta by biotite and phengite: Implications for the "missing Nb paradox": Geology, v. 41, p. 303–306, doi: 10.1130/G33781.1.
Stowell, H., Parker, K. O., Gatewood, M., Tulloch, A., and Koenig, A., 2014, Temporal links between pluton emplacement, garnet granulite metamorphism, partial melting and extensional collapse in the lower crust of a Cretaceous magmatic arc, Fiordland, New Zealand: *Journal of Metamorphic Geology*, v. *32*, p. 151–175, https://doi.org/10.1111/jmg.12064.
Stünitz, H., Fitz Gerald, J. D., and Tullis, J., 2003, Dislocation generation, slip systems, and dynamic recrystallization in experimentally deformed plagioclase single crystals: *Tectonophysics*, v. *372,* no. 3–4, p. 215–233, https://doi.org/10.1016/S0040-1951(03)00241-5.
Sutherland, R., Gurnis, M., Kamp, P. J. J., and House, M. A., 2009, Regional exhumation history of brittle crust during subduction initiation, Fiordland, southwest New Zealand, and implications for thermochronologic sampling and analysis strategies: *Geosphere*, v. *5,* no. 5, p. 409–425, https://doi.org/10.1130/ges00225.1.
Sutherland, R., Toy, V. G., Townend, J., Cox, S. C., Eccles, J. D., Faulkner, D. R., Prior, D.J., Norris, R.J., Mariani, E., Boulton, C., Carpenter, B.M., Menzies, C.D., Little, T.A., Hasting, M., De Pascale, G.P., Langridge, R.M., Scott, H.R., Lindroos, Z.R., Fleming, B., and Kopf, J., 2012, Drilling reveals fluid control on architecture and rupture of the Alpine fault, New Zealand: *Geology*, v. *40,* no. 12, p. 1143–1146, https://doi.org/10.1130/G33614.1
Sutherland, R., 1995, The Australia-Pacific in the SW Pacific: boundary and Cenozoic plate motions: *Tectonics*, v. *14, no.* 4, p. 819–831.
Sutherland, Rupert, Barnes, P., and Uruski, C., 2006, Miocene-recent deformation, surface elevation, and volcanic intrusion of the overriding plate during subduction initiation, offshore southern Fiordland, Puysegur margin, southwest New Zealand: *New Zealand Journal of Geology and Geophysics*, v. *49, no*. 1, p. 131–149, https://doi.org/10.1080/00288306.2006.9515154.
Svava Olsen, T., and Kohlstedt, D. L., 1985, Natural deformation and recrystallization of some intermediate plagioclase feldspars: *Tectonophysics*, v. *111, no.* 1–2, p. 107–131, https://doi.org/10.1016/0040-1951(85)90067-8.
Swiatnicki, W.A., Lojkowski, W., and Grabski, M.W., 1986, Inverstigation of grain boundary diffusion in polycrystals by means of extrinsic grain boundary dislocations spreading rate: Acta Metallurgica, v. 34, p. 599–605.
Syverson, D.D., Etschmann, B., Liu, W., Ram, R., Mei, Y., Lanzirotti, T., Mercadier, J., and Brugger, J., 2019, Oxidation state and coordination environment of Pb in U-bearing minerals: Geochimica Et Cosmochimica Acta, v. 265, p. 109–131, doi: 10.1016/j.gca.2019.08.039.
Thomas, J.B., and Sinha, A.K., 1999, Field, geochemical, and isotopic evidence for magma mixing and assimilation and fractional crystallization processes in the Quottoon

Igneous Complex, northwestern British Columbia and southeastern Alaska: Canadian Journal of Earth Sciences, v. 36, p. 819–831, doi: 10.1139/e99-001.
Timms, N.E., Kinny, P.D., and Reddy, S.M., 2006, Enhanced diffusion of Uranium and Thorium linked to crystal plasticity in zircon: Geochemical Transactions, v. 7, p. 1–16, doi: 10.1186/1467-4866-7-10.
Timms, N.., Kinny, P.., Reddy, S.M., Evans, K., Clark, C., and Healy, D., 2011, Relationship among titanium, rare earth elements, U-Pb ages and deformation microstructures in zircon: Implications for Ti-in-zircon thermometry: Chemical Geology, v. 280, p. 33–46.
Tippett, J. M., and Kamp, P. J. J., 1993, Fission Track Analysis of the Late Cenozoic Vertical Kinematics of Continental Pacific Crust, South Island, New Zealand: *Journal of Geophysical Research: Solid Earth*, v. *98.* no. B9, p. 16,119–16,148.
Tomaschek, F., Kennedy, A.K., Villa, I.M., Lagos, M., and Ballhaus, C., 2003, Zircons from Syros, Cyclades, Greece– Recrystallization and Mobilization of Zircon During High-Pressure Metamorphism: Journal of Petrology, v. 44, p. 1977–2002, doi: 10.1093/petrology/egg067.
Toy, V. G., Boulton, C. J., Sutherland, R., Townend, J., Norris, R. J., Little, T. A., Prior, D.J., Mariani, E., Faulkner, D., Menzies, C.D., Scott, H., and Carpenter, B. M., 2015, Fault rock lithologies and architecture of the central Alpine fault, New Zealand, revealed by DFDP-1 drilling: *Lithosphere*, v. *7, no*. 2, p. 155–173, https://doi.org/10.1130/L395.1
Tullis, J., and Yund, R.A., 1985, Dynamic recrystallization of feldspar: a mechanism for ductile shear zone formation.: Geology, v. 13, p. 238–241, doi: 10.1130/0091-7613(1985)13<238:DROFAM>2.0.CO;2.
Tullis, J., and Yund, R.A., 1987, Transition from cataclastic flow to dislocation creep of feldspar: mechanisms and microstructures.: Geology, v. 15, p. 606–609, doi: 10.1130/0091-7613(1987)15<606:TFCFTD>2.0.CO;2.
Tulloch, A. J., Ireland, T. R., Kimbrough, D. L., and Griffin, W. L., 2011, Autochthonous inheritance of zircon through Cretaceous partial melting of Carboniferous plutons: the Arthur River Complex, Fiordland, New Zealand: *Contributions to Mineralogy and Petrology*, v. *161*, p. 401–421, https://doi.org/10.1007/s00410-010-0539-6.
Tulloch, A. J., and Kimbrough, D. L., 2003, Paried plutonic belts in convergent margins and the development of high Sr/Y magmatism: Peninsular Ranges batholith of Baja-California and Median batholith of New Zealand: *Geological Society of America Special Paper*, v. *374*, p. 275–295.
Turnbull, D., and Hoffman, R., 1954, The effect of relative crystal and boundary orientations on grain boundary diffusion rates: Acta Metallurgica, v. 2, p. 419–426.
Vard, E., and Williams-jones, A.E., 1993, A fluid inclusion study of vug minerals in dawsonite-altered phonolite sills, Montreal, Quebec: implications for HFSE mobility: Contributions to Mineralogy and Petrology, v. 113, p. 410–423.
Vernon, R. H., 1981, Optical microstructure of partly recrystallized calcite in some naturally deformed marbles, *Tectonophysics*, v. *78,* no. 1–4, p. 601–612, https://doi.org/10.1016/0040-1951(81)90031-7.
Vidal, J. L., Kubin, L., Debat, P., and Soula, J. C., 1980, Deformation and dynamic recrystallization of K feldspar augen in orthogneiss from Montagne Noire, Occitania, Southern France: *Lithos*, v. *13,* no. 3, p. 247–255, https://doi.org/10.1016/0024-

4937(80)90070-5.
Vry, J. K., Baker, J., Maas, R., Little, T. A., Grapes, R., and Dixon, M., 2004, Zoned (Cretaceous and Cenozoic) garnet and the timing of high grade metamorphism, Southern Alps, New Zealand: *Journal of Metamorphic Geology*, v. *22, no*. 3, p. 137–157: https://doi.org/10.1111/j.1525-1314.2004.00504.x.
Walters, J.B., Cruz-Uribe, A.M., Song, W.J., Gerbi, C., and Biela, K., 2022, Strengths and limitations of in situ U–Pb titanite petrochronology in polymetamorphic rocks: An example from western Maine, USA: Journal of Metamorphic Geology, p. 1–24, doi: 10.1111/jmg.12657.
Walters, J.B., and Kohn, M.J., 2017, Protracted thrusting followed by late rapid cooling of the Greater Himalayan Sequence, Annapurna Himalaya, Central Nepal: Insights from titanite petrochronology: Journal of Metamorphic Geology, v. 35, p. 897–917, doi: 10.1111/jmg.12260.
Watson, E.B., and Liang, Y., 1995, A simple model for sector zoning in slowly grown crystals: Implications for growth rate and lattice diffusion, with emphasis on accessory minerals in crustal rocks: American Mineralogist, v. 80, p. 1179–1187, doi: https://doi.org/10.2138/am-1995-11-1209.
Weinberg, R.F., Wolfram, L.C., Nebel, O., Hasalova, P., Zavada, P., Kylander-clark, A.R.C., and Becchio, R., 2020, ScienceDirect Decoupled U-Pb date and chemical zonation of monazite in migmatites: The case for disturbance of isotopic systematics by coupled dissolution-reprecipitation: Geochimica et Cosmochimica Acta, v. 269, p. 398–412, doi: 10.1016/j.gca.2019.10.024.
Wells, M.L., Beyene, M.A., Spell, T.L., Kula, J.L., Miller, D.M., and Zanetti, K.A., 2005, The Pinto shear zone; a Laramide synconvergent extensional shear zone in the Mojave Desert region of the southwestern United States: Journal of Structural Geology, v. 27, p. 1697–1720, doi: 10.1016/j.jsg.2005.03.005.
Wells, M.L., and Hoisch, T.D., 2008, The role of mantle delamination in widespread Late Cretaceous extension and magmatism in the Cordilleran orogen, western United States: Geological Society of America Bulletin, v. 120, p. 515–530, doi: 10.1130/B26006.1.
Wendt, I., and Carl, C., 1991, The statistical distribution of the mean squared weighted deviation: *Chemical Geology: Isotope Geoscience Section*, v. *86,* no. 4, p. 275–285, https://doi.org/10.1016/0168-9622(91)90010-T.
White, S.H., and Knipe, R.J., 1978, Transformation- and reaction-enhanced ductility in rocks: Journal of the Geological Society, v. 135, p. 513–516, doi: 10.1144/gsjgs.135.5.0513.
Williams, I.S., 1998, U-Th-Pb geochronology by ion microprobe: Reviews in economic geology, v. 7, p. 1–35.
Williams, M.L., Jercinovic, M.J., Harlov, D.E., Budzy, B., and Hetherington, C.J., 2011, Resetting monazite ages during fl uid-related alteration: Chemical Geology, v. 283, p. 218–225, doi: 10.1016/j.chemgeo.2011.01.019.
Wintsch, R.P., and Yi, K., 2002, Dissolution and replacement creep: A significant deformation mechanism in mid-crustal rocks: Journal of Structural Geology, v. 24, p. 1179–1193, doi: 10.1016/S0191-8141(01)00100-6.
Wood, B. L., 1972, Metamorphosed ultramafites and associated formations near Milford Sound, New Zealand, *New Zealand Journal of Geology and Geophysics*, v. *15, no.* 1, p. 88–128, https://doi.org/10.1080/00288306.1972.10423948.

Wood, D.J., Stowell, H.H., Onstott, T.C., and Hollister, L.S., 1991, $^{40}Ar/^{39}Ar$ constraints on the emplacement, uplift, and cooling of the Coast Plutonic Complex sill, southeastern Alaska: Geological Society of America Bulletin, v. 103, p. 849–860.

Wooden, J.L., and Miller, D.M., 1990, Chronologic and Isotopic Framework for Early Proterozoic Crustal Evolution in the Eastern Mojave Desert Region , SE California: Journal of Geophysical Research, v. 95, p. 20, 133–20, 146, doi: 10.1029/JB095iB12p20133.

Zhang, C., Li, X., Behrens, H., and Holtz, F., 2022, Partitioning of OH-F-Cl between biotite and silicate melt: Experiments and an empirical model: Geochimica et Cosmochimica Acta, v. 317, p. 155–179, doi: 10.1016/j.gca.2021.10.031.

APPENDICES

APPENDIX 1

TEXT S1

Equations used to calculate Pb concentrations:

$$^{204}Pb\ ppm = (U\ ppm) \times \left(\frac{1\ mol\ U}{238.02891\ g\ U}\right) \times \left(\frac{0.9928\ mol\ ^{238}U}{1\ mol\ U}\right) \times \left(\frac{mol\ ^{206}Pb}{mol\ ^{238}U}\right)_m \times \left(\frac{mol\ ^{204}Pb}{mol\ ^{206}Pb}\right)_m \times \left(\frac{203.9730\ g\ ^{207}Pb}{1\ mol\ ^{207}Pb}\right)$$

$$^{206}Pb\ ppm = (U\ ppm) \times \left(\frac{1\ mol\ U}{238.02891\ g\ U}\right) \times \left(\frac{0.9928\ mol\ ^{238}U}{1\ mol\ U}\right) \times \left(\frac{mol\ ^{206}Pb}{mol\ ^{238}U}\right)_m \times \left(\frac{205.9745\ g\ ^{206}Pb}{1\ mol\ ^{206}Pb}\right)$$

$$^{207}Pb\ ppm = (U\ ppm) \times \left(\frac{1\ mol\ U}{238.02891\ g\ U}\right) \times \left(\frac{0.9928\ mol\ ^{238}U}{1\ mol\ U}\right) \times \left(\frac{mol\ ^{206}Pb}{mol\ ^{238}U}\right)_m \times \left(\frac{mol\ ^{207}Pb}{mol\ ^{206}Pb}\right)_m \times \left(\frac{206.9759\ g\ ^{207}Pb}{1\ mol\ ^{207}Pb}\right)$$

$$^{208}Pb\ ppm = (U\ ppm) \times \left(\frac{1\ mol\ U}{238.02891\ g\ U}\right) \times \left(\frac{0.9928\ mol\ ^{238}U}{1\ mol\ U}\right) \times \left(\frac{mol\ ^{206}Pb}{mol\ ^{238}U}\right)_m \times \left(\frac{mol\ ^{208}Pb}{mol\ ^{206}Pb}\right)_m \times \left(\frac{207.9757\ g\ ^{207}Pb}{1\ mol\ ^{207}Pb}\right)$$

Equations used to calculate fraction ^{206}Pb, ^{207}Pb, and ^{208}Pb that is common Pb:

$$^{206}Pb_c/^{206}Pb_t = ((^{207}Pb/^{206}Pb)_m - (^{207}Pb/^{206}Pb)^*)/((^{207}Pb/^{206}Pb)_c - (^{207}Pb/^{206}Pb)^*)$$

$$^{207}Pb_c/^{207}Pb_t = ^{206}Pb_c/^{206}Pb_t \times ((^{207}Pb/^{206}Pb)_c/(^{207}Pb/^{206}Pb)_m)$$

$$^{208}Pb_c/^{208}Pb_t = ^{206}Pb_c/^{206}Pb_t \times ((^{208}Pb/^{206}Pb)_c/(^{208}Pb/^{206}Pb)_m)$$

Where $^{20X}Pb_c/^{20X}Pb_t$ is the fraction 20XPb common, $(^{20X}Pb/^{20X}Pb)_m$ is the measured ratio, $(^{207}Pb/^{206}Pb)^*$ is the radiogenic Pb value for the ^{207}Pb-corrected ^{206}Pb–^{238}U date, and $(^{20X}Pb/^{20X}Pb)_c$ is the Stacey and Kramers (1975) two-stage terrestrial Pb model value.

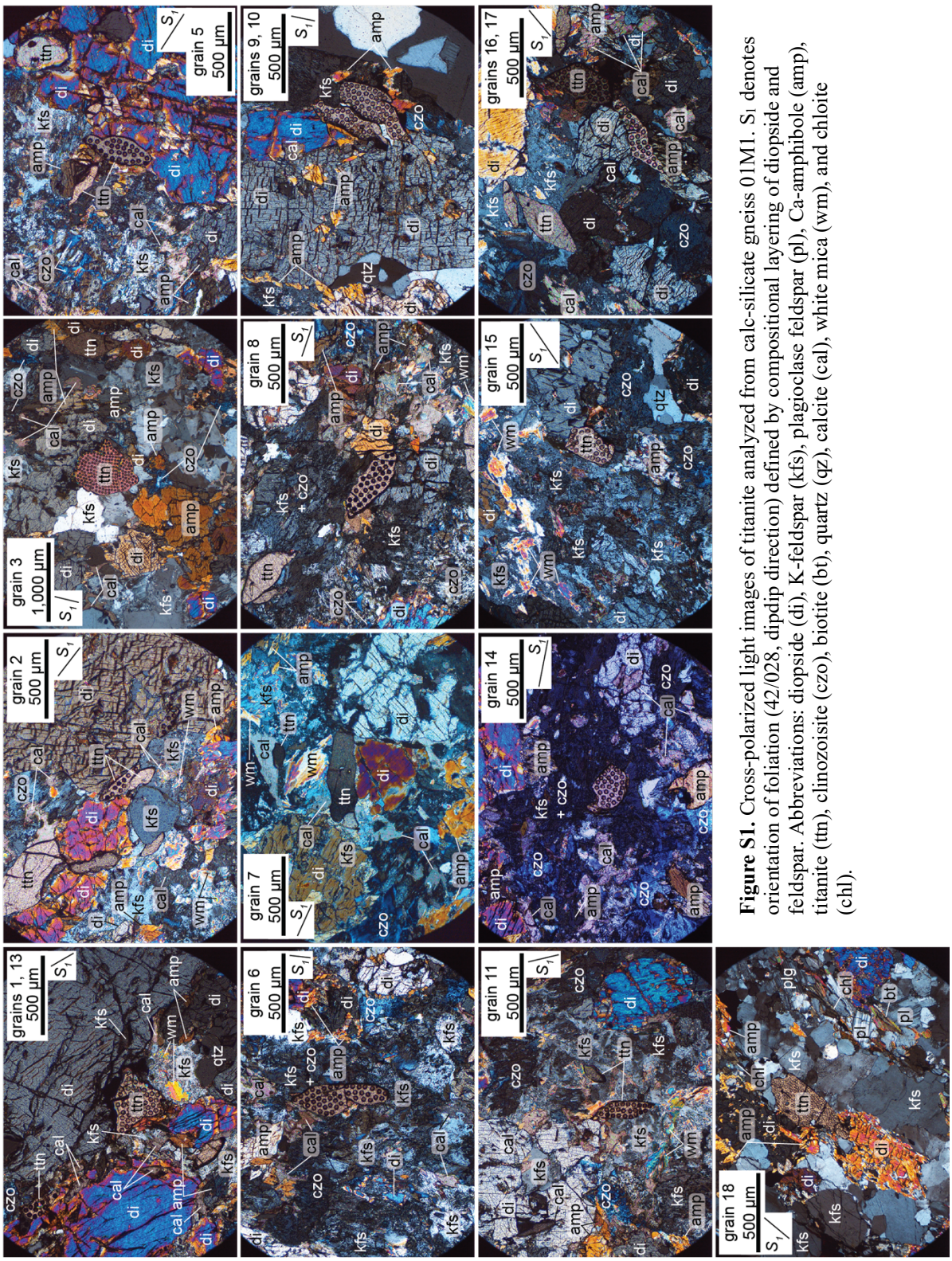

Figure S1. Cross-polarized light images of titanite analyzed from calc-silicate gneiss 01M1. S_1 denotes orientation of foliation (42/028, dipdip direction) defined by compositional layering of diopside and feldspar. Abbreviations: diopside (di), K-feldspar (kfs), plagioclase feldspar (pl), Ca-amphibole (amp), titanite (ttn), clinozoisite (czo), biotite (bt), quartz (qz), calcite (cal), white mica (wm), and chloite (chl).

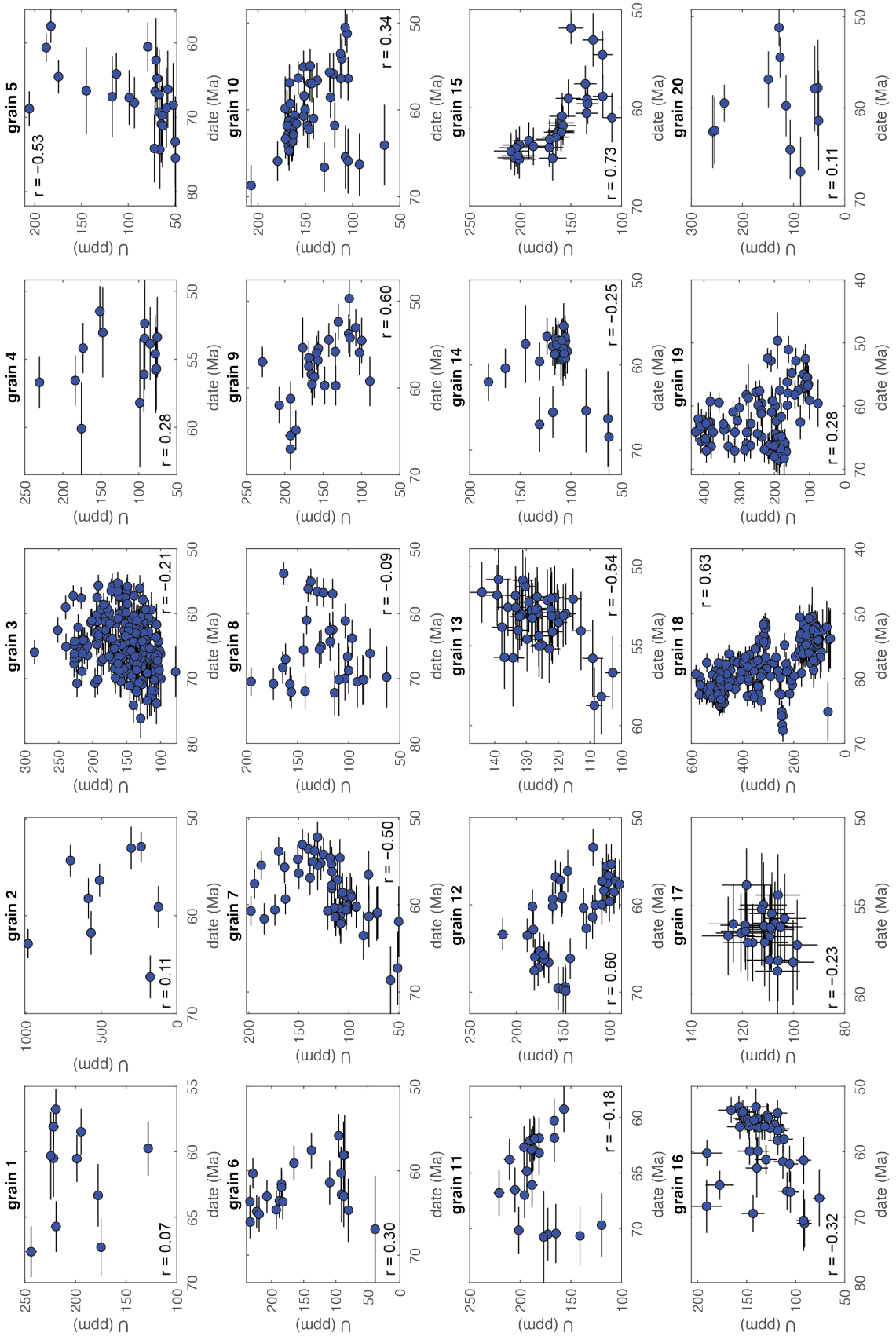

Figure S3. Date vs. U (ppm) for each of the analyzed titanite grains. Date uncertainties are in-run uncertainties.

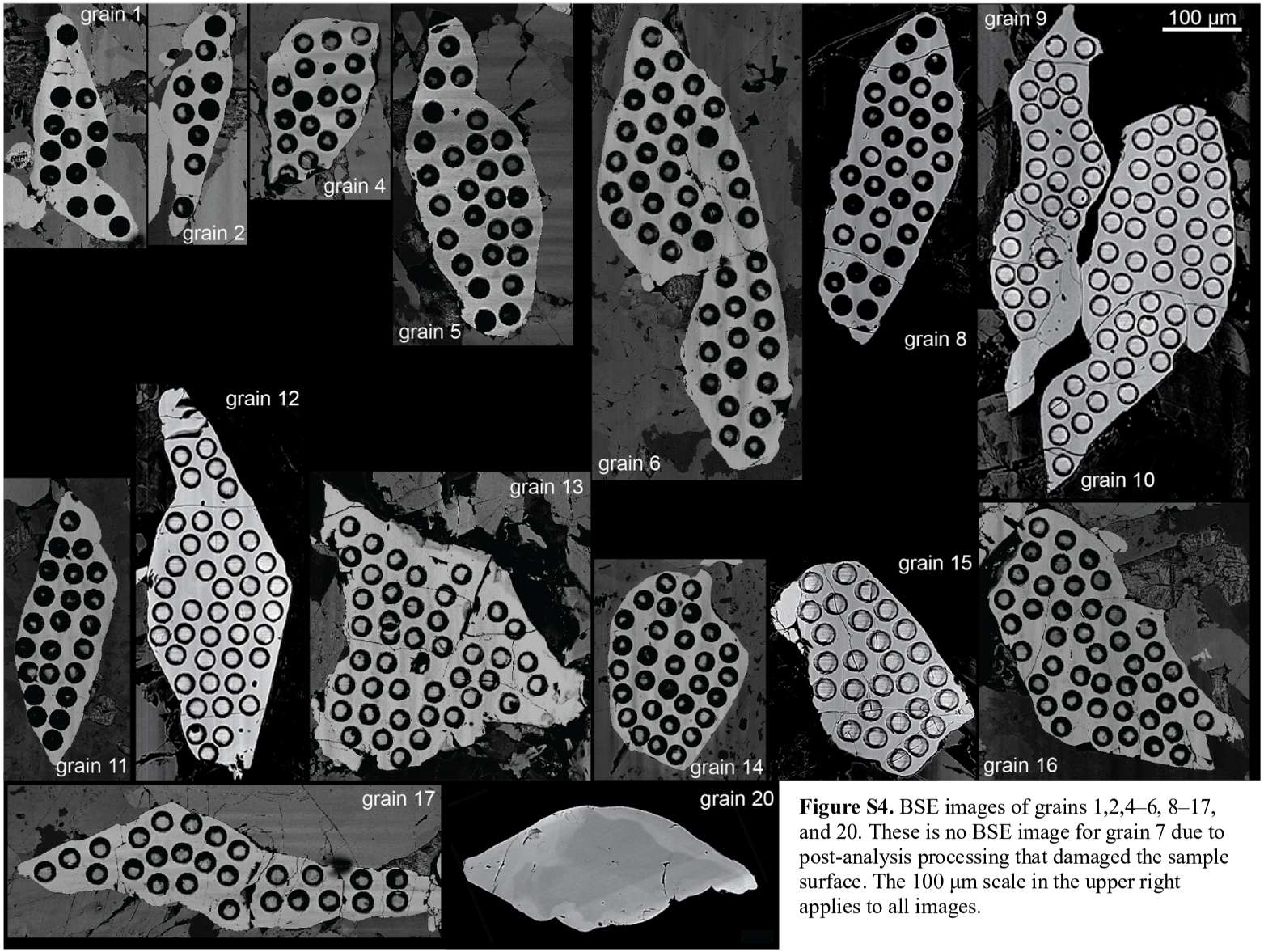

Figure S4. BSE images of grains 1,2,4–6, 8–17, and 20. These is no BSE image for grain 7 due to post-analysis processing that damaged the sample surface. The 100 µm scale in the upper right applies to all images.

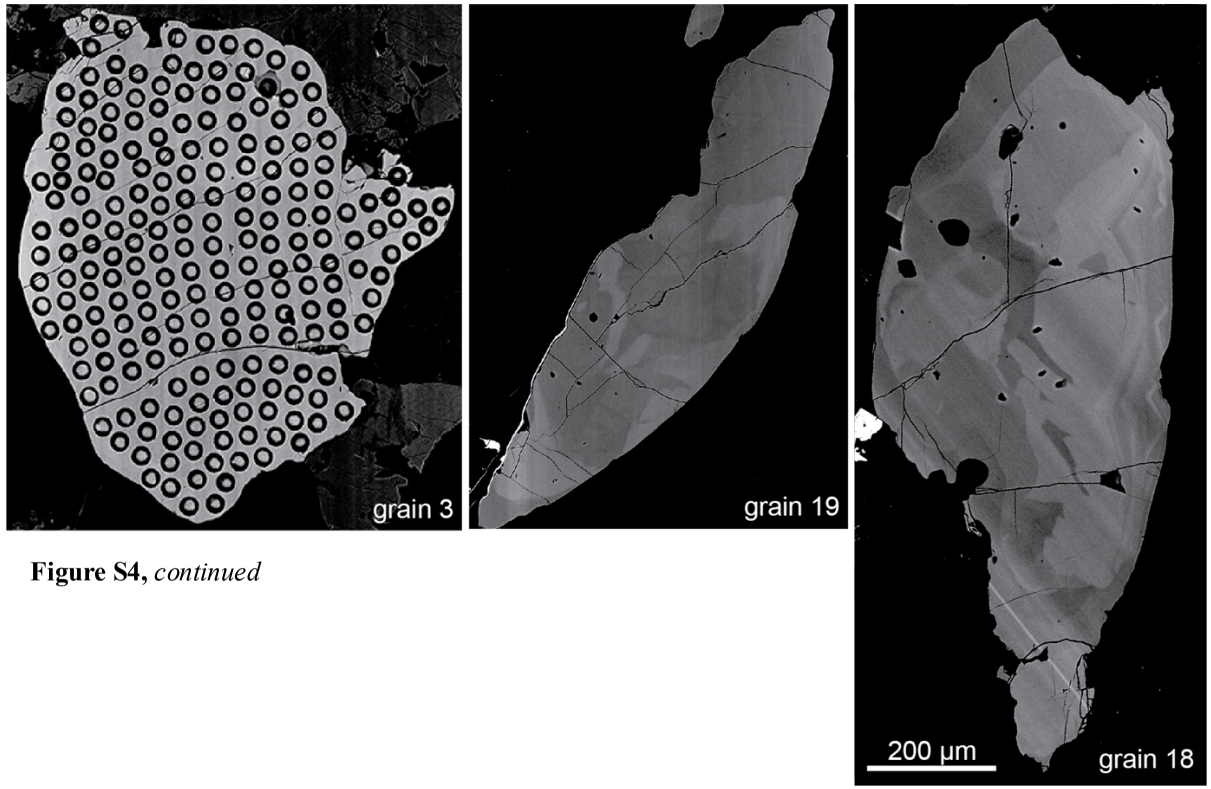

Figure S4, *continued*

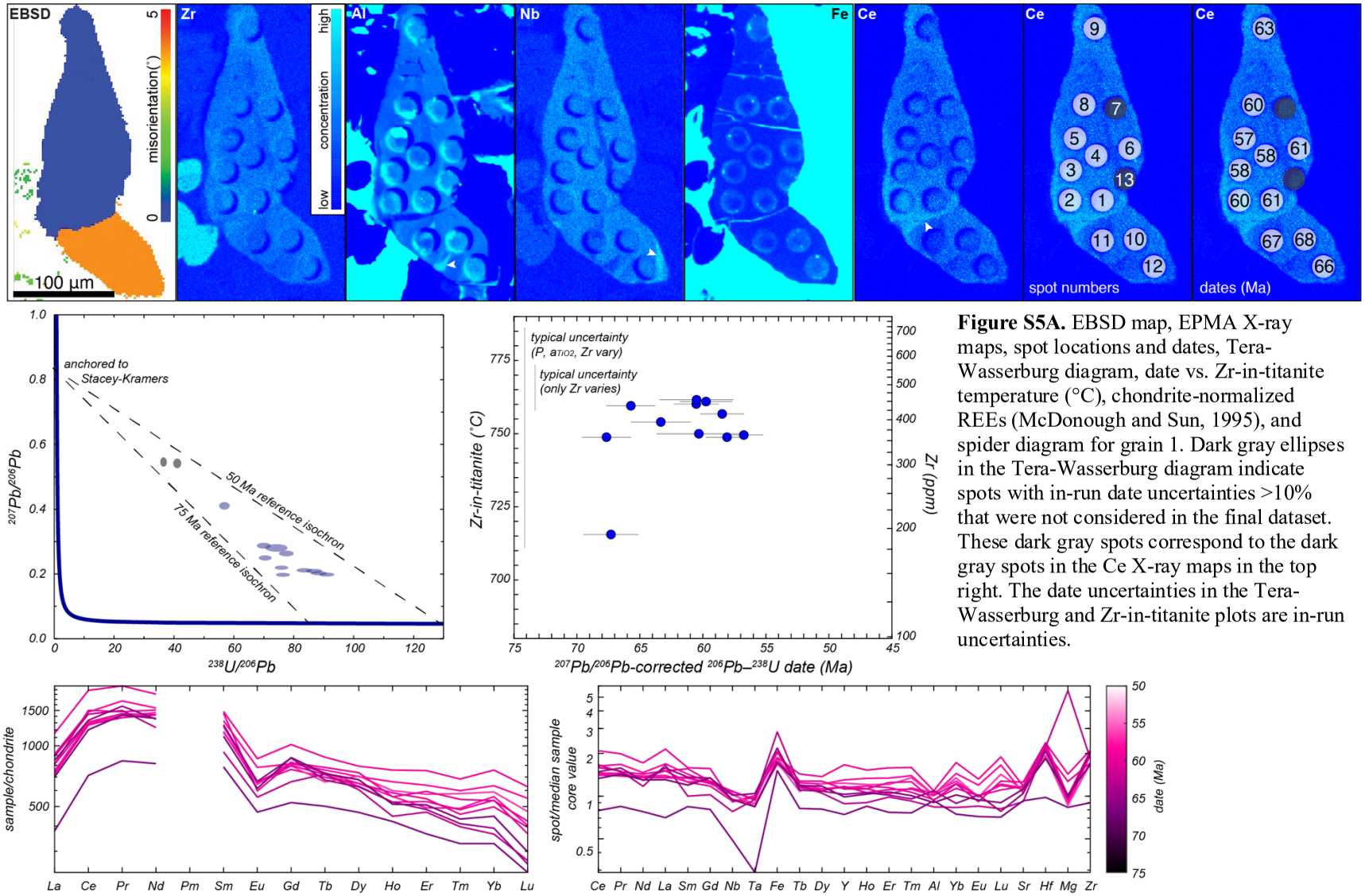

Figure S5A. EBSD map, EPMA X-ray maps, spot locations and dates, Tera-Wasserburg diagram, date vs. Zr-in-titanite temperature (°C), chondrite-normalized REEs (McDonough and Sun, 1995), and spider diagram for grain 1. Dark gray ellipses in the Tera-Wasserburg diagram indicate spots with in-run date uncertainties >10% that were not considered in the final dataset. These dark gray spots correspond to the dark gray spots in the Ce X-ray maps in the top right. The date uncertainties in the Tera-Wasserburg and Zr-in-titanite plots are in-run uncertainties.

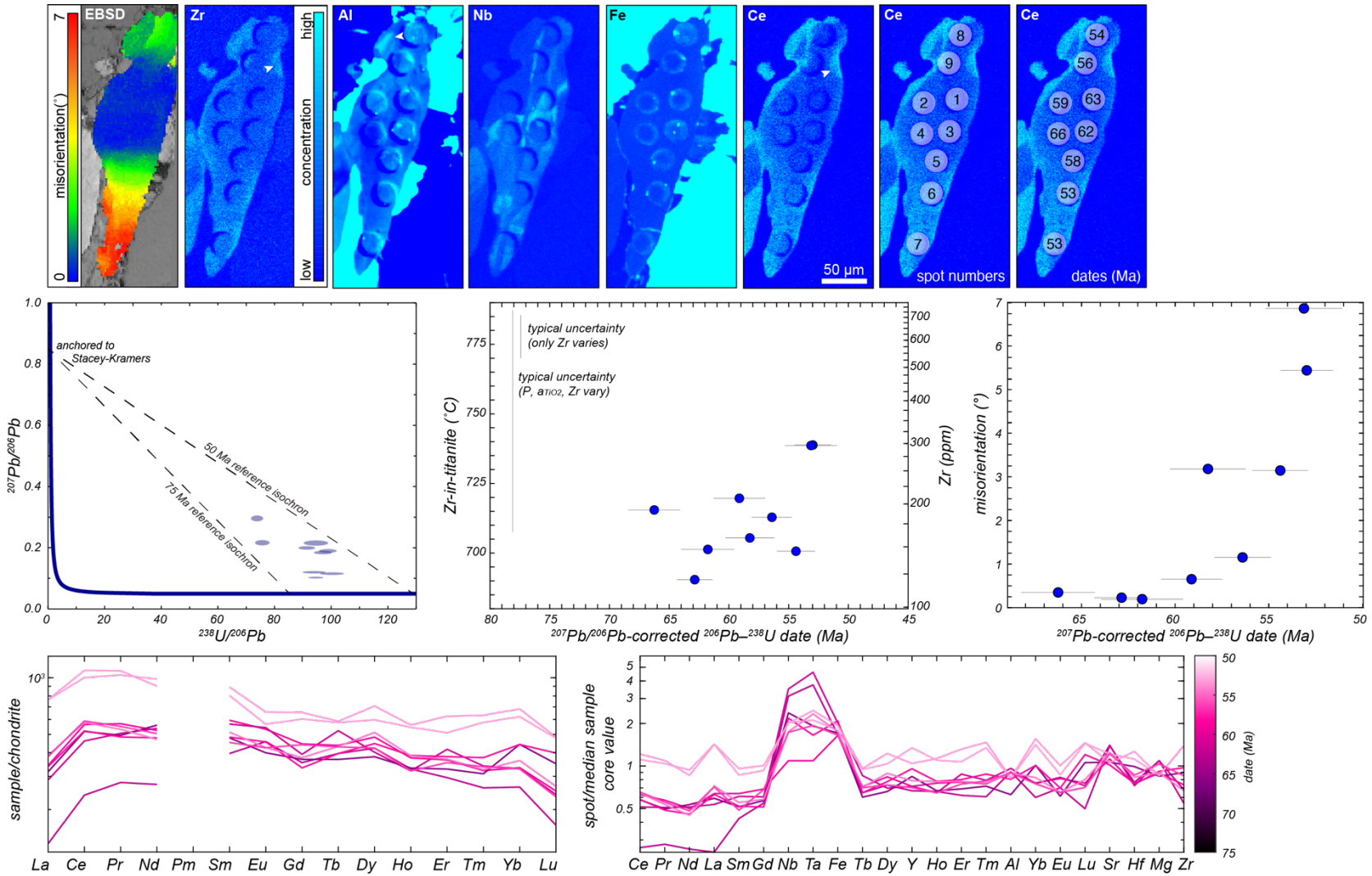

Figure 5B. Data for grain 2. Uncertainties in the Tera-Wasserburg diagrams and date uncertainties in the date vs. Zr-in-ttn plot and date vs. misorientation plot are in-run uncertainties. White arrows indicate patchy and lobate–cuspate compositional domains interpreted to have formed from dissolution–reprecipitation.

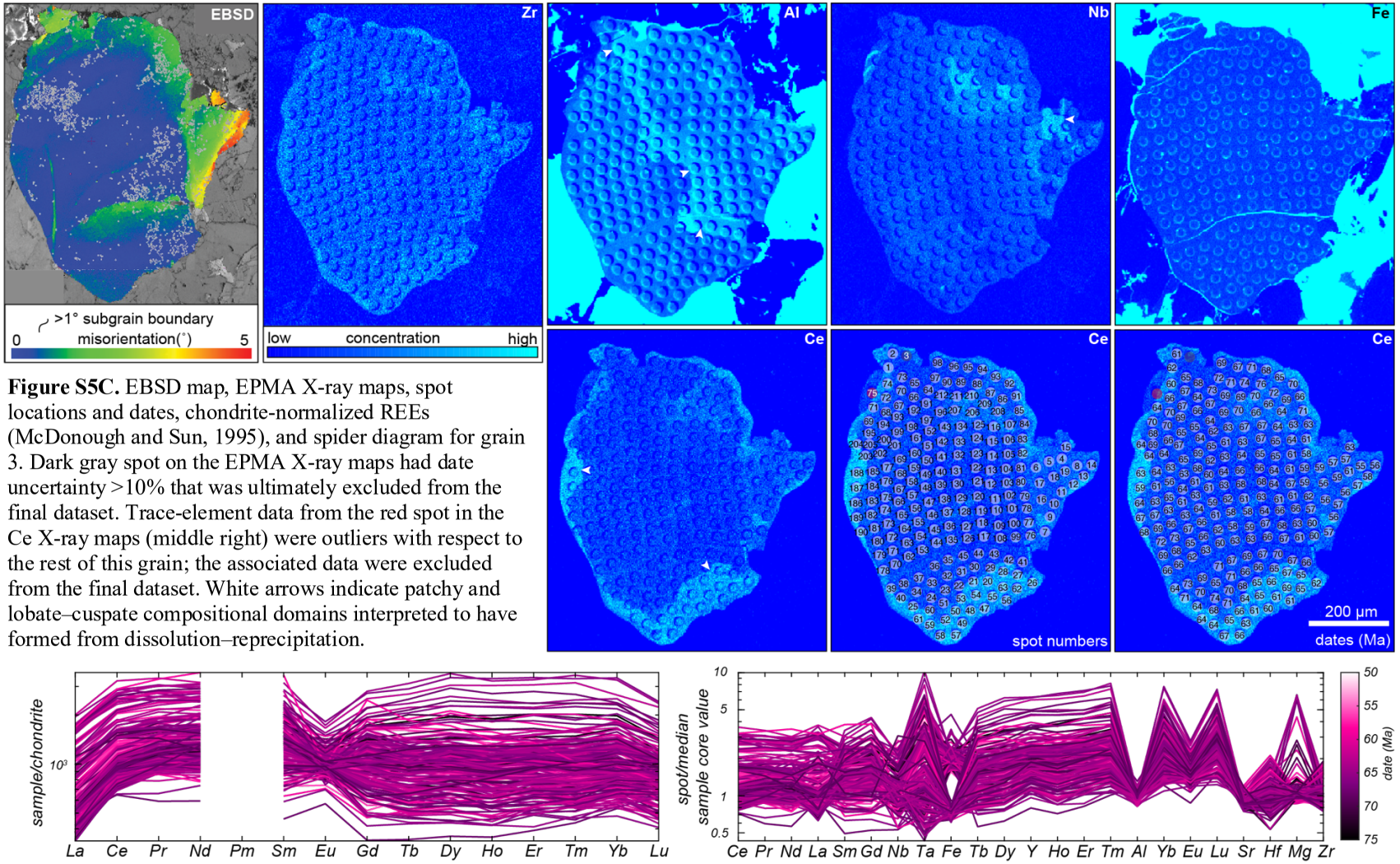

Figure S5C. EBSD map, EPMA X-ray maps, spot locations and dates, chondrite-normalized REEs (McDonough and Sun, 1995), and spider diagram for grain 3. Dark gray spot on the EPMA X-ray maps had date uncertainty >10% that was ultimately excluded from the final dataset. Trace-element data from the red spot in the Ce X-ray maps (middle right) were outliers with respect to the rest of this grain; the associated data were excluded from the final dataset. White arrows indicate patchy and lobate–cuspate compositional domains interpreted to have formed from dissolution–reprecipitation.

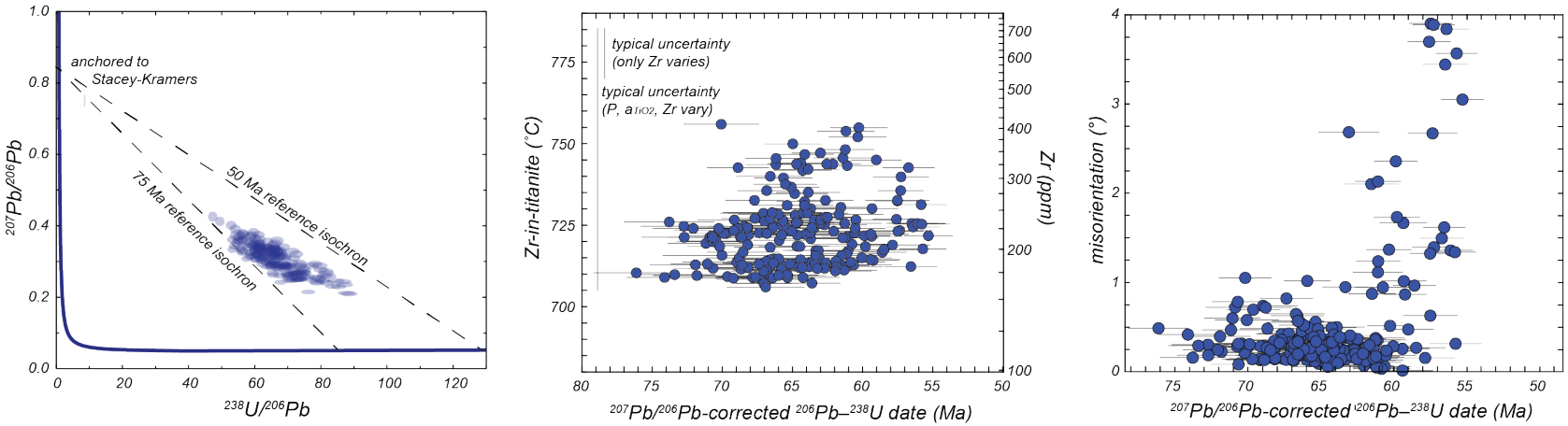

Figure 5C, continued. Date vs. misorientation, Tera-Wasserburg diagram, and date vs. Zr-in-titanite temperature (°C) for grain 3. The dark gray spot in the Tera-Wasserburg diagram indicates spot with in-run date uncertainty >10% that was not considered in the final dataset. This dark gray spot corresponds to the dark gray spot in the Ce X-ray maps on the previous page.

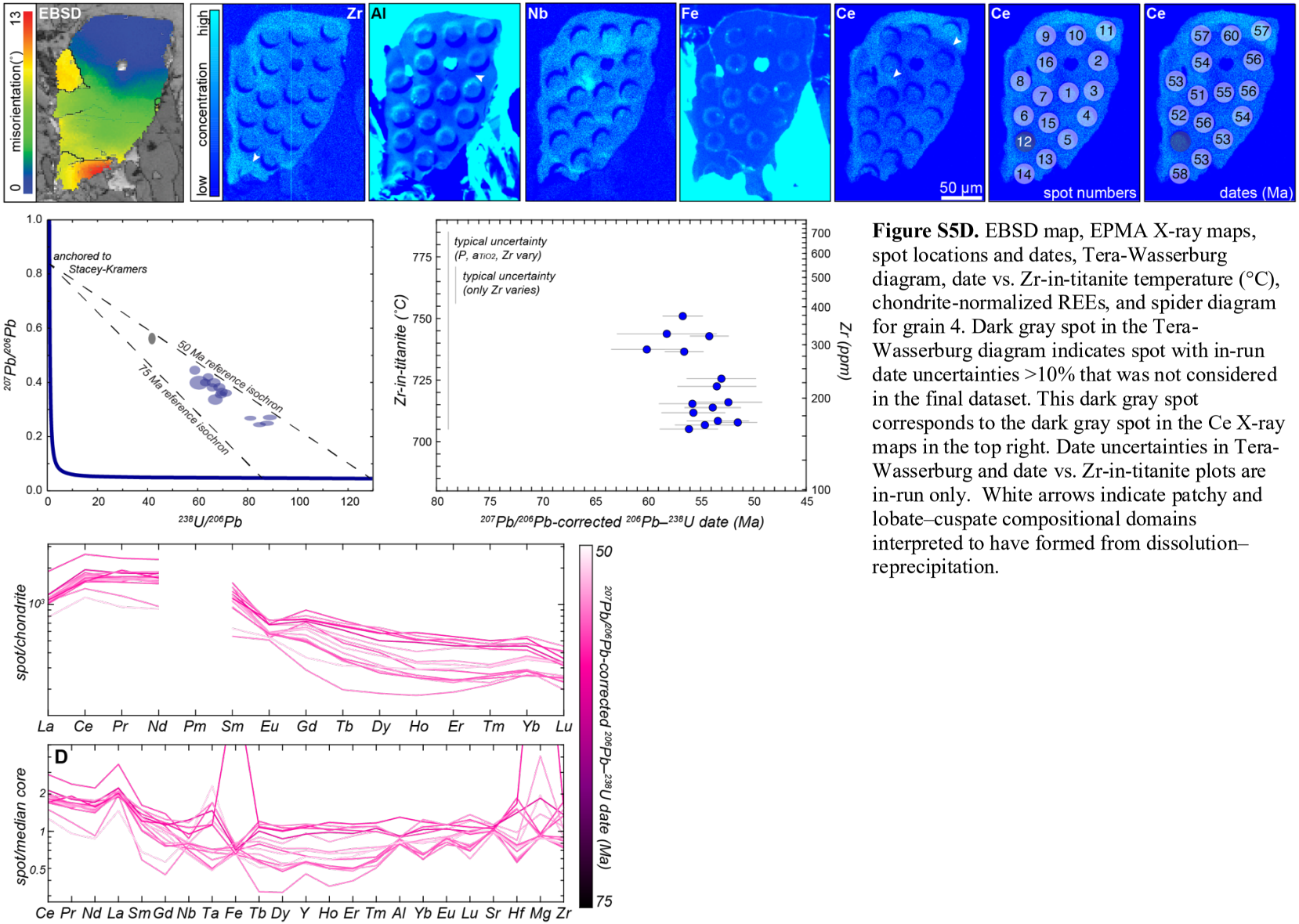

Figure S5D. EBSD map, EPMA X-ray maps, spot locations and dates, Tera-Wasserburg diagram, date vs. Zr-in-titanite temperature (°C), chondrite-normalized REEs, and spider diagram for grain 4. Dark gray spot in the Tera-Wasserburg diagram indicates spot with in-run date uncertainties >10% that was not considered in the final dataset. This dark gray spot corresponds to the dark gray spot in the Ce X-ray maps in the top right. Date uncertainties in Tera-Wasserburg and date vs. Zr-in-titanite plots are in-run only. White arrows indicate patchy and lobate–cuspate compositional domains interpreted to have formed from dissolution–reprecipitation.

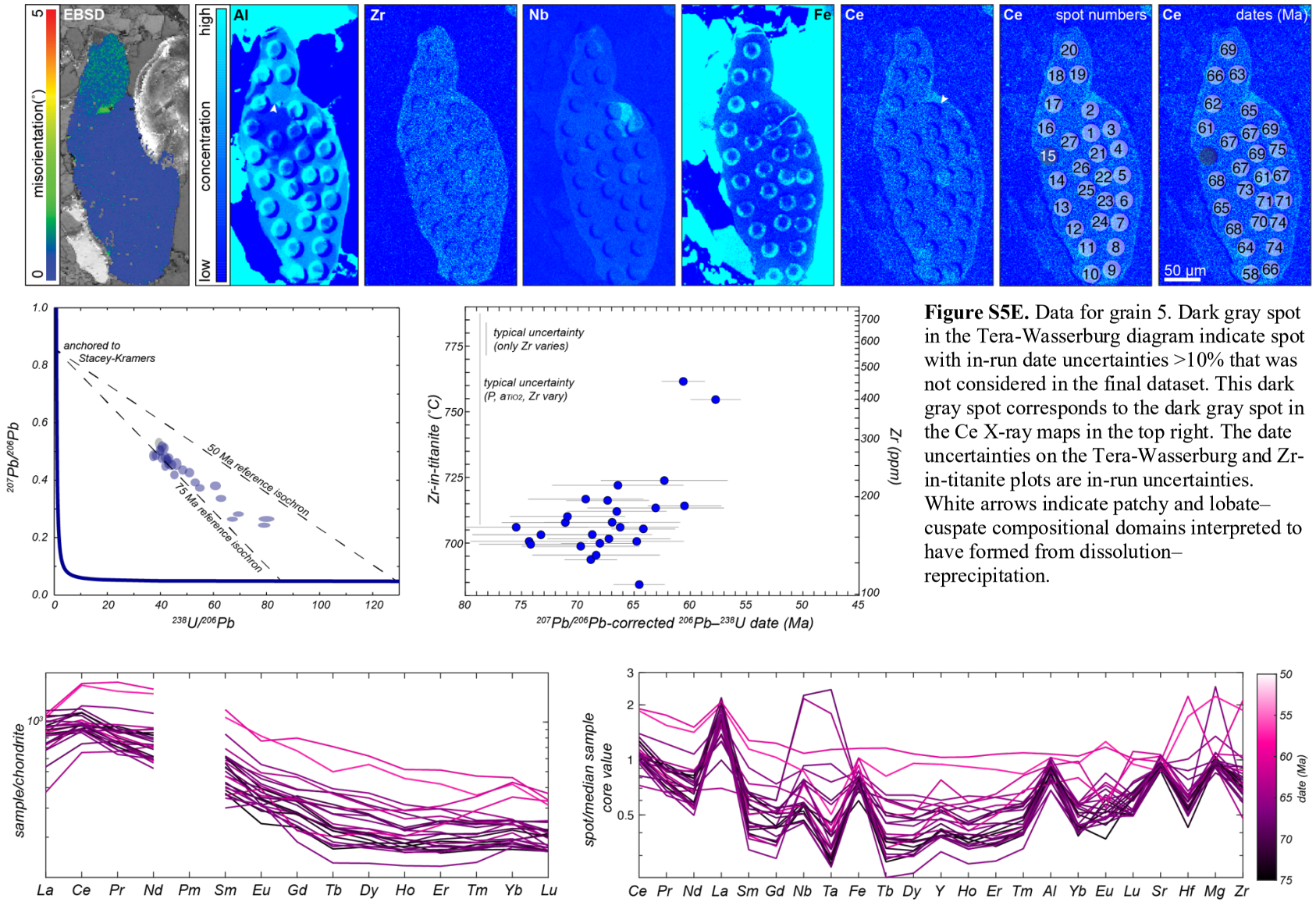

Figure S5E. Data for grain 5. Dark gray spot in the Tera-Wasserburg diagram indicate spot with in-run date uncertainties >10% that was not considered in the final dataset. This dark gray spot corresponds to the dark gray spot in the Ce X-ray maps in the top right. The date uncertainties on the Tera-Wasserburg and Zr-in-titanite plots are in-run uncertainties. White arrows indicate patchy and lobate–cuspate compositional domains interpreted to have formed from dissolution–reprecipitation.

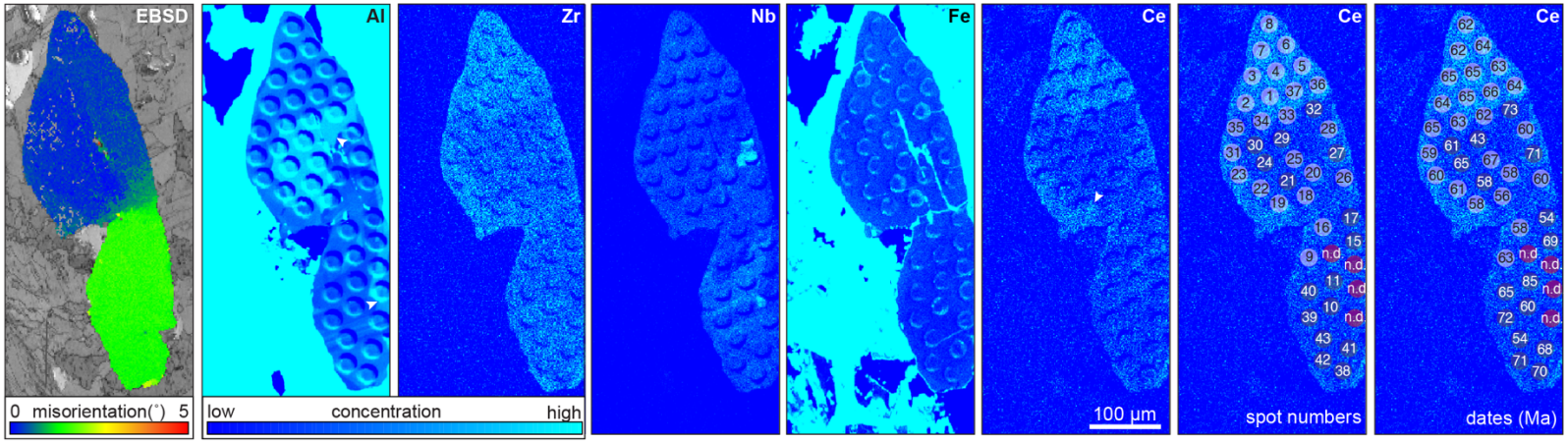

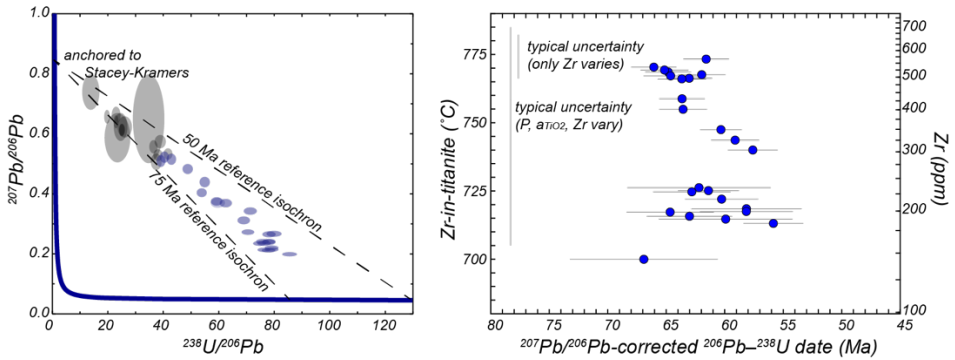

Figure S5F. Data for grain 6. Dark gray spots in the Tera-Wasserburg diagram indicate spots with in-run date uncertainties >10% that were not considered in the final dataset. These dark gray spots correspond to the dark gray spots in the Ce X-ray maps in the top right. Red spots labeled "n.d." in the Ce X-ray maps are spots where U concentration were too low to calculate a date. The date uncertainties in the Tera-Wasserburg and Zr-in-titanite plots are in-run uncertainties. White arrows indicate patchy and lobate–cuspate compositional domains interpreted to have formed from dissolution–reprecipitation.

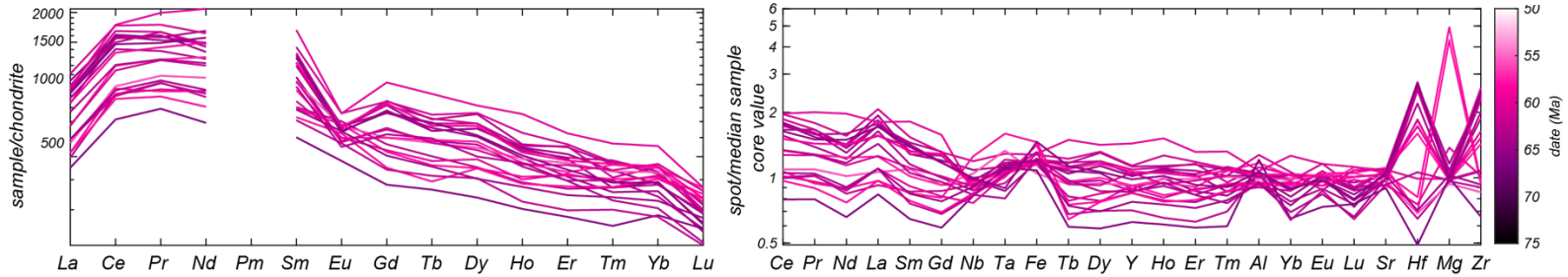

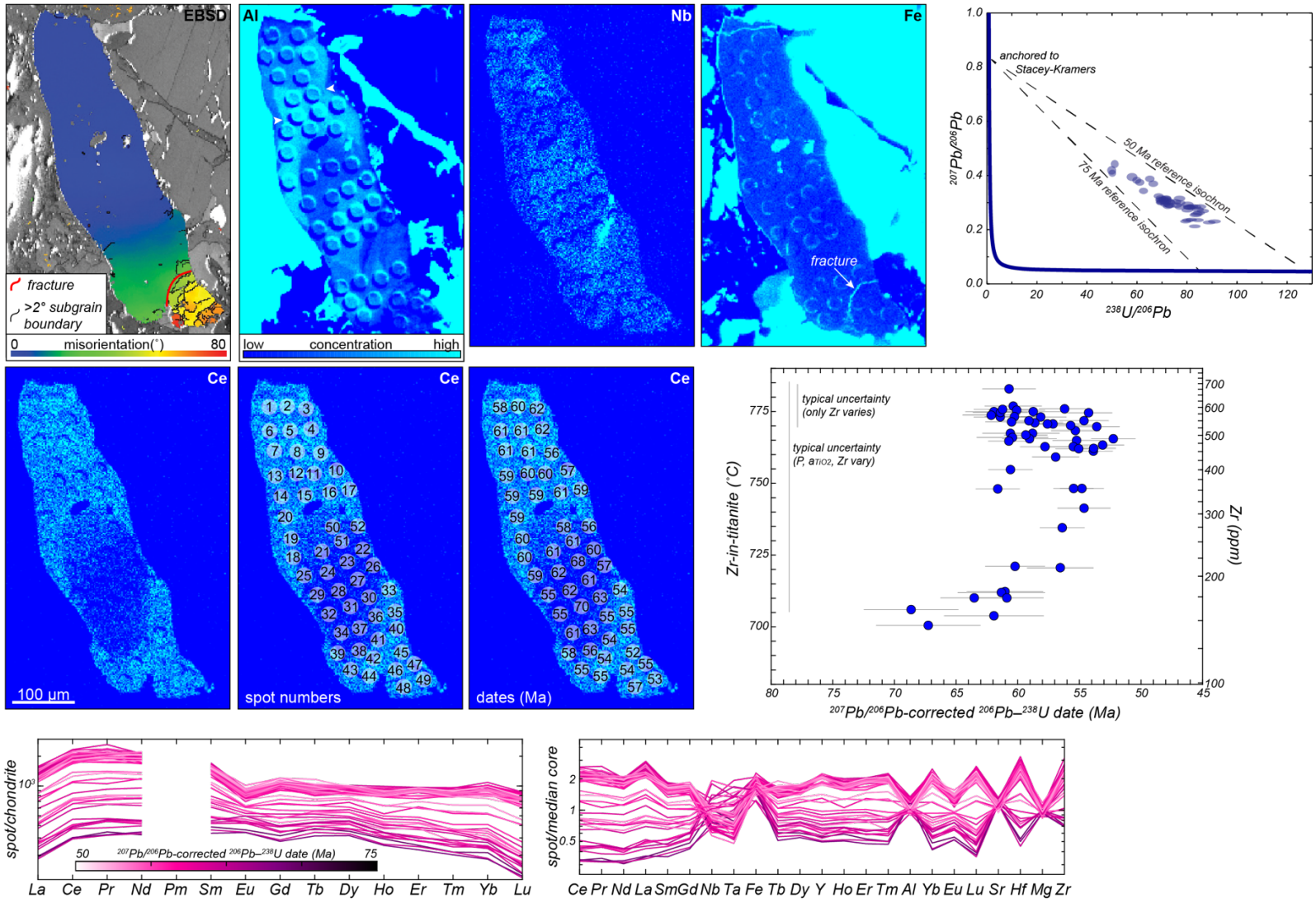

Figure S5G. Data for grain 7. Uncertainties are in-run uncertainties. White arrows indicate patchy and lobate–cuspate compositional domains interpreted to have formed from dissolution–reprecipitation.

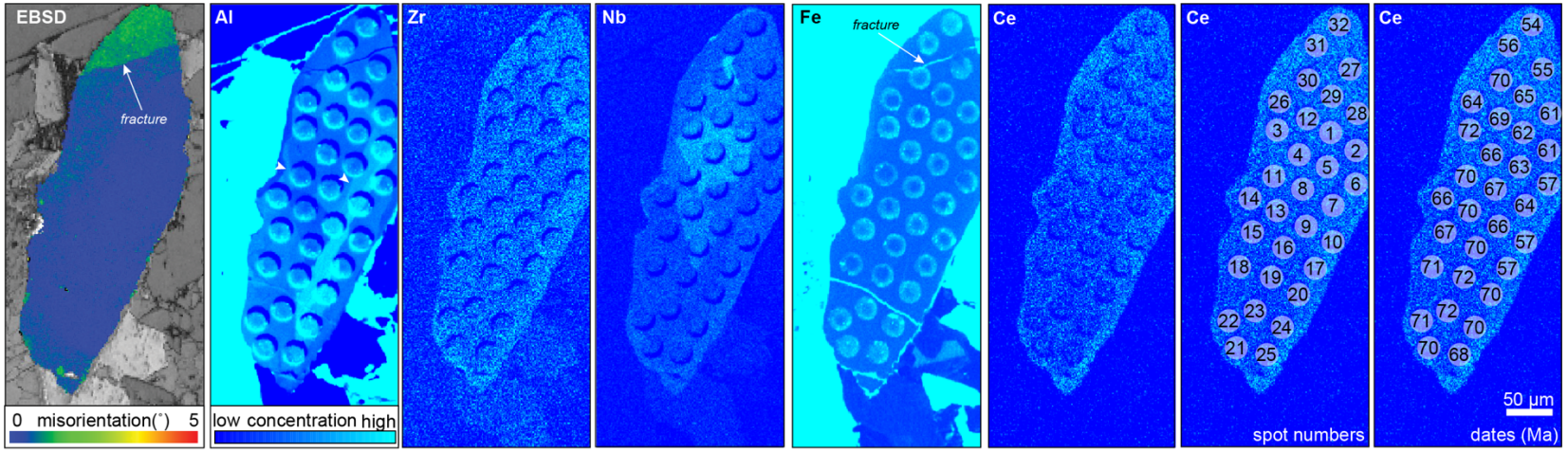

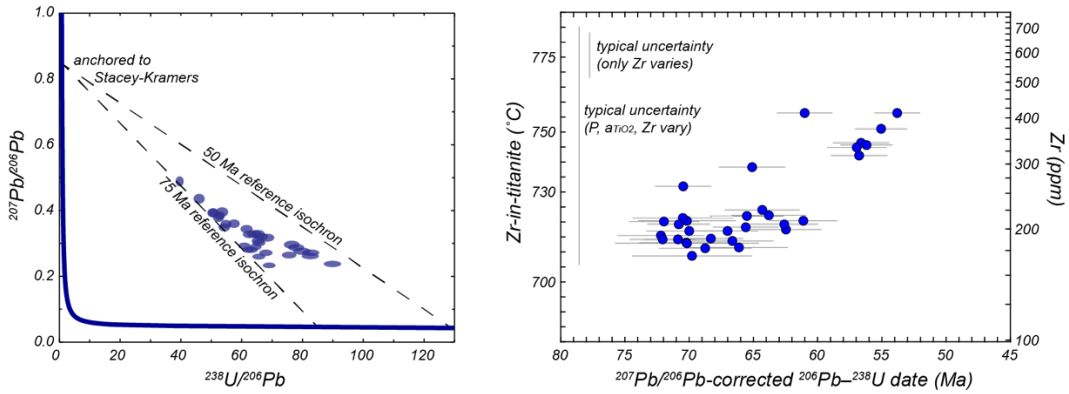

Figure S5H. EBSD map, EPMA X-ray map, spot locations and dates, Tera-Wasserburg diagram, date vs. Zr-in-titanite temperature (°C), chondrite-normalized REEs (McDonough and Sun, 1995), and spider diagram for grain 8. The uncertainties in the Tera-Wasserburg diagram and date uncertainties in the Zr-in-titanite plots are in-run uncertainties. White arrows indicate patchy and lobate–cuspate compositional domains interpreted to have formed from dissolution–reprecipitation.

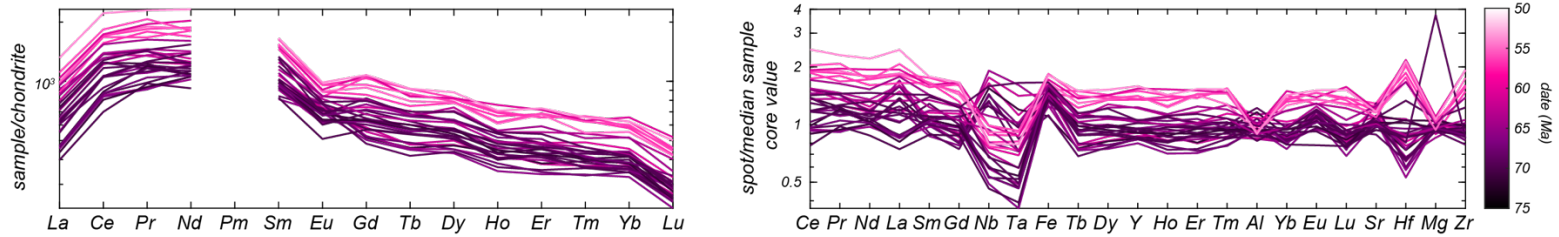

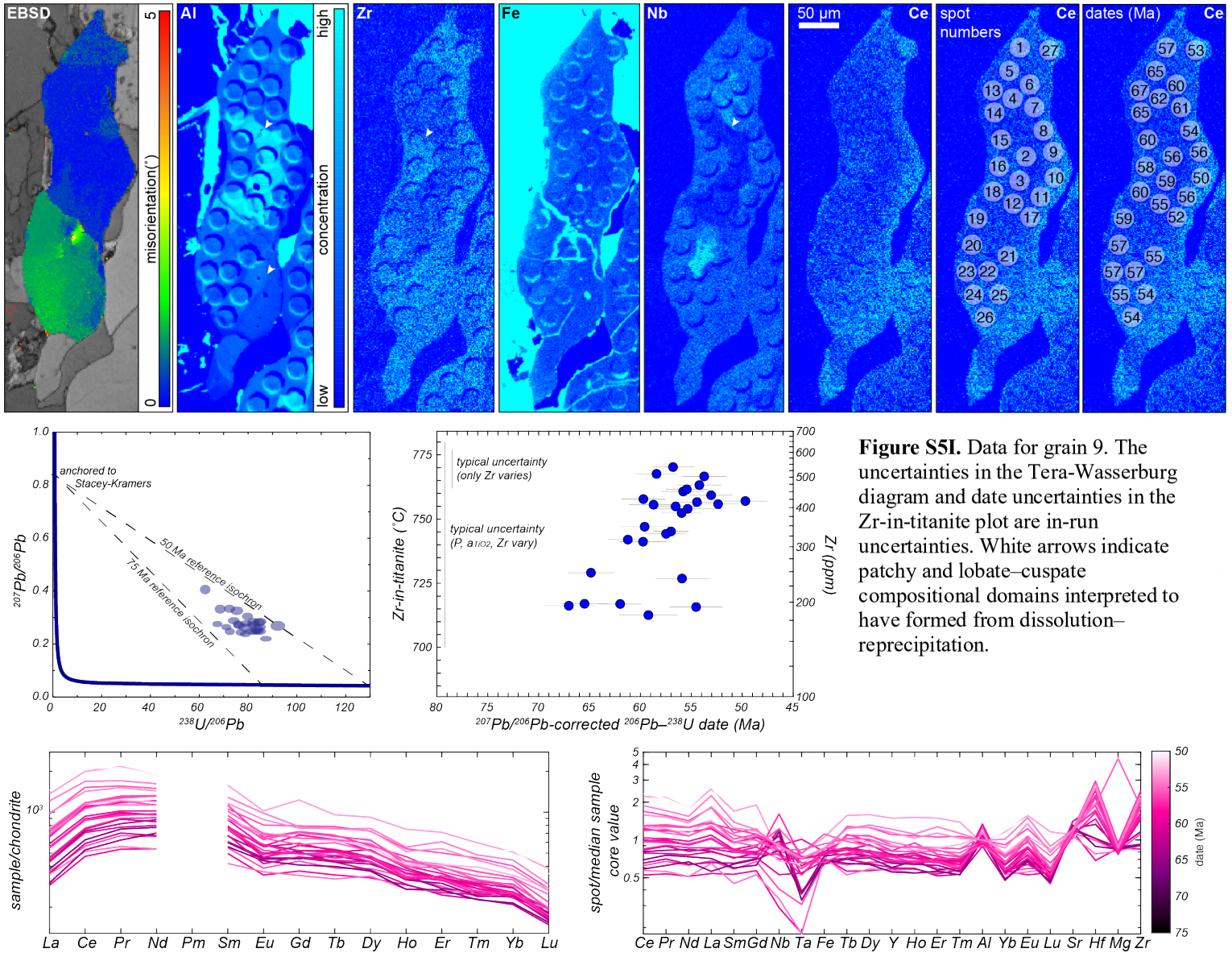

Figure S5I. Data for grain 9. The uncertainties in the Tera-Wasserburg diagram and date uncertainties in the Zr-in-titanite plot are in-run uncertainties. White arrows indicate patchy and lobate–cuspate compositional domains interpreted to have formed from dissolution–reprecipitation.

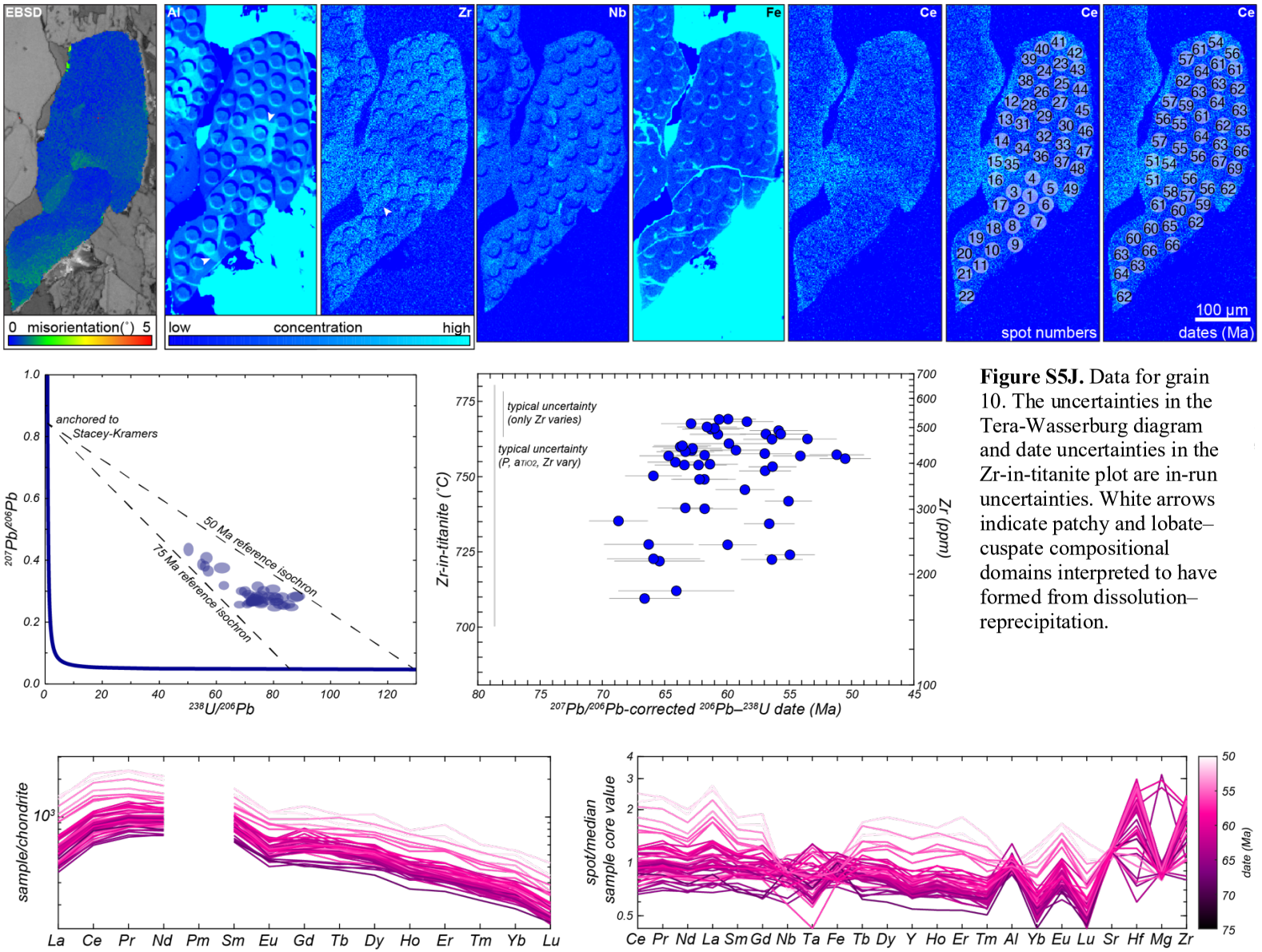

Figure S5J. Data for grain 10. The uncertainties in the Tera-Wasserburg diagram and date uncertainties in the Zr-in-titanite plot are in-run uncertainties. White arrows indicate patchy and lobate–cuspate compositional domains interpreted to have formed from dissolution–reprecipitation.

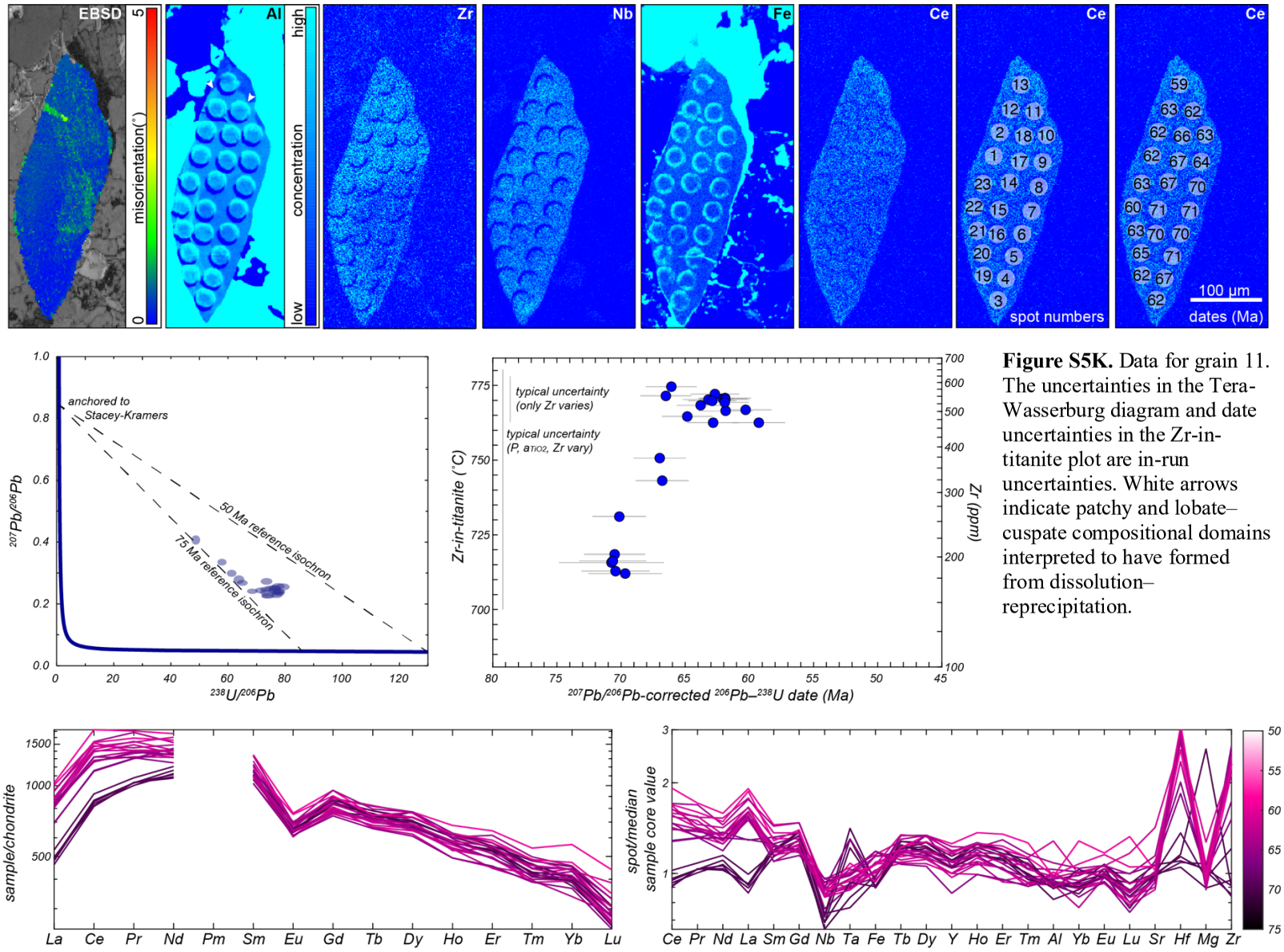

Figure S5K. Data for grain 11. The uncertainties in the Tera-Wasserburg diagram and date uncertainties in the Zr-in-titanite plot are in-run uncertainties. White arrows indicate patchy and lobate–cuspate compositional domains interpreted to have formed from dissolution–reprecipitation.

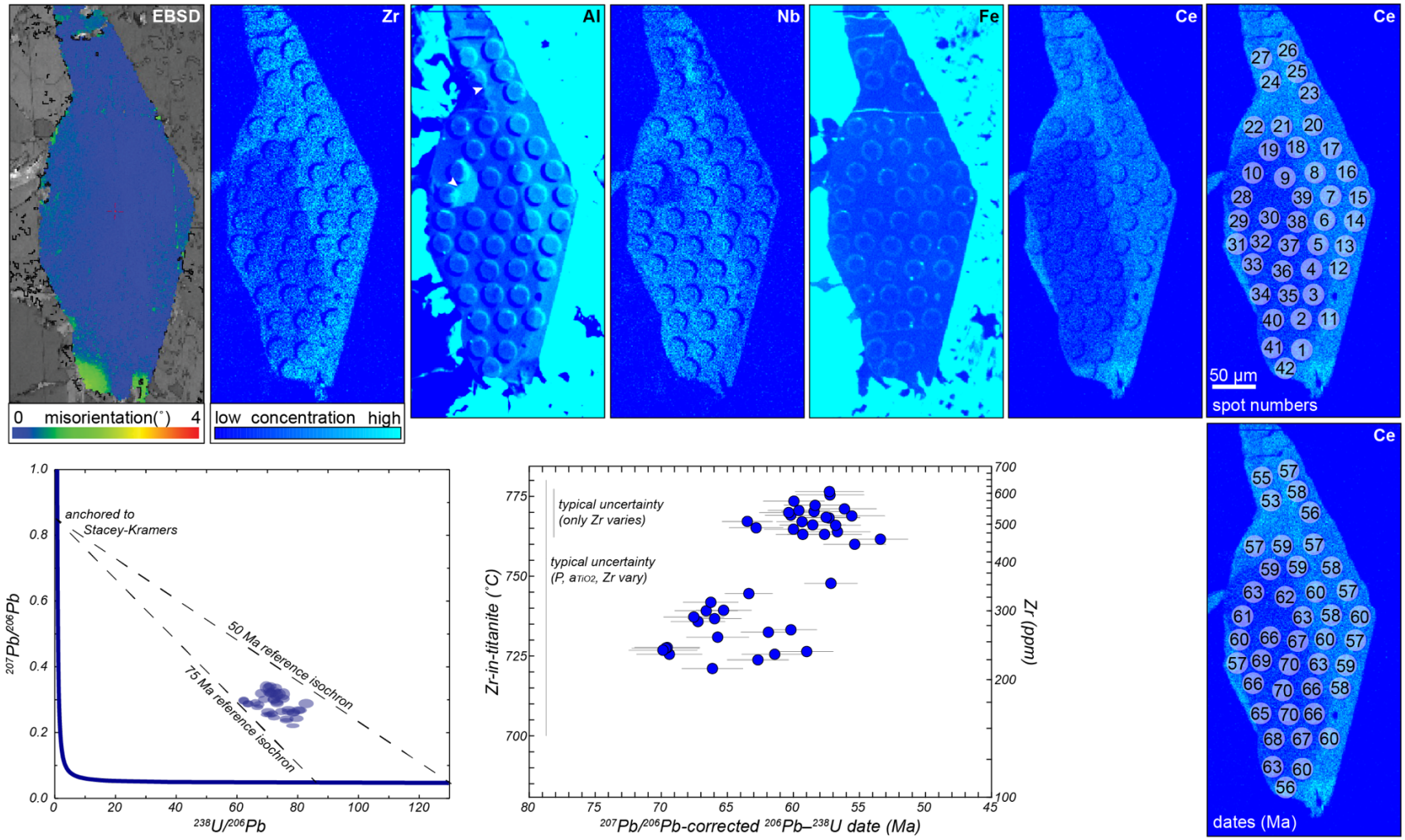

Figure S5L. Data for grain 12. The uncertainties in the Tera-Wasserburg diagram and date uncertainties in the Zr-in-titanite plot are in-run uncertainties. White arrows indicate patchy and lobate–cuspate compositional domains interpreted to have formed from dissolution–reprecipitation.

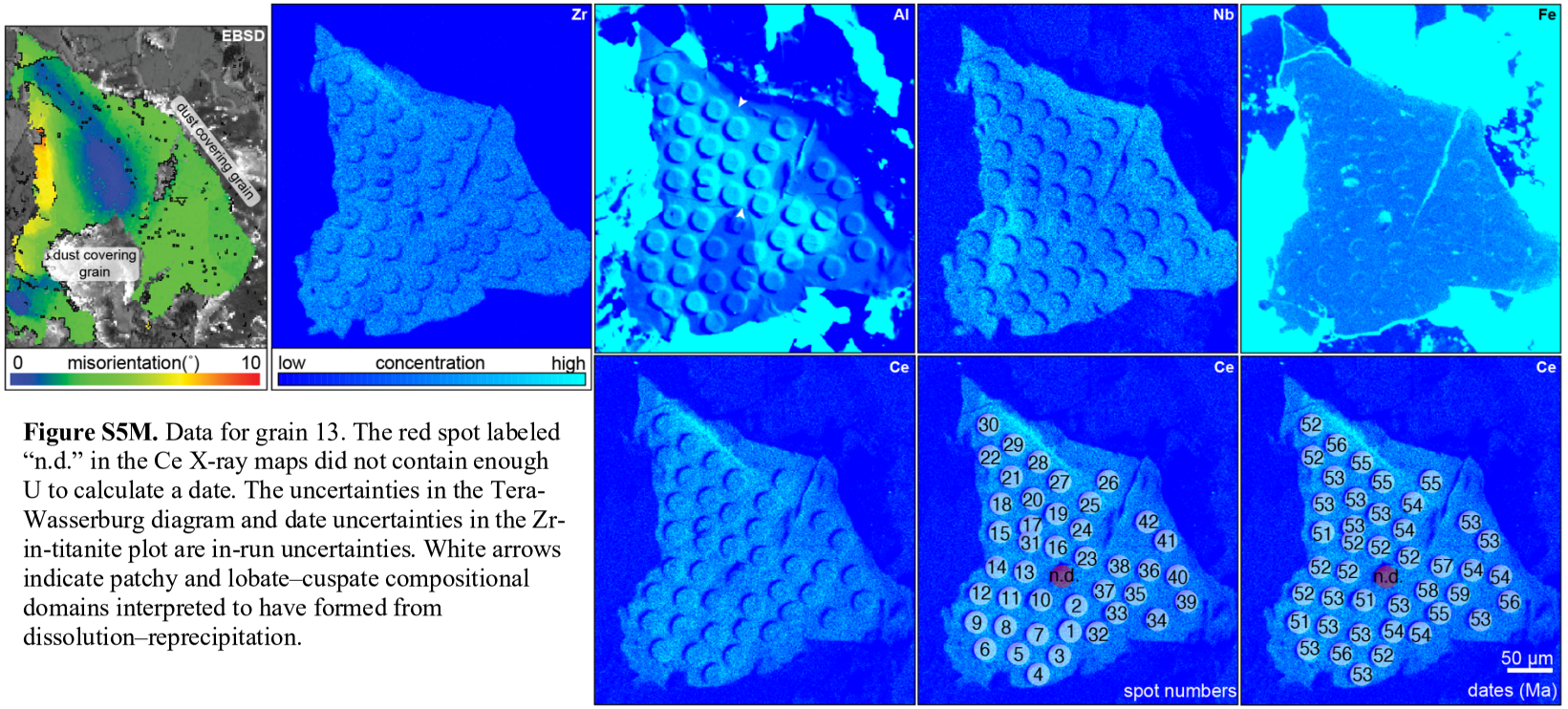

Figure S5M. Data for grain 13. The red spot labeled "n.d." in the Ce X-ray maps did not contain enough U to calculate a date. The uncertainties in the Tera-Wasserburg diagram and date uncertainties in the Zr-in-titanite plot are in-run uncertainties. White arrows indicate patchy and lobate–cuspate compositional domains interpreted to have formed from dissolution–reprecipitation.

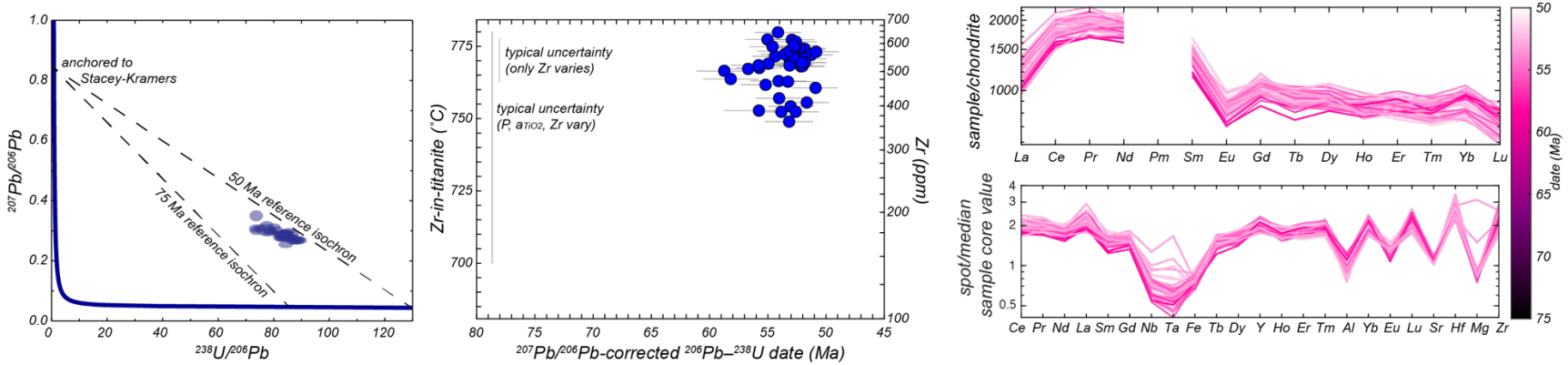

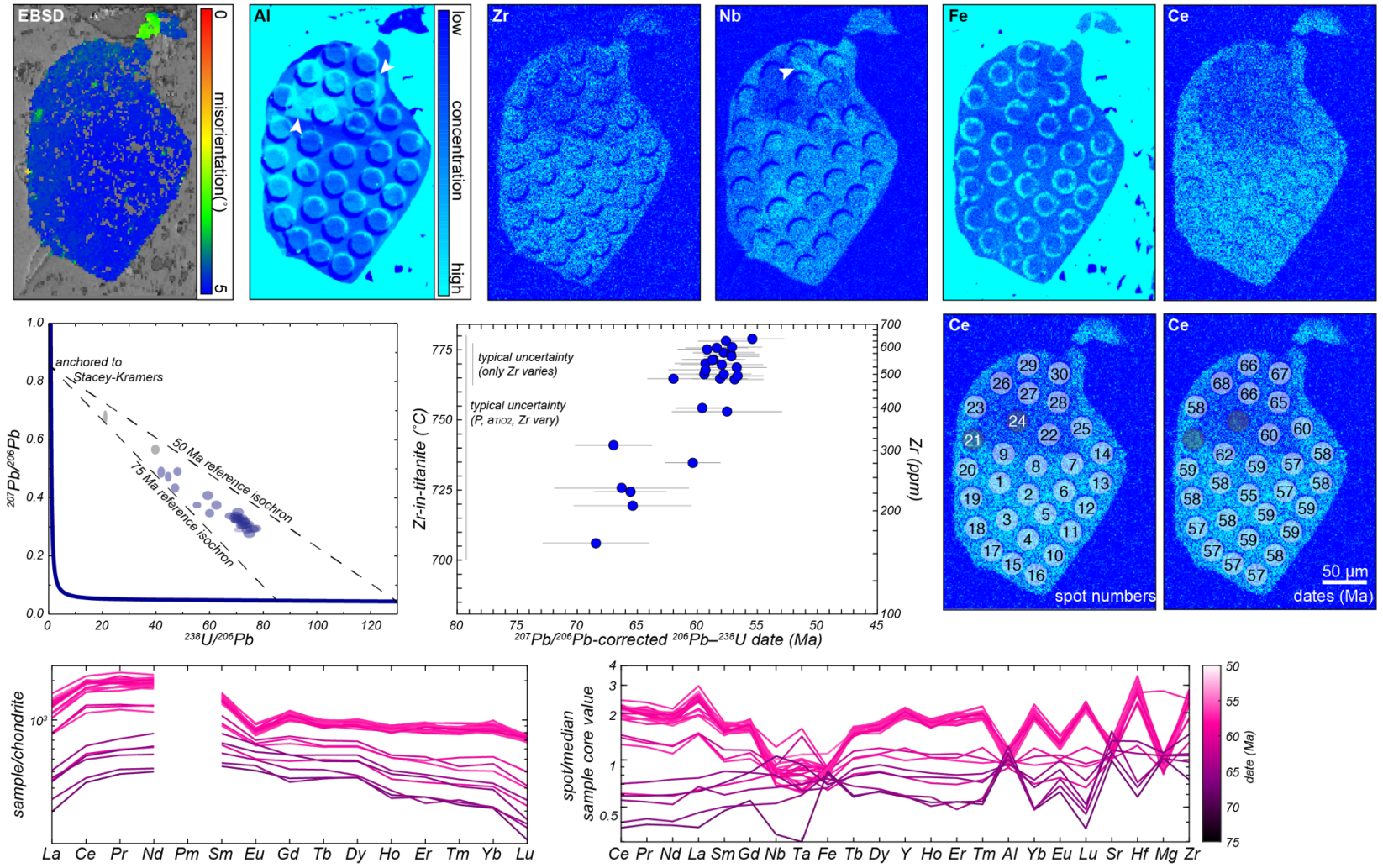

Figure S5N. Data for grain 14. Dark gray spots in the Tera-Wasserburg diagram and maps indicate spots with in-run date uncertainties >10% that were not considered in the final dataset. The uncertainties in the Tera-Wasserburg and date uncertainties in the Zr-in-titanite plot are in-run uncertainties. White arrows indicate patchy and lobate–cuspate compositional domains interpreted to have formed from dissolution–reprecipitation.

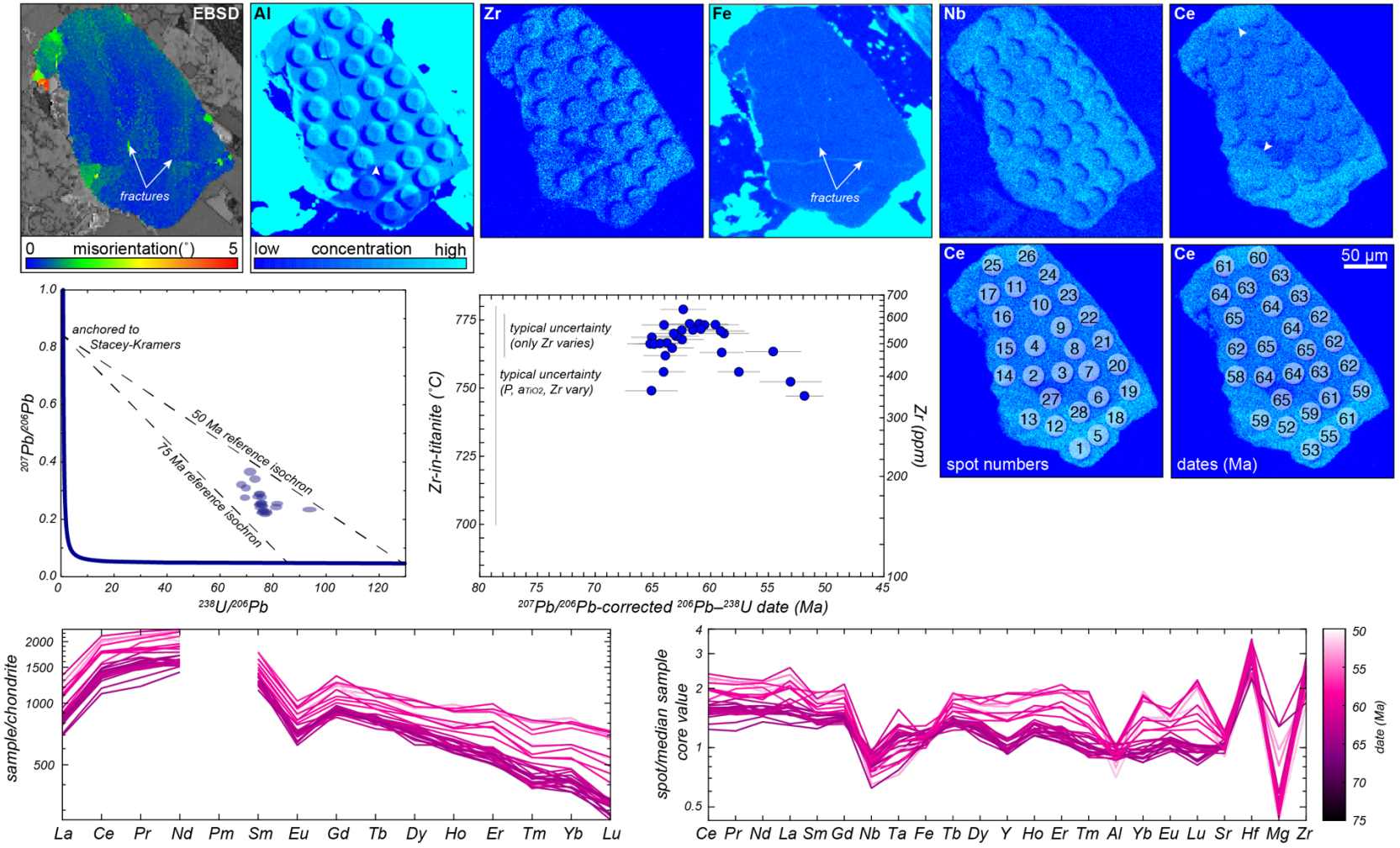

Figure S5O. Data for grain 15. Dark gray spots in the Tera-Wasserburg diagram and maps indicate spots with in-run date uncertainties >10% that were not considered in the final dataset. The uncertainties in the Tera-Wasserburg and date uncertainties in the Zr-in-titanite plot are in-run uncertainties. White arrows indicate patchy and lobate–cuspate compositional domains interpreted to have formed from dissolution–reprecipitation.

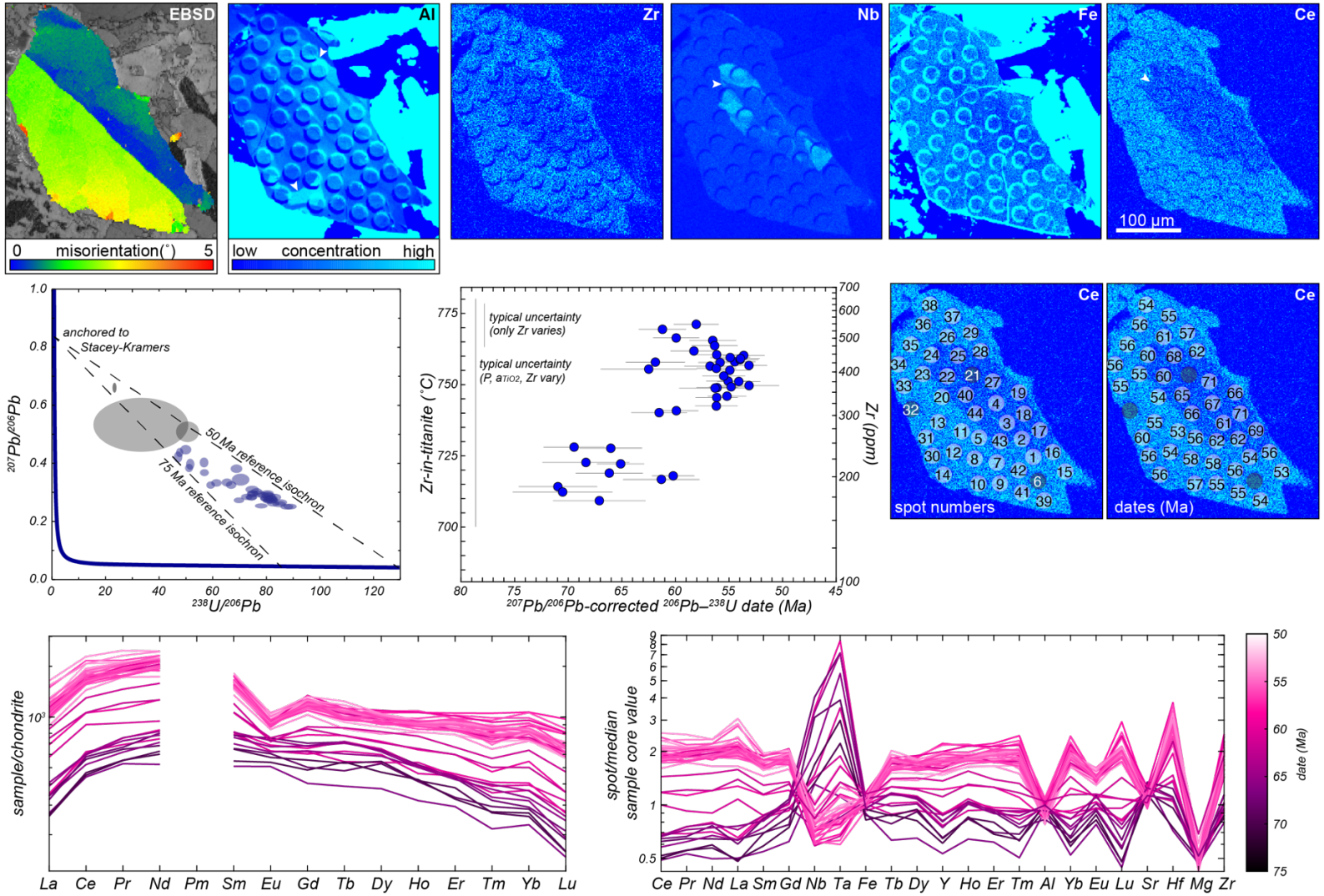

Figure S5P. Data for grain 16. Dark gray spots in the Tera-Wasserburg diagram and maps indicate spots with in-run date uncertainties >10% that were not considered in the final dataset. The uncertainties in the Tera-Wasserburg and date uncertainties in the Zr-in-titanite plot are in-run uncertainties. White arrows indicate patchy and lobate–cuspate compositional domains interpreted to have formed from dissolution–reprecipitation.

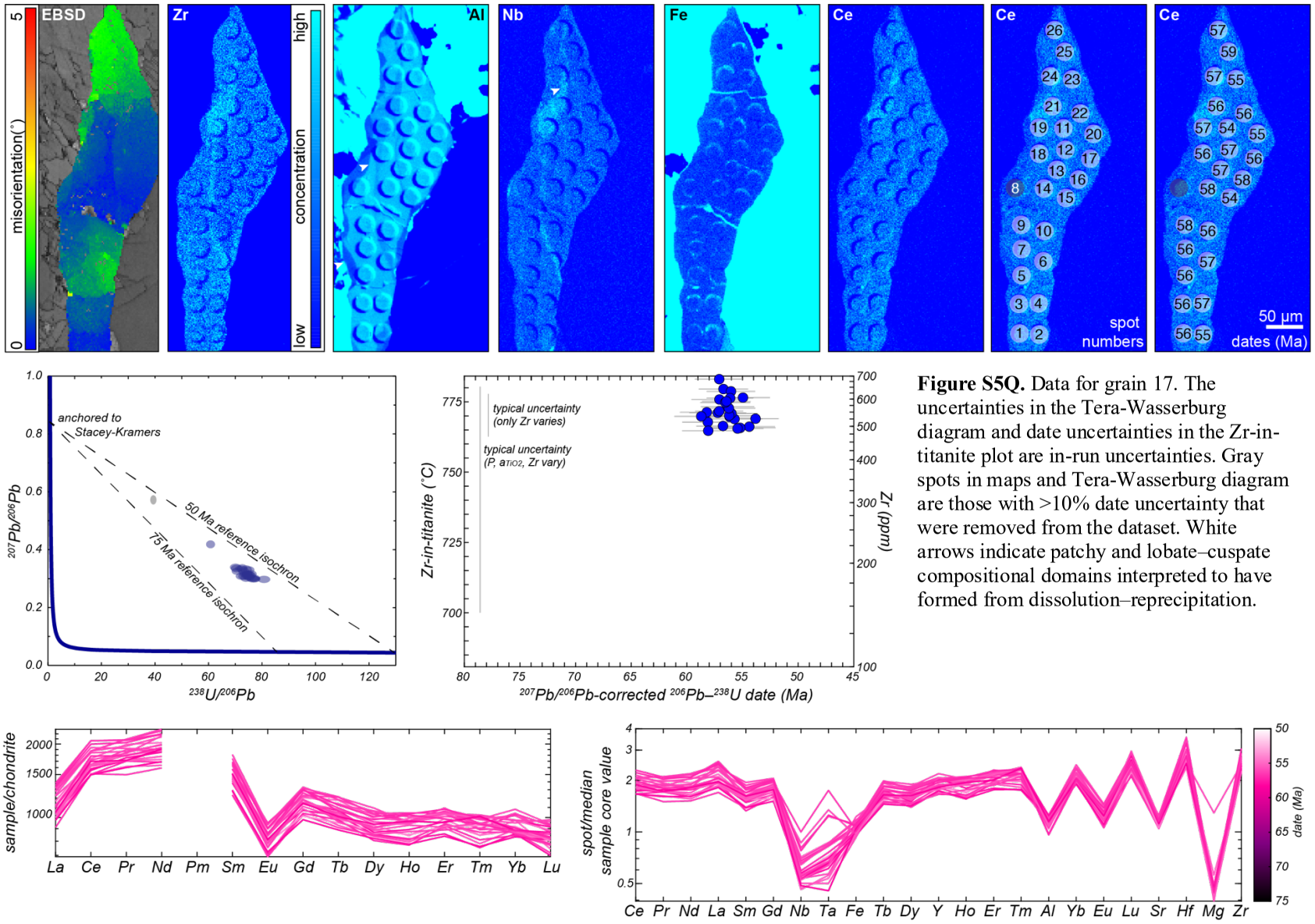

Figure S5Q. Data for grain 17. The uncertainties in the Tera-Wasserburg diagram and date uncertainties in the Zr-in-titanite plot are in-run uncertainties. Gray spots in maps and Tera-Wasserburg diagram are those with >10% date uncertainty that were removed from the dataset. White arrows indicate patchy and lobate–cuspate compositional domains interpreted to have formed from dissolution–reprecipitation.

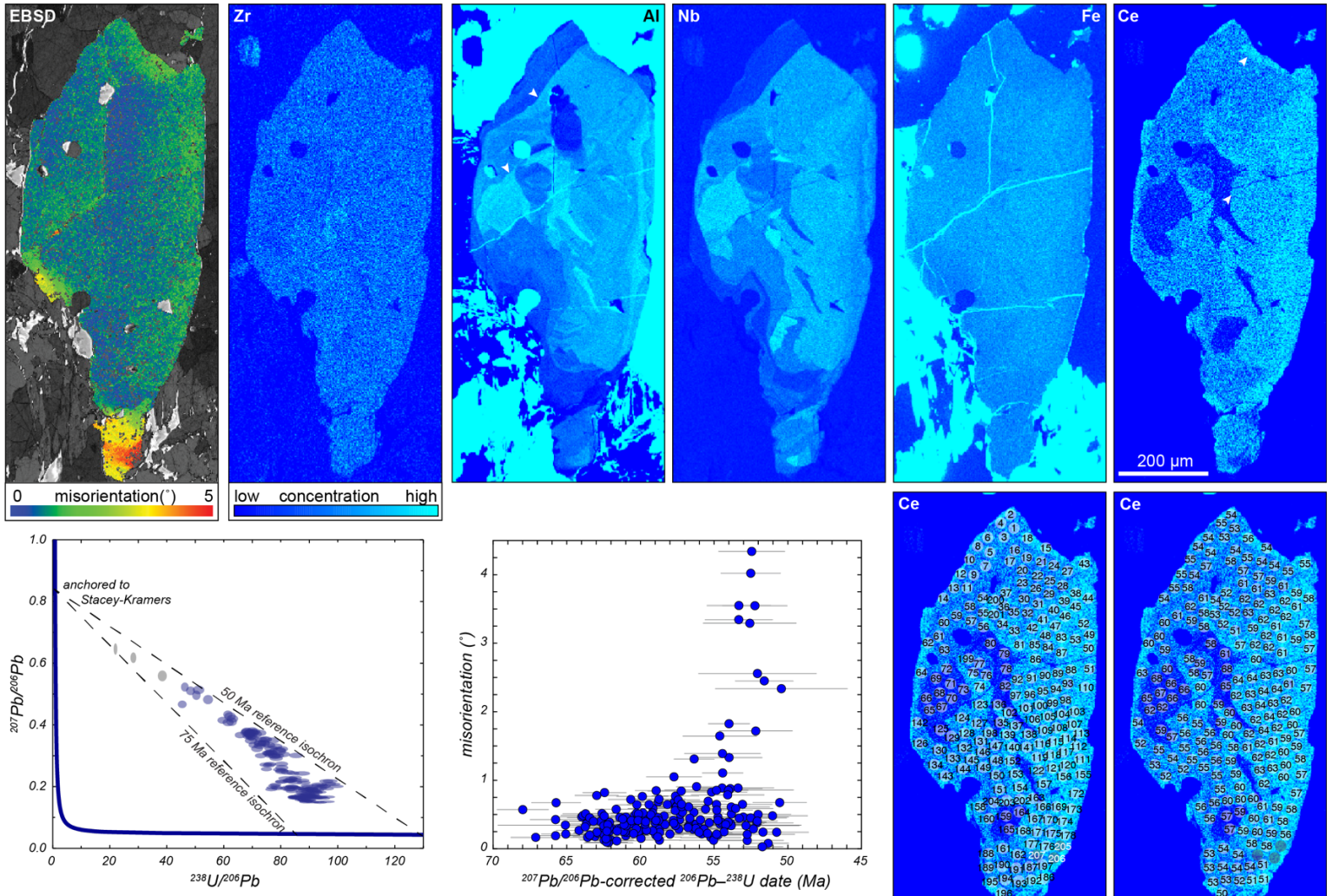

Figure S5R. Data for grain 18. Dark gray spots in the Tera-Wasserburg diagram and maps indicate spots with in-run date uncertainties >10% that were not considered in the final dataset. Uncertainties are in-run uncertainties. White arrows indicate patchy and lobate–cuspate compositional domains interpreted to have formed from dissolution–reprecipitation.

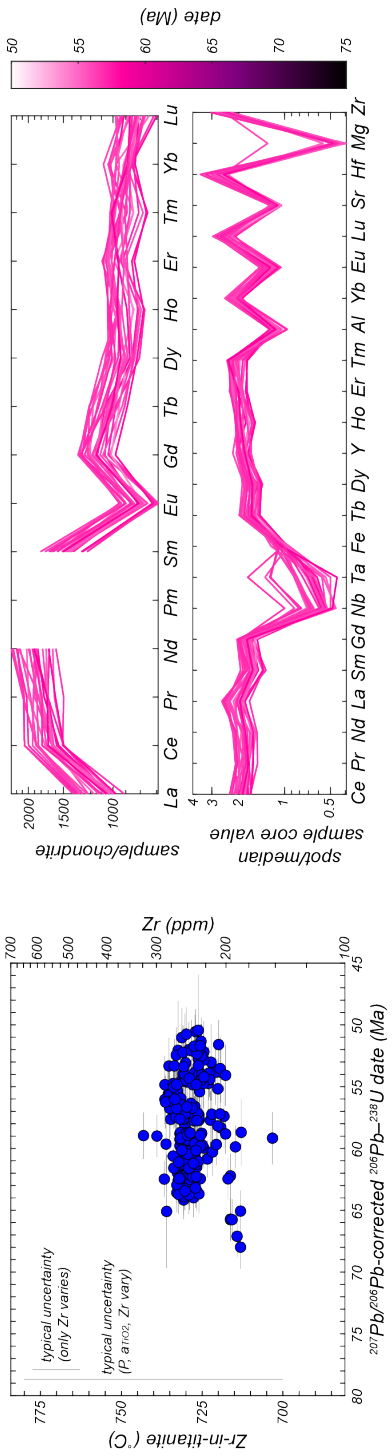

Figure S5R, *continued*

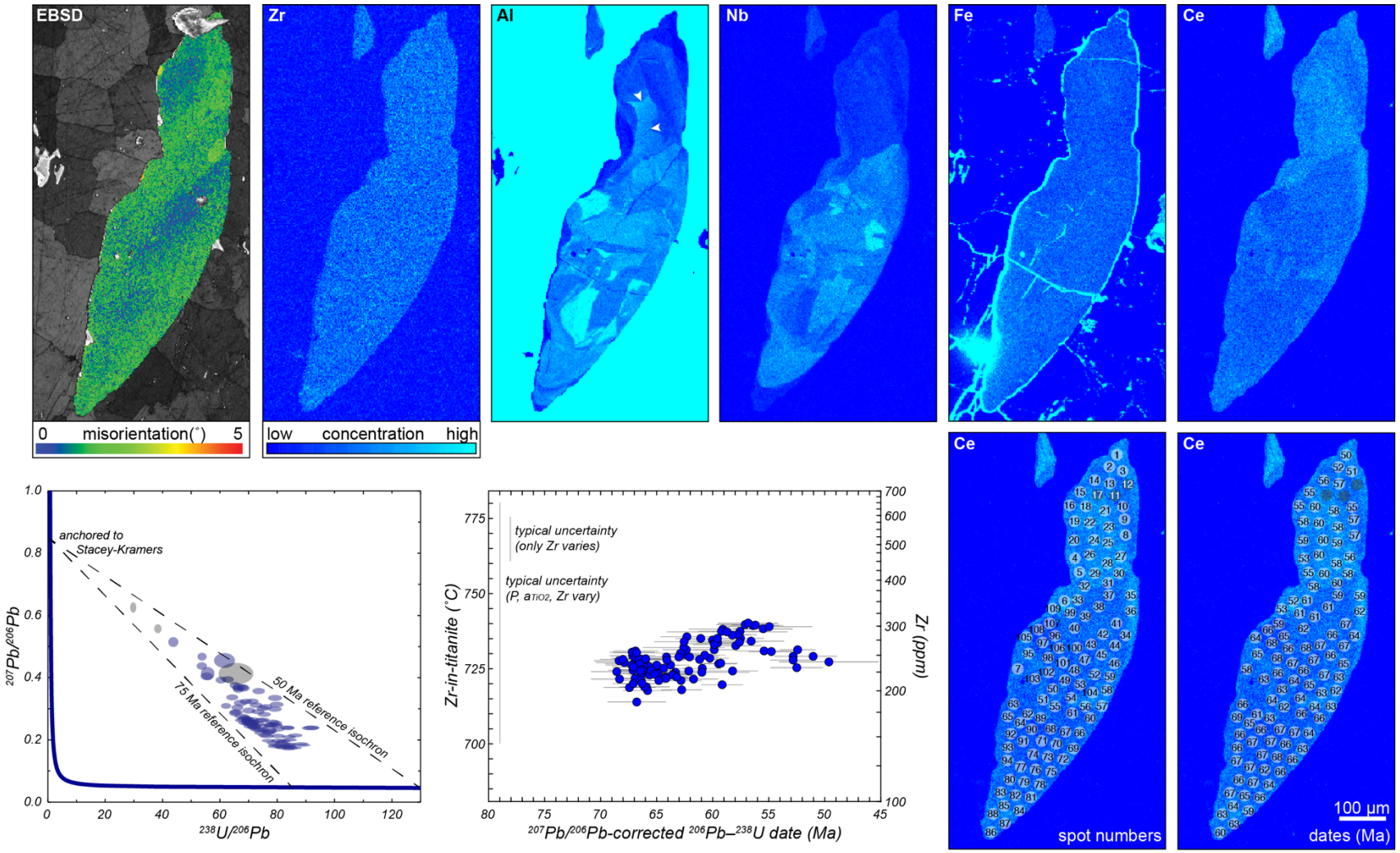

Figure S5S. Data for grain 19. Dark gray spots in the Tera-Wasserburg diagram and maps indicate spots with in-run date uncertainties >10% that were not considered in the final dataset. Uncertainties are in-run uncertainties. White arrows indicate patchy and lobate–cuspate compositional domains interpreted to have formed from dissolution–reprecipitation.

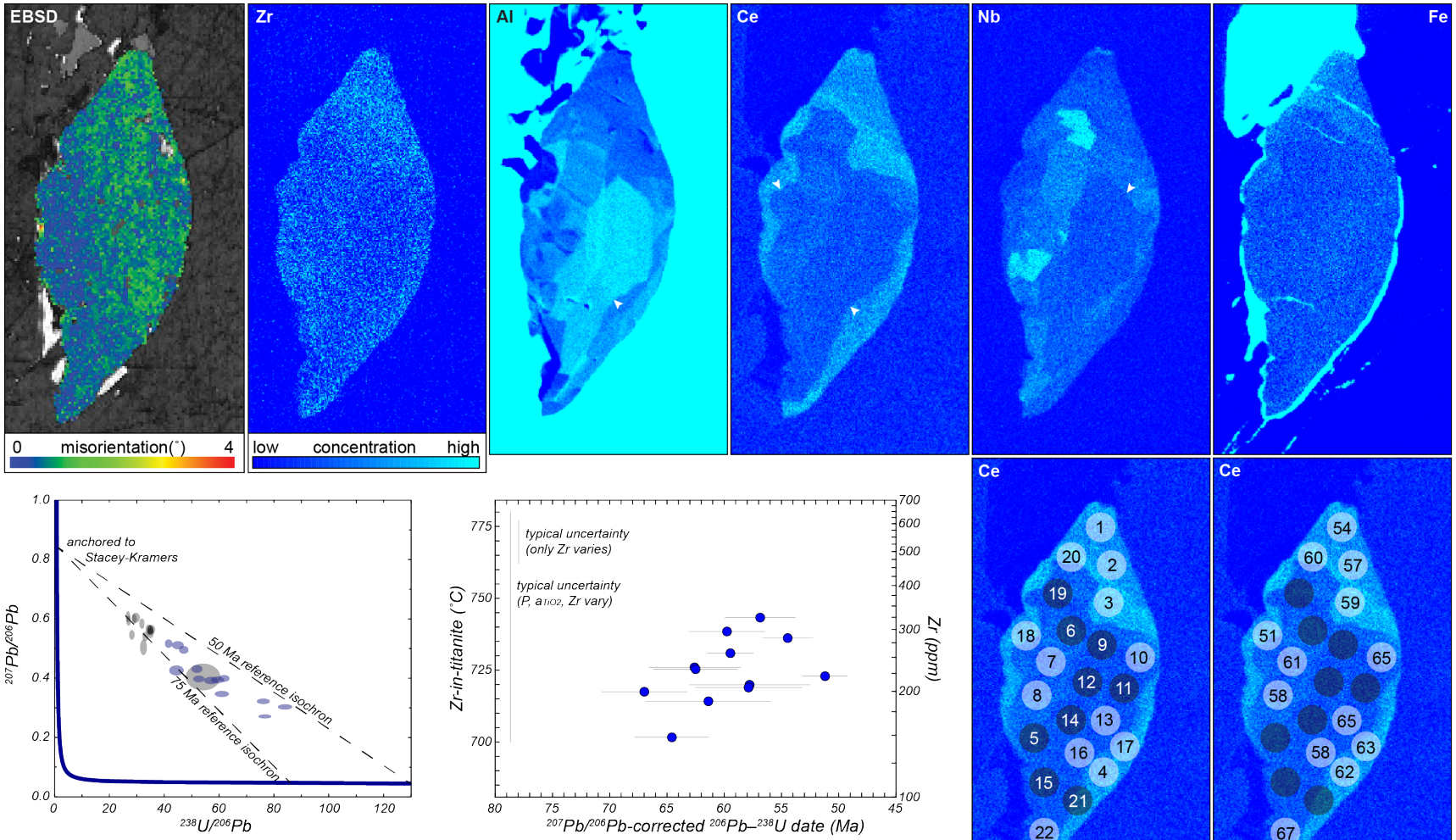

Figure S5T. Data for grain 20. Dark gray spots in the Tera-Wasserburg diagram and maps indicate spots with in-run date uncertainties >10% that were not considered in the final dataset. Uncertainties are in-run uncertainties. White arrows indicate patchy and lobate–cuspate compositional domains interpreted to have formed from dissolution–reprecipitation.

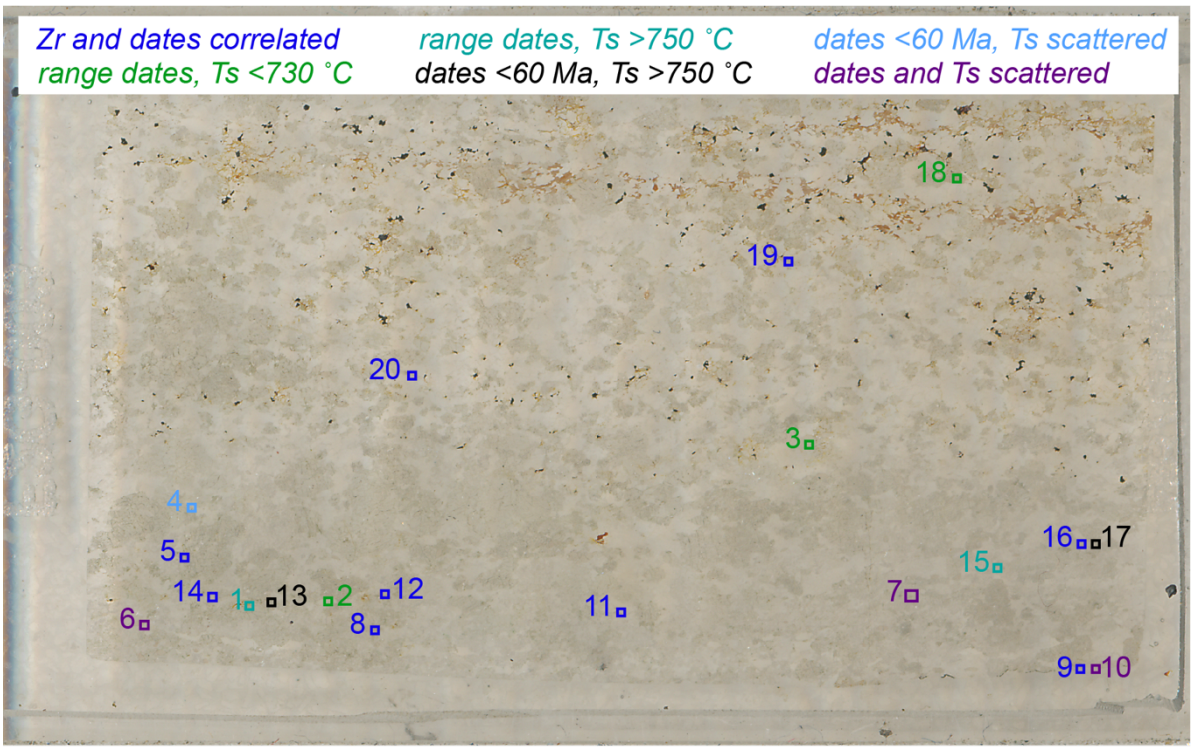

Figure S6. Locations of analyzed titanite grains within the studied thin section. Grain numbers are colored by Zr-in-titanite-date patterns.

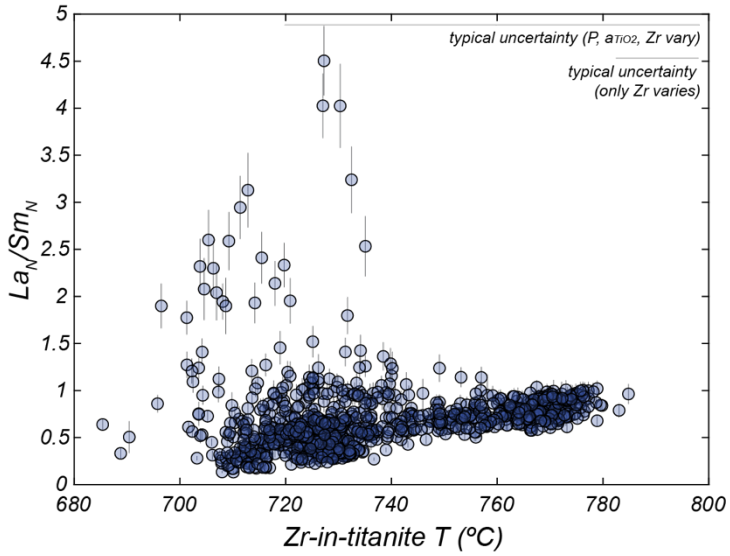

Figure S7. Chondrite-normalized La/Sm as a function of Zr-in-titanite temperature for sample M8701M1. Excluding outliers, La_N/Sm_N increases with increasing Zr-in-titanite temperature, supporting the likely F-bearing composition of the metamorphic fluid.

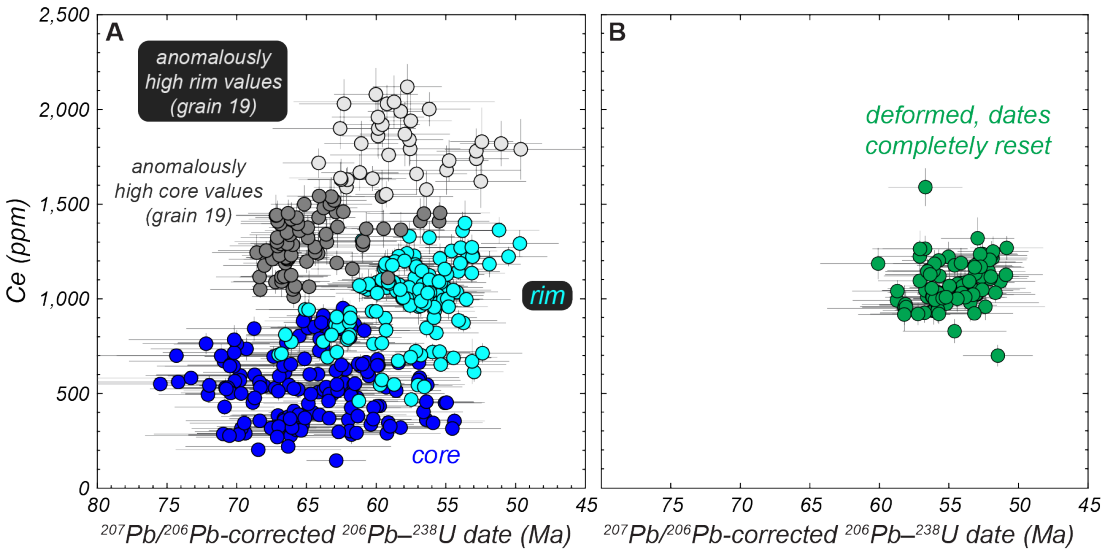

Figure S8. Date vs. Ce concentration plots for (A) the 11 grains wherein Ce concentrations increase with younging date (see Tables 1 and S2) and (B) the three bent grains wherein all dates are younger than 60 Ma (see Table 1). Grayed-out data points in (A) are anomalously high core and rim values from grain 19 that obscure the broad relationship between dates and Ce concentrations in the remaining grains. Ce concentrations from the three bent grains that yielded exclusively <60 Ma dates (B) fall within the range of Ce concentrations from the fluid-recrystallized rims (A).

APPENDIX 2

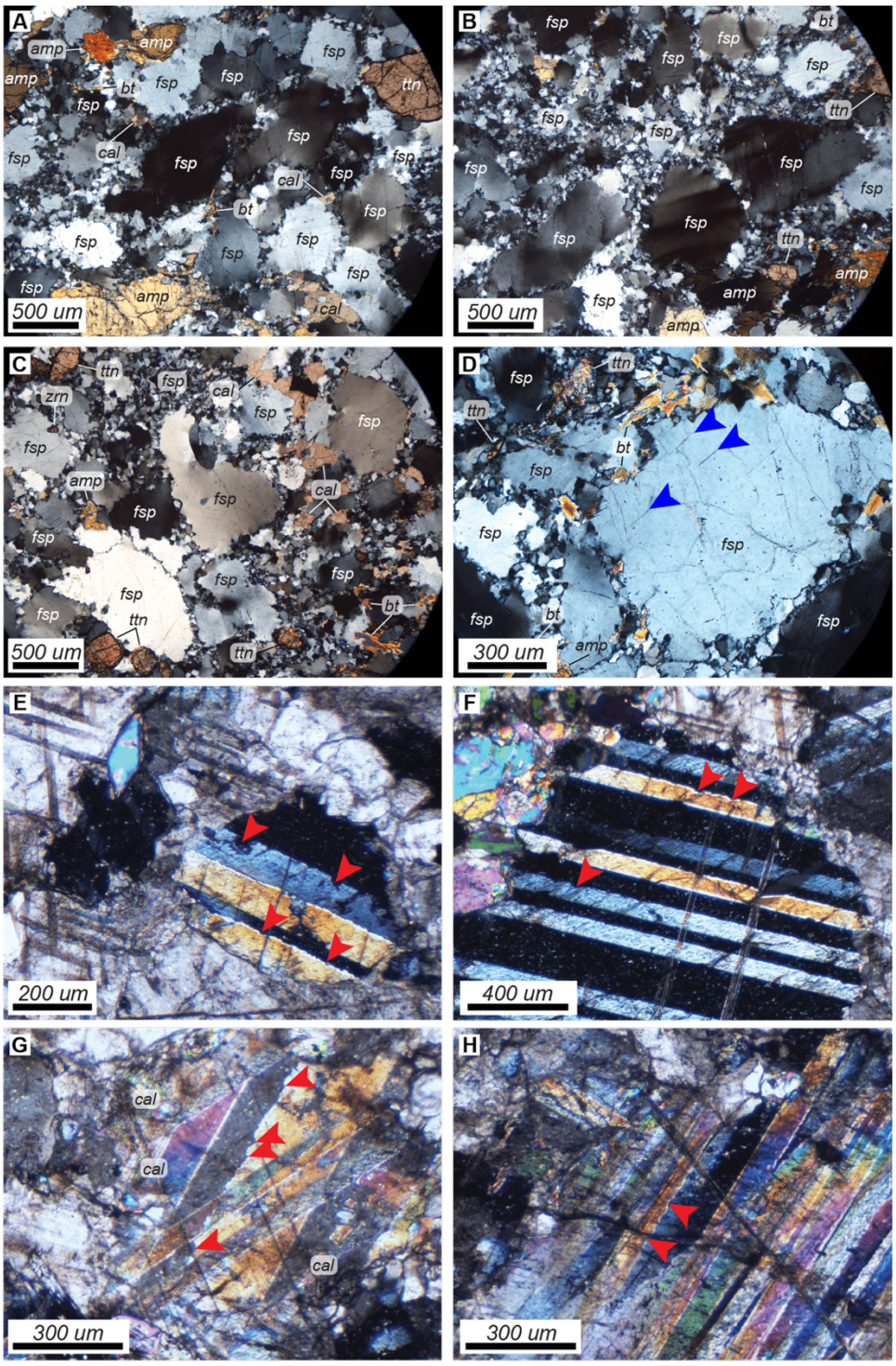

Figure S1. Additional thin section photomicrographs of feldspar deformation microstructures from sample 48A (A–D) and calcite deformation twins from sample 47A (E–F). Blue arrows in (D) indicate minor fractures whose orientations are consistent with their occurrence along cleavage planes. Red arrows in (E–H) denote serrated edge of twins that are indicative of type IV calcite deformation twins.

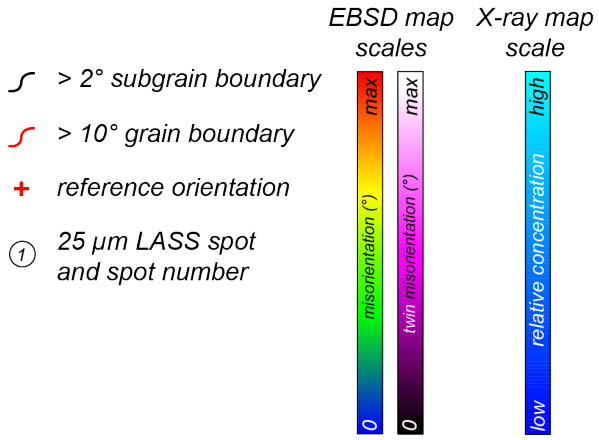

Figure S2. (following pages) EBSD misorientation maps, WDS X-ray maps, spot locations, date vs. (misorientation, Ce, Fe, Zr), and Tera–Wasserburg concordia diagrams for "Cretaceous–Miocene" grains in sample 48A. Legend for this figure is above and is relevant for each grain. The 25 µm LASS spot serves as scale for each grain. Number at top of EBSD and WDS maps is grain number for reference to Table S2. The maximum misorientation for each grain is listed at the top and is applicable to the host grain and the deformation twins. The plots on the pages that follow the maps are those for the preceding grain. Grains without date vs. misorientation plots are those that are unbent.

48A-0129-5; max misorient 12°

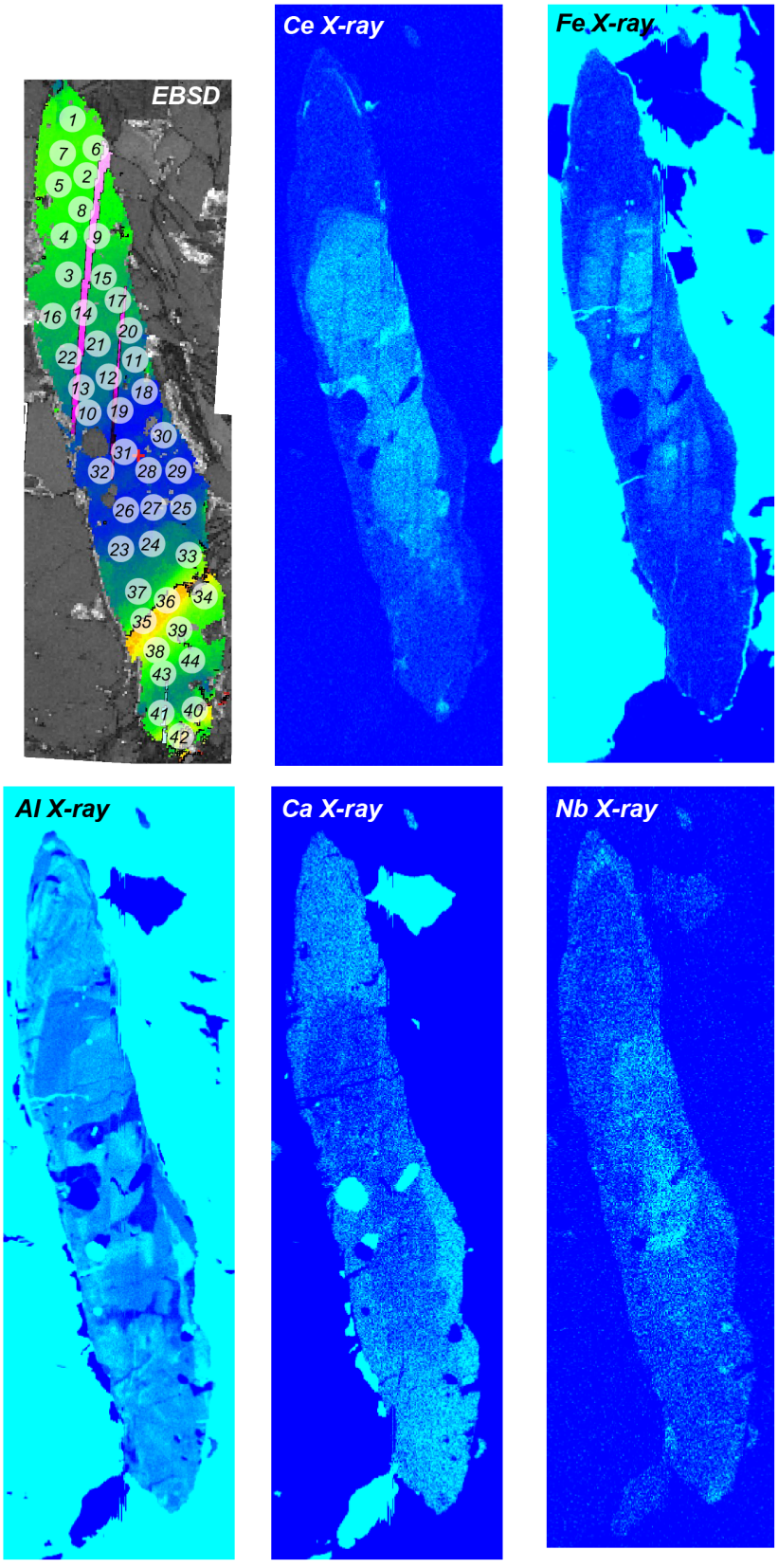

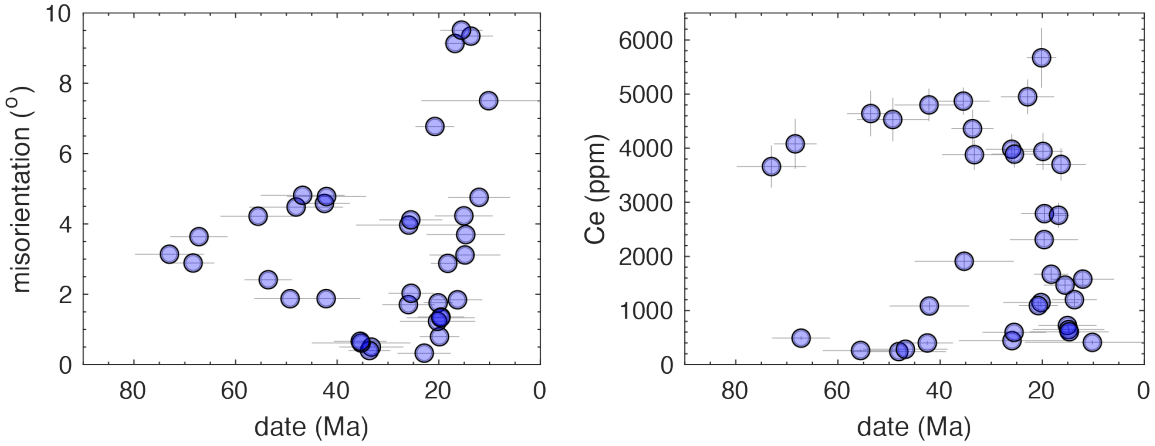
misorientation (°)
date (Ma)

Ce (ppm)
date (Ma)

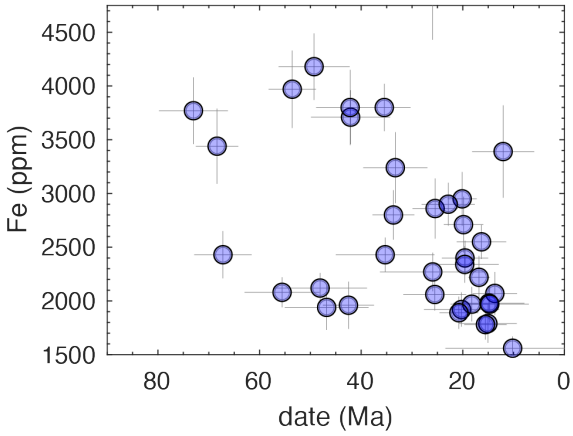
Fe (ppm)
date (Ma)

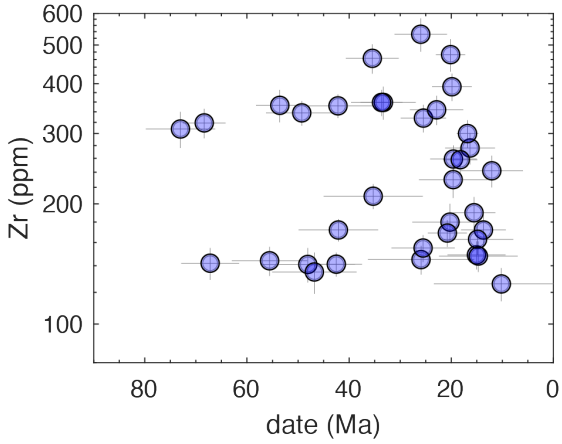
Zr (ppm)
date (Ma)

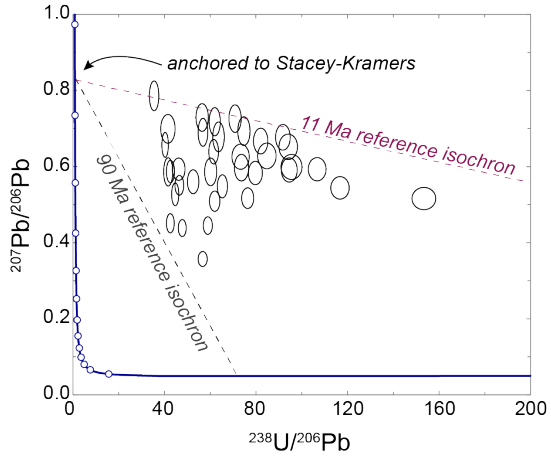
anchored to Stacey-Kramers
11 Ma reference isochron
90 Ma reference isochron
207Pb/206Pb
238U/206Pb

48A-0129-9; max misorient 5°

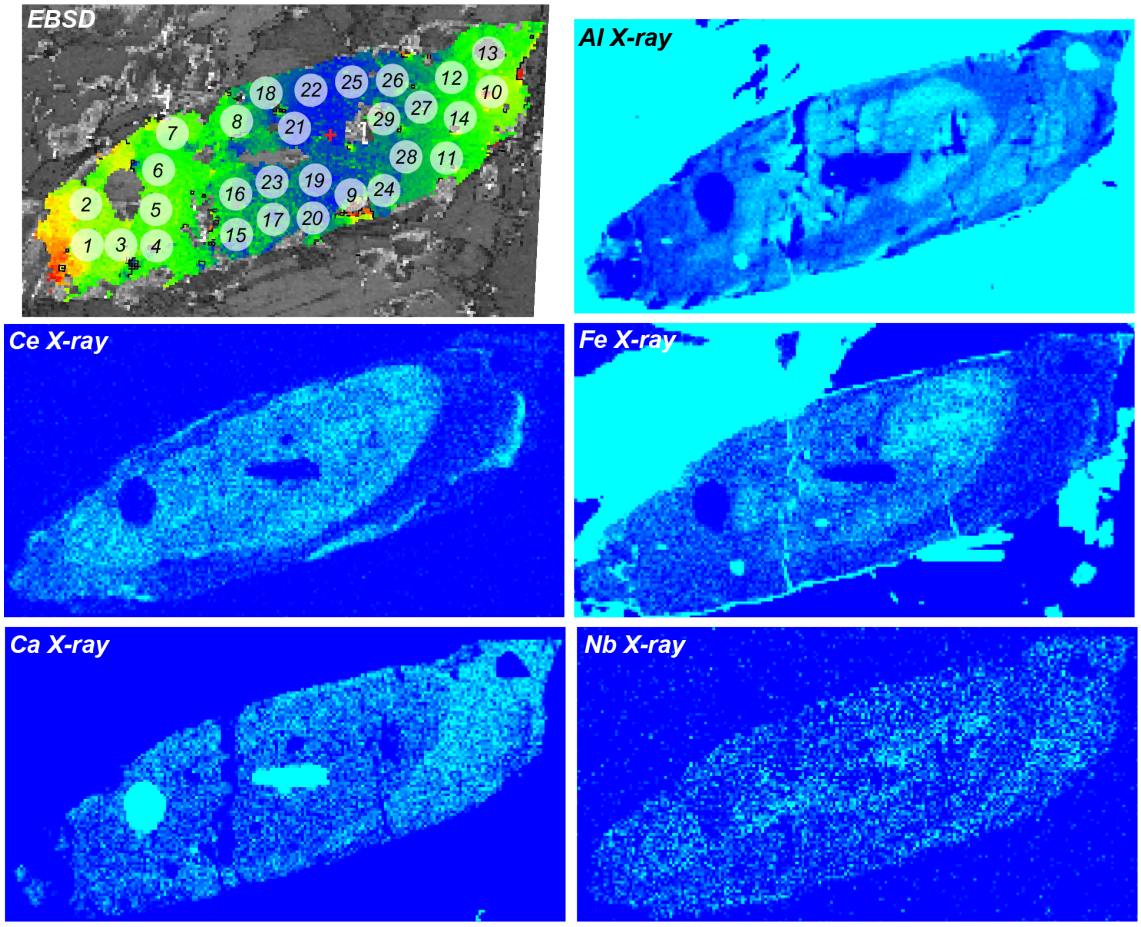

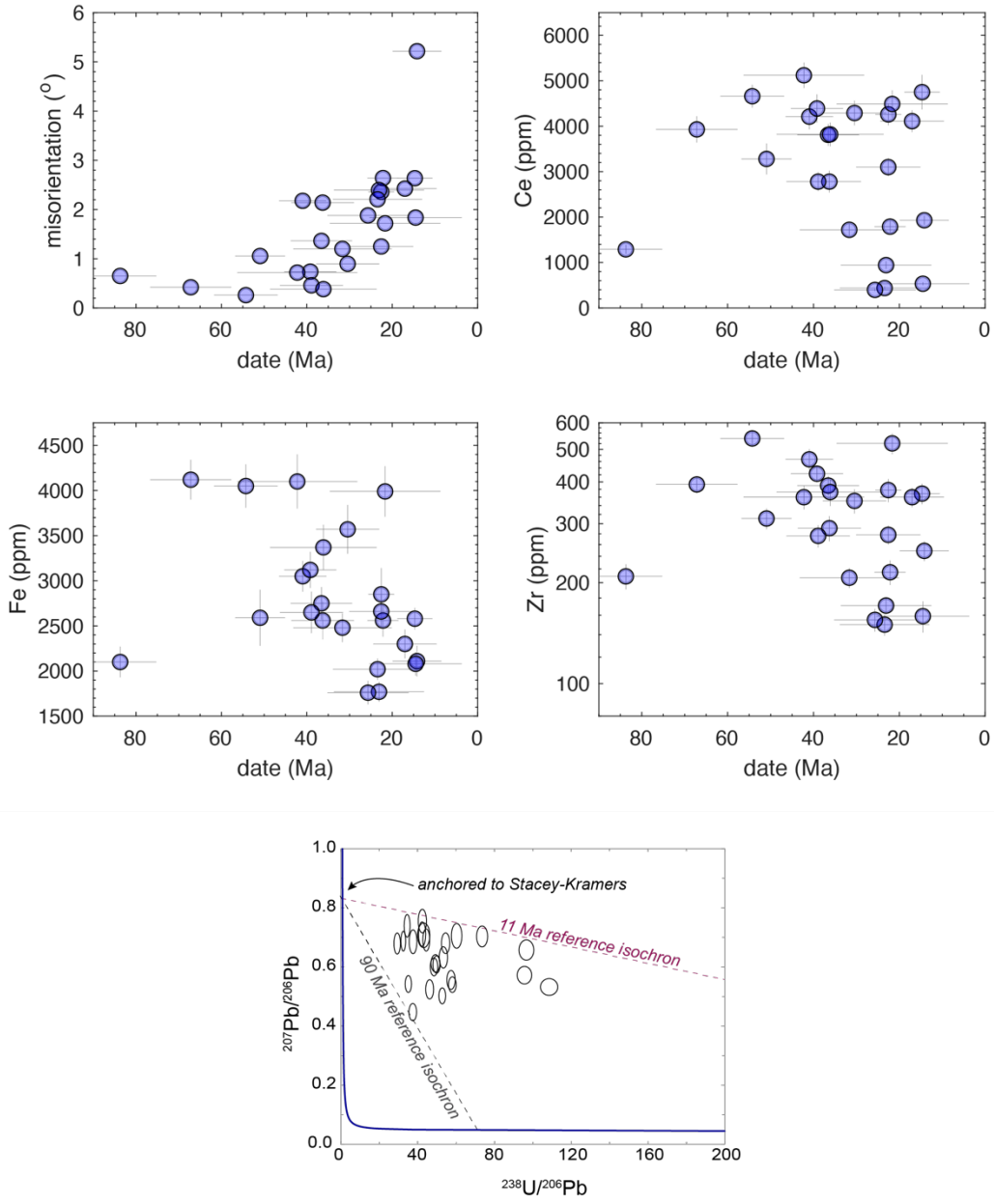
misorientation (°)
date (Ma)
Ce (ppm)
Fe (ppm)
Zr (ppm)
anchored to Stacey-Kramers
11 Ma reference isochron
90 Ma reference isochron
207Pb/206Pb
238U/206Pb

48A-0202-24; max misorient 20°

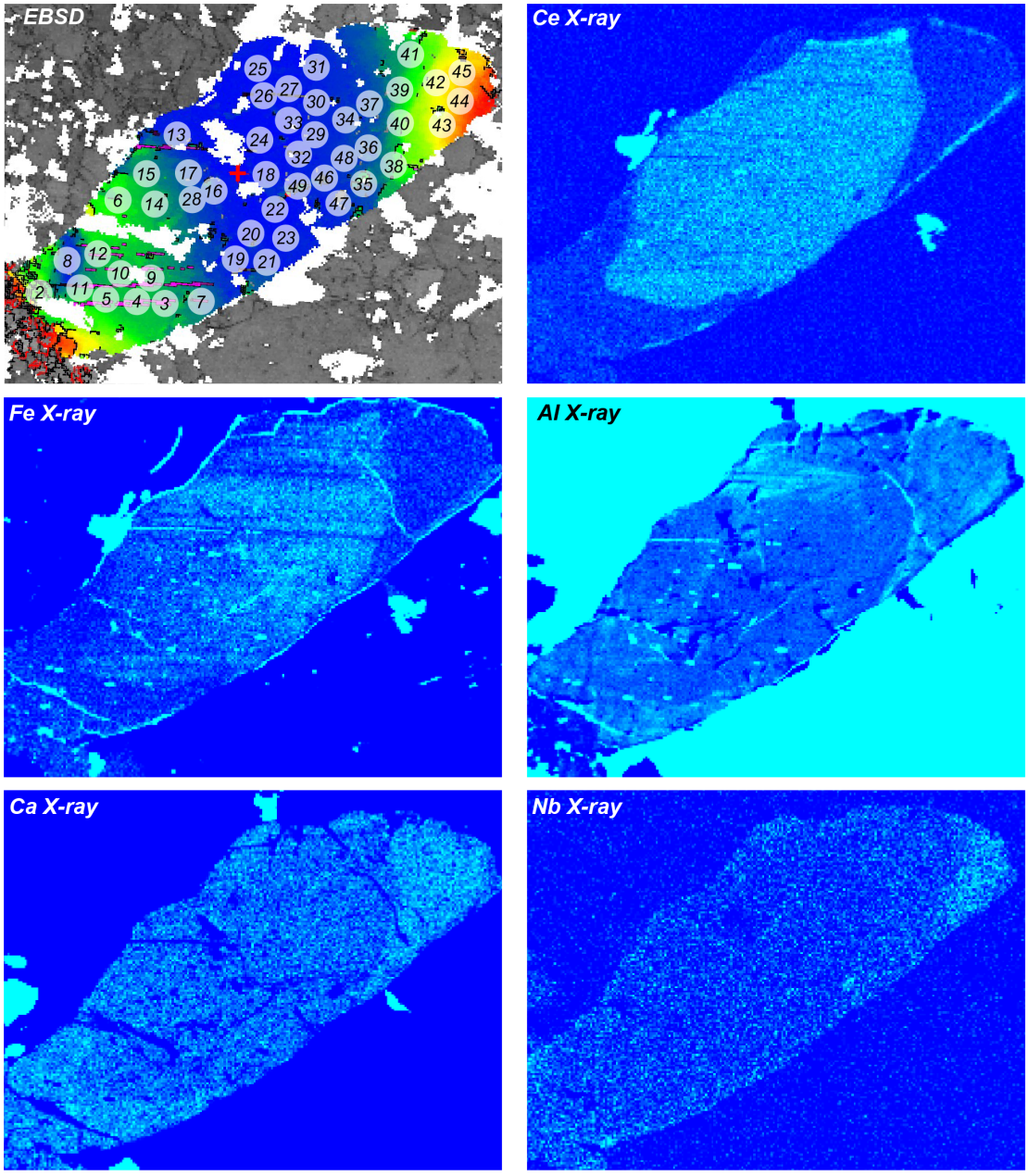

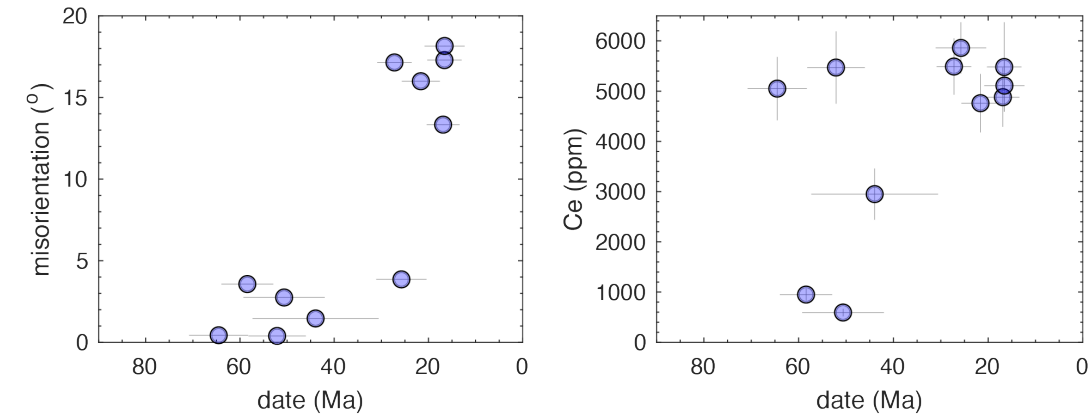
misorientation (°)
date (Ma)

Ce (ppm)
date (Ma)

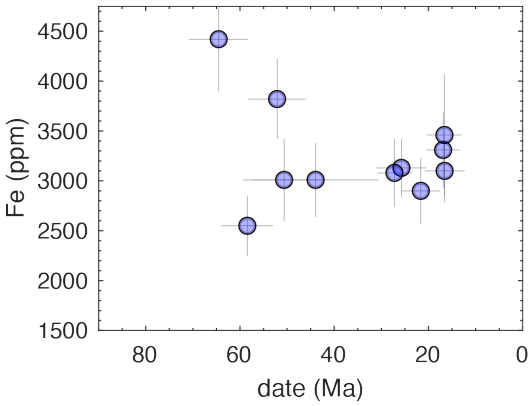
Fe (ppm)
date (Ma)

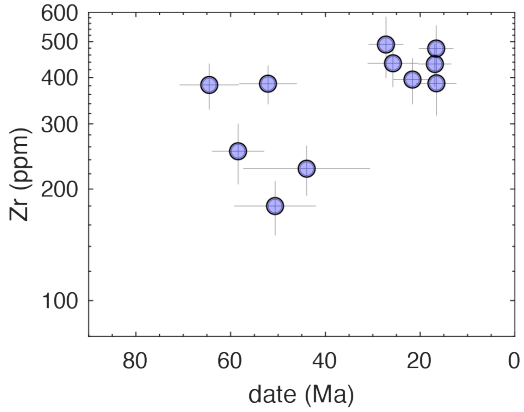
Zr (ppm)
date (Ma)

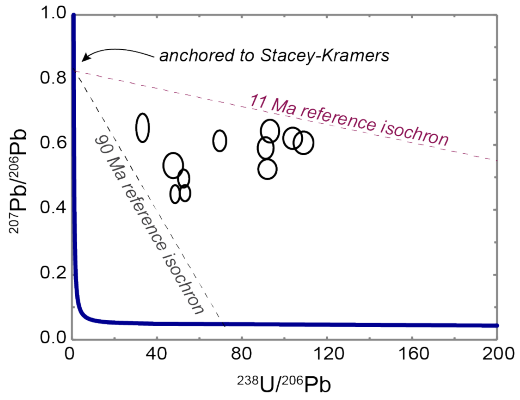
anchored to Stacey-Kramers
11 Ma reference isochron
90 Ma reference isochron
207Pb/206Pb
238U/206Pb

48A-1003-6; max misorient 20°

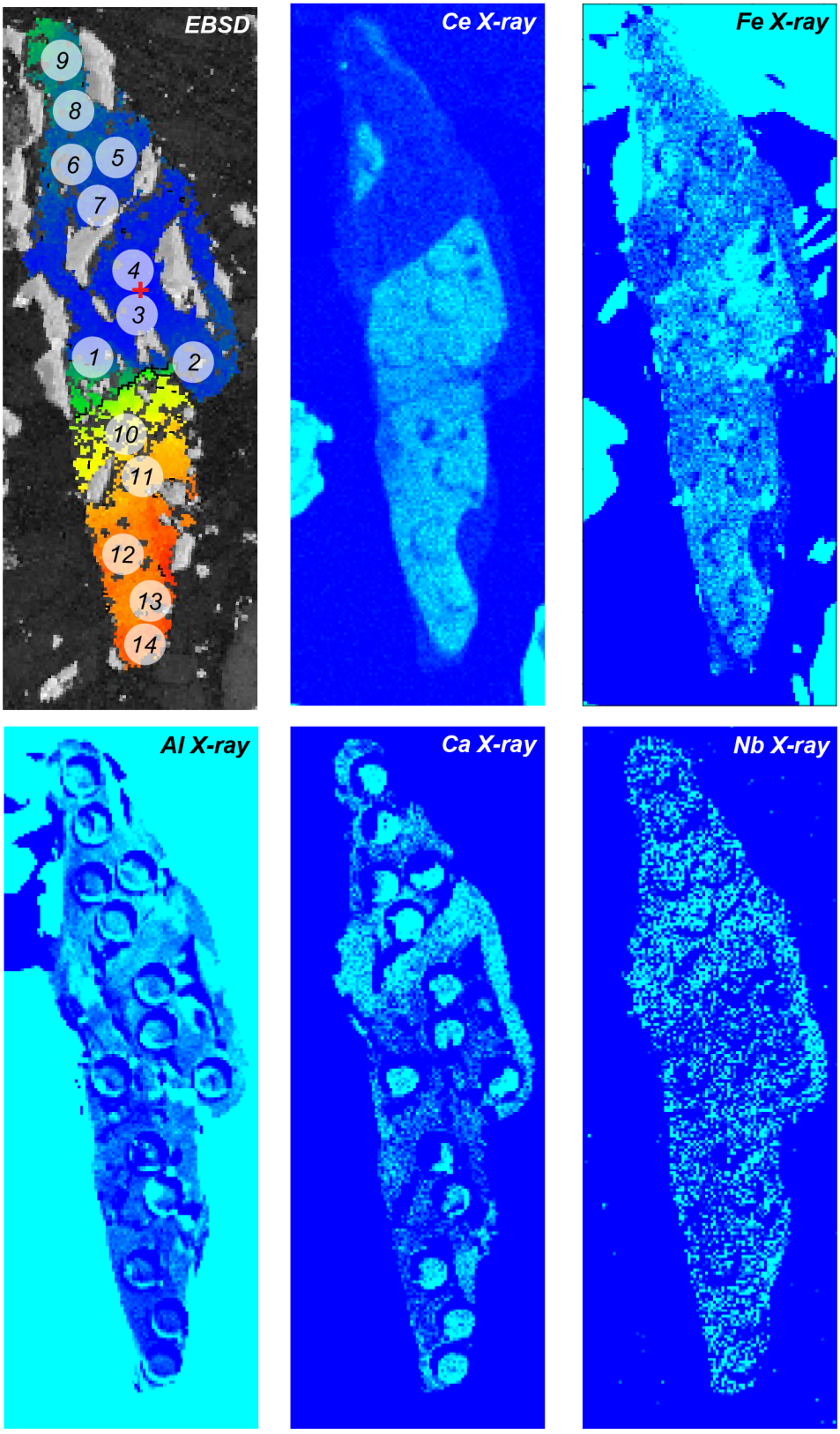

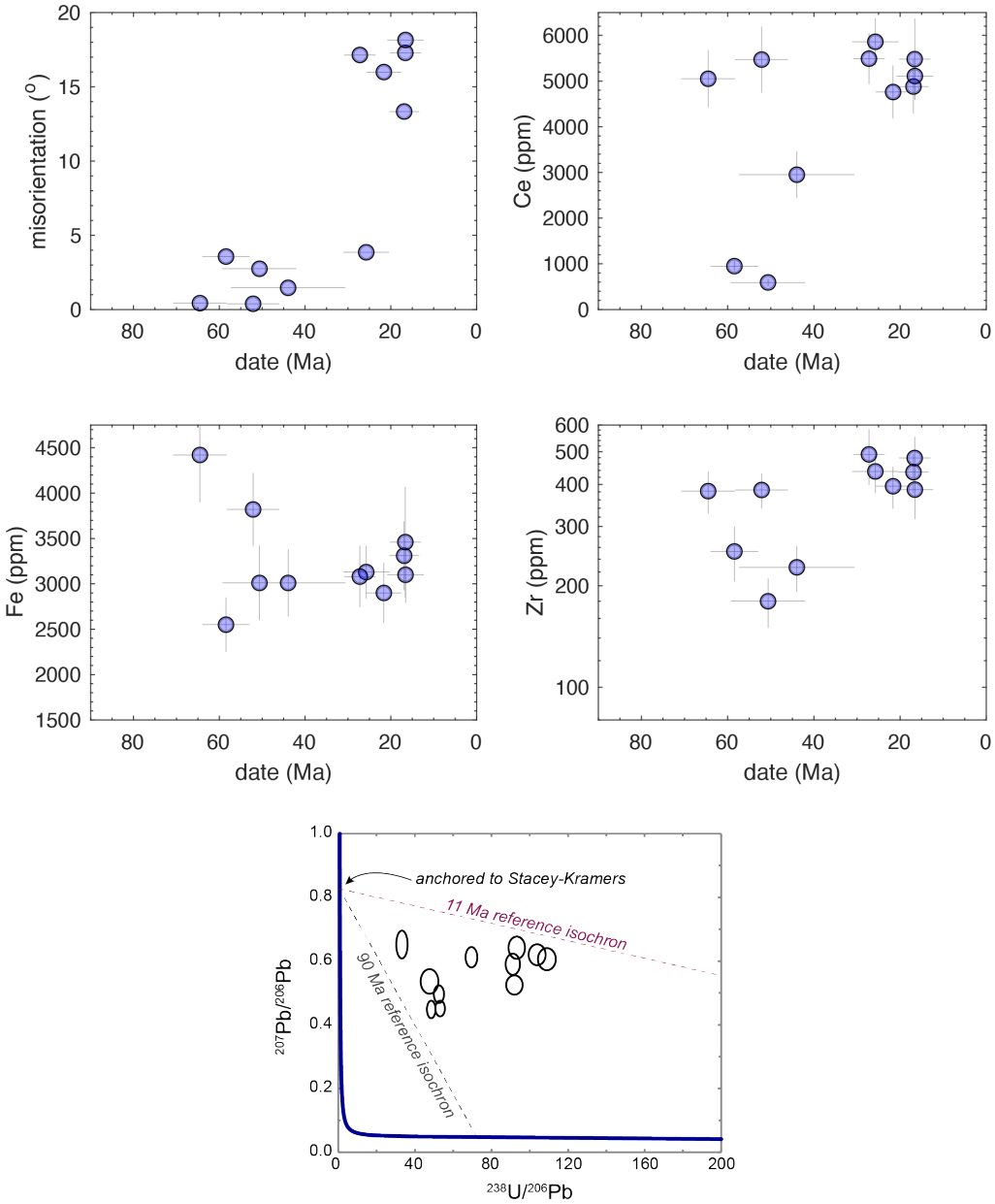
misorientation (°)
date (Ma)
Ce (ppm)
date (Ma)
Fe (ppm)
date (Ma)
Zr (ppm)
date (Ma)
anchored to Stacey-Kramers
11 Ma reference isochron
90 Ma reference isochron
207Pb/206Pb
238U/206Pb

48A-1003-16; max misorient 25°

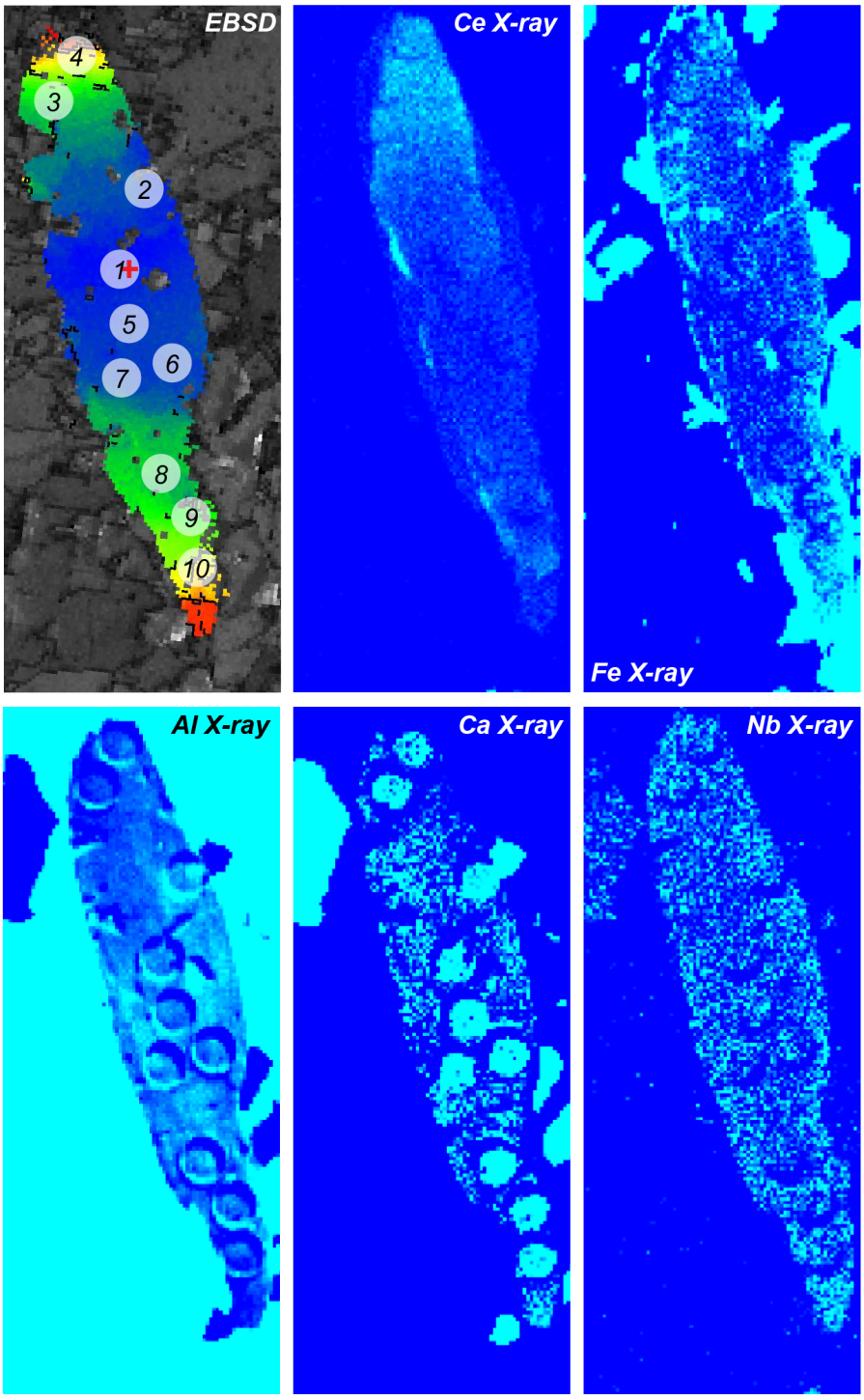

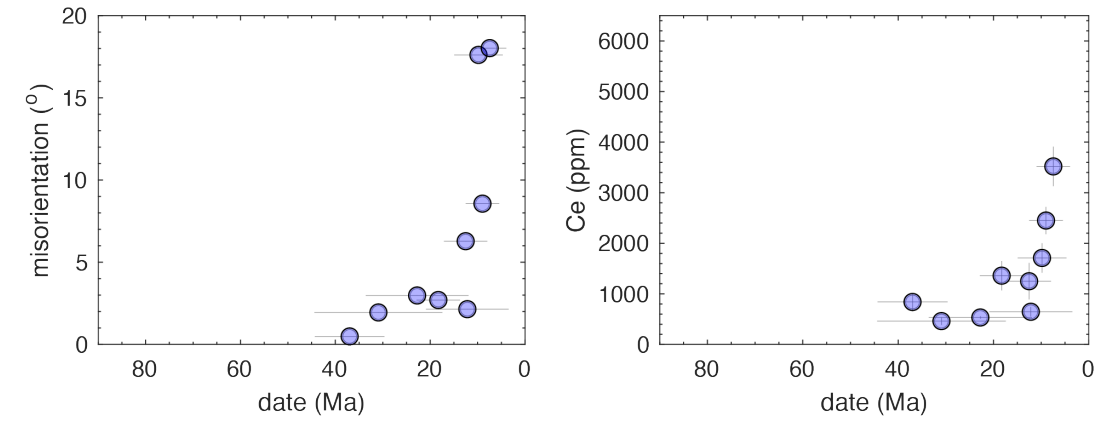
misorientation (°)
date (Ma)
Ce (ppm)
date (Ma)

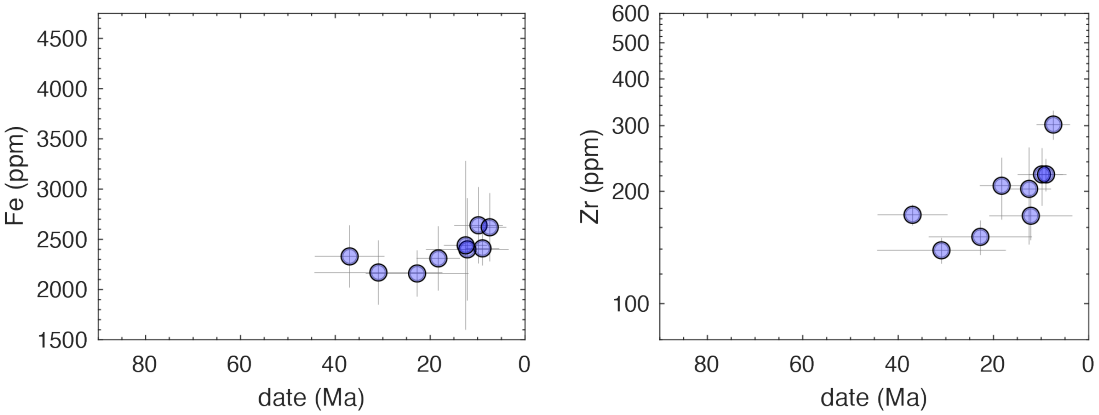
Fe (ppm)
date (Ma)
Zr (ppm)
date (Ma)

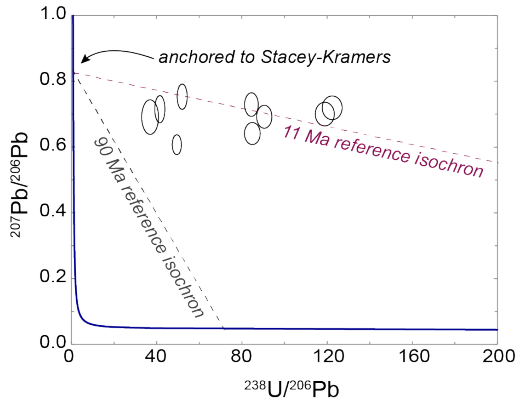
anchored to Stacey-Kramers
11 Ma reference isochron
90 Ma reference isochron
207Pb/206Pb
238U/206Pb

48A-1003-28; max misorient 22°

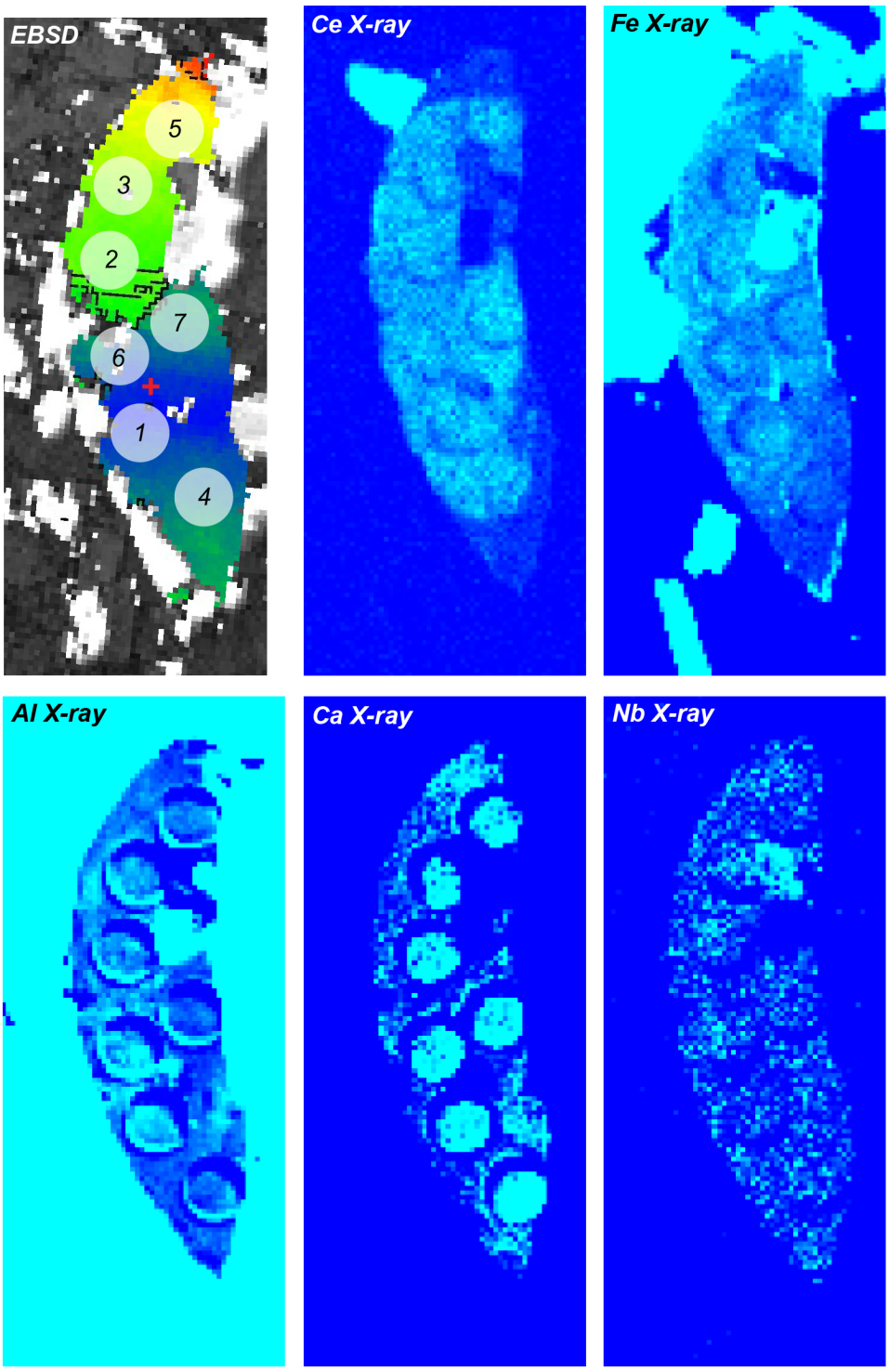

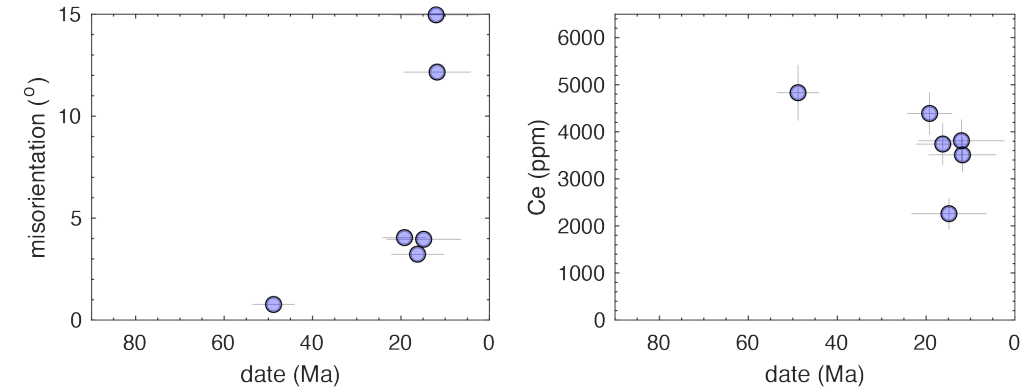
misorientation (°)
15
10
5
0
80
60
40
20
0
date (Ma)

Ce (ppm)
6000
5000
4000
3000
2000
1000
0
80
60
40
20
0
date (Ma)

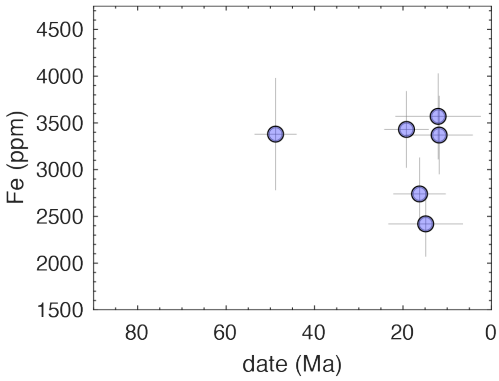
Fe (ppm)
4500
4000
3500
3000
2500
2000
1500
80
60
40
20
0
date (Ma)

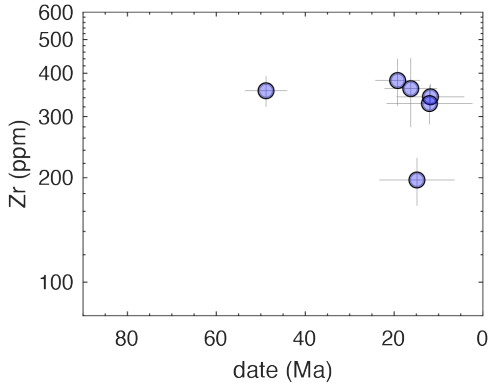
Zr (ppm)
600
500
400
300
200
100
80
60
40
20
0
date (Ma)

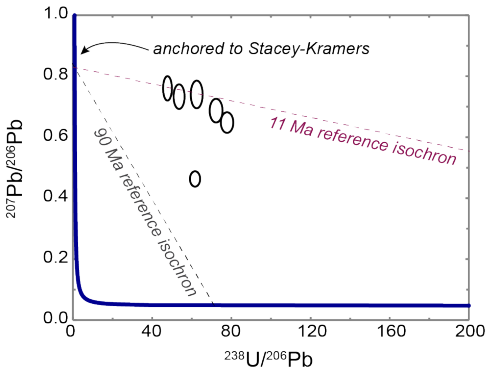
anchored to Stacey-Kramers
11 Ma reference isochron
90 Ma reference isochron
207Pb/206Pb
1.0
0.8
0.6
0.4
0.2
0.0
0
40
80
120
160
200
238U/206Pb

48A-1003-29; max misorient 20°

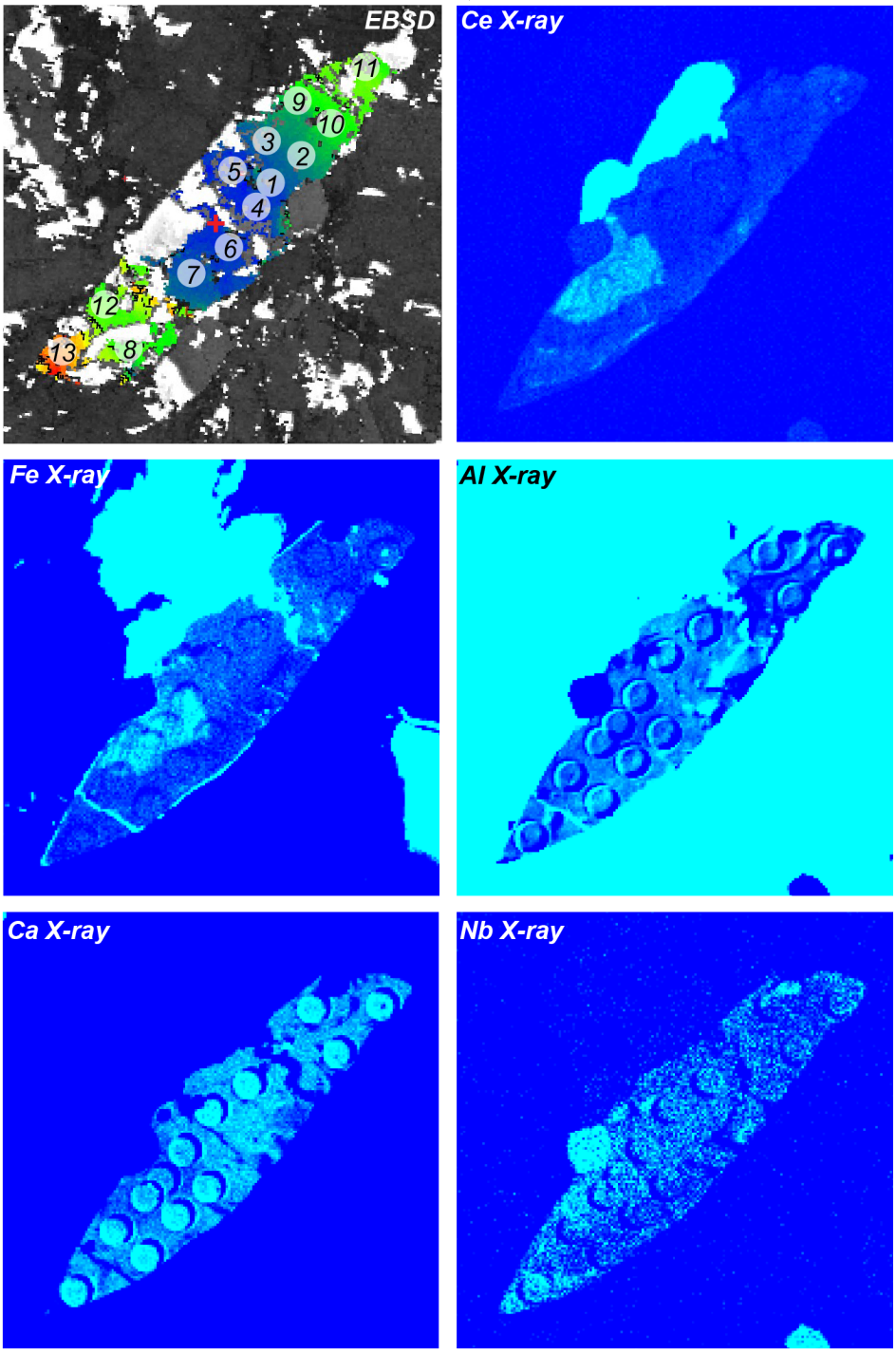

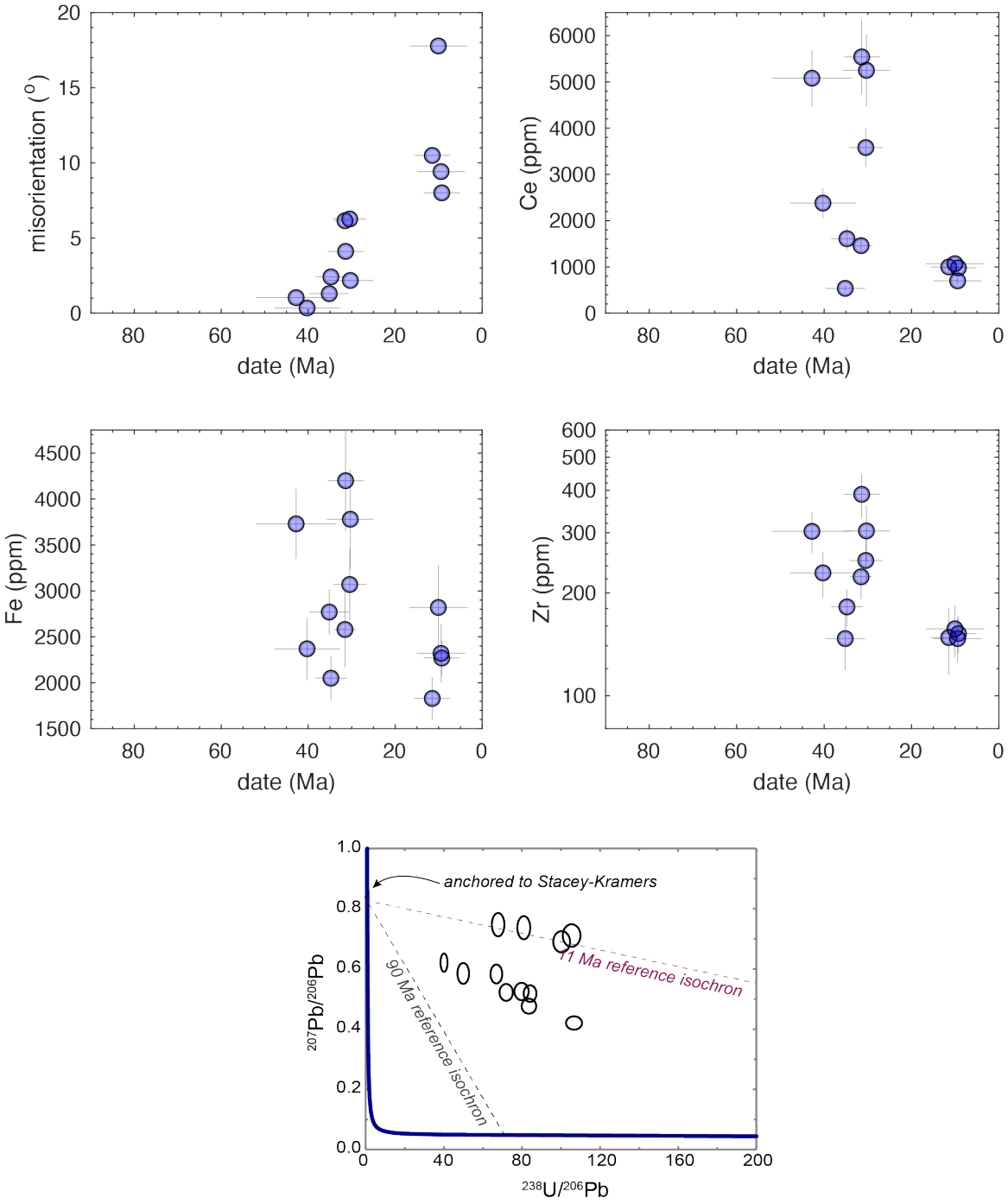
misorientation (°)
date (Ma)
Ce (ppm)
Fe (ppm)
Zr (ppm)
anchored to Stacey-Kramers
11 Ma reference isochron
90 Ma reference isochron
207Pb/206Pb
238U/206Pb

48A-0202-19; max misorient 5°

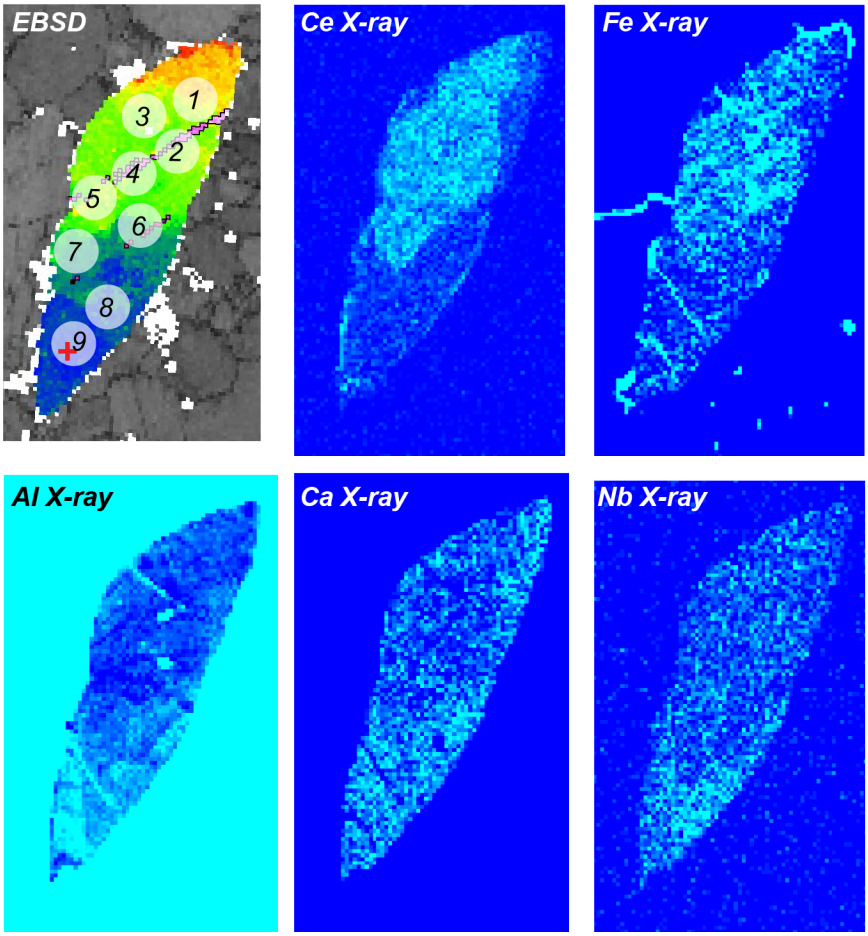

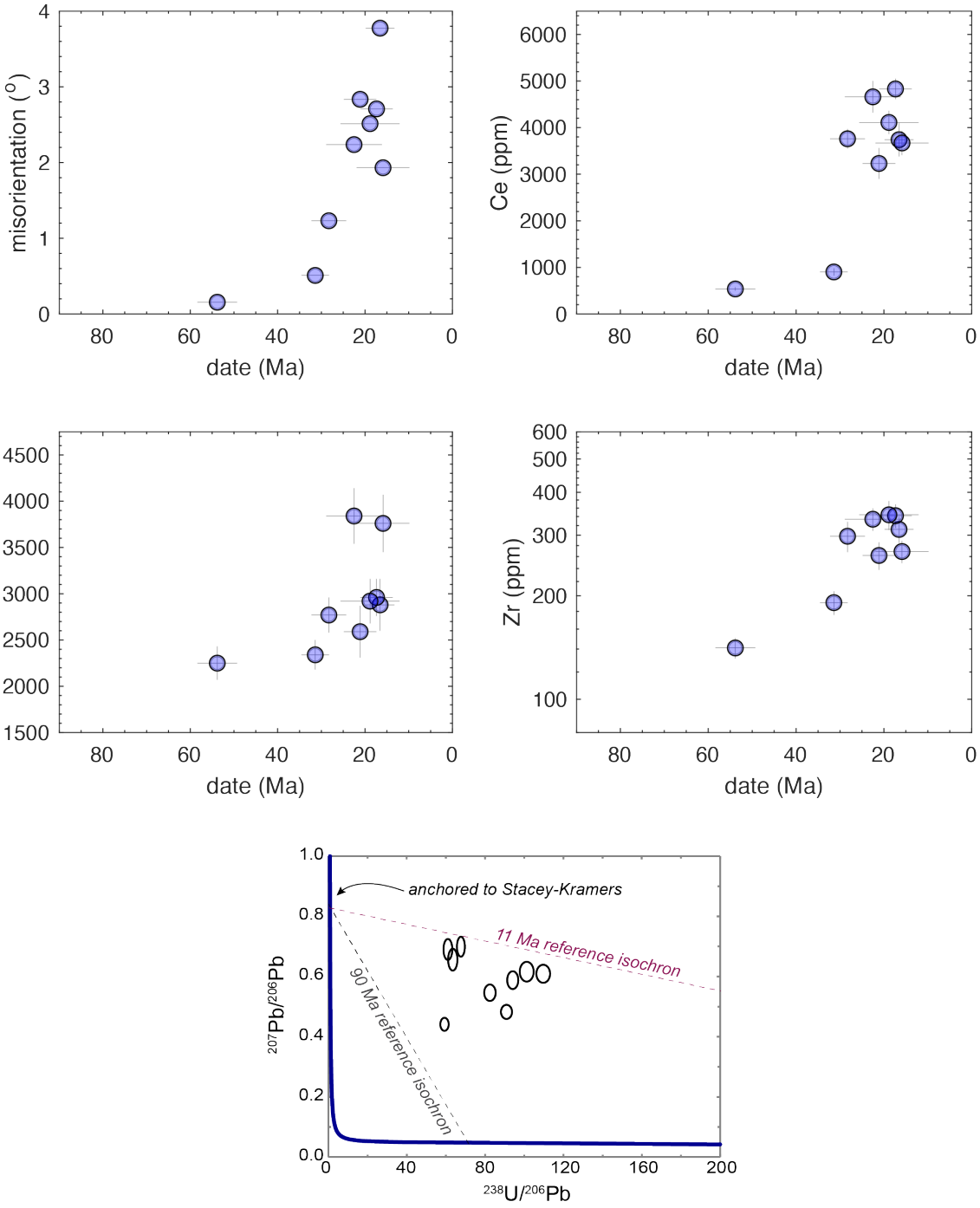
misorientation (°)
date (Ma)
Ce (ppm)
Fe (ppm)
Zr (ppm)
anchored to Stacey-Kramers
11 Ma reference isochron
90 Ma reference isochron
$^{207}Pb/^{206}Pb$
$^{238}U/^{206}Pb$

48A-0202-25; max misorient 30°

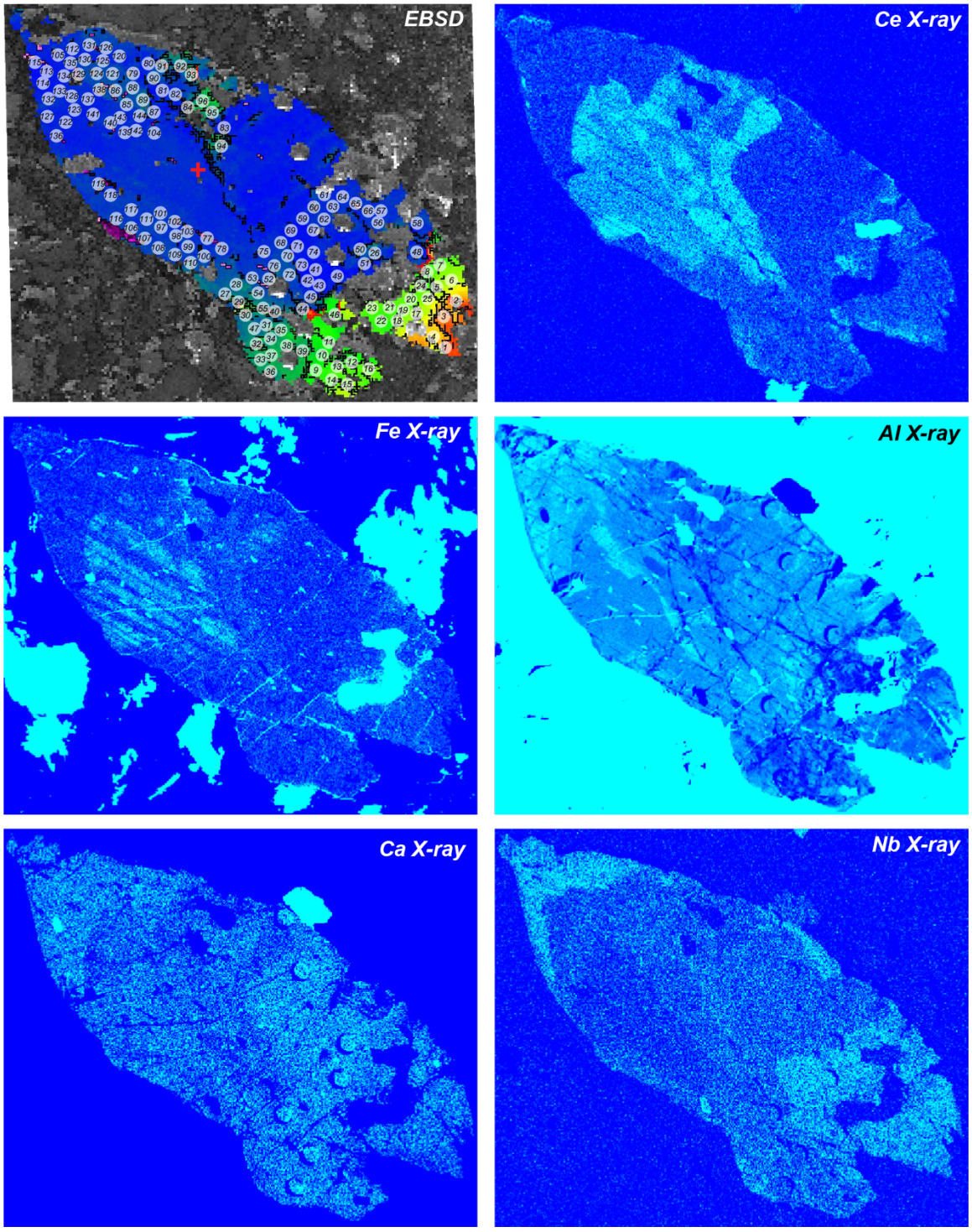

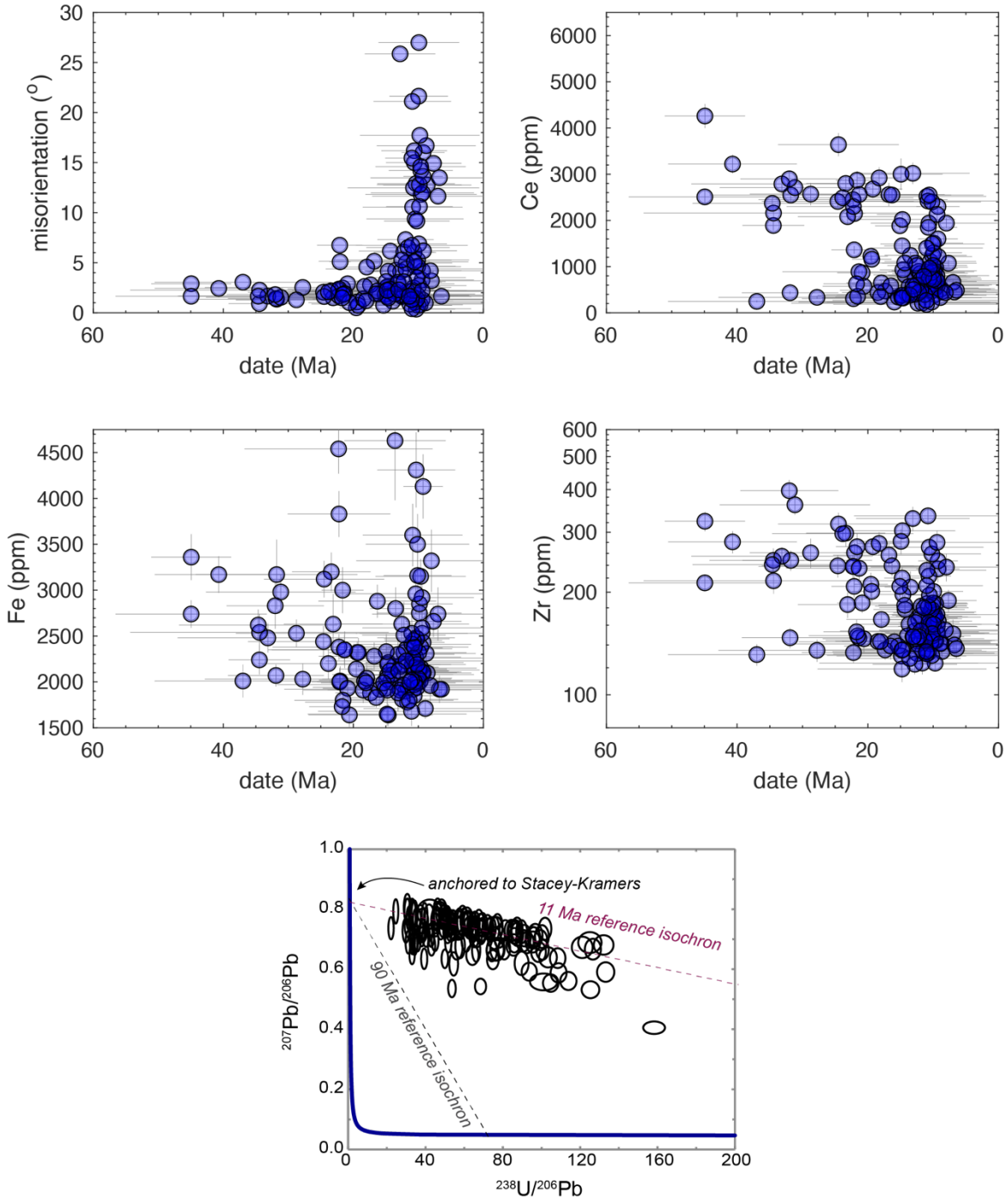
misorientation (°)
date (Ma)
Ce (ppm)
Fe (ppm)
Zr (ppm)
anchored to Stacey-Kramers
11 Ma reference isochron
90 Ma reference isochron
207Pb/206Pb
238U/206Pb

48A-0129-11; max misorient 11°

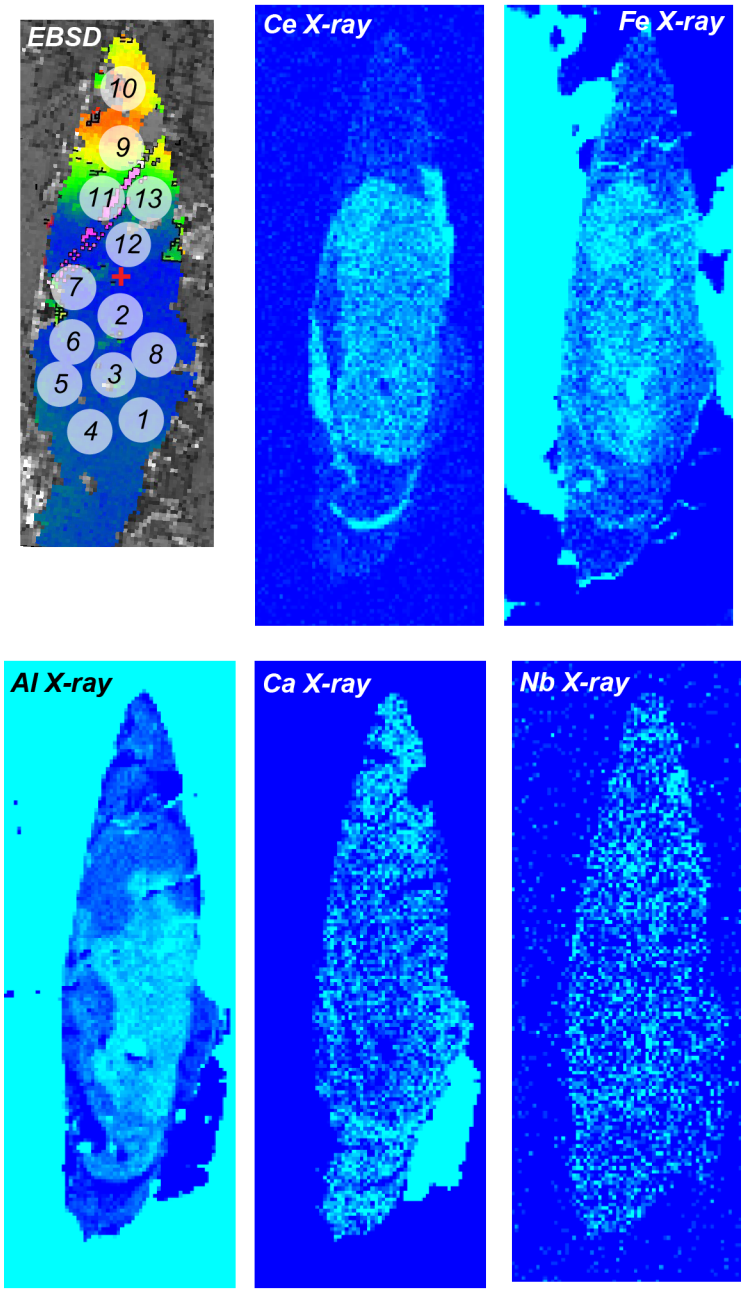

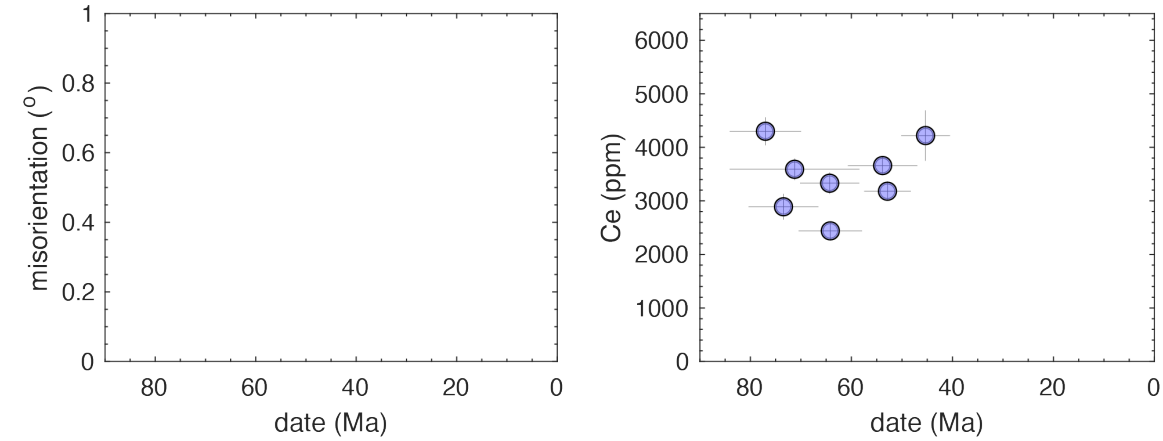
misorientation (°)
1
0.8
0.6
0.4
0.2
0
80
60
40
20
0
date (Ma)

Ce (ppm)
6000
5000
4000
3000
2000
1000
0
80
60
40
20
0
date (Ma)

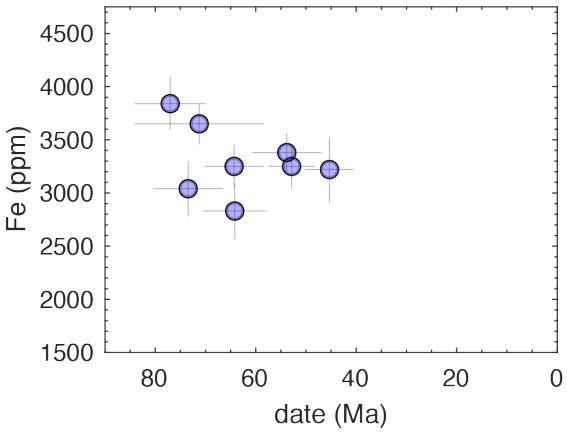
Fe (ppm)
4500
4000
3500
3000
2500
2000
1500
80
60
40
20
0
date (Ma)

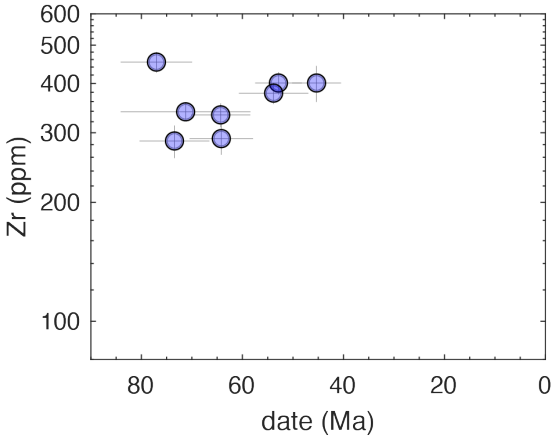
Zr (ppm)
600
500
400
300
200
100
80
60
40
20
0
date (Ma)

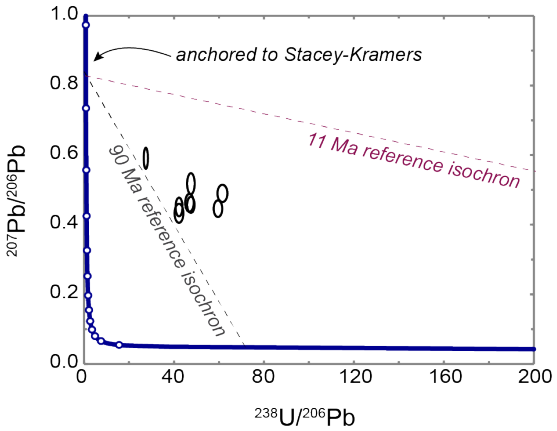
anchored to Stacey-Kramers
11 Ma reference isochron
90 Ma reference isochron
207Pb/206Pb
1.0
0.8
0.6
0.4
0.2
0.0
0
40
80
120
160
200
238U/206Pb

0202-23; max misorient 10°

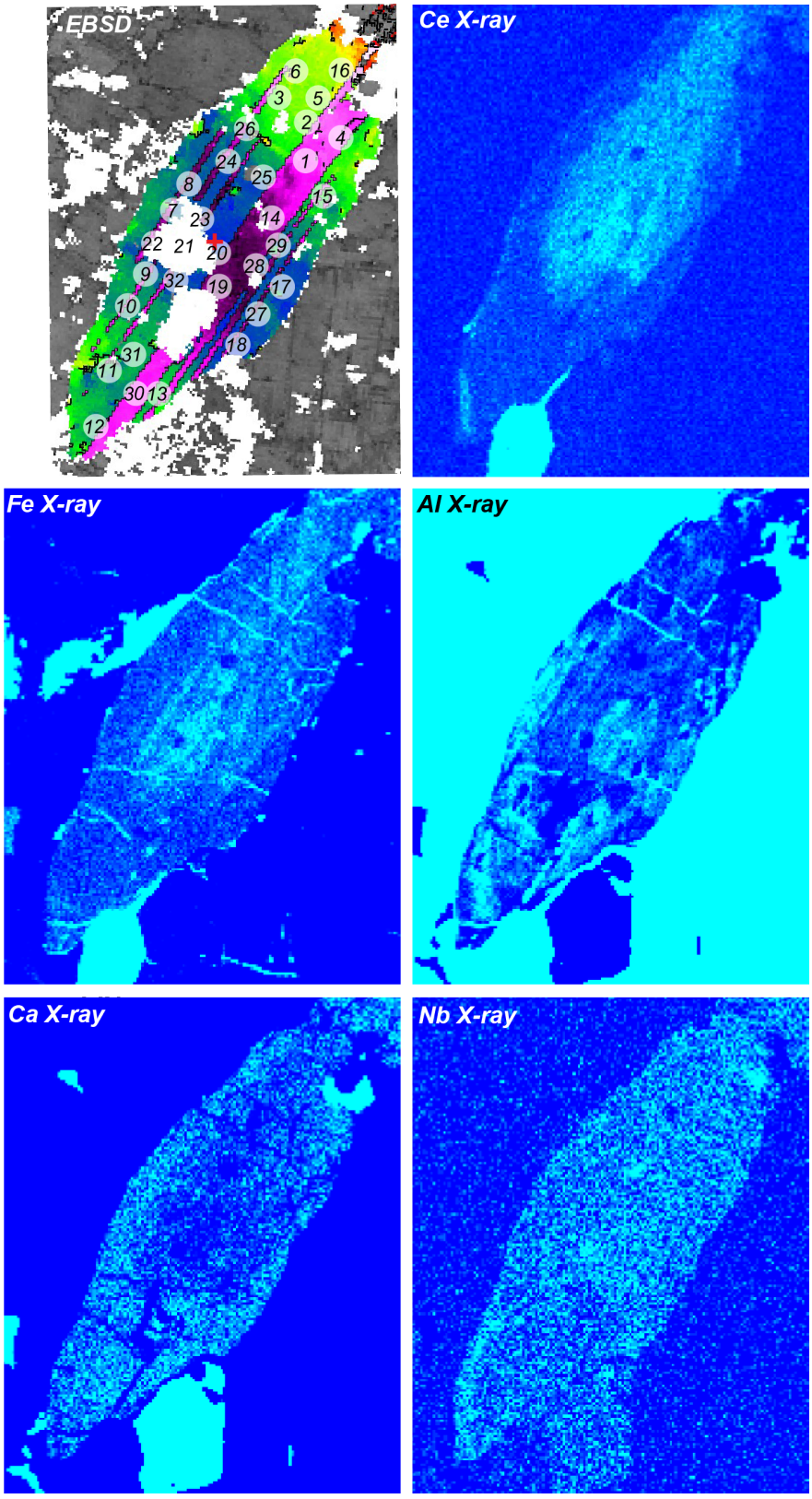

0129-1; max misorient 34°

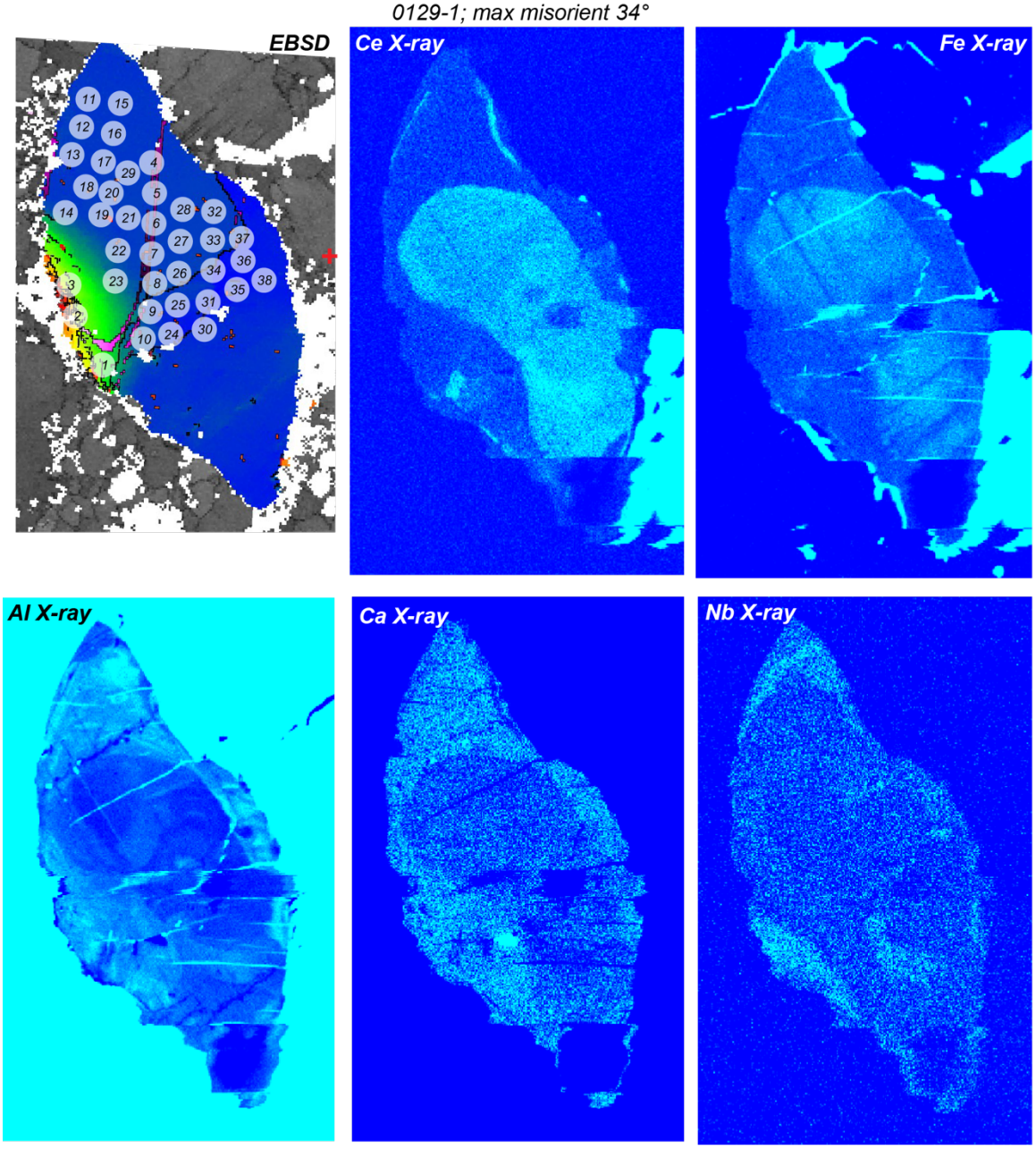

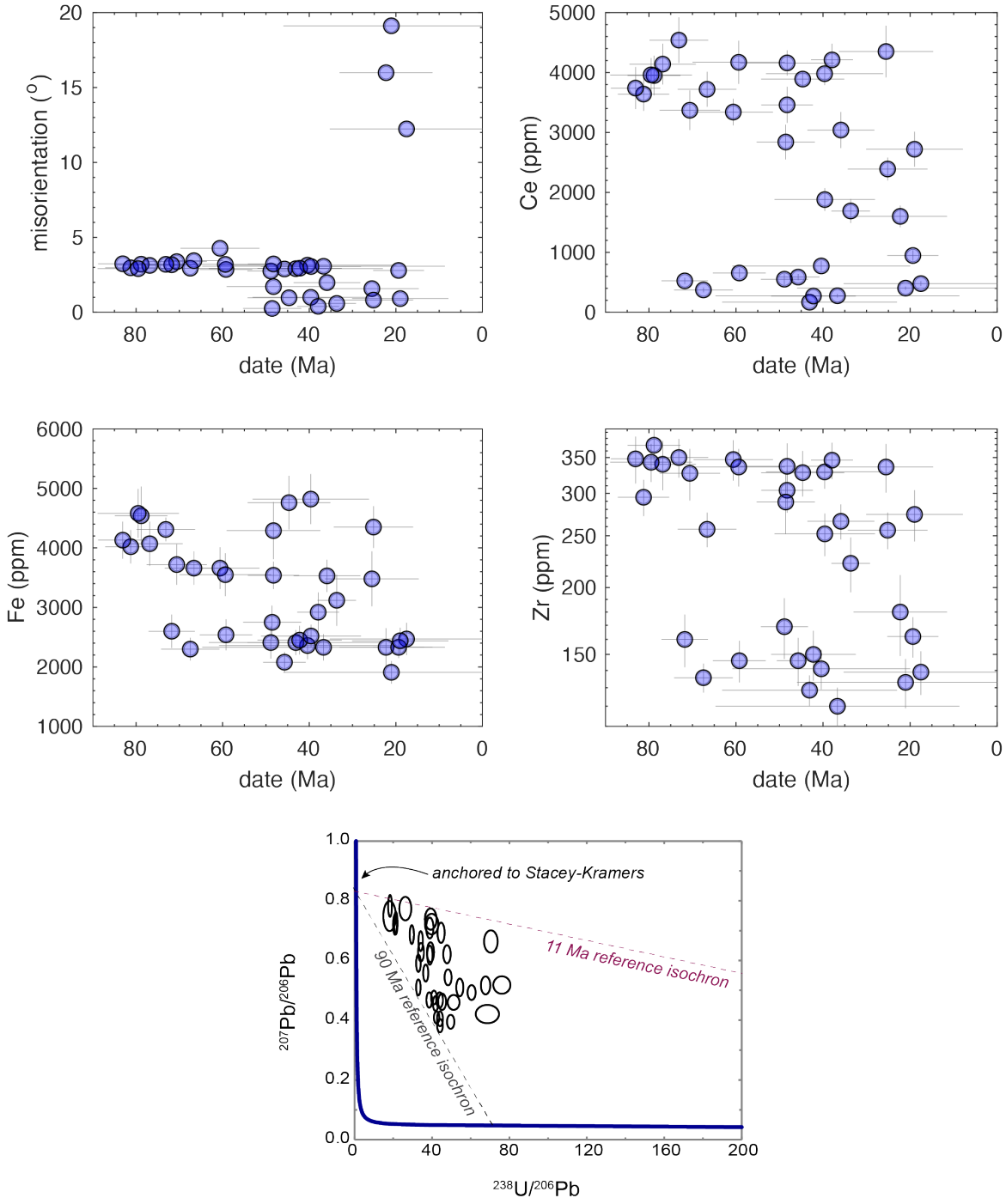
misorientation (°)
date (Ma)
Ce (ppm)
Fe (ppm)
Zr (ppm)
anchored to Stacey-Kramers
11 Ma reference isochron
90 Ma reference isochron
207Pb/206Pb
238U/206Pb

48A-0129-3; max misorient 10°

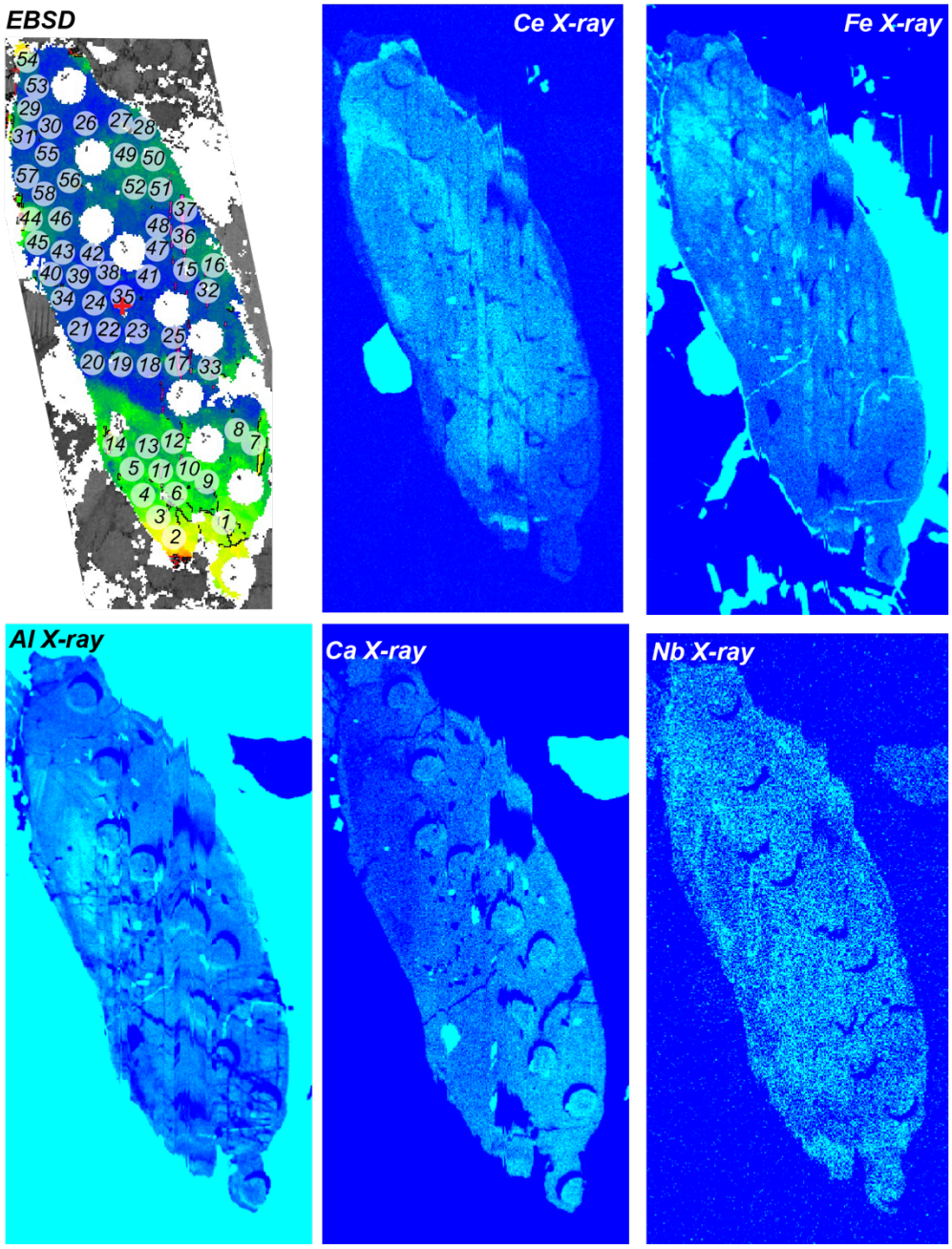

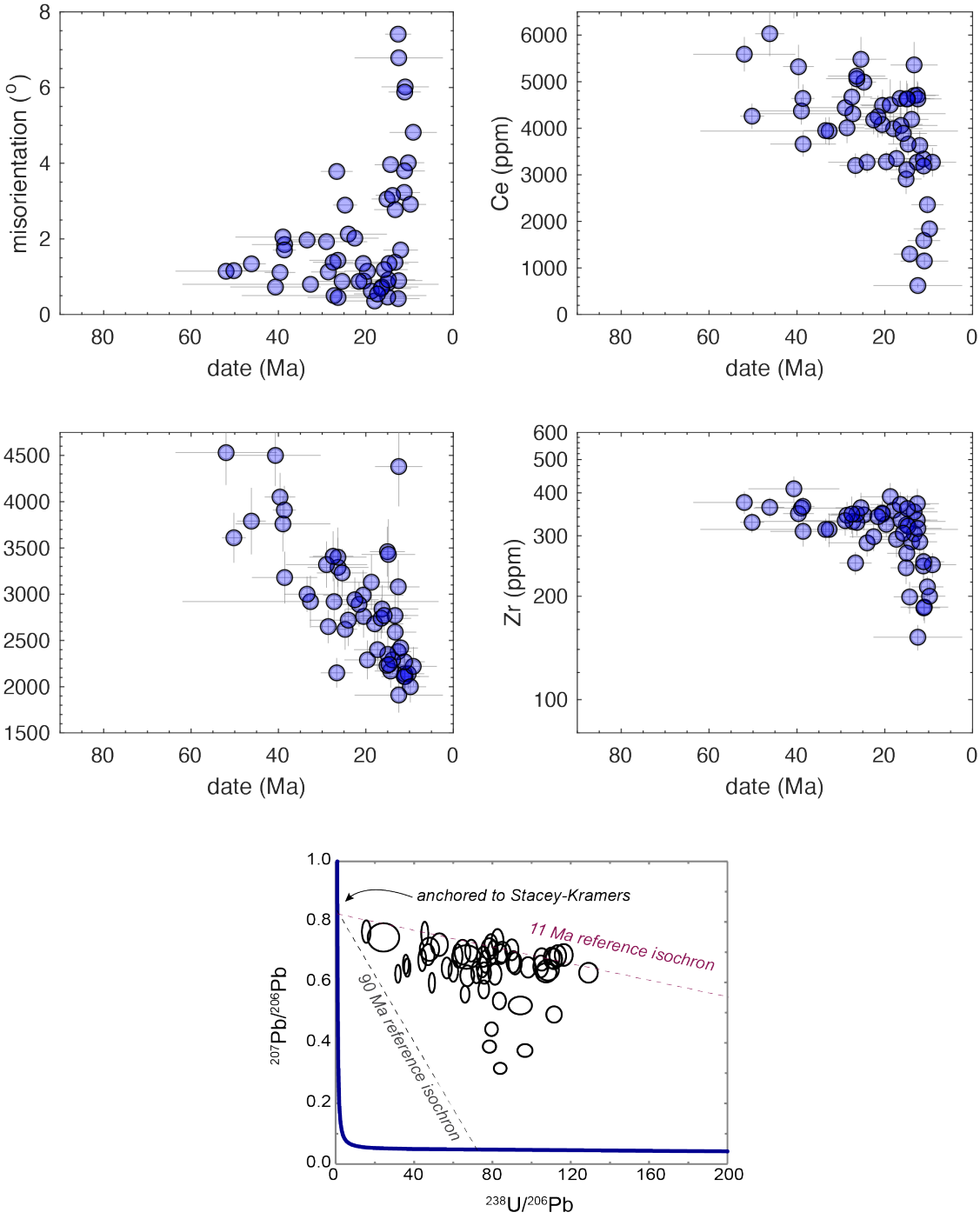
misorientation (°)
date (Ma)
Ce (ppm)
Fe (ppm)
Zr (ppm)
anchored to Stacey-Kramers
11 Ma reference isochron
90 Ma reference isochron
$^{207}Pb/^{206}Pb$
$^{238}U/^{206}Pb$

48A-0129-8; max misorient 3.5°

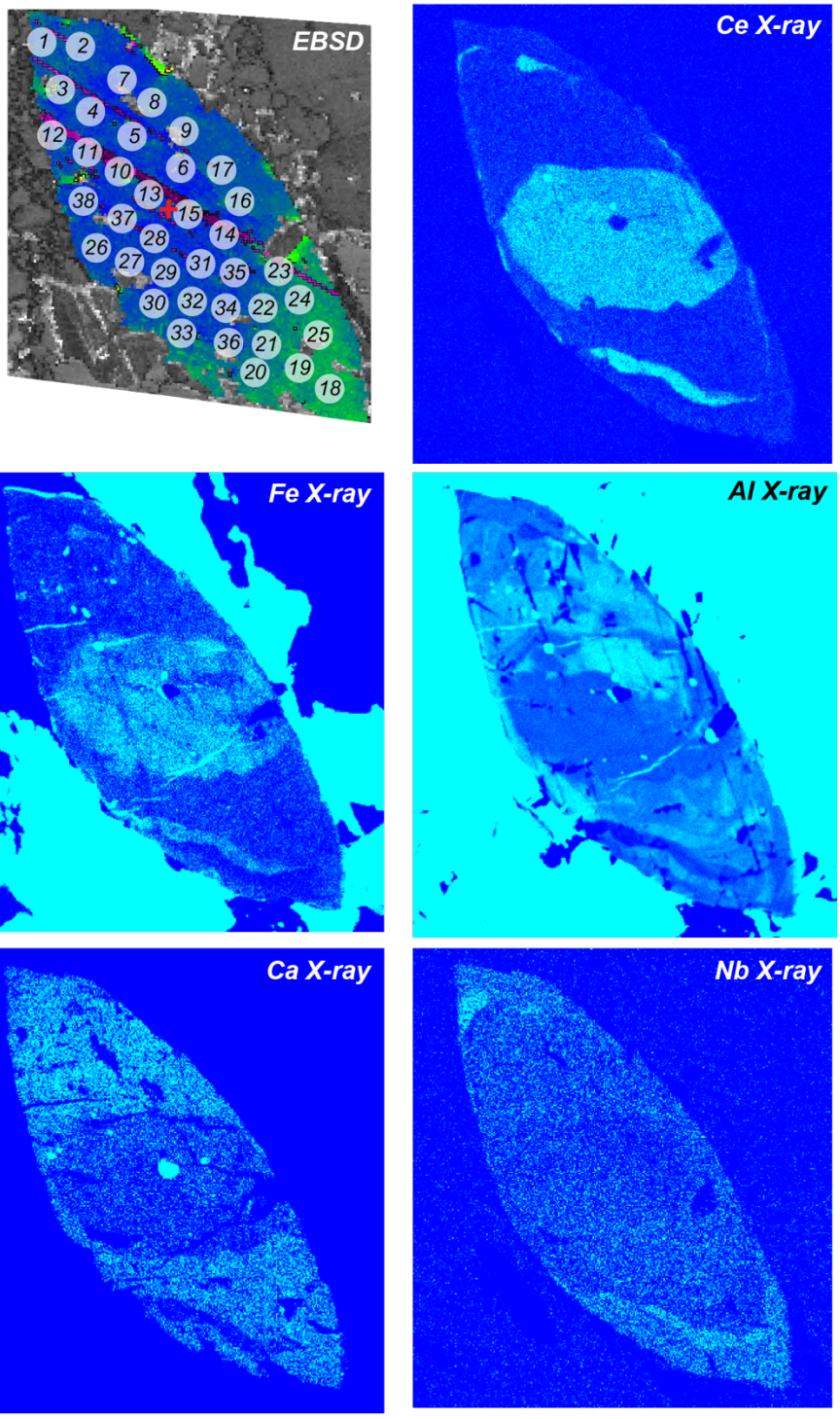

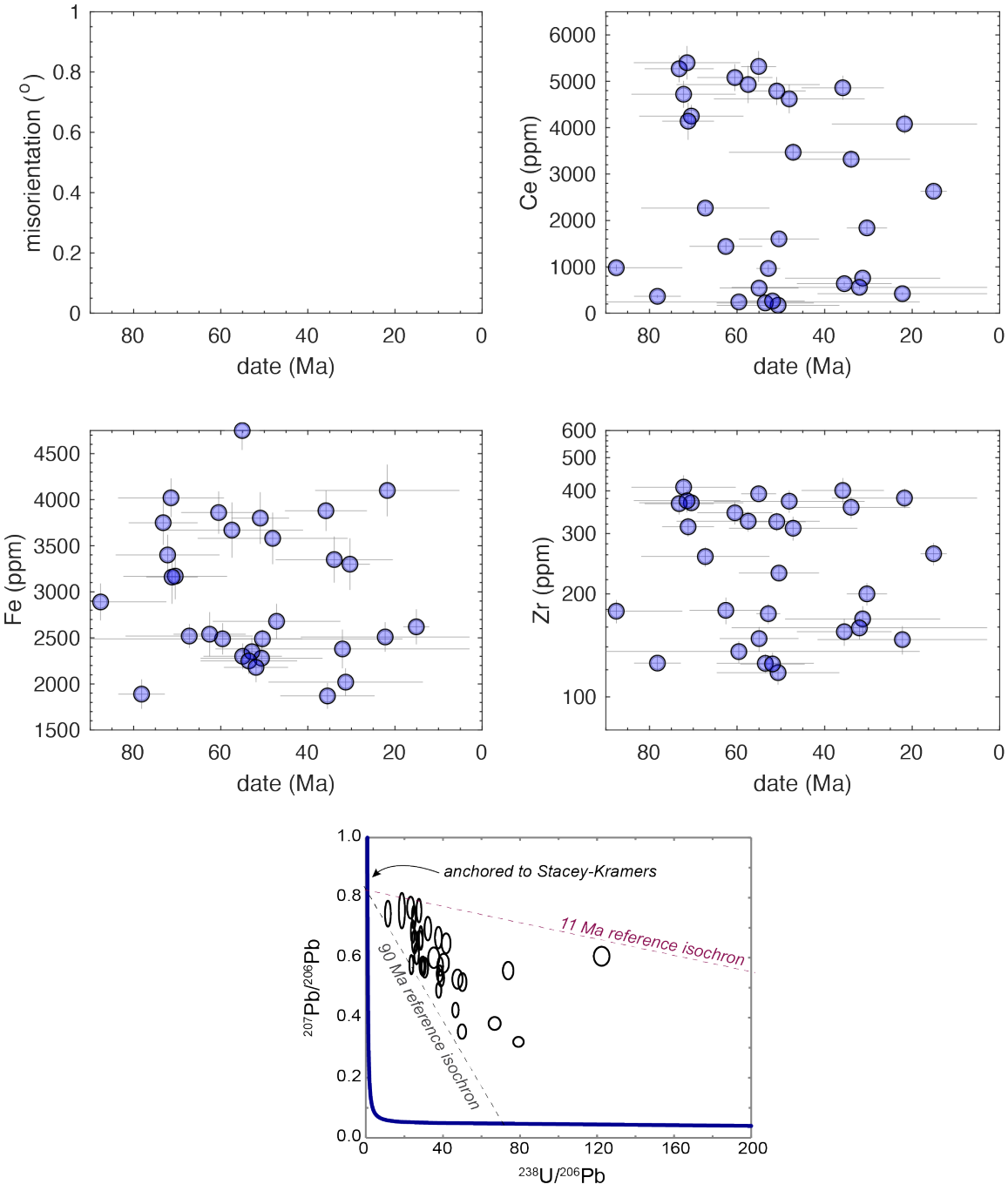
misorientation (°)
date (Ma)
Ce (ppm)
Fe (ppm)
Zr (ppm)
anchored to Stacey-Kramers
11 Ma reference isochron
90 Ma reference isochron
207Pb/206Pb
238U/206Pb

48A-0129-14; max misorient 15°

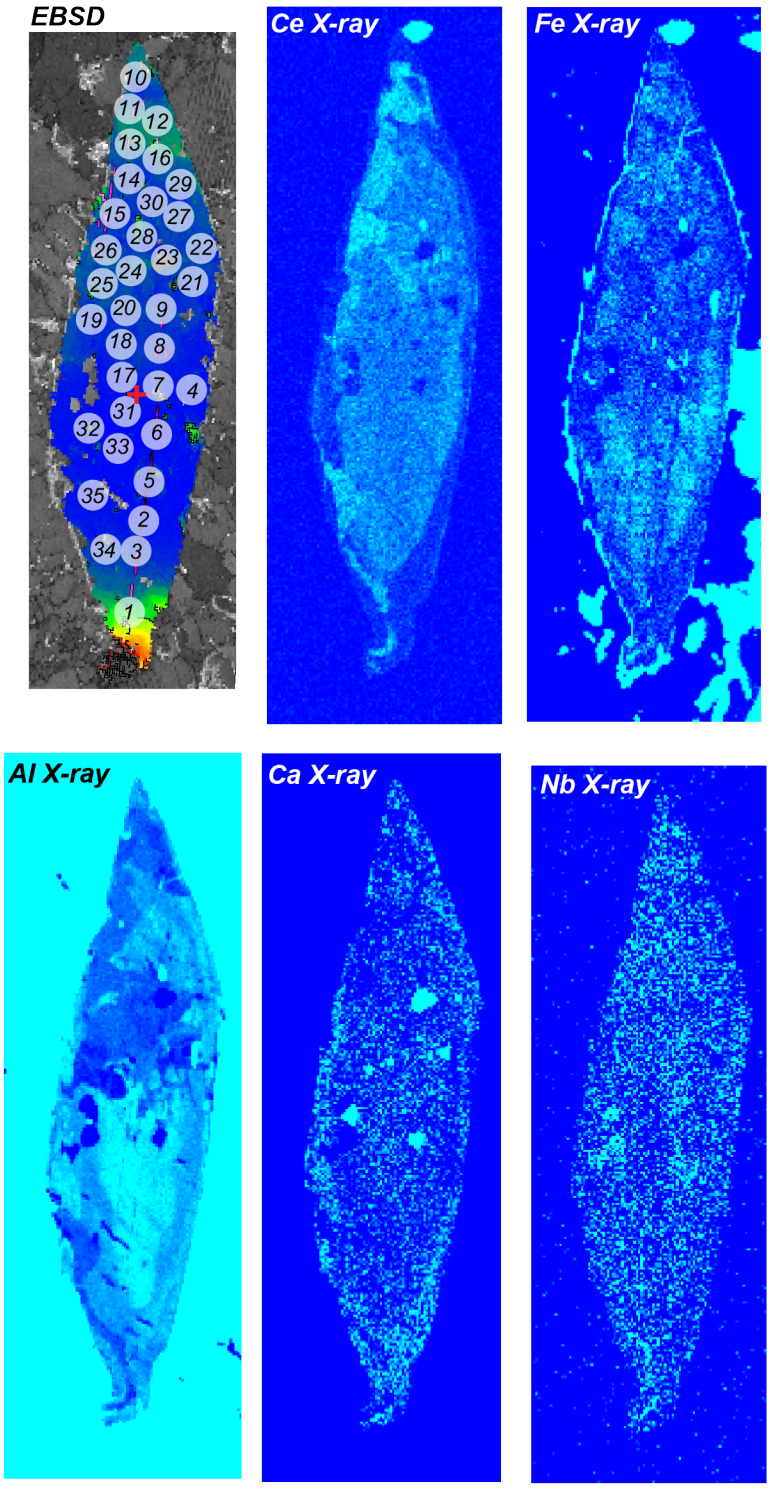

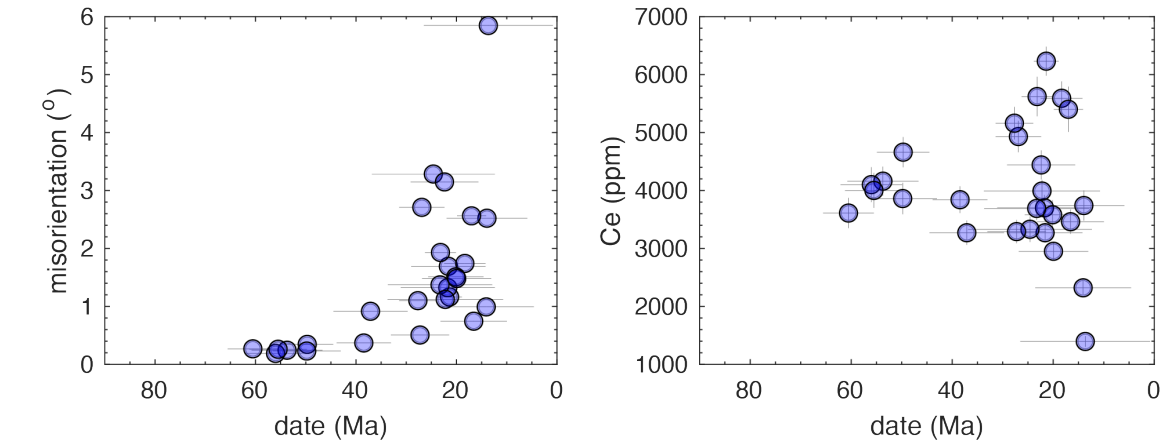
misorientation (°)
date (Ma)

Ce (ppm)
date (Ma)

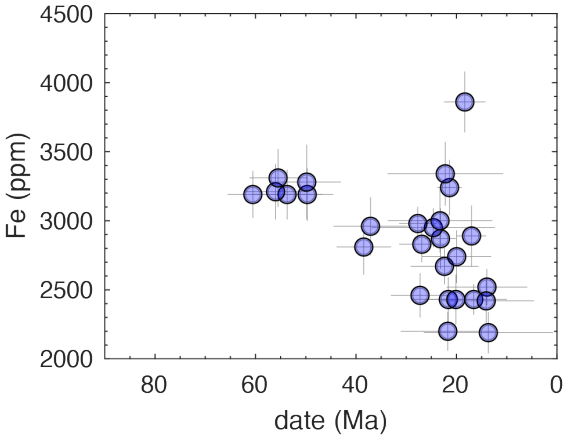
Fe (ppm)
date (Ma)

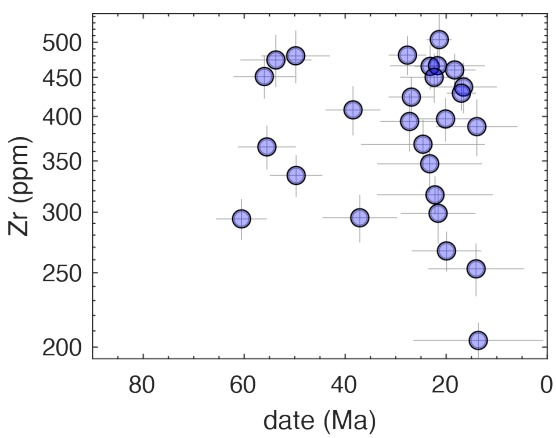
Zr (ppm)
date (Ma)

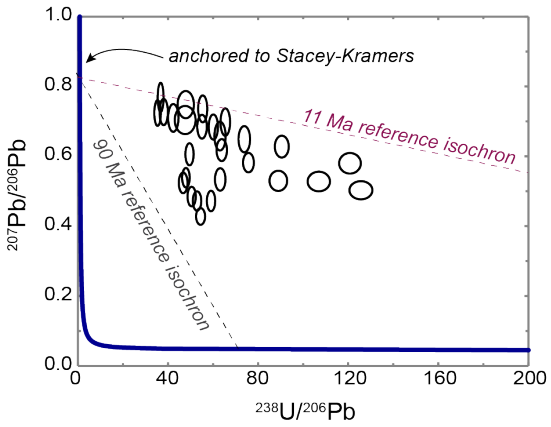
anchored to Stacey-Kramers
11 Ma reference isochron
90 Ma reference isochron
207Pb/206Pb
238U/206Pb

48A-0129-15; max misorient 3.5°

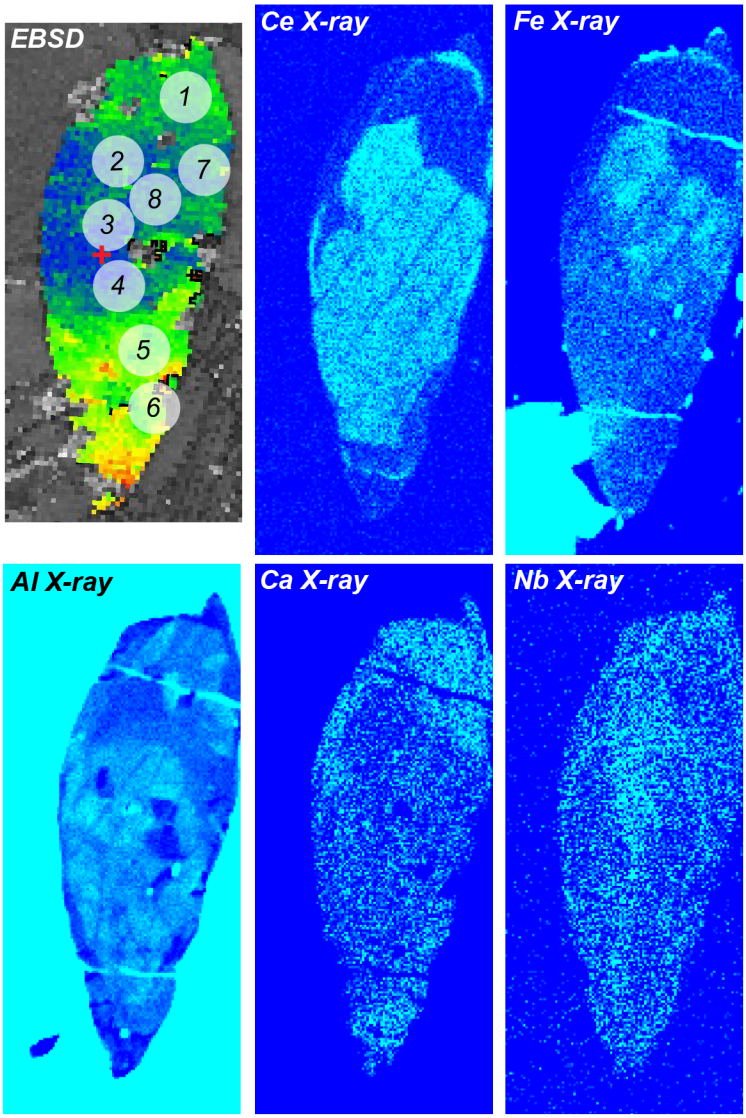

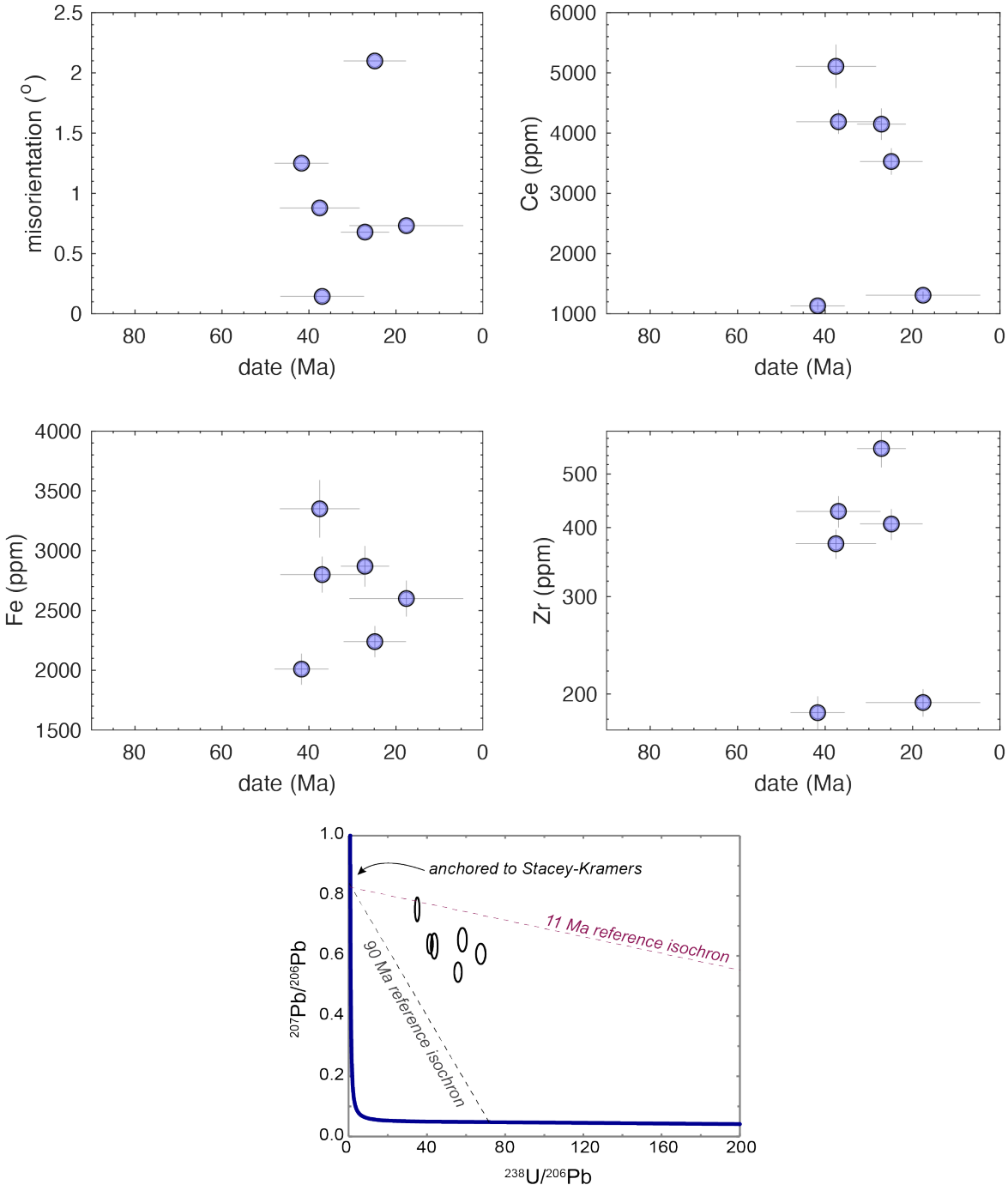
misorientation (°)
date (Ma)
Ce (ppm)
Fe (ppm)
Zr (ppm)
anchored to Stacey-Kramers
11 Ma reference isochron
90 Ma reference isochron
207Pb/206Pb
238U/206Pb

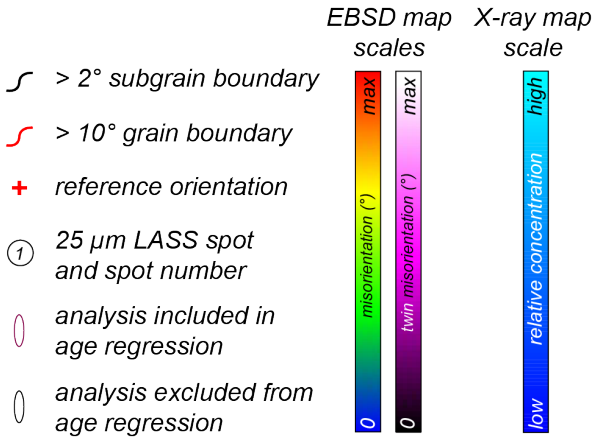

Figure S3. (following pages) EBSD misorientation maps, WDS X-ray maps, Tera–Wasserburg concordia diagrams, and spot locations for "zoned Miocene" grains from sample 48A. Legend for this figure is above and is not repeated for each grain. The 25 µm LASS spot serves as scale for each grain. Number at top of EBSD map is grain number for reference to Table S2. The maximum misorientation for each grain is listed at the top of the maps and is applicable to the host grain and the deformation twins.

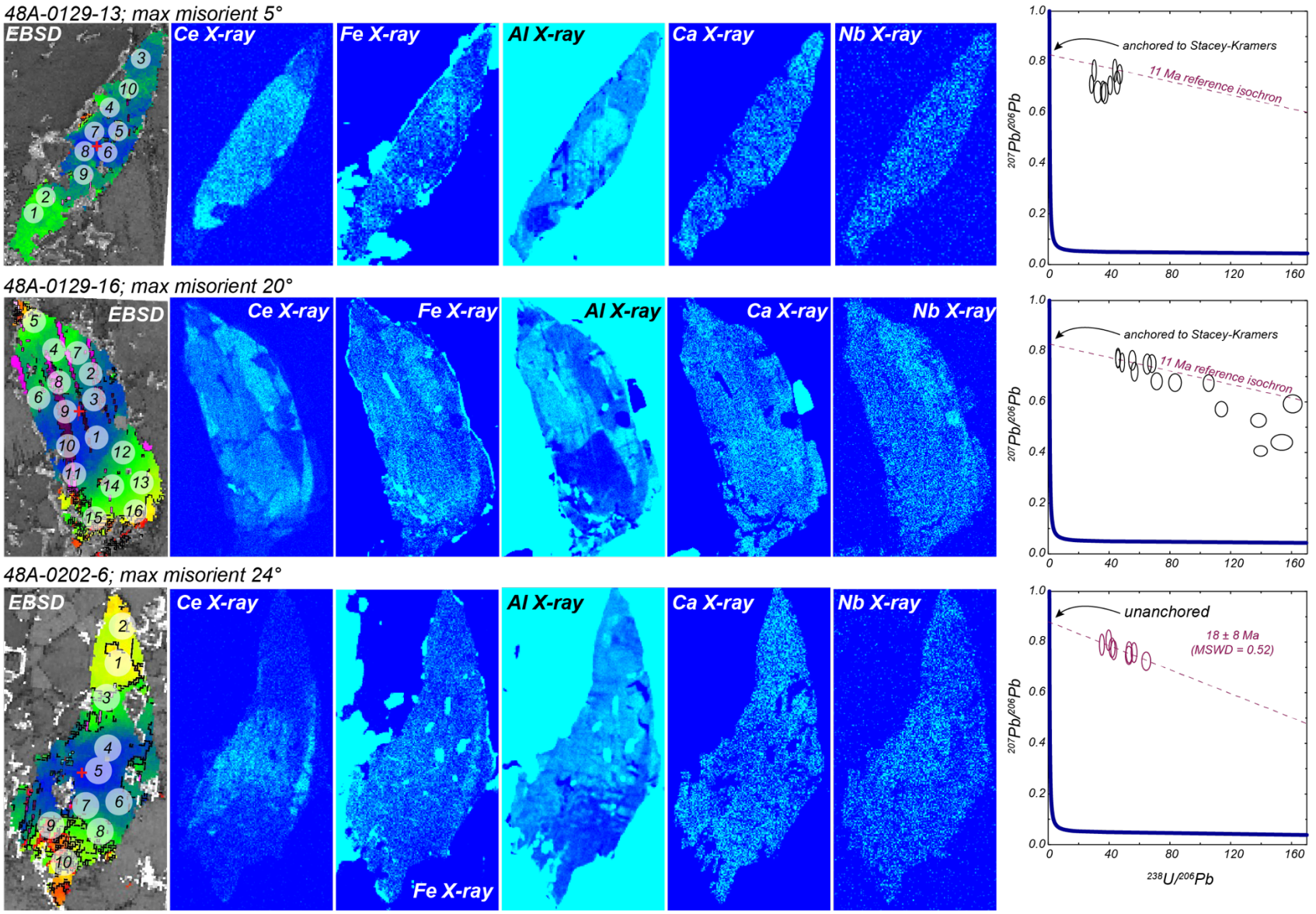
48A-0129-13; max misorient 5°
EBSD
Ce X-ray
Fe X-ray
Al X-ray
Ca X-ray
Nb X-ray
anchored to Stacey-Kramers
11 Ma reference isochron
48A-0129-16; max misorient 20°
EBSD
Ce X-ray
Fe X-ray
Al X-ray
Ca X-ray
Nb X-ray
anchored to Stacey-Kramers
11 Ma reference isochron
48A-0202-6; max misorient 24°
EBSD
Ce X-ray
Fe X-ray
Al X-ray
Ca X-ray
Nb X-ray
unanchored
18 ± 8 Ma
(MSWD = 0.52)
207Pb/206Pb
238U/206Pb

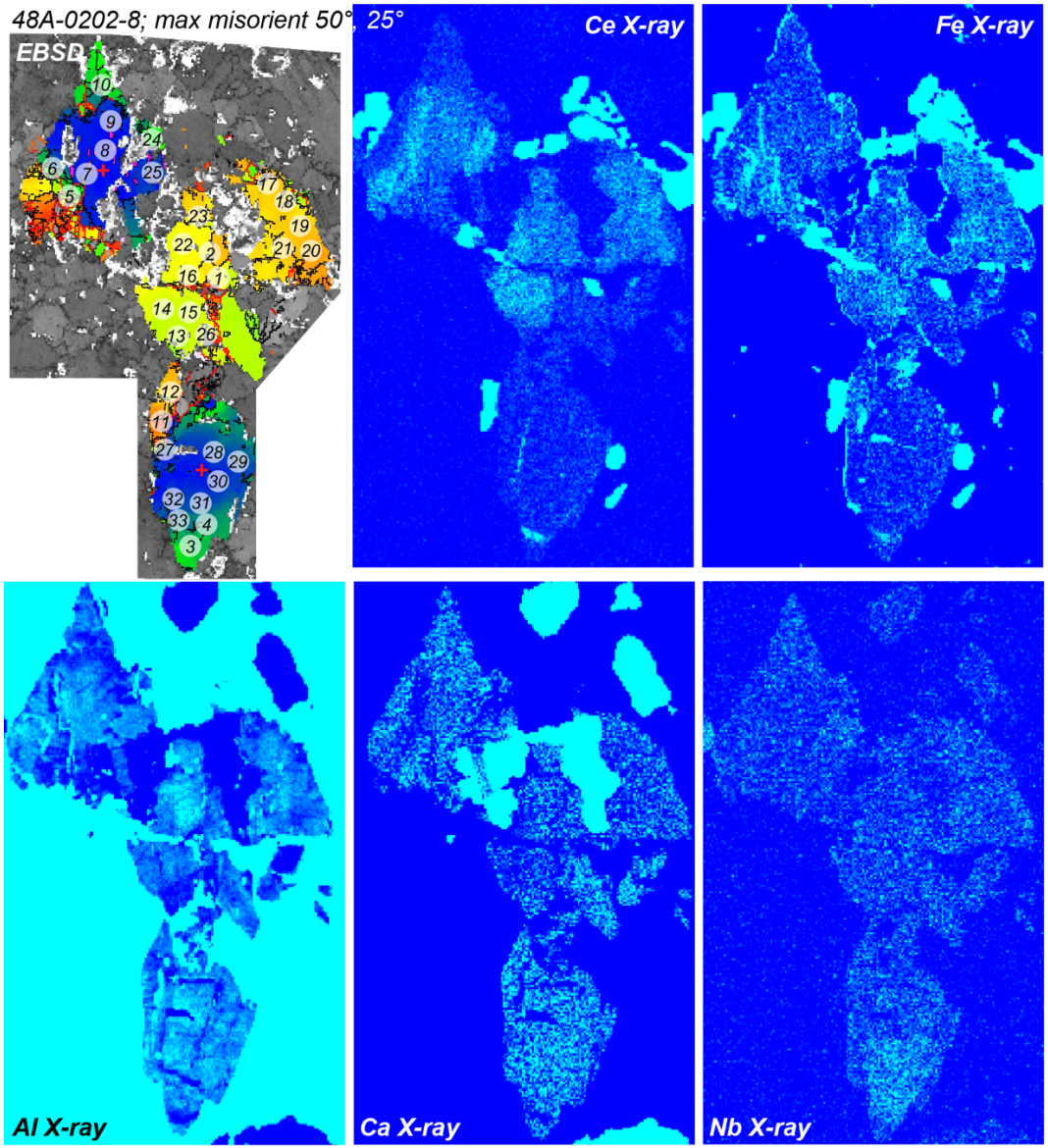
48A-0202-8; max misorient 50°, 25°
EBSD
Ce X-ray
Fe X-ray
Al X-ray
Ca X-ray
Nb X-ray

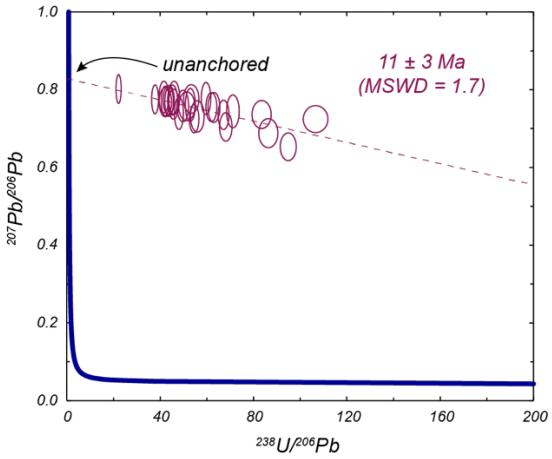
unanchored
11 ± 3 Ma
(MSWD = 1.7)
$^{207}Pb/^{206}Pb$
$^{238}U/^{206}Pb$
1.0
0.8
0.6
0.4
0.2
0.0
0
40
80
120
160
200

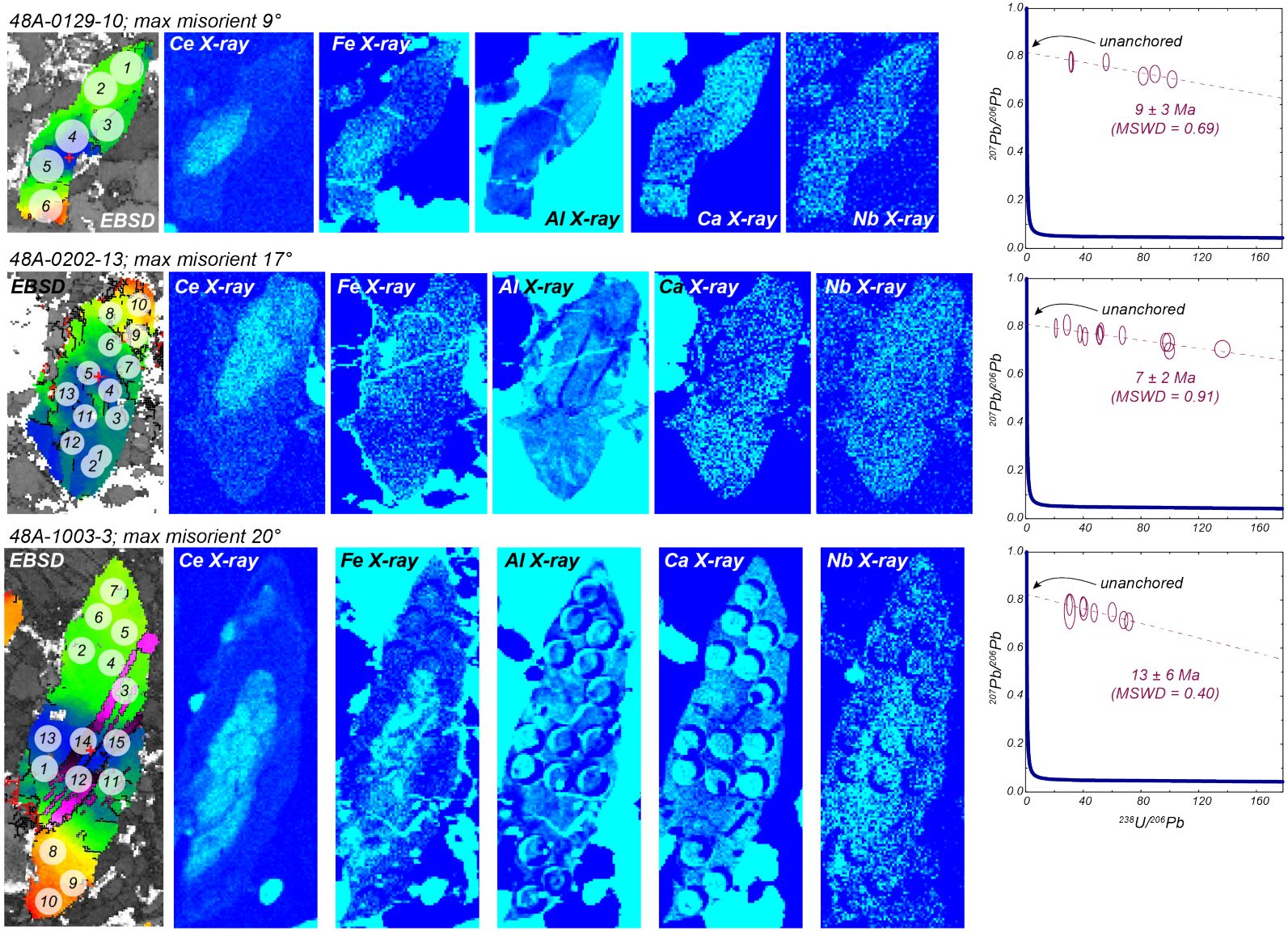
48A-0129-10; max misorient 9°
EBSD
Ce X-ray
Fe X-ray
Al X-ray
Ca X-ray
Nb X-ray
unanchored
9 ± 3 Ma
(MSWD = 0.69)
48A-0202-13; max misorient 17°
EBSD
Ce X-ray
Fe X-ray
Al X-ray
Ca X-ray
Nb X-ray
unanchored
7 ± 2 Ma
(MSWD = 0.91)
48A-1003-3; max misorient 20°
EBSD
Ce X-ray
Fe X-ray
Al X-ray
Ca X-ray
Nb X-ray
unanchored
13 ± 6 Ma
(MSWD = 0.40)
207Pb/206Pb
238U/206Pb

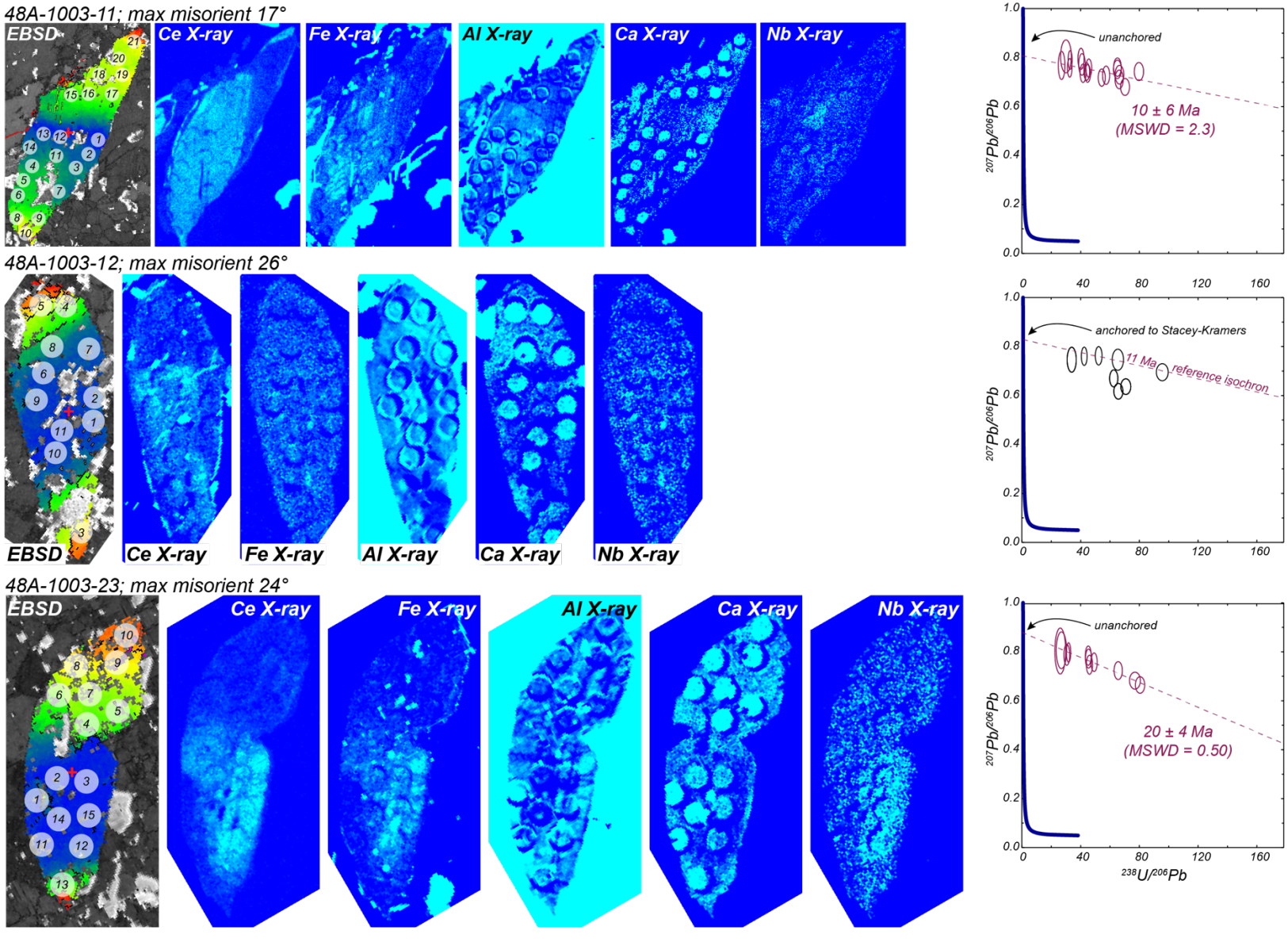
48A-1003-11; max misorient 17°
EBSD
Ce X-ray
Fe X-ray
Al X-ray
Ca X-ray
Nb X-ray
unanchored
10 ± 6 Ma
(MSWD = 2.3)
48A-1003-12; max misorient 26°
EBSD
Ce X-ray
Fe X-ray
Al X-ray
Ca X-ray
Nb X-ray
anchored to Stacey-Kramers
11 Ma reference isochron
48A-1003-23; max misorient 24°
EBSD
Ce X-ray
Fe X-ray
Al X-ray
Ca X-ray
Nb X-ray
unanchored
20 ± 4 Ma
(MSWD = 0.50)
207Pb/206Pb
238U/206Pb

48A-1003-13; max misorient 33°

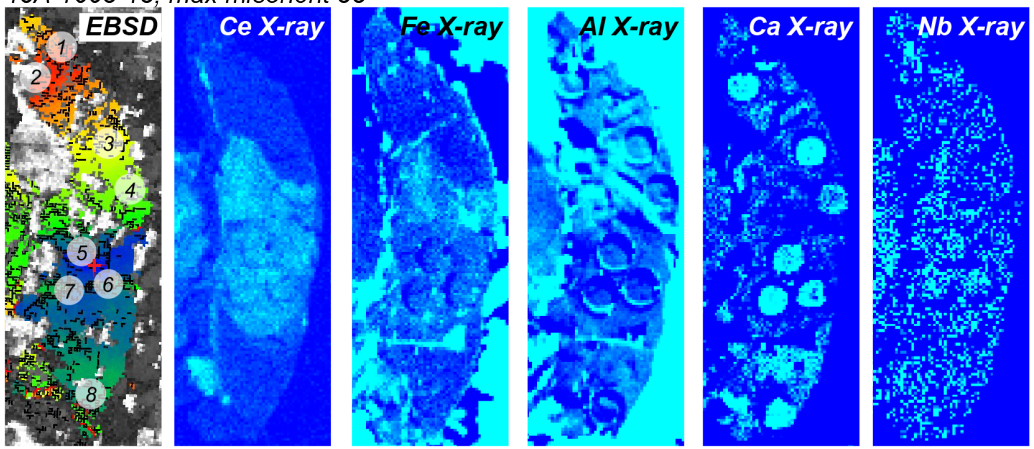

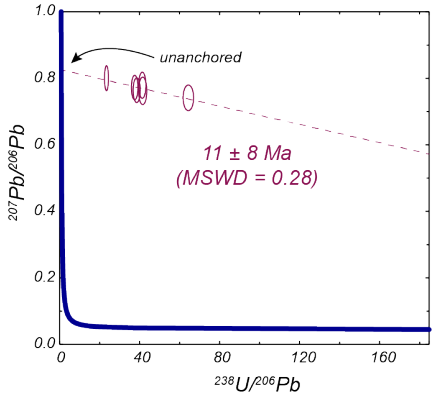

48A-1003-22; max misorient 80°

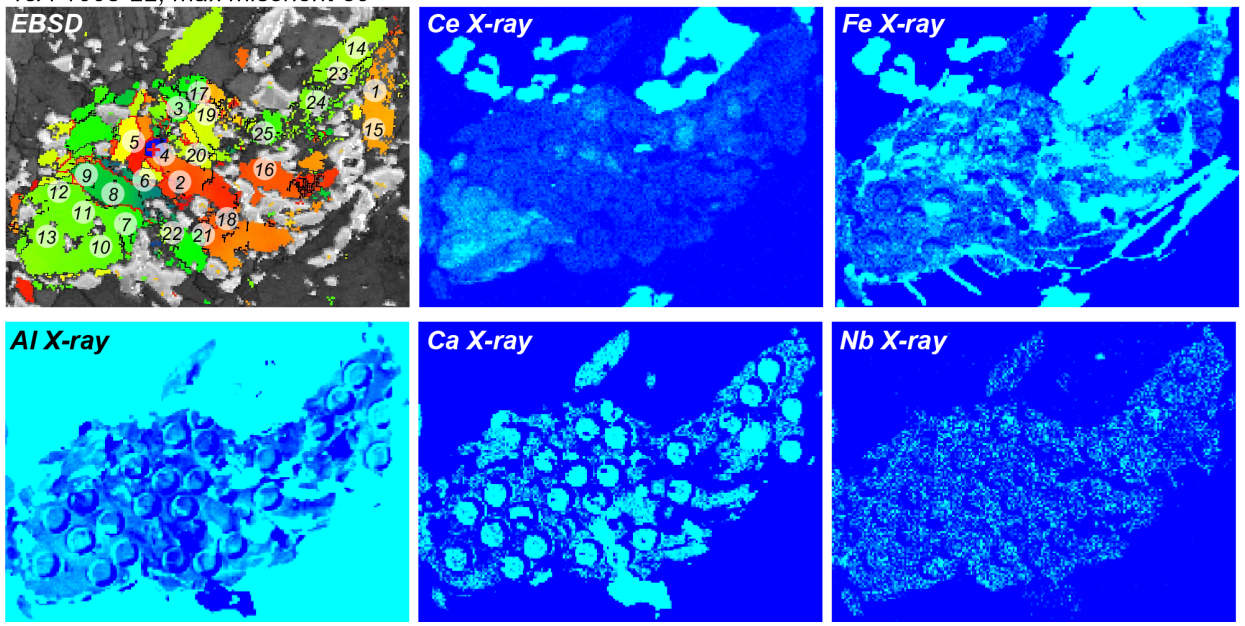

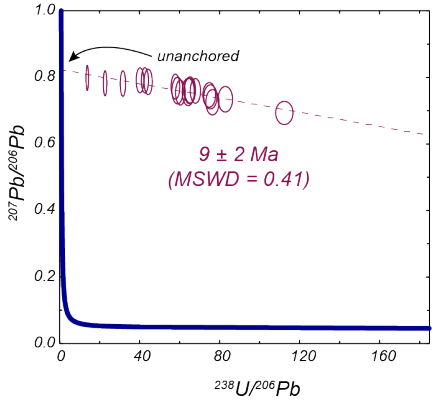

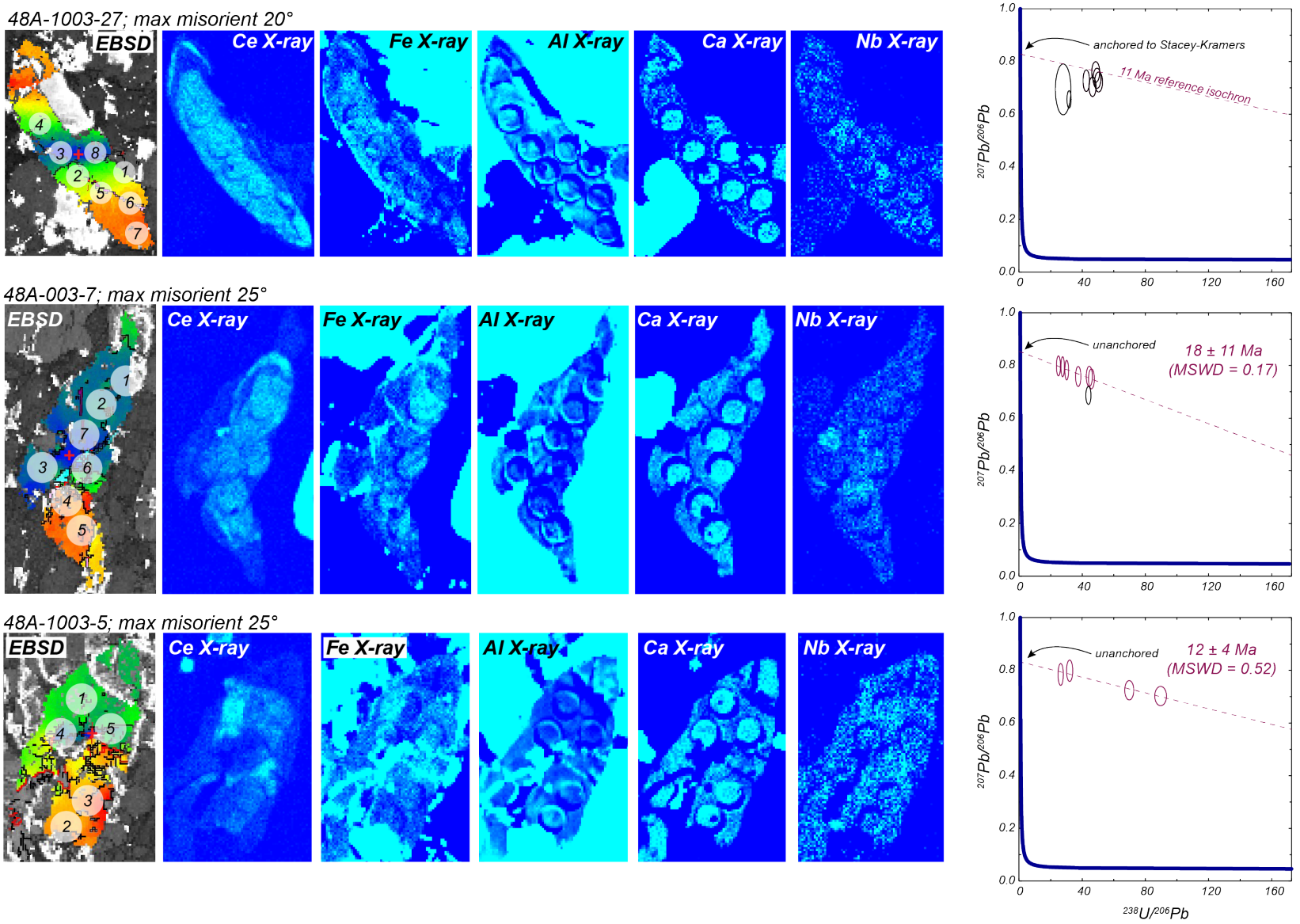
48A-1003-27; max misorient 20°
EBSD
Ce X-ray
Fe X-ray
Al X-ray
Ca X-ray
Nb X-ray
anchored to Stacey-Kramers
11 Ma reference isochron
48A-003-7; max misorient 25°
unanchored
18 ± 11 Ma
(MSWD = 0.17)
48A-1003-5; max misorient 25°
12 ± 4 Ma
(MSWD = 0.52)
207Pb/206Pb
238U/206Pb

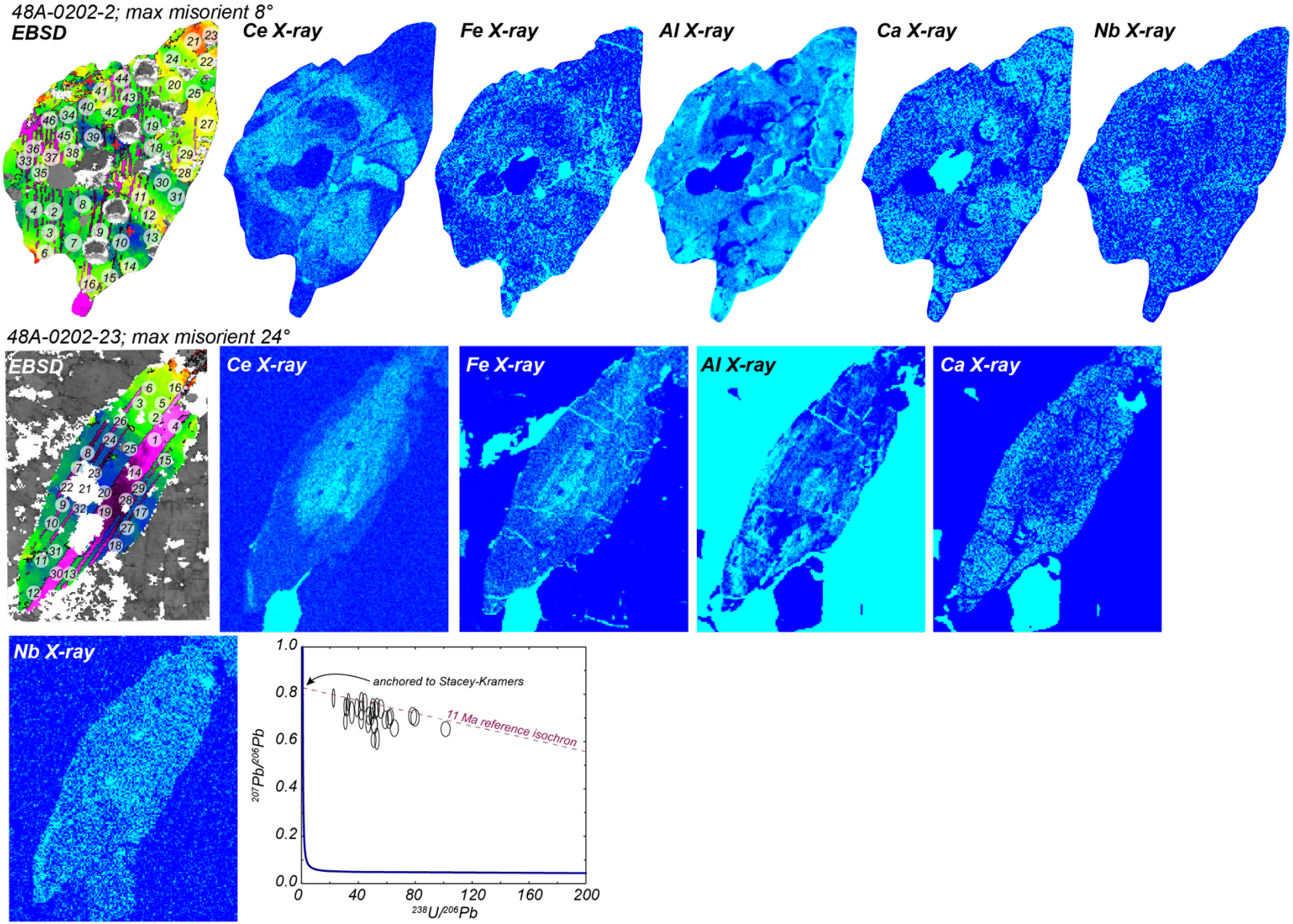
48A-0202-2; max misorient 8°
EBSD
Ce X-ray
Fe X-ray
Al X-ray
Ca X-ray
Nb X-ray
48A-0202-23; max misorient 24°
EBSD
Ce X-ray
Fe X-ray
Al X-ray
Ca X-ray
Nb X-ray
anchored to Stacey-Kramers
11 Ma reference isochron
207Pb/206Pb
238U/206Pb
1.0
0.8
0.6
0.4
0.2
0.0
0
40
80
120
160
200

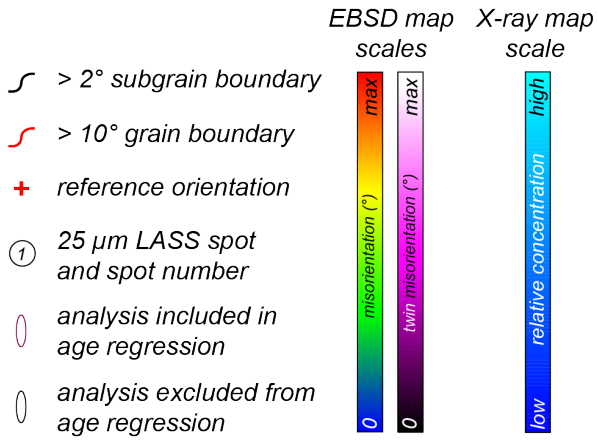

Figure S4. (following pages) EBSD misorientation maps, WDS X-ray maps, Tera–Wasserburg concordia diagrams, and spot locations for "homogeneous Miocene" grains from sample 48A. Legend for this figure is above and is not repeated for each grain. The 25 µm LASS spot serves as scale for each grain. Number at top of EBSD map is grain number for reference to Table S2. The maximum misorientation for each grain is listed at the top of the maps and is applicable to the host grain and the deformation twins.

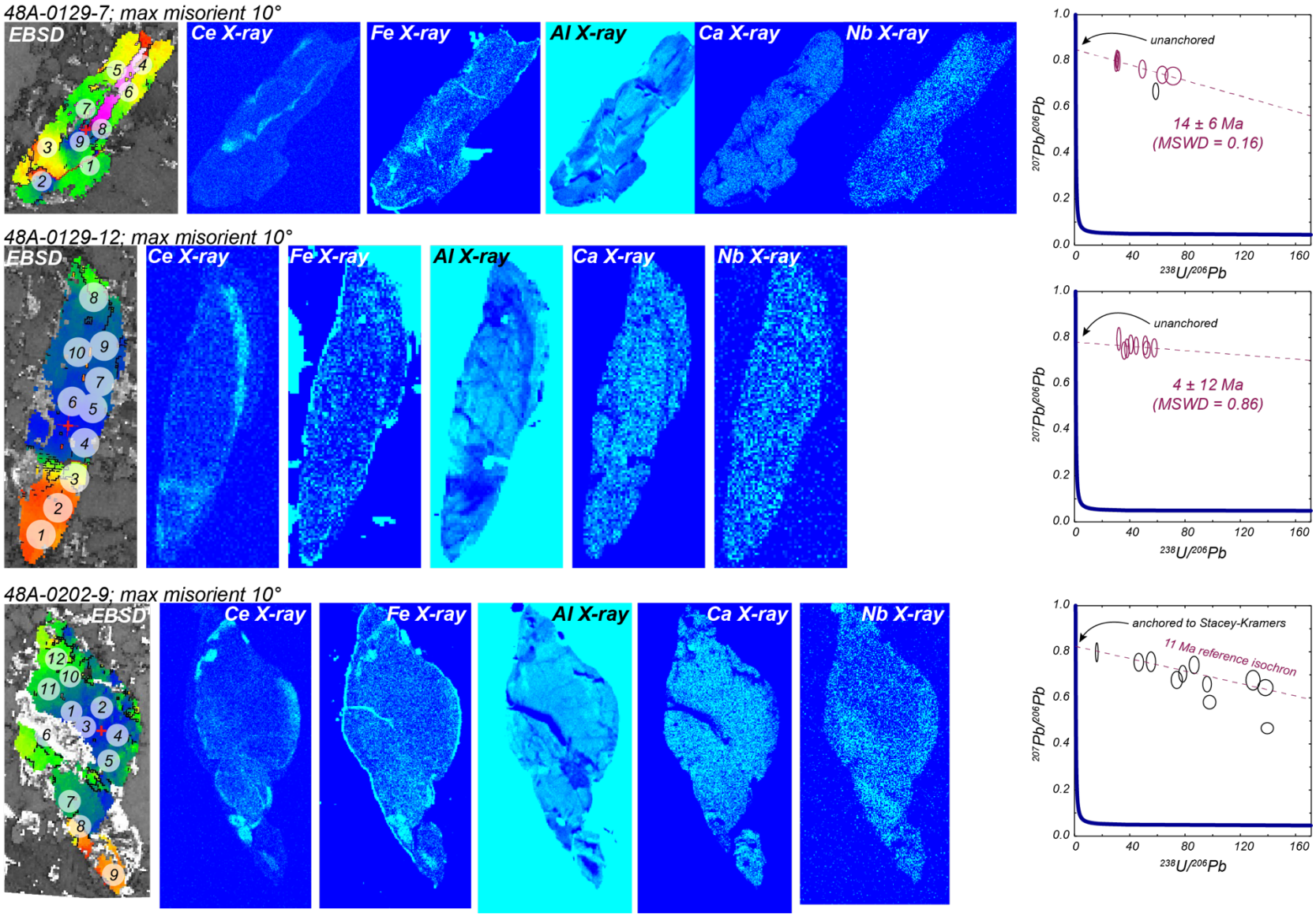
48A-0129-7; max misorient 10°
EBSD
Ce X-ray
Fe X-ray
Al X-ray
Ca X-ray
Nb X-ray
48A-0129-12; max misorient 10°
EBSD
Ce X-ray
Fe X-ray
Al X-ray
Ca X-ray
Nb X-ray
48A-0202-9; max misorient 10°
EBSD
Ce X-ray
Fe X-ray
Al X-ray
Ca X-ray
Nb X-ray
unanchored
14 ± 6 Ma
(MSWD = 0.16)
unanchored
4 ± 12 Ma
(MSWD = 0.86)
anchored to Stacey-Kramers
11 Ma reference isochron
207Pb/206Pb
238U/206Pb

48A-0202-12; max misorient 10°

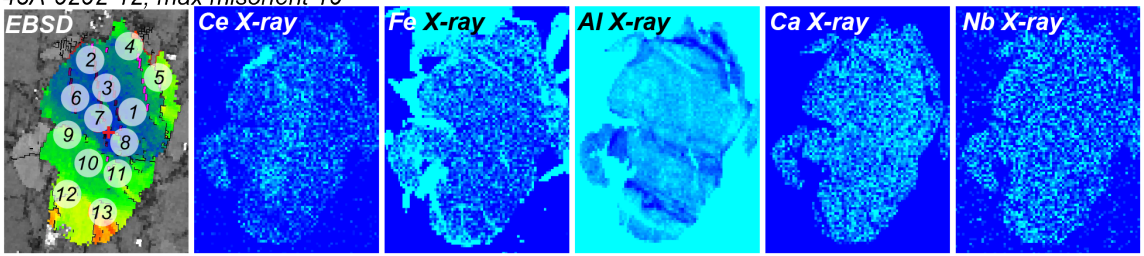

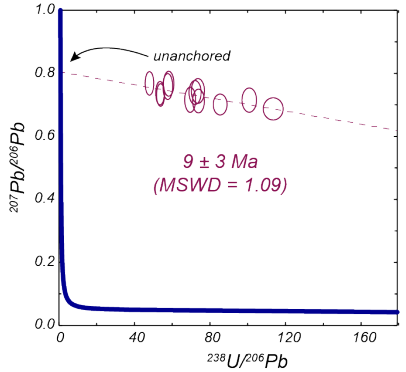

48A-1003-8; max misorient 40°

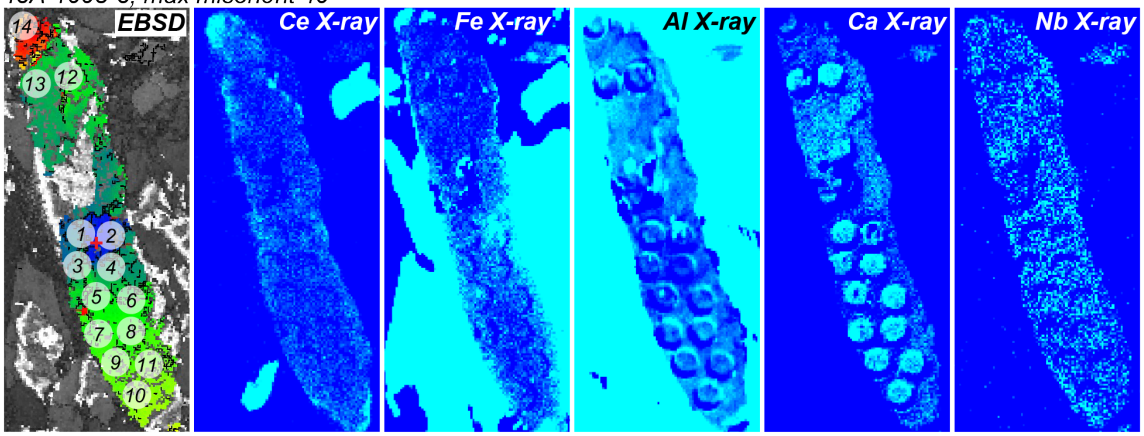

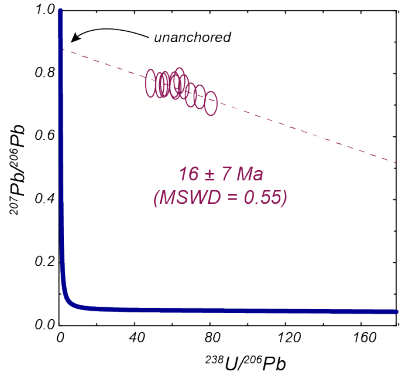

48A-1003-21; max misorient 13°

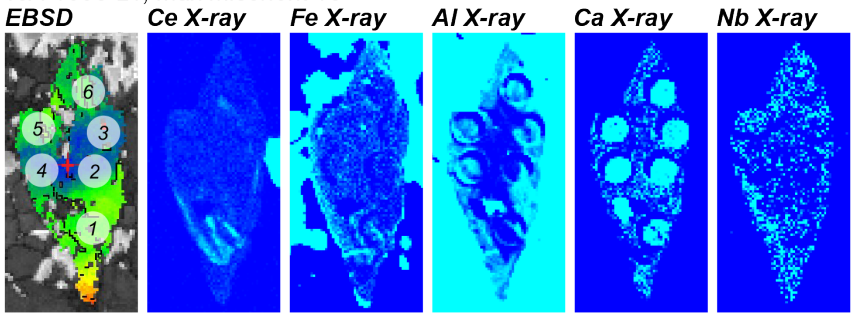

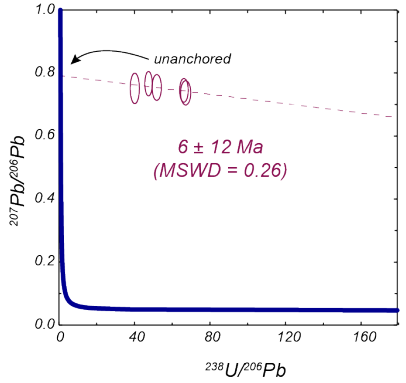

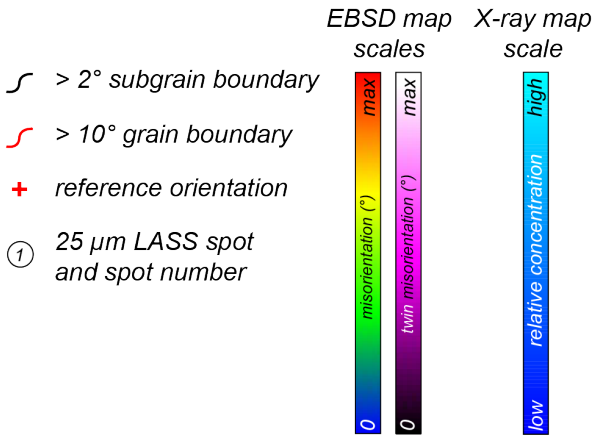

Figure S5. (following pages) EBSD misorientation maps, WDS X-ray maps, spot locations, date vs. (misorientation, Ce, Fe, Zr), and Tera–Wasserburg concordia diagrams for grains from sample 45C where dates and composition are correlated. Legend for this figure is above and is relevant for each grain. The 25 µm LASS spot serves as scale for each grain. Number at top of EBSD and WDS maps is grain number for reference to Table S2. The maximum misorientation for each grain is listed at the top and is applicable to the host grain and the deformation twins. The plots on the pages that follow the maps are those for the preceding grain.

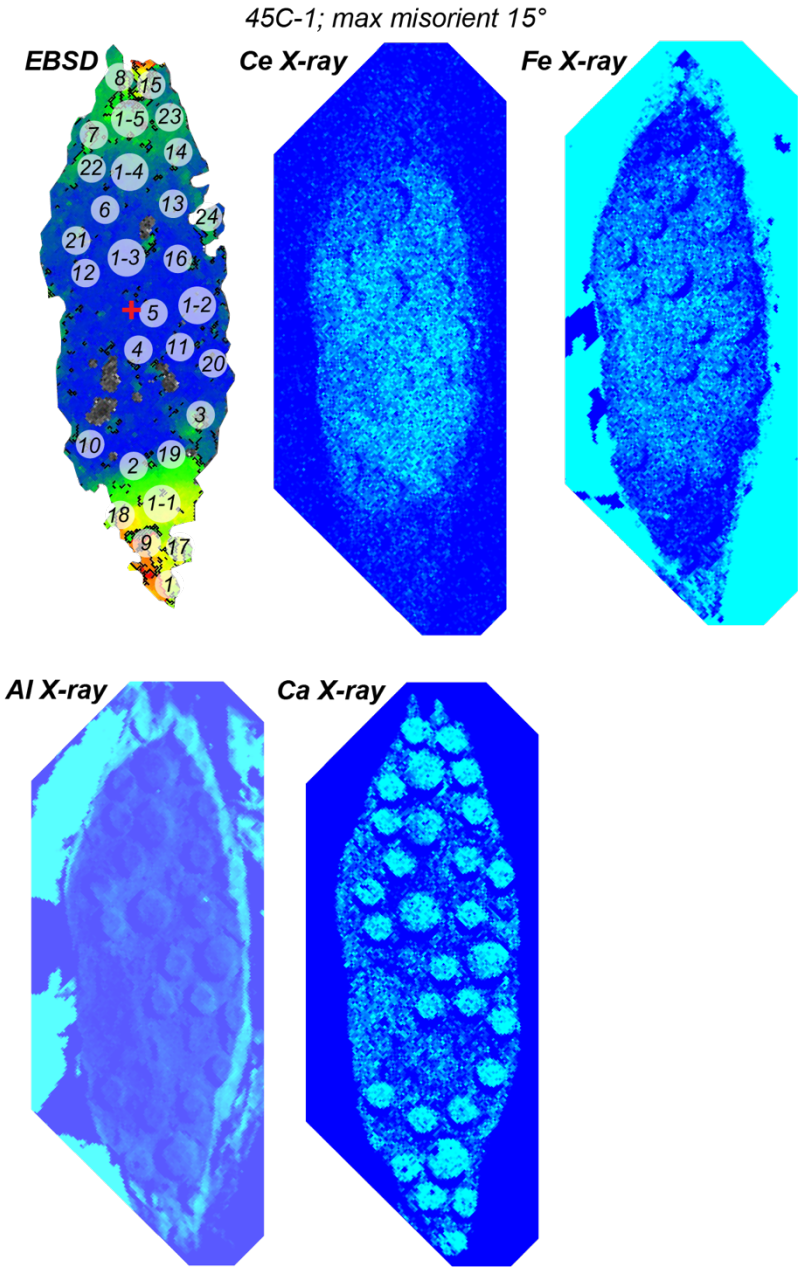
45C-1; max misorient 15°
EBSD
Ce X-ray
Fe X-ray
Al X-ray
Ca X-ray
8
15
1-5
23
7
14
22
1-4
6
13
24
21
1-3
16
12
5
1-2
4
11
20
3
10
19
2
1-1
18
9
17
1

45C-0615-33; max misorient 11°

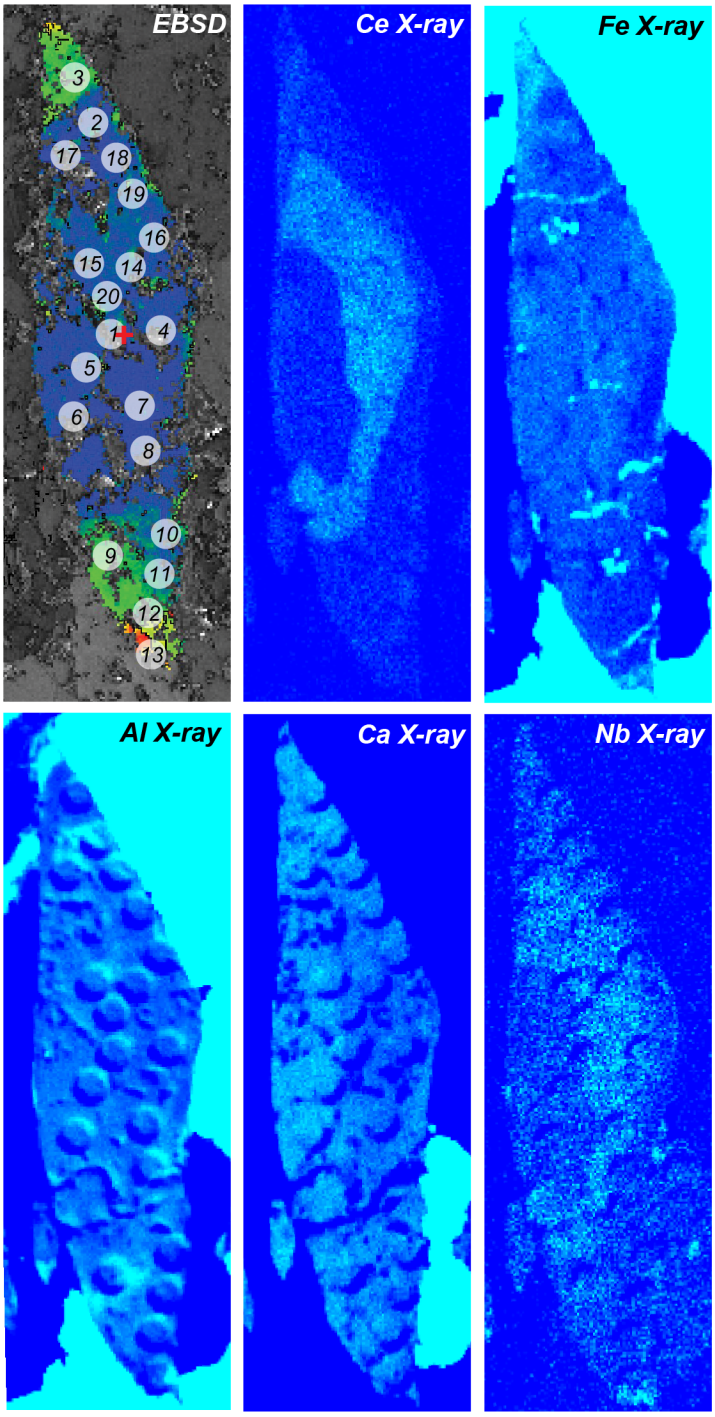

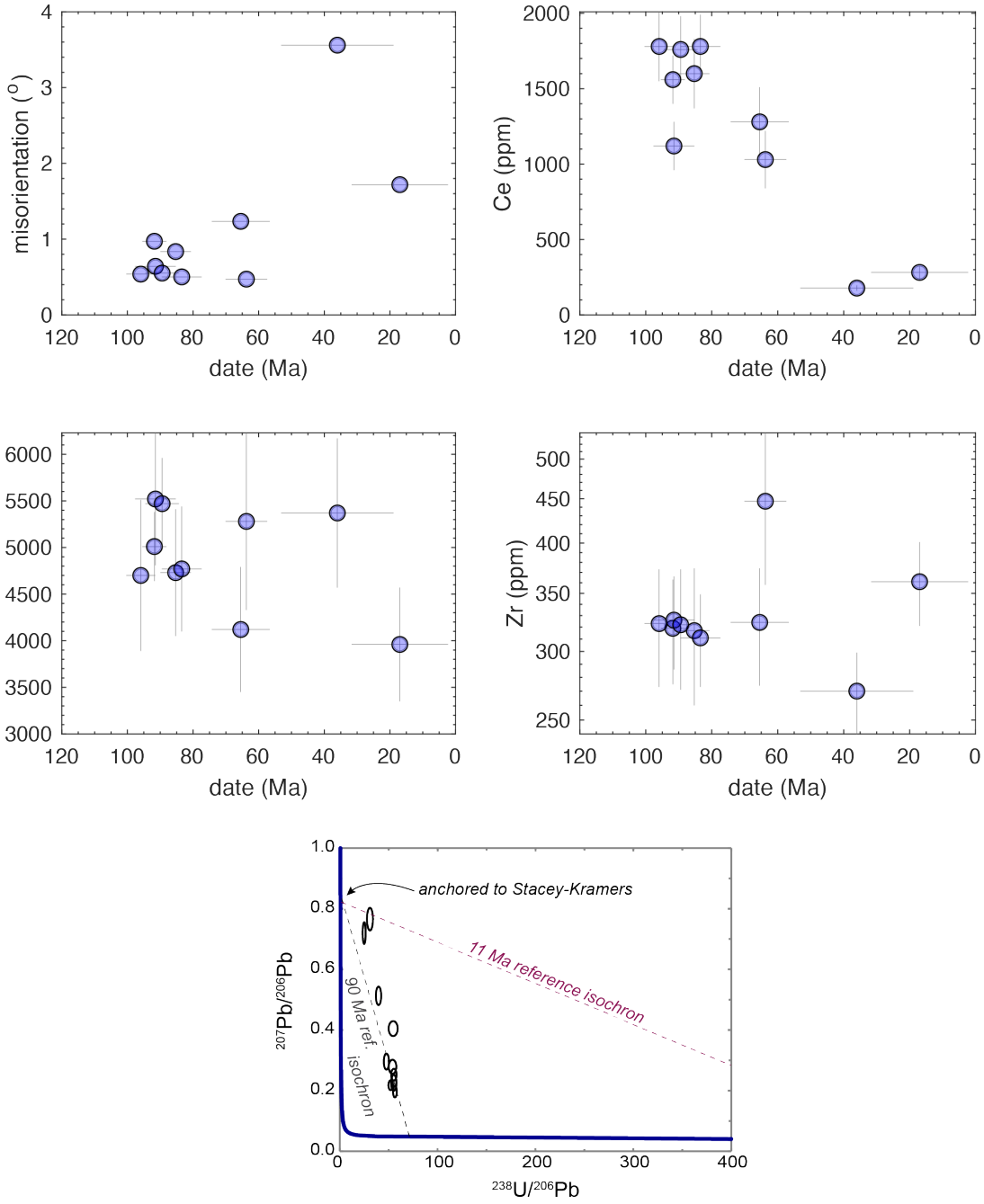
misorientation (°)
date (Ma)
Ce (ppm)
Fe (ppm)
Zr (ppm)
anchored to Stacey-Kramers
11 Ma reference isochron
90 Ma ref. isochron
$^{207}Pb/^{206}Pb$
$^{238}U/^{206}Pb$

45C-0615-38; max misorient 14°

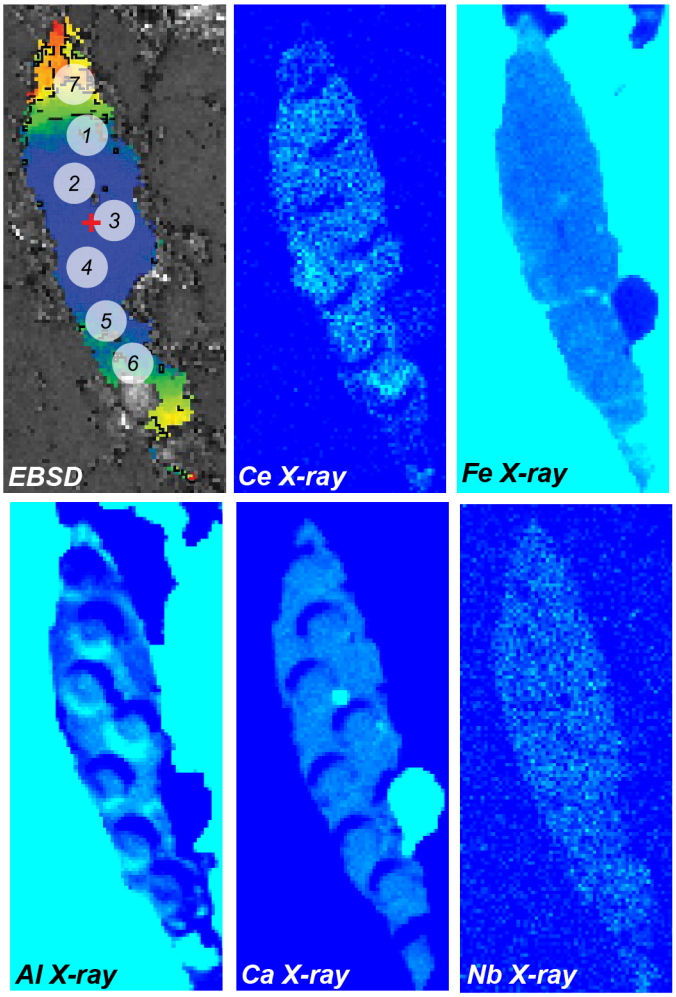

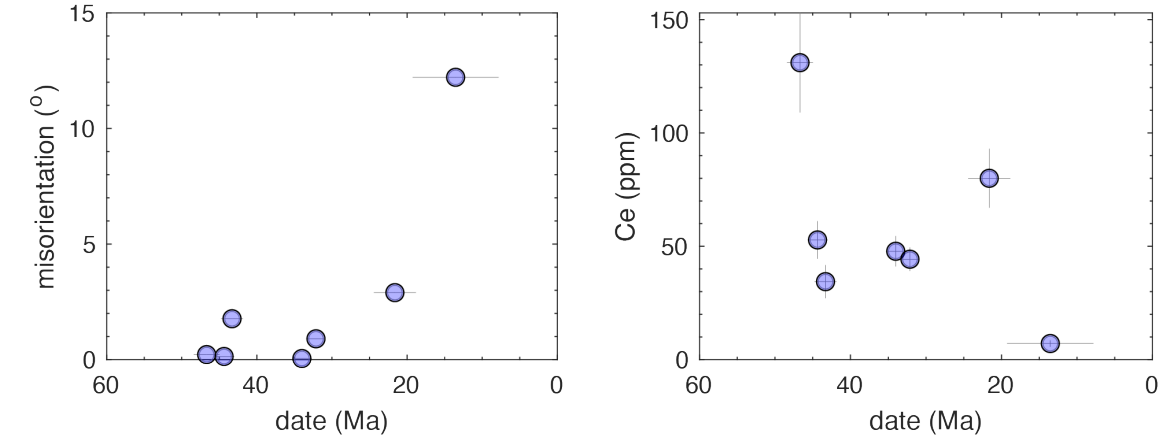
misorientation (°)
15
10
5
0
60
40
20
0
date (Ma)

Ce (ppm)
150
100
50
0
60
40
20
0
date (Ma)

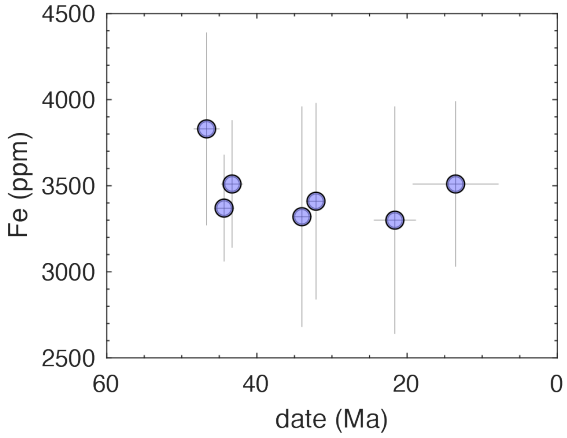
Fe (ppm)
4500
4000
3500
3000
2500
60
40
20
0
date (Ma)

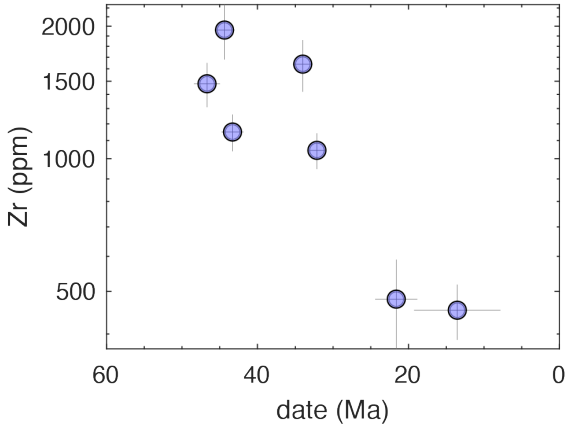
Zr (ppm)
2000
1500
1000
500
60
40
20
0
date (Ma)

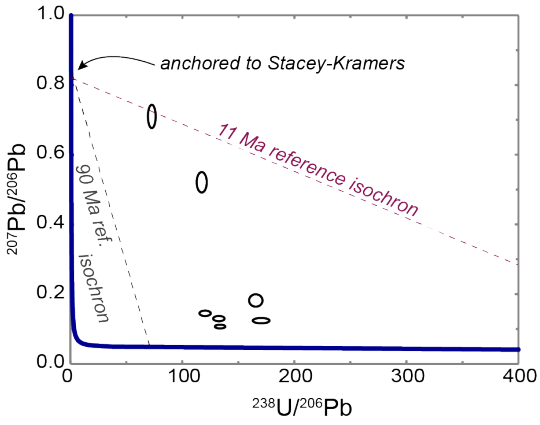
anchored to Stacey-Kramers
11 Ma reference isochron
90 Ma ref. isochron
207Pb/206Pb
1.0
0.8
0.6
0.4
0.2
0.0
0
100
200
300
400
238U/206Pb

45C-0615-45; max misorient 17°

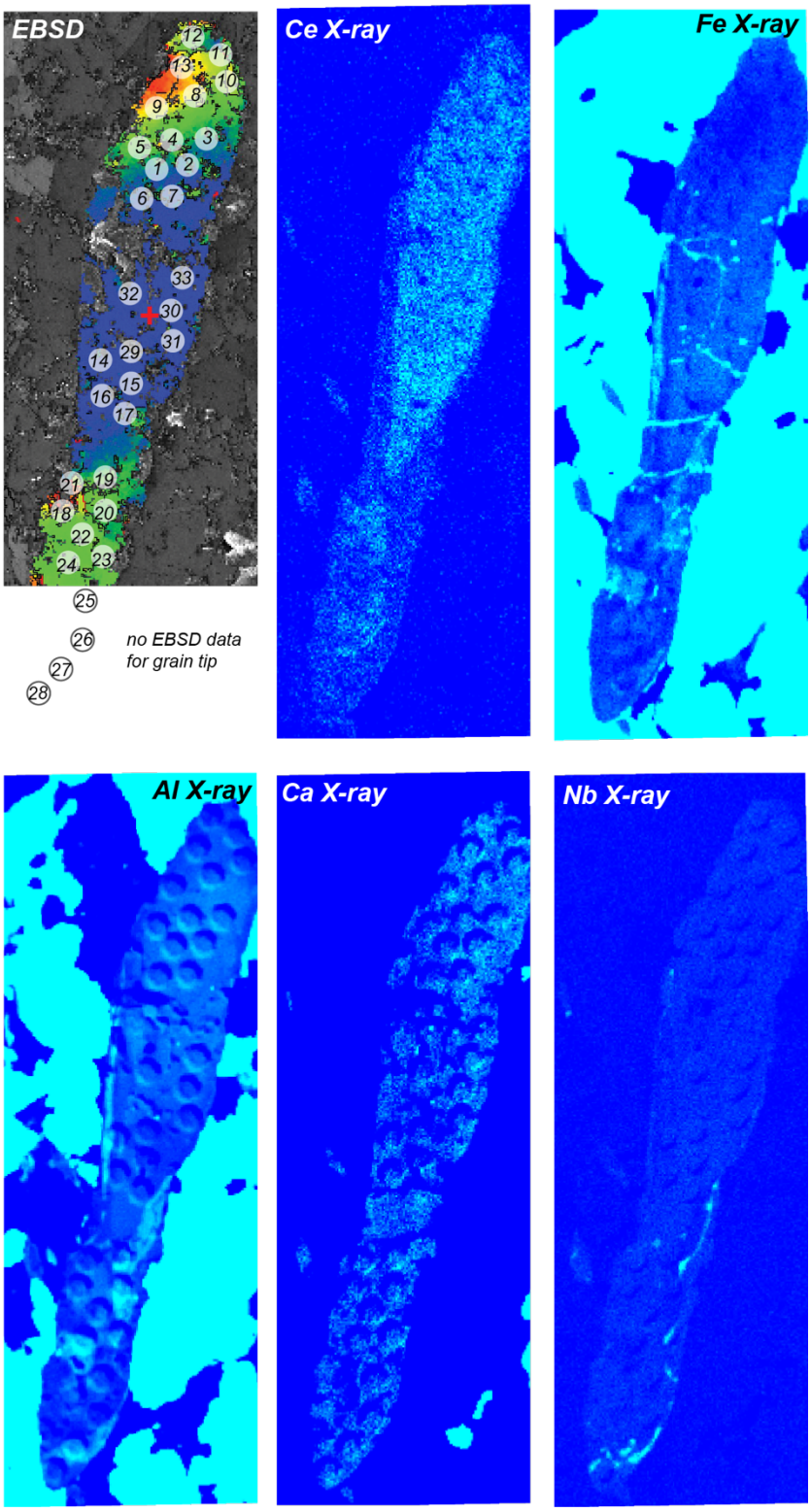

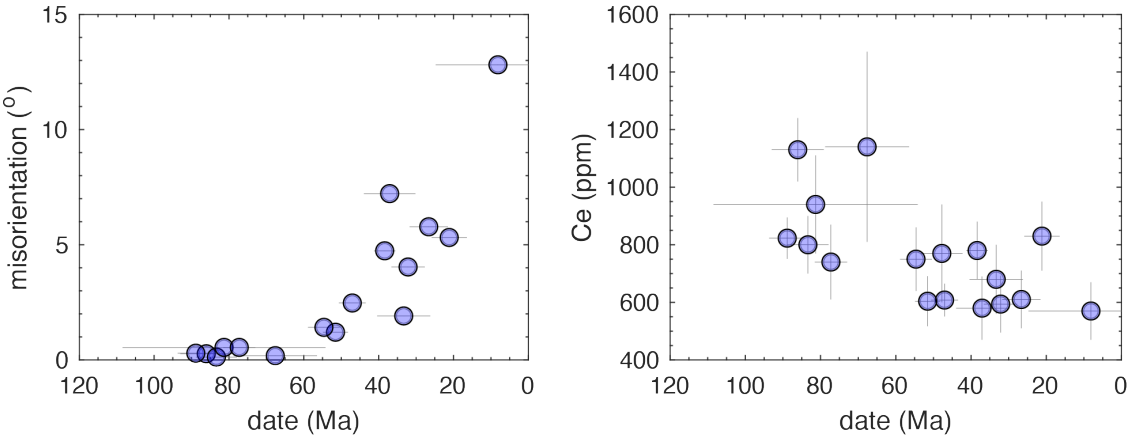
misorientation (°)
date (Ma)
Ce (ppm)
date (Ma)

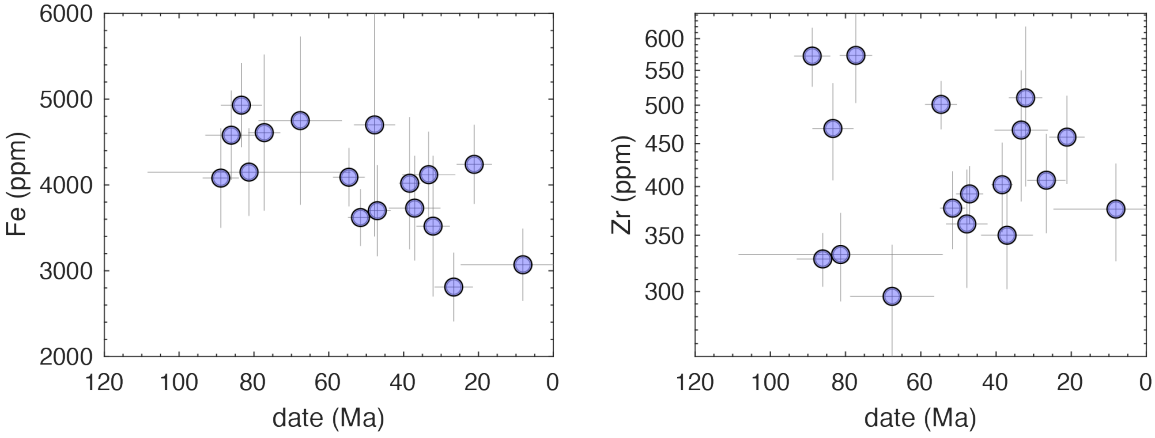
Fe (ppm)
date (Ma)
Zr (ppm)
date (Ma)

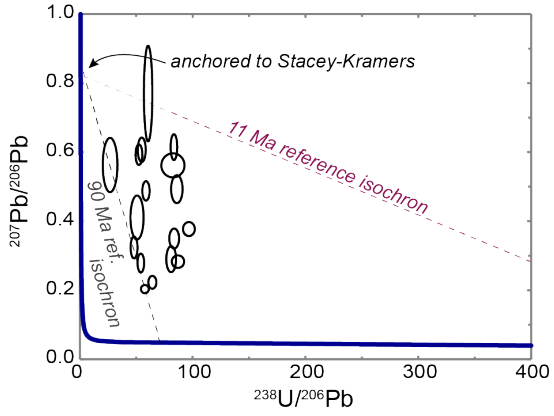
anchored to Stacey-Kramers
11 Ma reference isochron
90 Ma ref. isochron
207Pb/206Pb
238U/206Pb

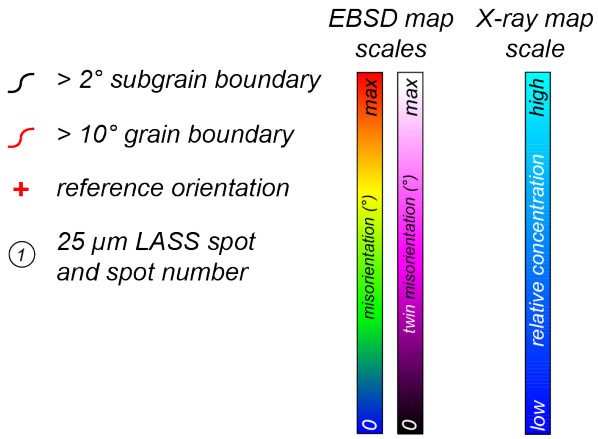

Figure S6. (following pages) EBSD misorientation maps, WDS X-ray maps, spot locations, date vs. (misorientation, Ce, Fe, Zr), and Tera–Wasserburg concordia diagrams for grains from sample 45C where dates and composition are not correlated. Legend for this figure is above and is relevant for each grain. The 25 µm LASS spot serves as scale for each grain. Number at top of EBSD and WDS maps is grain number for reference to Table S2. The maximum misorientation for each grain is listed at the top and is applicable to the host grain and the deformation twins. The plots on the pages that follow the maps are those for the preceding grain.

45C-0615-20; max misorient 15°

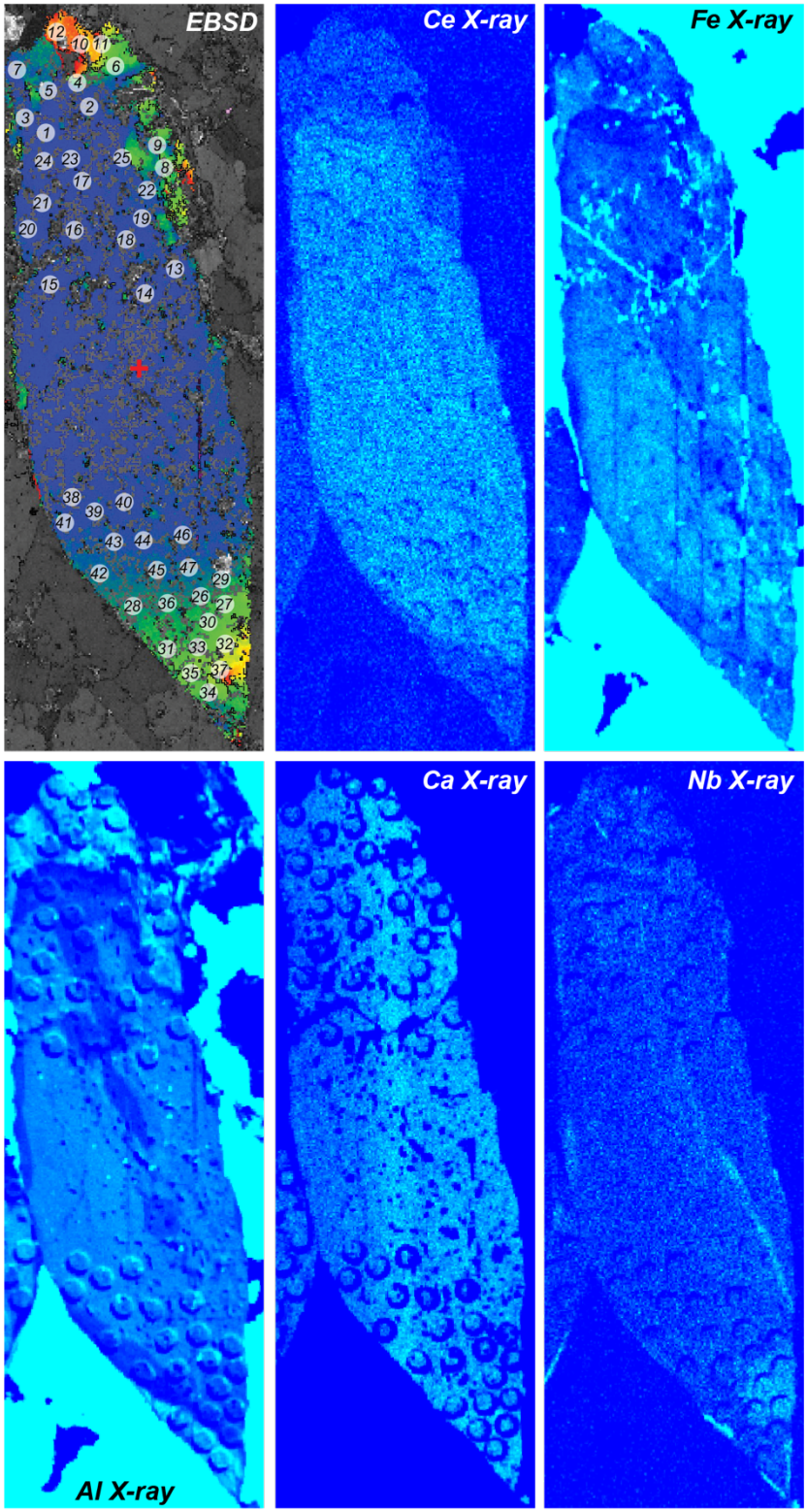

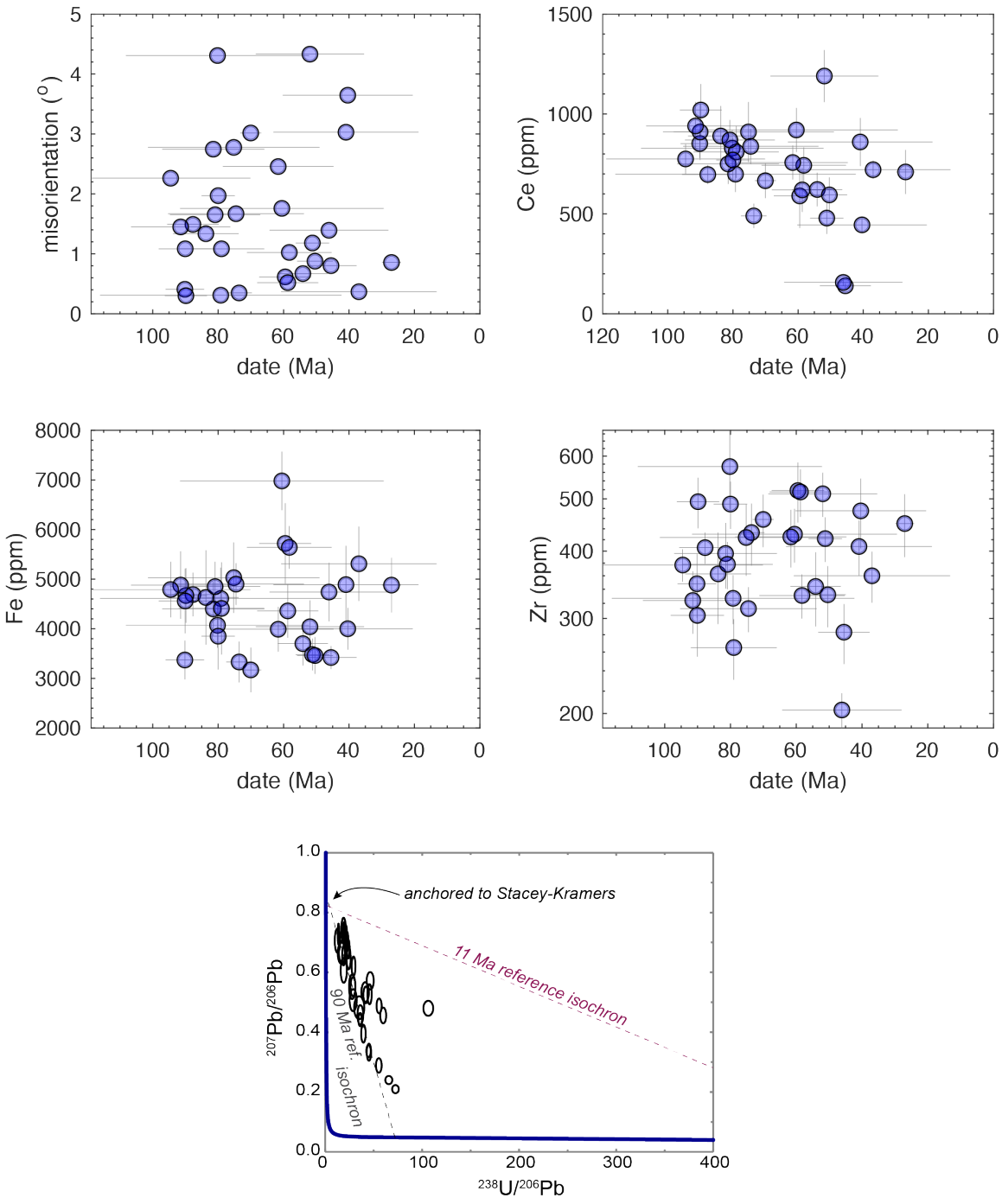
misorientation (°)
date (Ma)
Ce (ppm)
Fe (ppm)
Zr (ppm)
anchored to Stacey-Kramers
11 Ma reference isochron
90 Ma ref. isochron
207Pb/206Pb
238U/206Pb

45C-0615-24; max misorient 25°

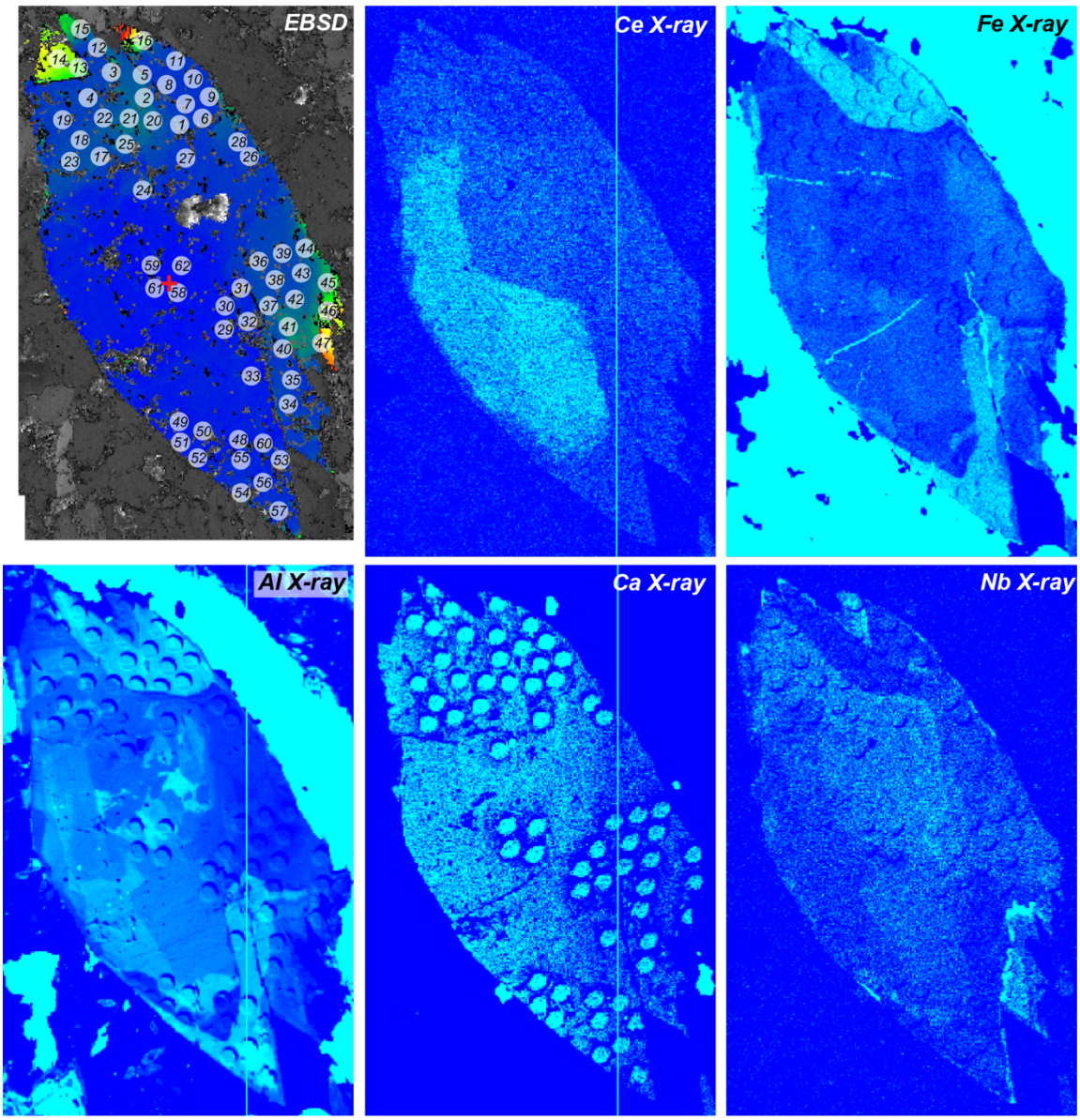

45C-0615-29; max misorient 10°

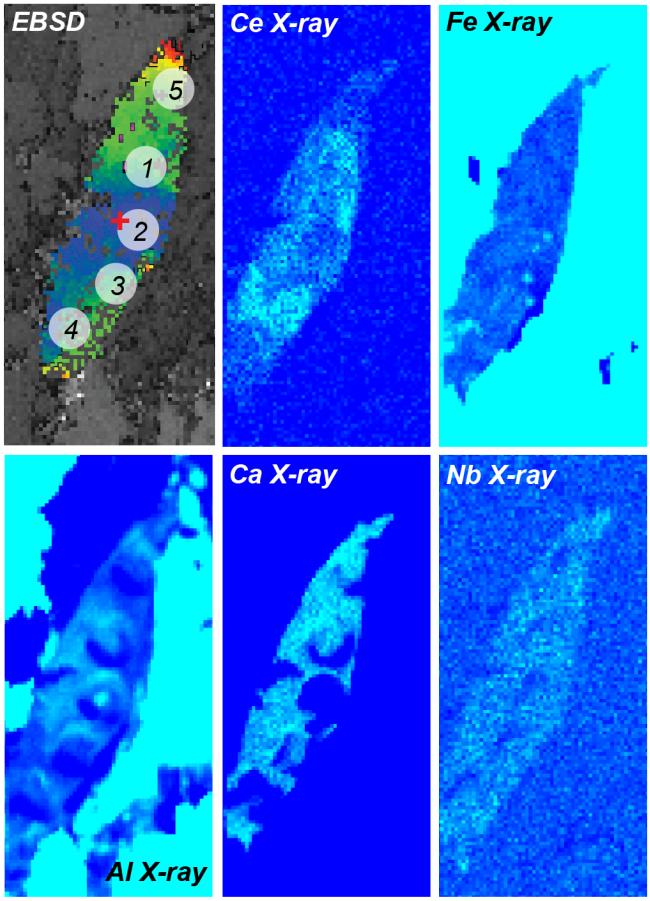

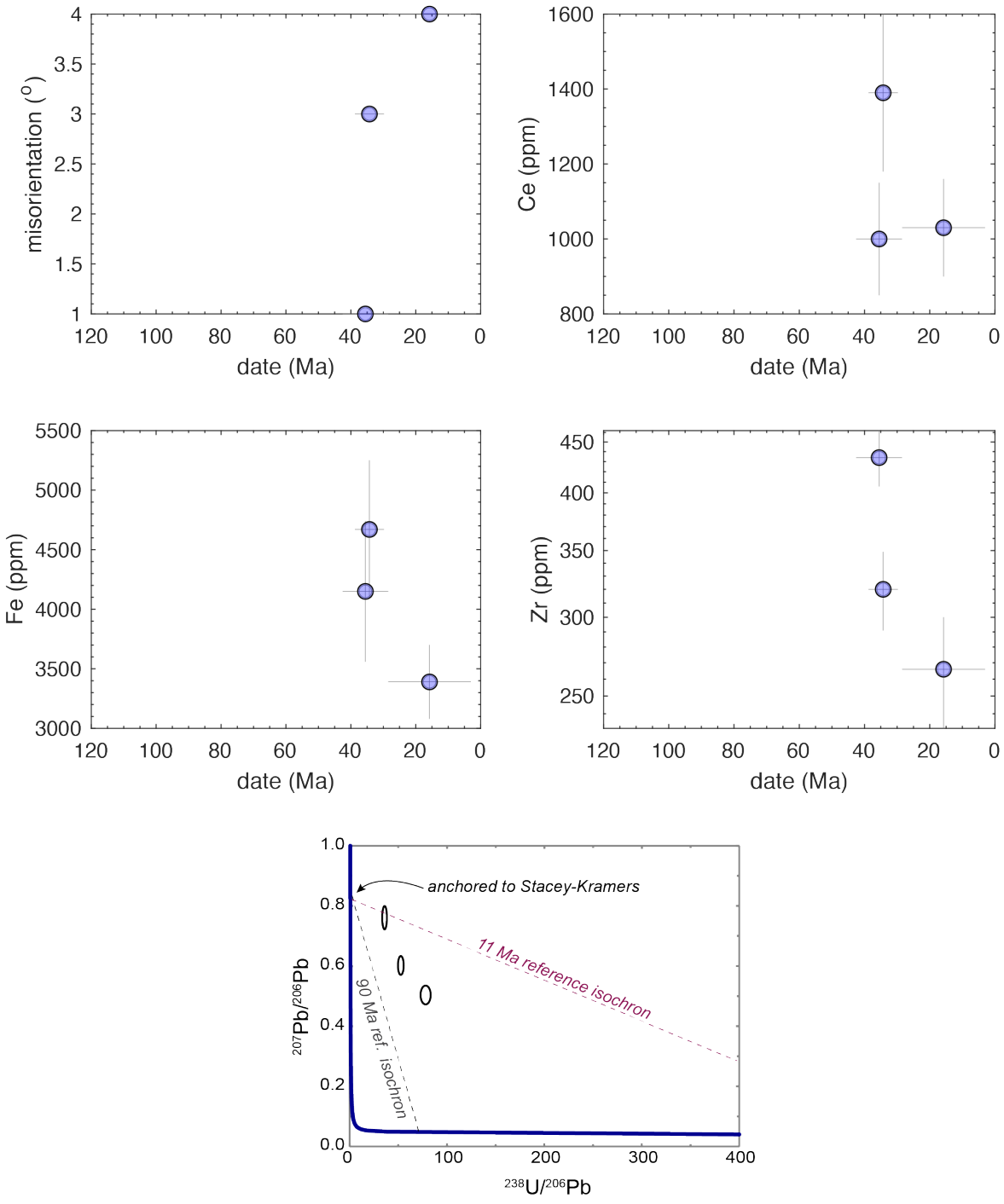
misorientation (°)
date (Ma)
Ce (ppm)
Fe (ppm)
Zr (ppm)
anchored to Stacey-Kramers
11 Ma reference isochron
90 Ma ref. isochron
207Pb/206Pb
238U/206Pb

45C-0615-31; max misorient 10°

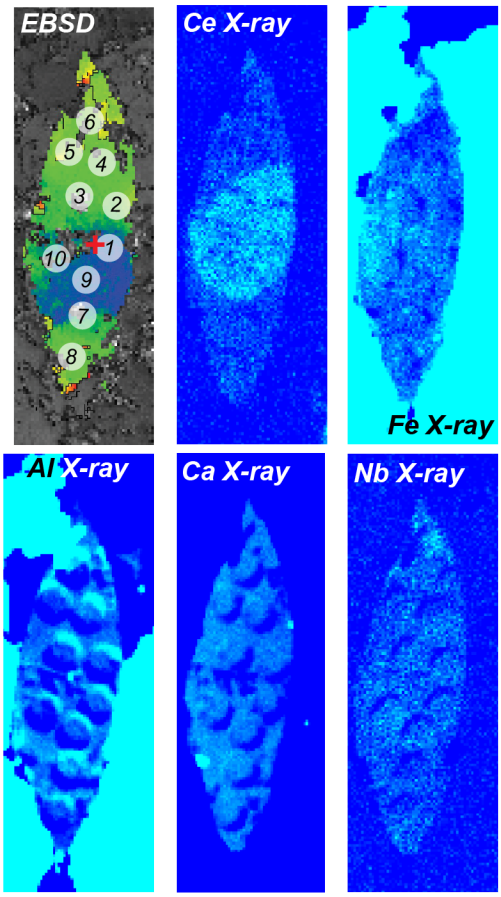

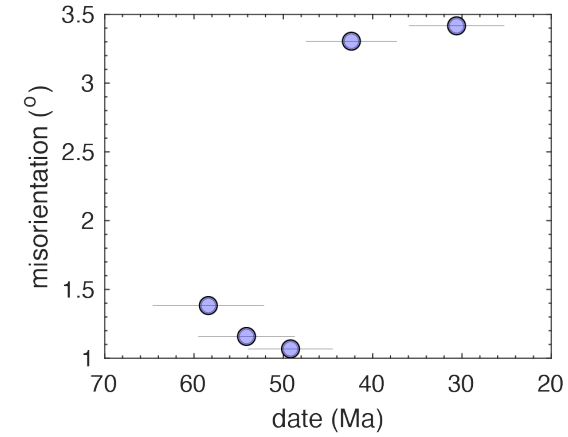
misorientation (°)
3.5
3
2.5
2
1.5
1
70
60
50
40
30
20
date (Ma)

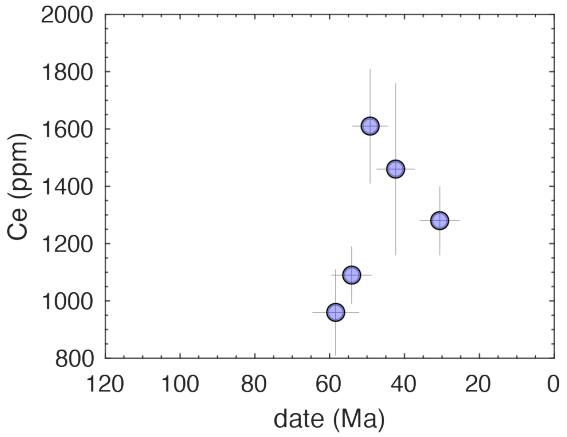
Ce (ppm)
2000
1800
1600
1400
1200
1000
800
120
100
80
60
40
20
0
date (Ma)

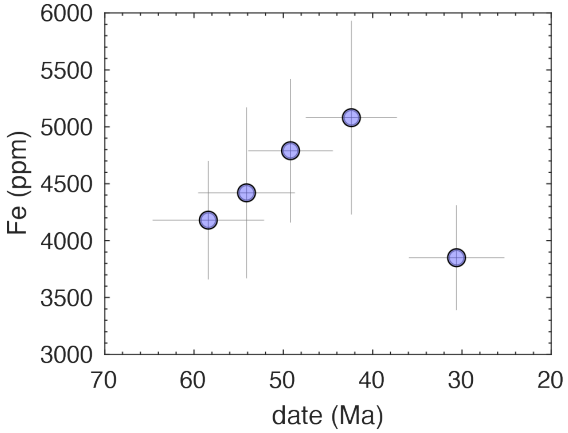
Fe (ppm)
6000
5500
5000
4500
4000
3500
3000
70
60
50
40
30
20
date (Ma)

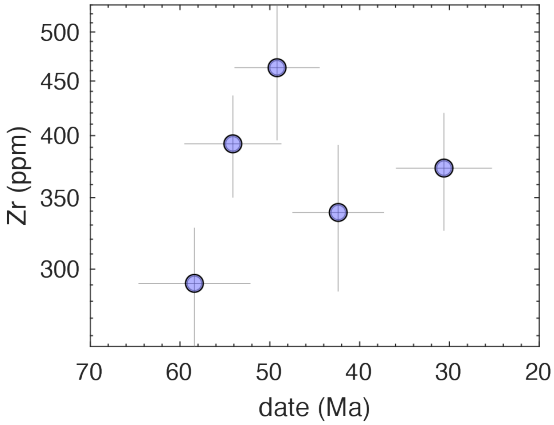
Zr (ppm)
500
450
400
350
300
70
60
50
40
30
20
date (Ma)

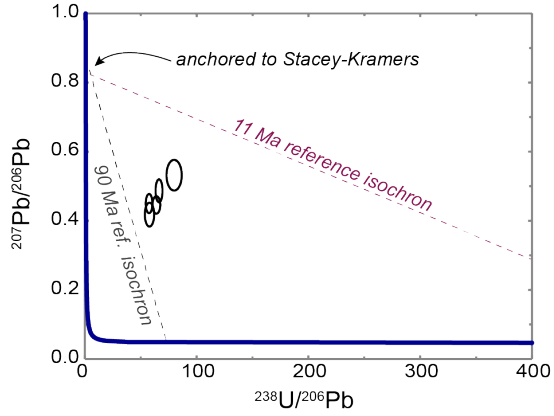
anchored to Stacey-Kramers
11 Ma reference isochron
90 Ma ref. isochron
207Pb/206Pb
1.0
0.8
0.6
0.4
0.2
0.0
0
100
200
300
400
238U/206Pb

45C-0615-40; max misorient 8°

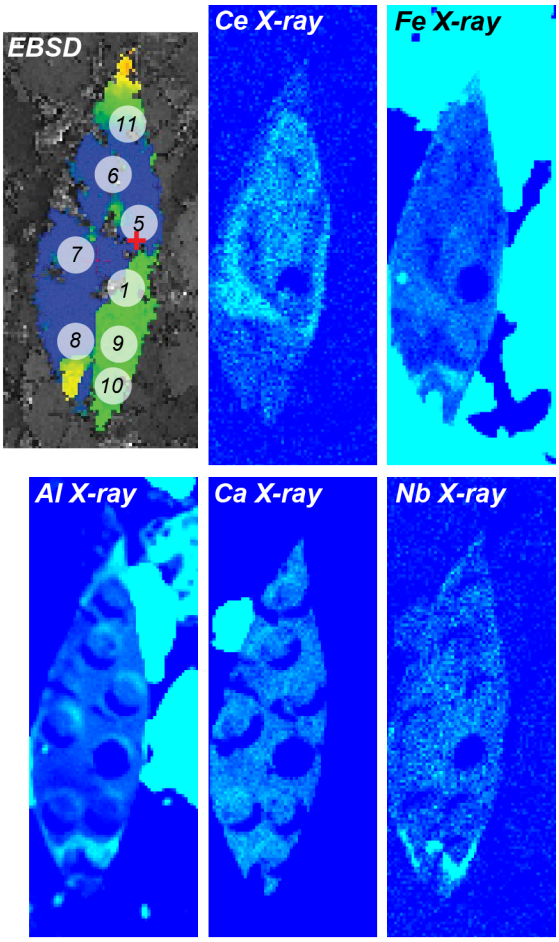

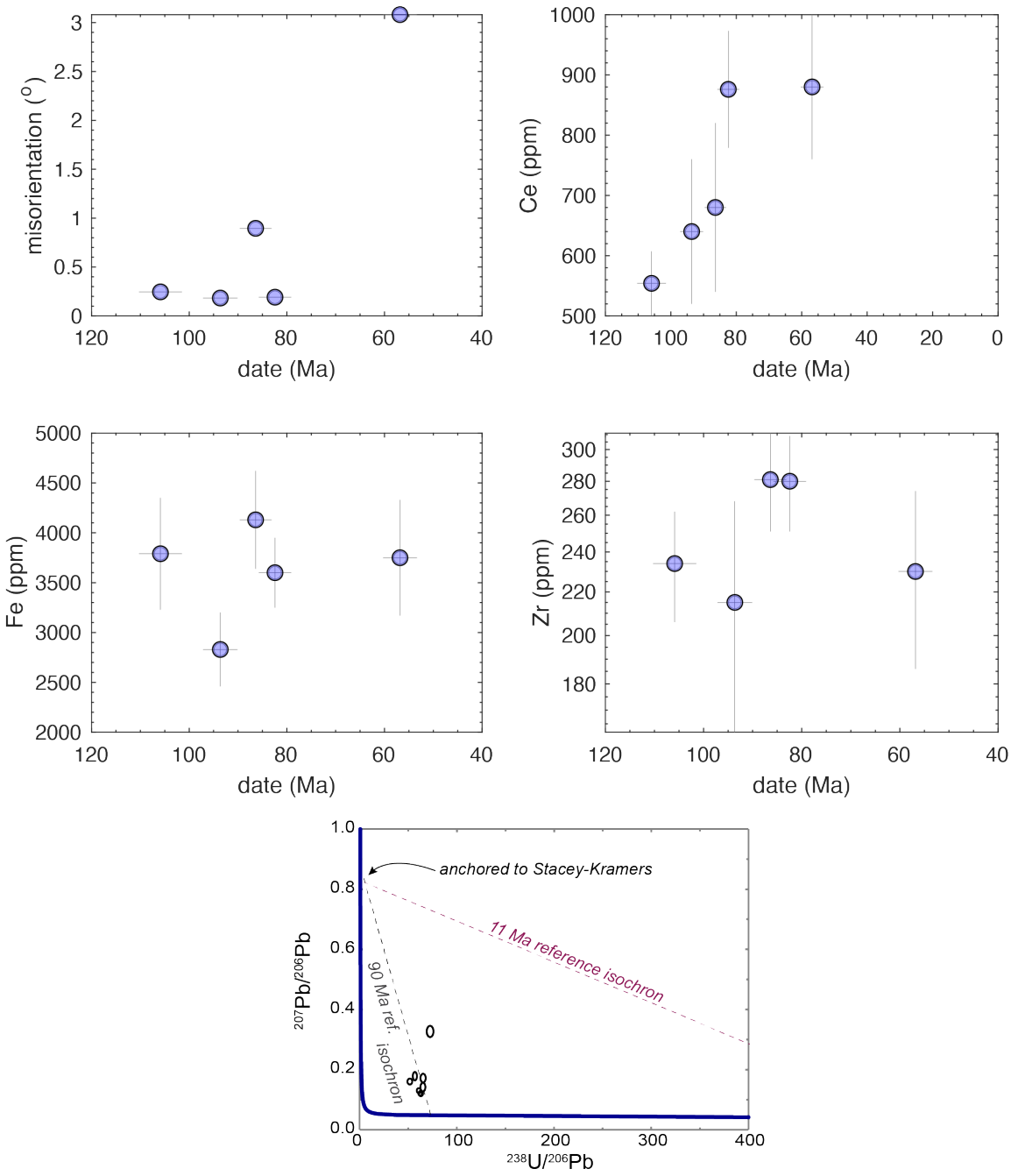
misorientation (°)
date (Ma)
Ce (ppm)
Fe (ppm)
Zr (ppm)
anchored to Stacey-Kramers
11 Ma reference isochron
90 Ma ref. isochron
0
$^{207}Pb/^{206}Pb$
$^{238}U/^{206}Pb$

45C-0615-48; max misorient 10°

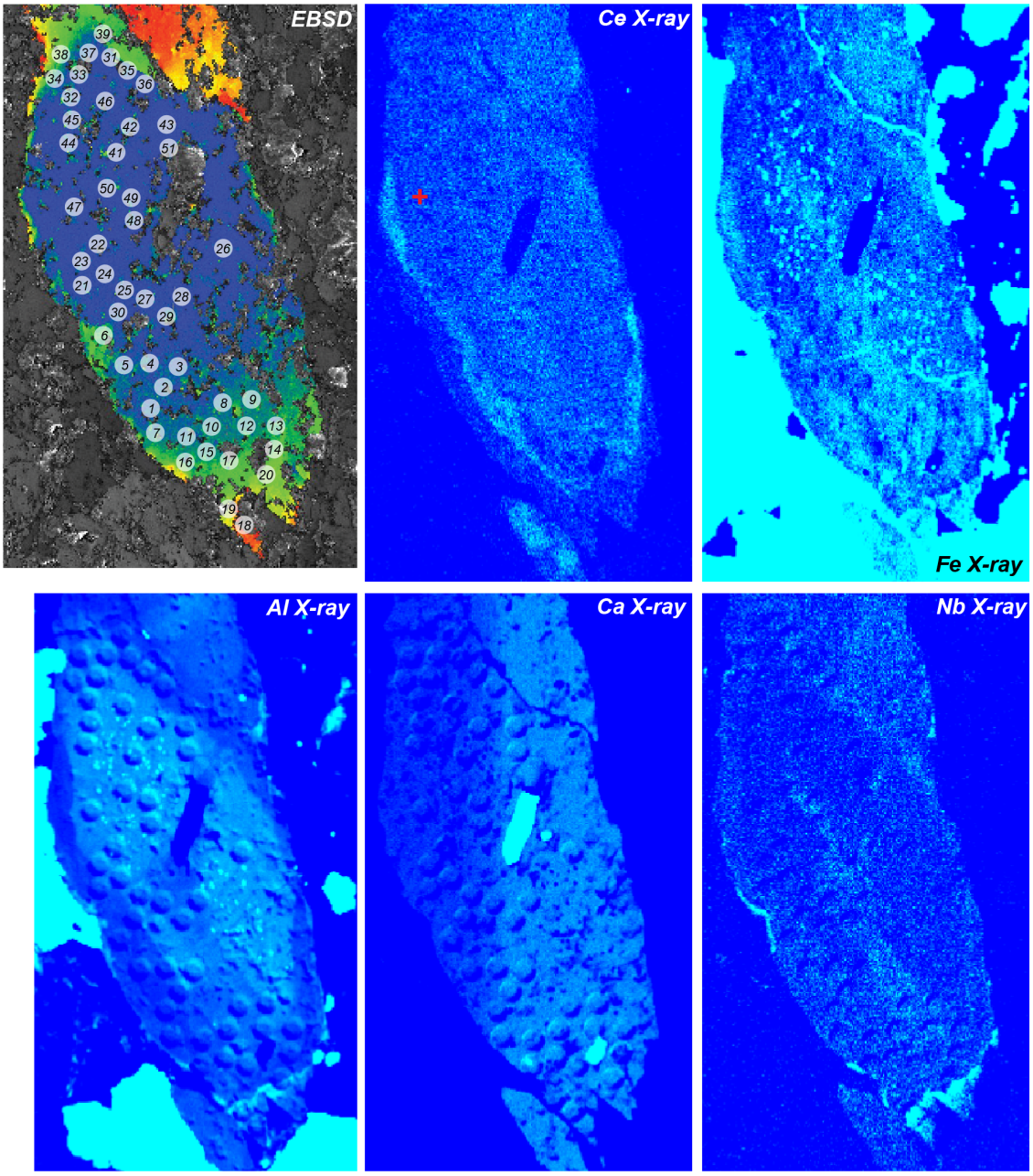

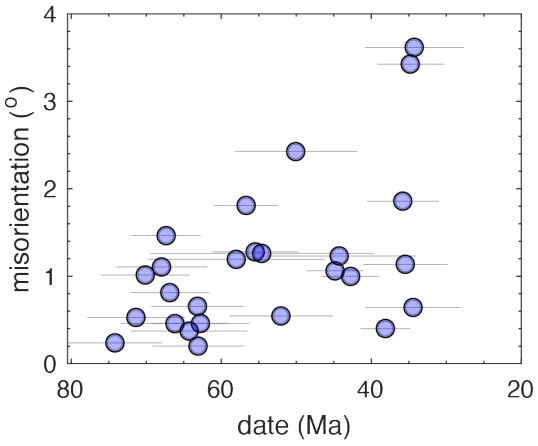
misorientation (°)
date (Ma)

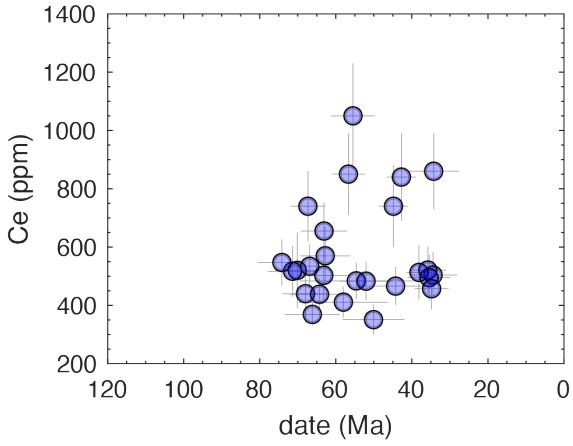
Ce (ppm)
date (Ma)

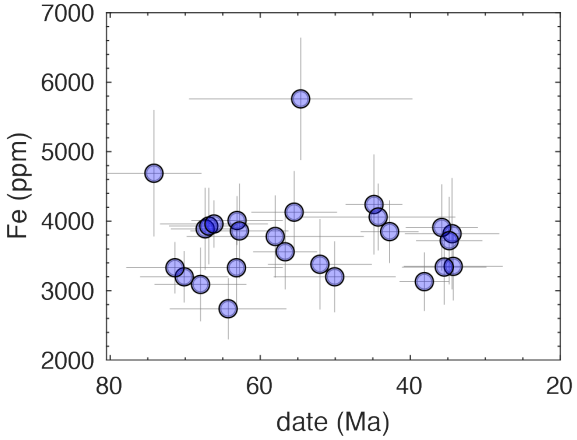
Fe (ppm)
date (Ma)

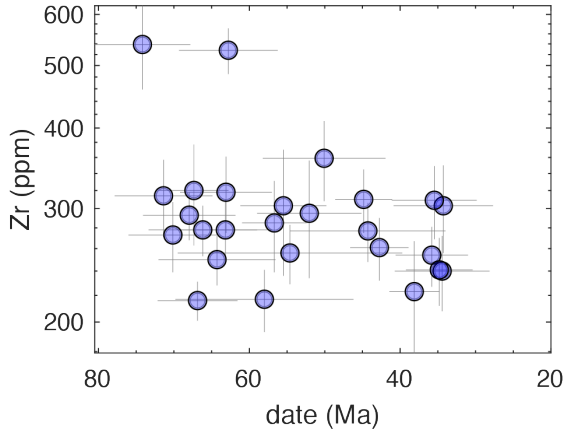
Zr (ppm)
date (Ma)

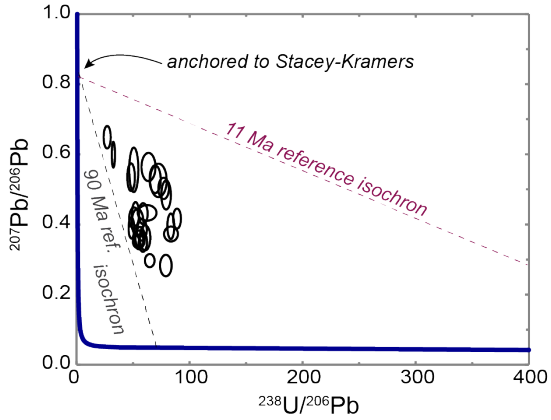
anchored to Stacey-Kramers
11 Ma reference isochron
90 Ma ref. isochron
207Pb/206Pb
238U/206Pb

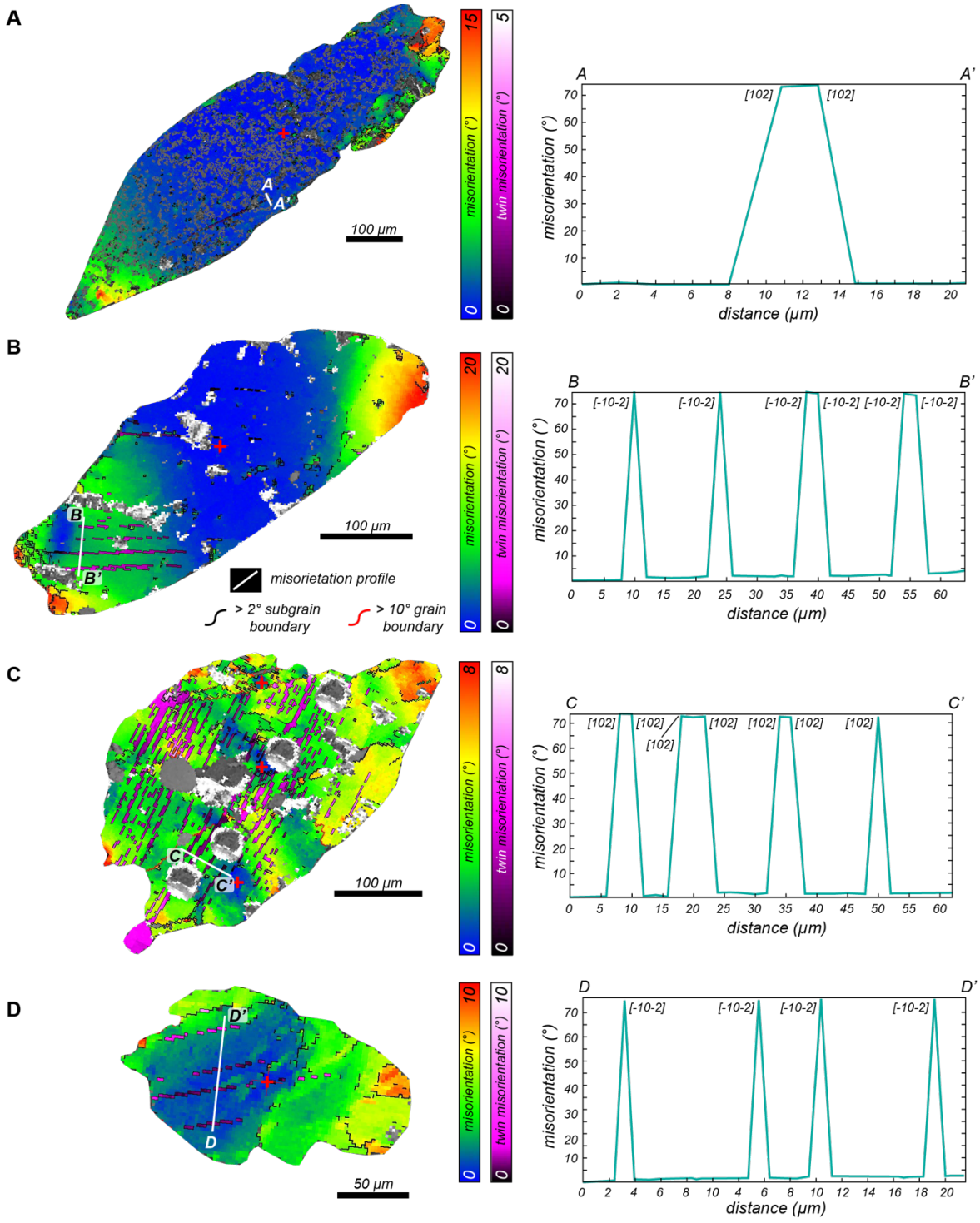

Figure S8. Misorientation transects showing misorientation axis-angle relationships across twins. (A) Singular grain from sample 45C with deformation twins. (B–D) Grains from 48A shown in main text (Figs. 5, 6, 7). Relationships are consistent with the 74°/<102> misorientation axis-angle relationship expected from titanite deformation twins. Misorientation angle is with respect to starting point.

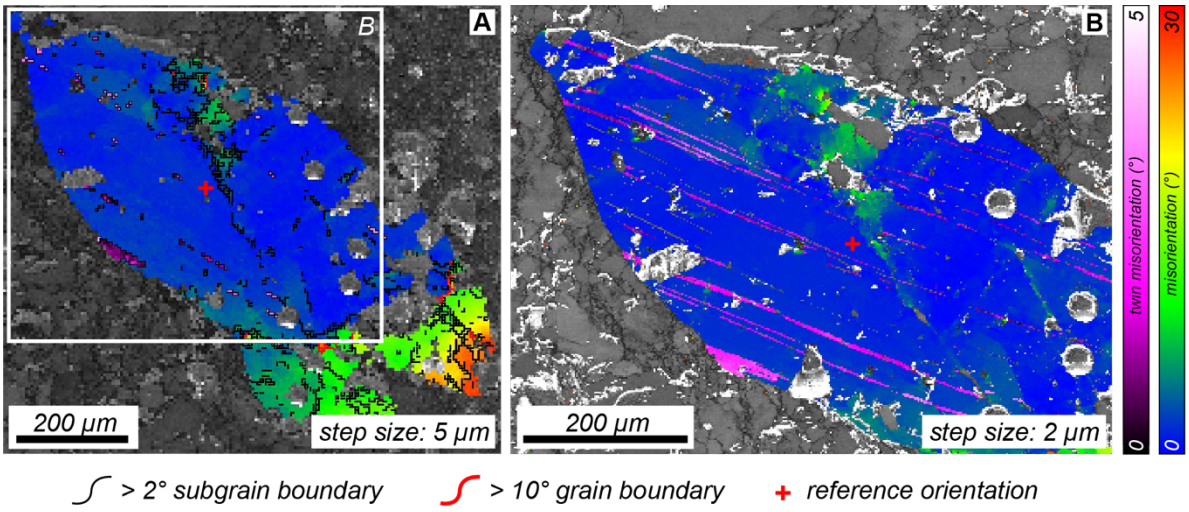

Figure S10. EBSD relative misorientation maps acquired at two different step sizes (left: 5 µm; right: 2 µm) demonstrating that for some grains, the data acquisition step size may have been too coarse to capture all deformation twins.

APPENDIX 3

S1.1 Volume diffusion assessment

Approach

Titanite U-Pb dates are often suggested to be cooling ages, recording the end of thermally mediated Pb volume diffusion (e.g., Dodson, 1973). Experimental data suggest that the nominal closure temperature for Pb in titanite should be ~600 °C (Cherniak, 1993). Datasets from nature, however, demonstrate that the titanite Pb closure temperature is much higher, likely >750 °C (Kohn and Corrie, 2011; Spencer et al., 2013; Stearns et al., 2016; Kohn, 2017; Marsh and Smye, 2017; Smye et al., 2018; Hartnady et al., 2019; Holder et al., 2019). Titanite U-Pb dates may therefore remain unaffected by thermally mediated volume diffusion at all but the most extreme temperatures (i.e., granulite-facies conditions) and should not be interpreted as cooling ages without accompanying evidence (e.g. Bonamici et al., 2015; Kirkland et al., 2016; Olierook et al., 2019)

Crank (1975) defines a volume-diffusion related concentration gradient as:

$$\left(\frac{C - C_r}{C_c - C_r}\right) = erf\left(\frac{x}{\sqrt{4Dt}}\right)$$

C is the concentration of a given element at a given location, C_r is the concentration of that element in the rim, C_c is the concentration of that element in the core, x is the location of the spot along the concentration gradient (i.e., distance from the edge of the grain), D is the diffusivity of the element of interest, and t is time (in seconds). Taking the inverse error function of this equation results in:

$$erf^{-1}\left(\frac{C - C_r}{C_c - C_r}\right) = \frac{x}{\sqrt{4Dt}}$$

The erf^{-1} of a normalized concentration gradient produced by volume diffusion is therefore a line with slope:

$$m = \frac{1}{\sqrt{4Dt}}$$

The erf^{-1} of a concentration gradient that is the result of volume diffusion *at the grain scale* should define a line with respect to distance from the edge of the grain.

To assess whether the titanite U-Pb dates reported herein could be explained by thermally mediated volume diffusion of Pb, we evaluated whether dates and Pb concentrations define an *erf* with respect to distance from the edge of the grain by calculating the erf^{-1} of the normalized Pb concentration gradients and date gradients. We also evaluated the concentration gradients of all measured elements to determine whether any measured element moved by thermally mediated volume diffusion. Pearson's r (correlation coefficient) and r^2 of linear regressions (using the fitlm function in MATLAB) of the normalized erf^{-1} data were calculated to evaluate whether such data are linear and could plausibly be explained by volume diffusion. For the linear regression calculations, each of the normalized concentration values were assigned a percent uncertainty equivalent to those reported for the dates and trace-element concentrations. For each element, we define C_c and C_r as the maximum and minimum concentrations, respectively, which is a reasonable approximation given that most elements are enriched in cores compared to rims (Fig. 8C).

Erf^{-1} of the normalized concentration gradients were only calculated for the sub- to euhedral grains in sample 5-1A (e.g., Figs. 6, 7) as the aggregate grains did not show any

variation in date. This approach can only assess the role of thermally mediated volume diffusion at the grain scale and cannot account for volume diffusion that may have occurred at spatial scales smaller than the analytical spot size (i.e., 25 μm).

U and Th concentration concentrations used in the *erf*$^{-1}$ calculations are those measured from the Nu Instruments Plasma HR-ES multi-collector ICP and calculated in Iolite with MKED1 (Spandler et al., 2016) as the primary reference material. Additional uncertainty was added to unknown U and Th concentrations to make secondary U and Th concentration reference material NIST SRM 612 values a single population (2.9% for U and 2.6% for Th). Measured U concentrations in NIST SRM 612 were within the known values. Measured Th concentrations in NIST SRM 612 deviate from the known value by ~10%, but concentrations were homogeneous in-run suggesting that unknown Th concentrations are systematically different from the true values and are thus comparable.

Pb concentrations produced in iolite using MKED1 as the primary reference material assumes the same isotopic ratios in the reference material and the unknowns. This method calculates inaccurate Pb concentrations when the analyzed materials contain substantive radiogenic Pb. Individual Pb isotope concentrations were thus recalculated using the following equations:

$$^{204}Pb\ ppm = (U\ ppm) \times \left(\frac{1\ mol\ U}{238.02891\ g\ U}\right) \times \left(\frac{0.9928\ mol\ ^{238}U}{1\ mol\ U}\right) \times \left(\frac{mol\ ^{206}Pb}{mol\ ^{238}U}\right)_m \times \left(\frac{mol\ ^{204}Pb}{mol\ ^{206}Pb}\right)_m \times \left(\frac{203.9730\ g\ ^{207}Pb}{1\ mol\ ^{207}Pb}\right)$$

$$^{206}Pb\ ppm = (U\ ppm) \times \left(\frac{1\ mol\ U}{238.02891\ g\ U}\right) \times \left(\frac{0.9928\ mol\ ^{238}U}{1\ mol\ U}\right) \times \left(\frac{mol\ ^{206}Pb}{mol\ ^{238}U}\right)_m \times \left(\frac{205.9745\ g\ ^{206}Pb}{1\ mol\ ^{206}Pb}\right)$$

$$^{207}Pb\ ppm = (U\ ppm) \times \left(\frac{1\ mol\ U}{238.02891\ g\ U}\right) \times \left(\frac{0.9928\ mol\ ^{238}U}{1\ mol\ U}\right) \times \left(\frac{mol\ ^{206}Pb}{mol\ ^{238}U}\right)_m \times \left(\frac{mol\ ^{207}Pb}{mol\ ^{206}Pb}\right)_m \times \left(\frac{206.9759\ g\ ^{207}Pb}{1\ mol\ ^{207}Pb}\right)$$

$$^{208}Pb\ ppm = (U\ ppm) \times \left(\frac{1\ mol\ U}{238.02891\ g\ U}\right) \times \left(\frac{0.9928\ mol\ ^{238}U}{1\ mol\ U}\right) \times \left(\frac{mol\ ^{206}Pb}{mol\ ^{238}U}\right)_m \times \left(\frac{mol\ ^{208}Pb}{mol\ ^{206}Pb}\right)_m \times \left(\frac{207.9757\ g\ ^{207}Pb}{1\ mol\ ^{207}Pb}\right)$$

The $^{206}Pb/^{238}U$, $^{207}Pb/^{206}Pb$, and $^{208}Pb/^{206}Pb$ ratios are the downhole-corrected values using MKED1 as the primary reference material. Like the $^{206}Pb/^{238}U$ and $^{207}Pb/^{206}Pb$ in the main text, additional uncertainty was added to $^{208}Pb/^{206}Pb$ to make secondary reference material BLR a single population (2.0%). The $^{204}Pb/^{206}Pb$ values used in the calculations are the raw $^{204}Pb/^{206}Pb$ values scaled by a factor to make raw NIST SRM 612 $^{204}Pb/^{206}Pb$ the known value (3.0). Additional uncertainty was added to $^{204}Pb/^{206}Pb$ to make the NIST SRM 612 values a single population (3.2%). The Pb concentration uncertainties were propagated in quadrature using the uncertainties in U concentrations and the uncertainties in the ratios involved in each isotope concentration. The total uncertainty reported for the Pb concentrations includes those for ^{204}Pb, ^{206}Pb, ^{207}Pb, and ^{208}Pb added in quadrature. The Pb concentrations calculated this way for secondary reference material BLR are within previously reported values (Aleinikoff et al., 2007) and within 4.1% for NIST SRM 612 (Table S1).

In addition to Pb concentrations, the concentrations for radiogenic and common Pb were calculated for each spot in order to evaluate their potentially differing behavior. The fraction of common ^{206}Pb, ^{207}Pb, and ^{206}Pb were calculated using the following equations:

$$^{206}Pb_c/^{206}Pb_t = ((^{207}Pb/^{206}Pb)_m - (^{207}Pb/^{206}Pb)^*)/((^{207}Pb/^{206}Pb)_c - (^{207}Pb/^{206}Pb)^*)$$

$$^{207}Pb_c/^{207}Pb_t = {}^{206}Pb_c/^{206}Pb_t \times ((^{207}Pb/^{206}Pb)_c/(^{207}Pb/^{206}Pb)_m)$$

$$^{208}Pb_c/^{208}Pb_t = {}^{206}Pb_c/^{206}Pb_t \times ((^{208}Pb/^{206}Pb)_c/(^{208}Pb/^{206}Pb)_m)$$

$^{20X}Pb_c/^{20X}Pb_t$ is represents the fraction of that Pb isotope that is initial Pb, $(^{20X}Pb/^{20X}Pb)_m$ is the measured ratio in the unknown, $(^{207}Pb/^{206}Pb)^*$ is the calculated radiogenic $^{207}Pb/^{206}Pb$ for the measured ^{207}Pb-corrected $^{206}Pb–^{238}U$ date, and $(^{20X}Pb/^{20X}Pb)_c$ is the assumed common Pb ratio, which was 0.86 for $^{207}Pb/^{206}Pb$ (see main text for discussion) and 2.08 for $^{208}Pb/^{206}Pb$ (Stacey and Kramers, 1975 two-stage terrestrial Pb model value). Calculating the proportions of common and radiogenic Pb in this way avoids assumptions about concordance as well as the precision and accuracy inherent in a ^{204}Pb correction.

Results and discussion

The results of the erf^{-1} calculations are presented in Fig. S3. Negative r^2 values, though counterintuitive, indicate instances in which a horizontal line is a better fit to the data than the calculated linear regression. Negative Pearson's r values represent grains in which elemental concentrations increase rather than decrease towards grain rims and result from how C_c and C_r were defined in our calculations. The erf^{-1} calculations for five of the eight euhedral grains produced low r^2 and r values (i.e., both r^2 and $r < 0.5$) for normalized date, total Pb concentration, common Pb concentration, and radiogenic Pb concentration (Fig. S3A, D, E, G, H). The range in dates produced by these grains is therefore not readily explained by thermally mediated volume diffusion of Pb. Three grains produced an r^2 or r value greater than 0.5 for at least one of normalized date, total Pb concentration, common Pb concentration, and/or radiogenic Pb concentration (Fig. S3B, C, F). However, in these same three grains, the erf^{-1} of normalized Sr concentration gradients is not linearly correlated with

distance. Sr and Pb have similar charge/radius ratios and are expected to have similar diffusivities; these elements should behave similarly if a grain underwent thermally mediated volume diffusion (LaTourrette et al., 1996; Marsh and Smye, 2017). Despite the *erf*-like correlations between distance and at least one of date, total Pb concentration, common Pb concentration, and radiogenic Pb concentration in these three grains, the discrepancies between these values and normalized Sr concentrations suggest that these relationships do not result from thermally mediated volume diffusion. The fact that such correlations are also not consistent grain to grain further supports the contention that none of the titanite U-Pb can be interpreted as cooling ages.

Five of the eight sub-to euhedral grains do not yield any convincingly *erf*-like relationships between distance and any measured trace element (r^2 or $r < 0.5$ for every element; Fig. S3A, D–G). The five remaining grains, however, yield some erf-like relationships between date and trace-element concentration (both r^2 and $r > 5$, indicating that variables are correlated, and that the correlation is linear Fig. S3B, C, H). The elements that produce these relationships, however, are not consistent from grain to grain. For example, Zr and Hf have erf-life relationships with distance in S3B, Mg and Mn decrease in an erf-like fashion with respect to distance in S3C, and concentration gradients of Pr and HREEs have an erf-like correlation with distance in S3H. The lack of consistent *erf*-like relationships between date and trace-element concentrations suggests that no element moved via thermally mediated volume diffusion at the grain scale. *Erf*-life concentration gradients in some elements in some grains likely reflect fluid-related zoning (observed in BSE, see main text Figs. 6, 7) with variable geometry and thickness among the analyzed grains (Fig. S5).

S1.2 Zircon U-Pb methods

Zircon U-Pb isotopic analyses were performed by LA-ICP-MS at the Arizona LaserChron Center (ALC). All analyses were completed on polished epoxy mounts. Zircons were first imaged by Cathodoluminescence (CL) using a Hitachi 3400N SEM paired to a Gatan CL2 detector to guide laser spot placement. U and Pb isotopes were analyzed on an Element2 HR single collector ICP-MS using the method outline by Gehrels et al. (2008), Gehrels and Pecha (2014), and Pullen et al. (2018). The zircons were ablated using a Photon Machines Analyte G2 193 nm excimer laser coupled to a HelEx ablation cell, using a 20 μm spot size and ~7 Jcm^{-2} laser fluence at 7 Hz for 10 s. The resulting laser pit was ~10 μm deep. Each ablation is bracketed by two 8 s pauses to measure backgrounds and for the signal to washout. Measured isotopes included ^{238}U, ^{235}U, ^{232}Th, ^{208}Pb, ^{207}Pb, ^{206}Pb, $^{204}(Pb + Hg)$, and ^{202}Hg. Total integration time for each output data point was 3.0 s for ^{238}U, 4.5 s for ^{235}U, 0.7 s for ^{232}Th, 0.7 s for ^{208}Pb, 8.3 s for ^{207}Pb, 5.9 s for ^{206}Pb, 2.3 s for $^{204}(Pb + Hg)$, and 1.5 s for ^{202}Hg. SLM zircon was used as the primary reference material and FC-1 and R33 zircon were analyzed as secondary reference materials.

The zircon isotopic data were reduced using ALC in-house python code and excel macro E2agecalc. Details of this python code are available from the Dat File Decoder link on the ALC web page (under Tools). E2agecalc first calculates backgrounds for each mass based on the 8 s prior to each ablation. The backgrounds are subtracted from the mass intensities from each integration. ^{204}Pb intensities are calculated using the natural $^{202}Hg/^{204}Hg$ of 4.3. Typically, the Hg correction is not significant as Hg backgrounds are low (~150 cps). A preliminary ^{206}Pb-^{238}U date is calculated from which to determine the appropriate Stacey and Kramers (1975) initial Pb ratios to apply in the common Pb correction. E2agecalc then

applies a common Pb correction to ^{208}Pb, ^{207}Pb, and ^{206}Pb based on the measured $^{206}Pb/^{204}Pb$ and the assumed Stacey and Kramers (1975) initial Pb. Fractionation factors for $^{206}Pb/^{238}U$, $^{206}Pb/^{207}Pb$, and $^{208}Pb/^{232}Th$ are calculated based on the measured and known ratios of the reference materials. Additional uncertainty required to explain the excess dispersion in the measured values of the standards is then determined. The fractionation factors of $^{206}Pb/^{238}U$, $^{206}Pb/^{207}Pb$, and $^{208}Pb/^{232}Th$ are applied to the unknows using a sliding window that averages ~8 standard analyses. Ratio and date uncertainties include propagated measurement uncertainties (for $^{206}Pb/^{238}U$ and $^{208}Pb/^{232}Th$), standard deviation of measured values (for $^{206}Pb/^{207}Pb$ and $^{206}Pb/^{204}Pb$), and the overdispersion factor. Reported uncertainties include systematic uncertainties on the scatter of reference material analyses, uncertainties on the absolute age of the reference materials, uncertainties in the assumed initial Pb values, and uncertainties in the ^{238}U and ^{235}U decay constants. The down-hole slope of $^{206}Pb/^{238}U$ is calculated to determine whether individual analyses transected cracks or inclusions. The reported U and Th values for the unknowns are calculated based on secondary reference material FC-1.

The relative discordance (based on $^{206}Pb/^{238}U$ and $^{207}Pb/^{206}Pb$ dates for analyses >1000 Ma; based on $^{206}Pb/^{238}U$ dates and $^{207}Pb/^{235}U$ dates for analyses <1000 Ma) were calculated for each analysis. Analyses that had an absolute value of relative discordance >6% were deemed “discordant” and excluded from final age interpretations. “Preferred date (Ma)” reported in table S3 is the $^{207}Pb/^{206}Pb$ date for analyses older than 1000 Ma and the $^{206}Pb/^{238}U$ date for analyses younger than 1000 Ma.

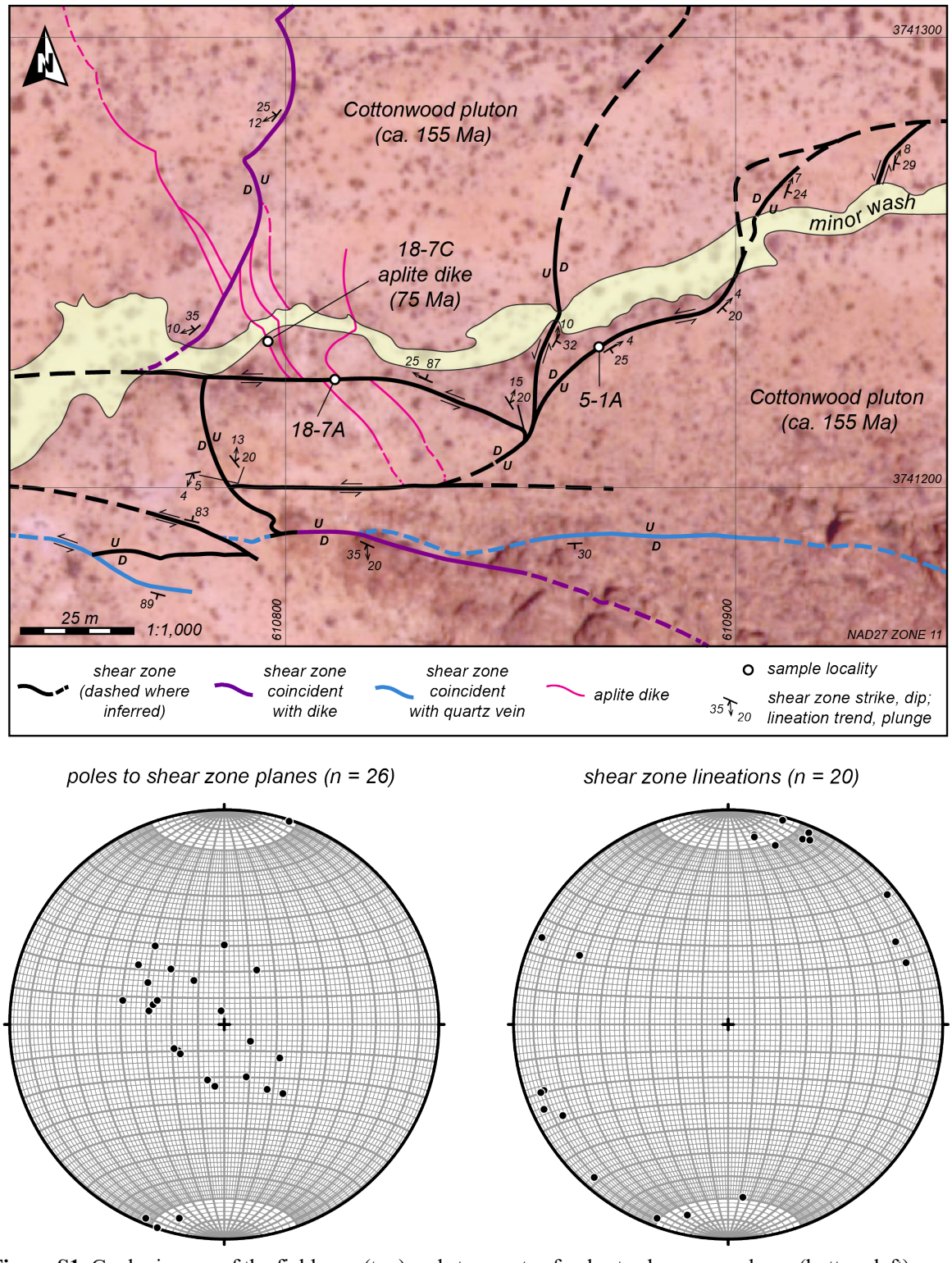

Figure S1. Geologic map of the field area (top) and stereonets of poles to shear zone planes (bottom left) and shear zone lineations (bottom right).

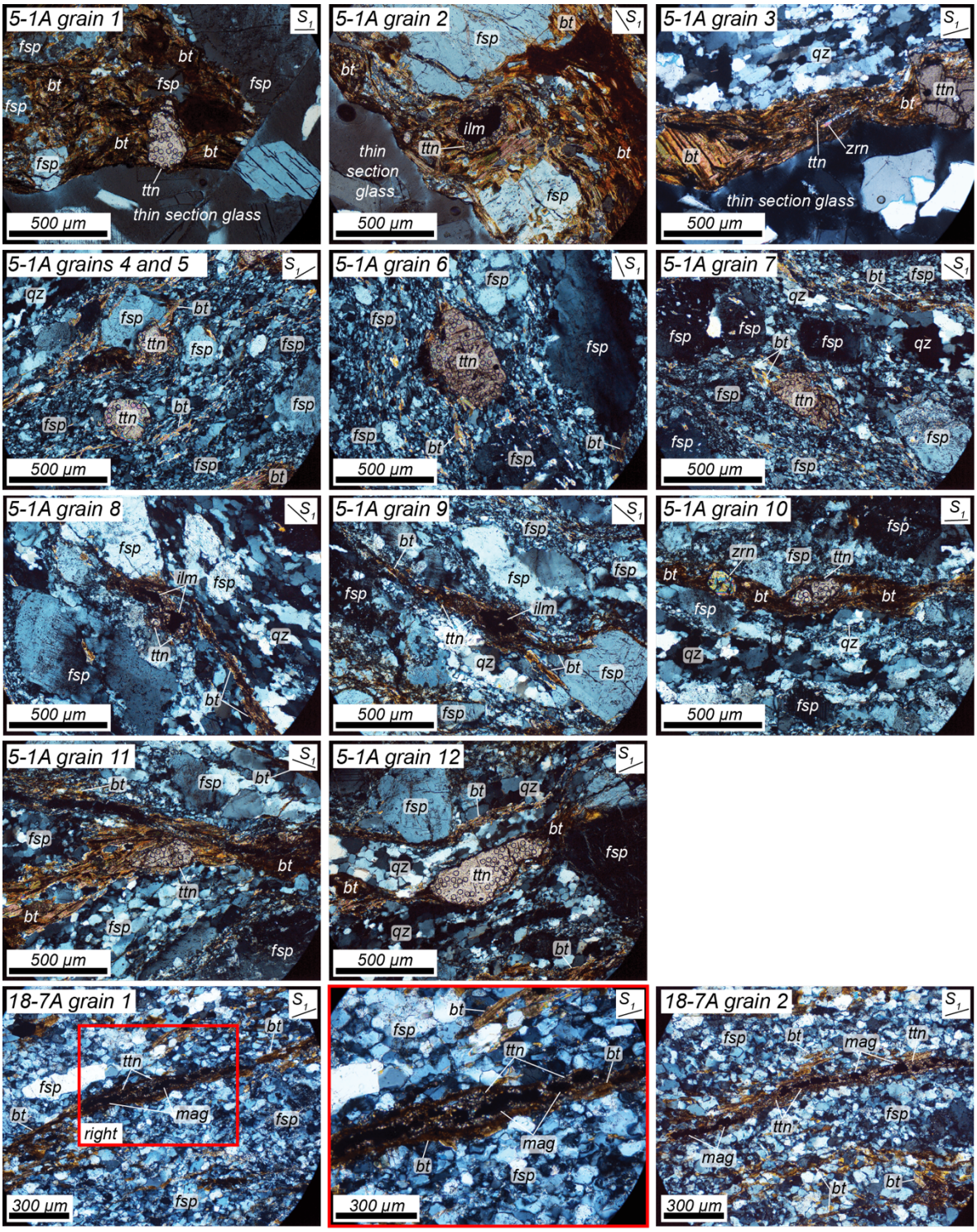

Figure S2. Thin section photomicrographs of analyzed titanite grains from samples 5-1A and 18–7A. S1 denotes orientation of foliation (dip, dip direction 25/130 for 5-1A and 90/010 for 18-7A. Feldspar (fsp); biotite (bt); titanite (ttn); ilmenite (ilm); quartz (qz); zircon (zrn); magnetite (mag).

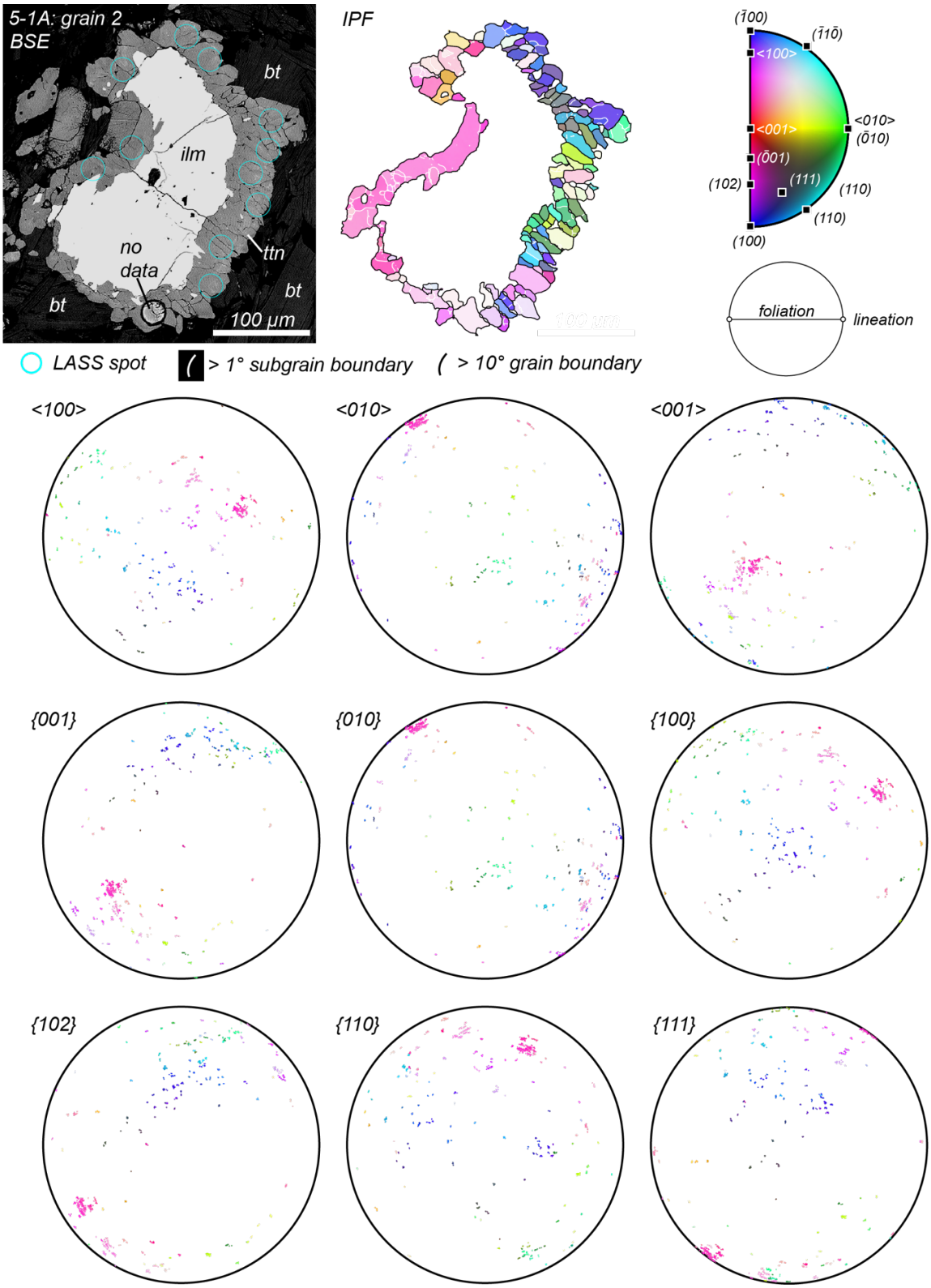

Figure S4. (following pages). Summary of textures, zoning, and microstructure for aggregate titanite grains.

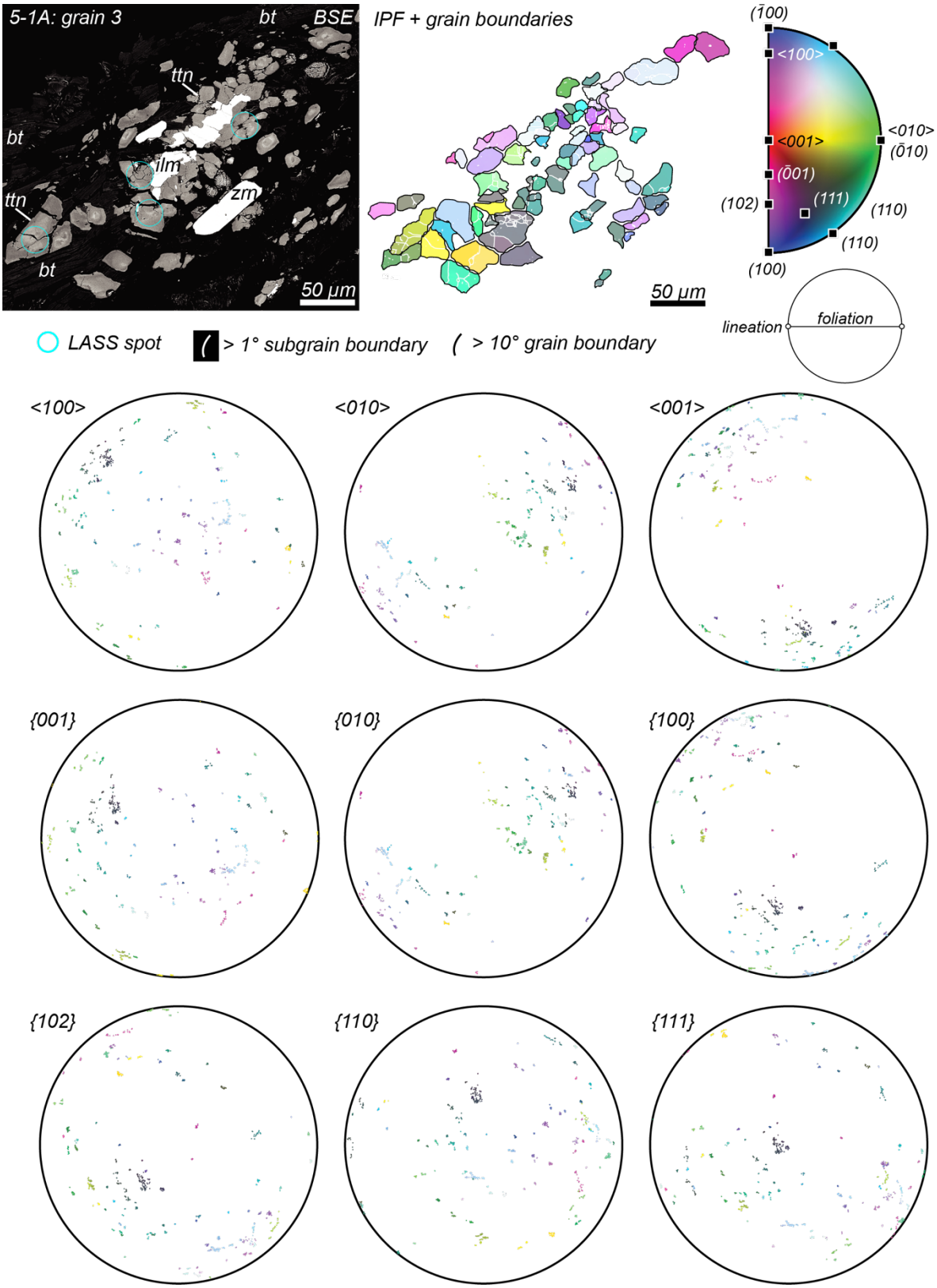
5-1A: grain 3
bt
BSE
ttn
bt
ilm
ttn
zm
bt
50 µm
IPF + grain boundaries
50 µm
(1̄00)
<100>
<001>
<010>
(0̄10)
(0̄01)
(102)
(111)
(110)
(110)
(100)
lineation
foliation
LASS spot
> 1° subgrain boundary
> 10° grain boundary
<100>
<010>
<001>
{001}
{010}
{100}
{102}
{110}
{111}

5-1A: grain 9

BSE and IPF map for this grain can be found in Figure 5 in the main text.

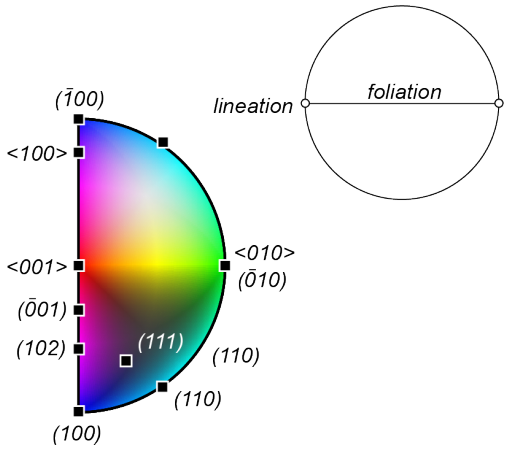

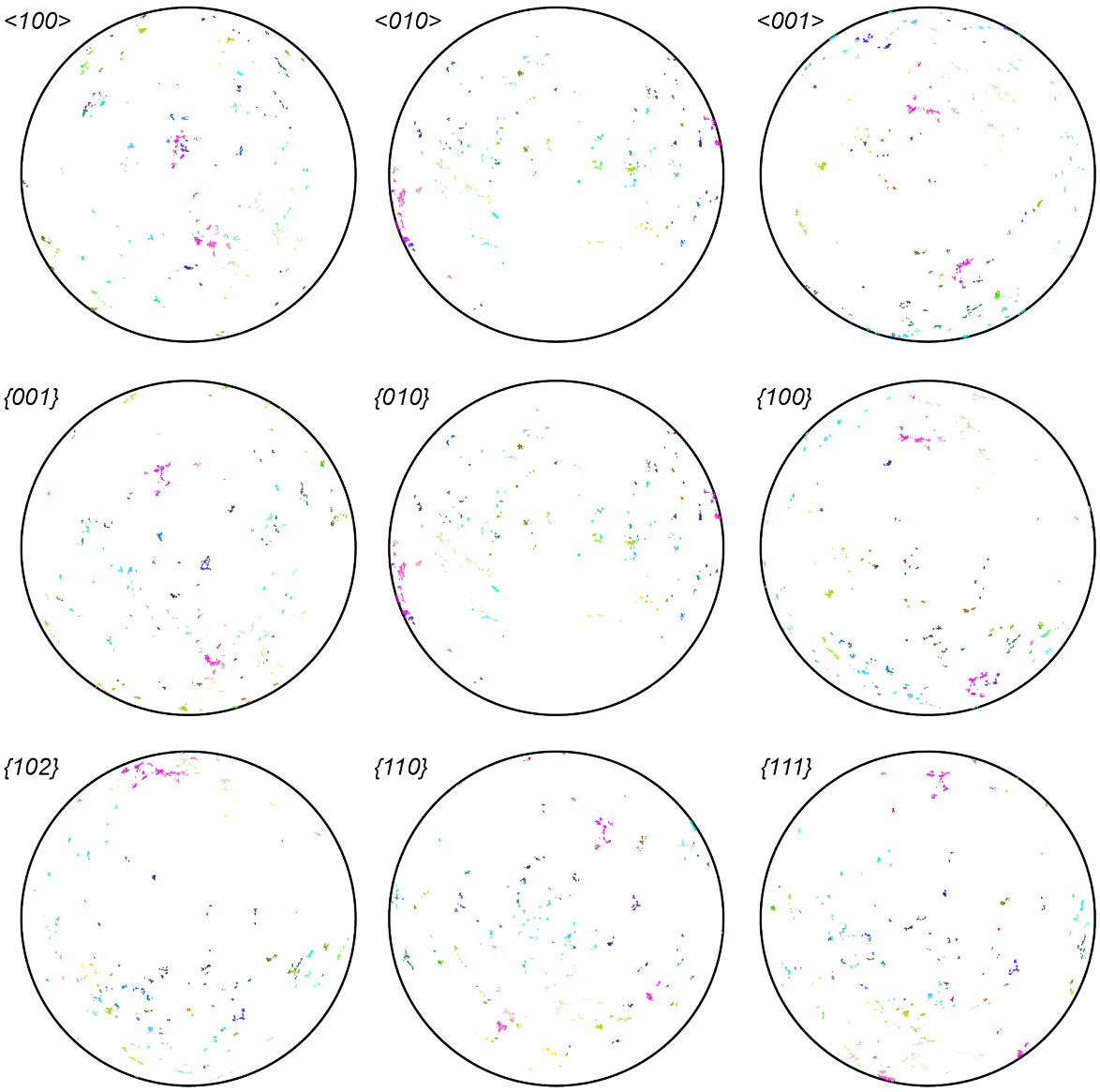

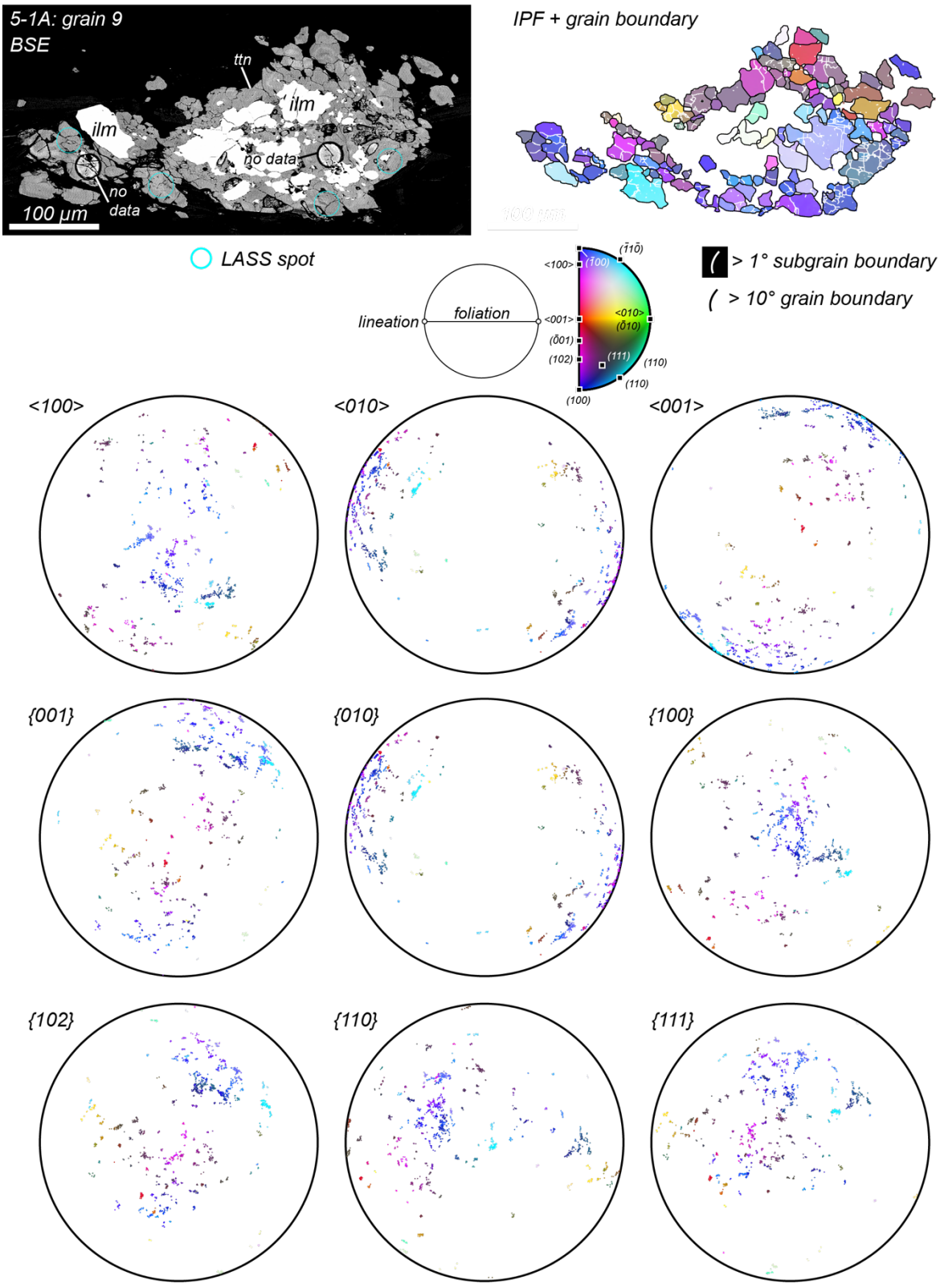
5-1A: grain 9
BSE
ttn
ilm
ilm
no data
no data
100 µm
IPF + grain boundary
100 µm
LASS spot
lineation
foliation
<100>
<001>
(0̄01)
(102)
(100)
(1̄10̄)
(010)
<010>
(0̄10)
(111)
(110)
(110)
> 1° subgrain boundary
> 10° grain boundary
<100>
<010>
<001>
{001}
{010}
{100}
{102}
{110}
{111}

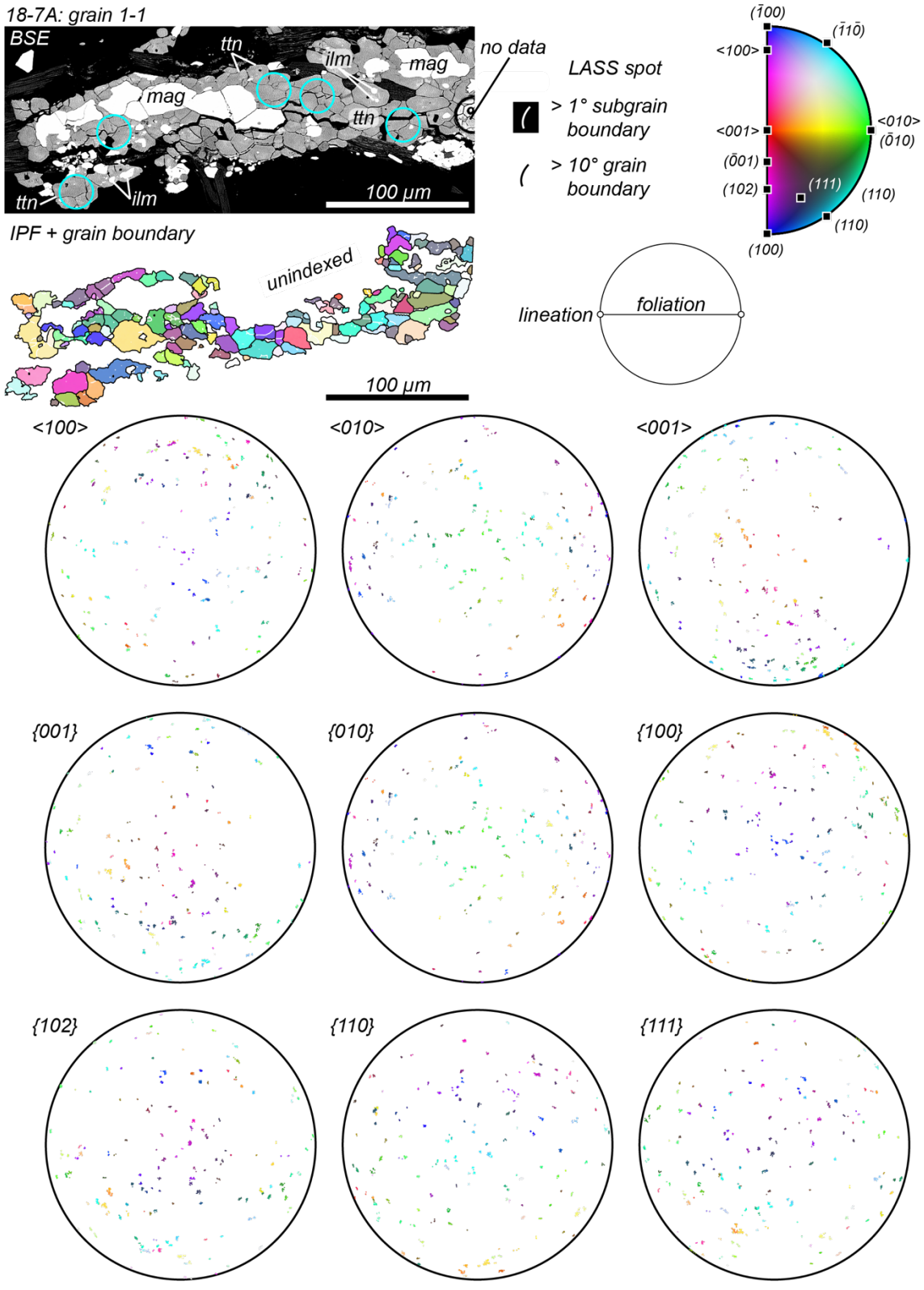
18-7A: grain 1-1
BSE
ttn
ilm
mag
mag
ttn
ttn
ilm
100 µm
no data
LASS spot
> 1° subgrain boundary
> 10° grain boundary
(1̄00)
(1̄1̄0)
<100>
<010>
(01̄0)
<001>
(001̄)
(102)
(111)
(110)
(110)
(100)
IPF + grain boundary
unindexed
100 µm
lineation
foliation
<100>
<010>
<001>
{001}
{010}
{100}
{102}
{110}
{111}

18-7A: grain 1-2

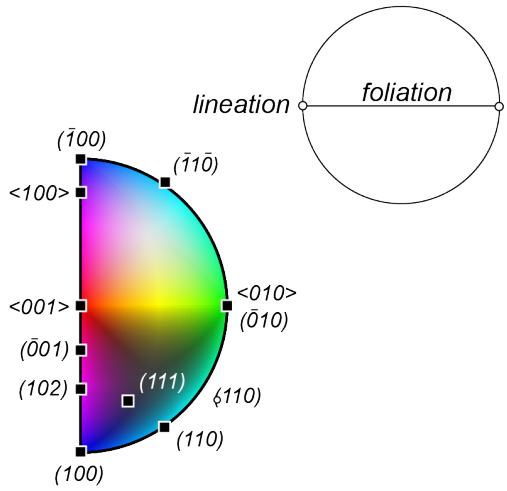

BSE and IPF map for this grain can be found in Figure 5 in the main text.

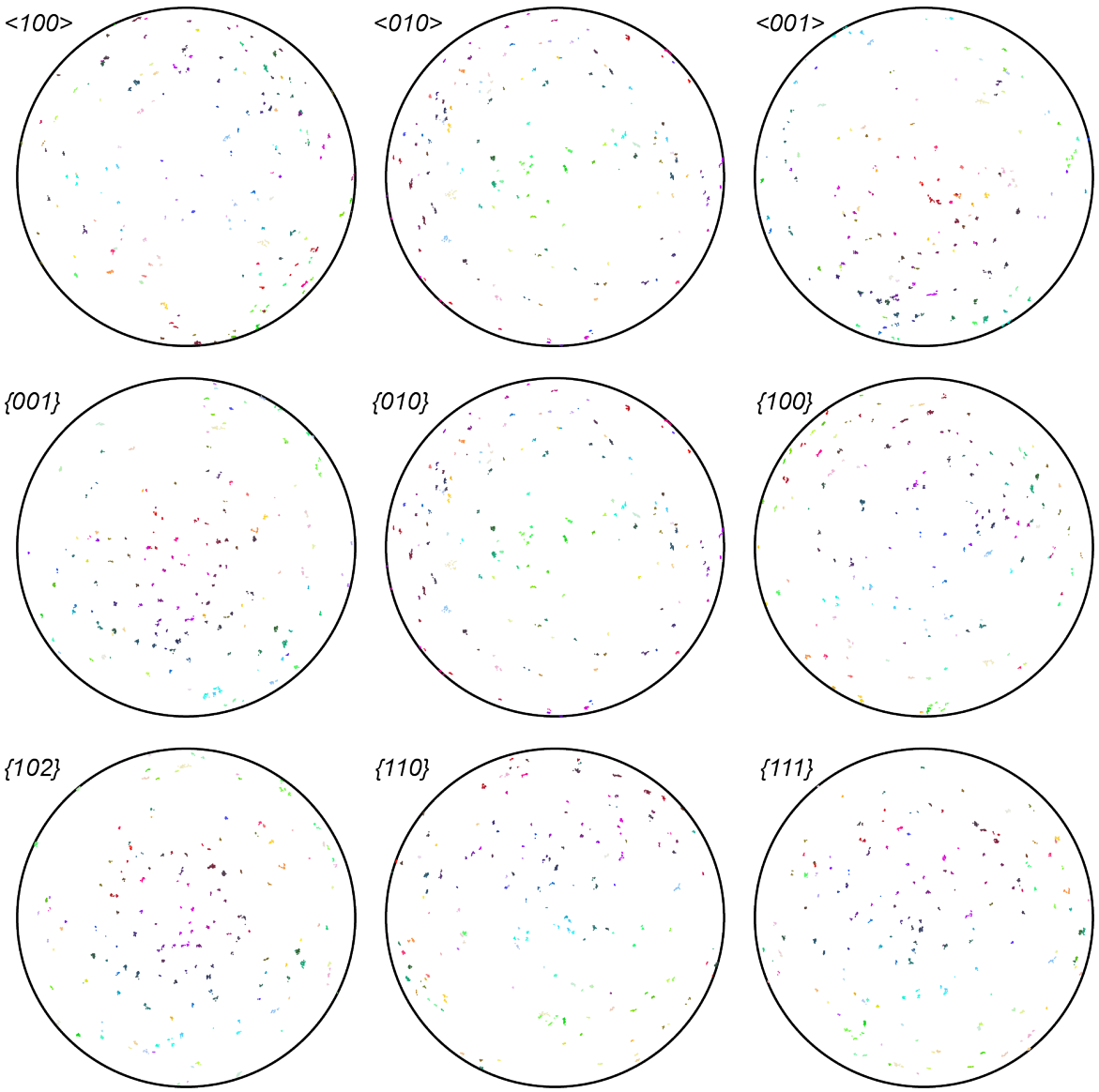

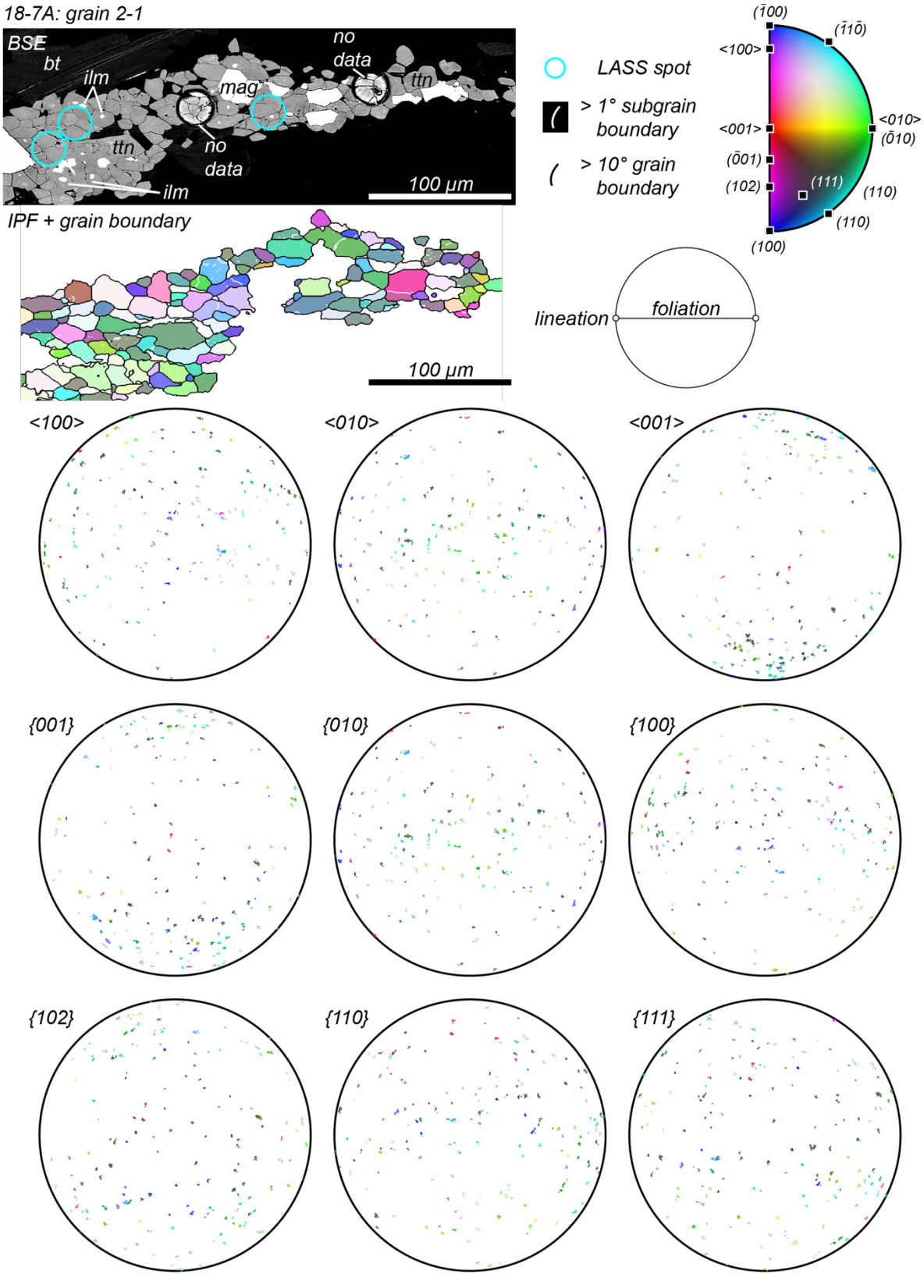
18-7A: grain 2-1
BSE
bt
ilm
ttn
mag
no data
ttn
no data
ilm
100 µm
IPF + grain boundary
100 µm
LASS spot
> 1° subgrain boundary
> 10° grain boundary
(1̄00)
(1̄1̄0)
<100>
<010>
(01̄0)
<001>
(001̄)
(102)
(111)
(110)
(110)
(100)
lineation
foliation
<100>
<010>
<001>
{001}
{010}
{100}
{102}
{110}
{111}

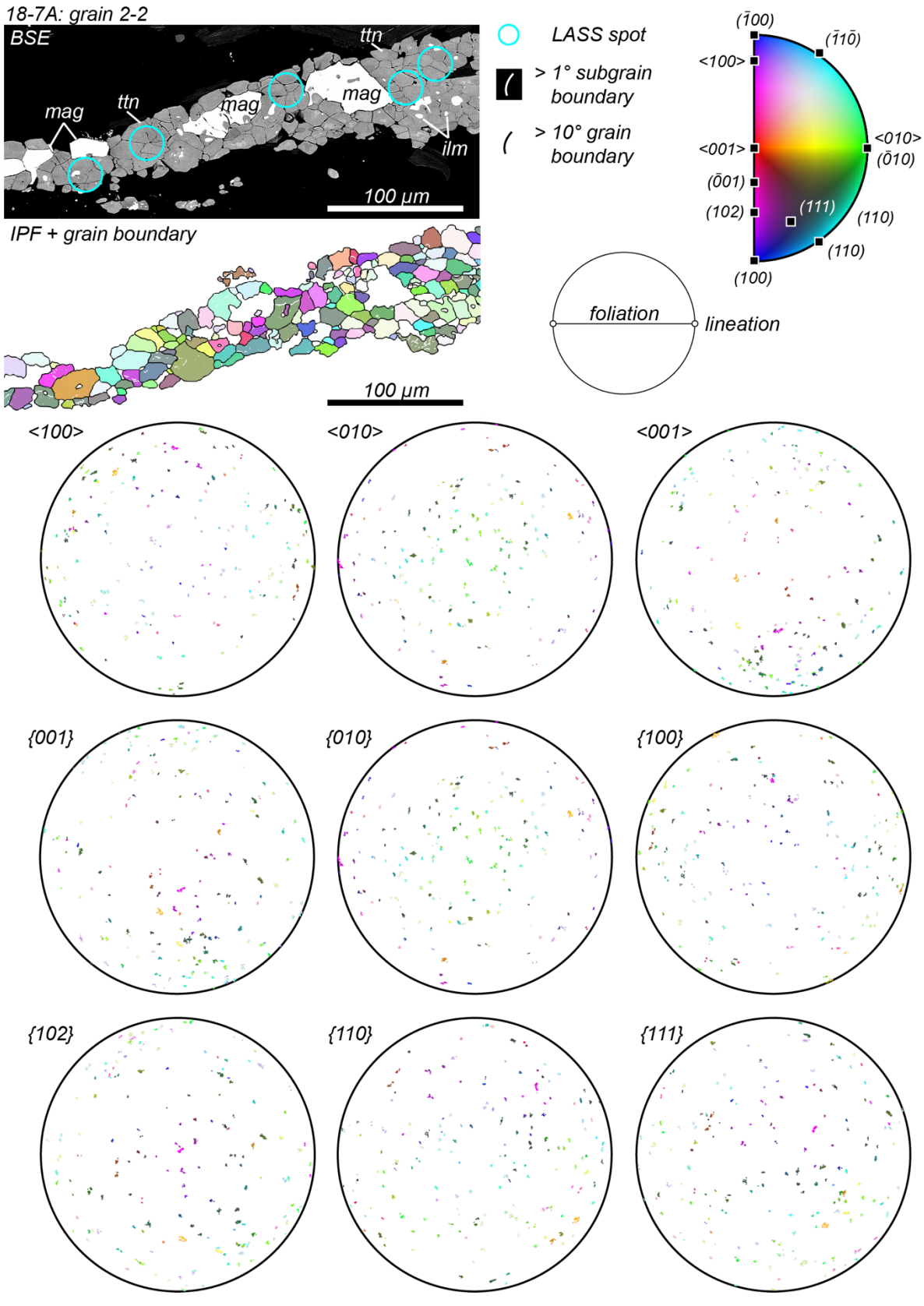
18-7A: grain 2-2
BSE
ttn
mag
ttn
mag
mag
ilm
100 µm
IPF + grain boundary
100 µm
LASS spot
> 1° subgrain boundary
> 10° grain boundary
(1̄00)
(1̄10̄)
<100>
<001>
<010>
(010̄)
(001̄)
(102)
(111)
(110)
(110)
(100)
foliation
lineation
<100>
<010>
<001>
{001}
{010}
{100}
{102}
{110}
{111}

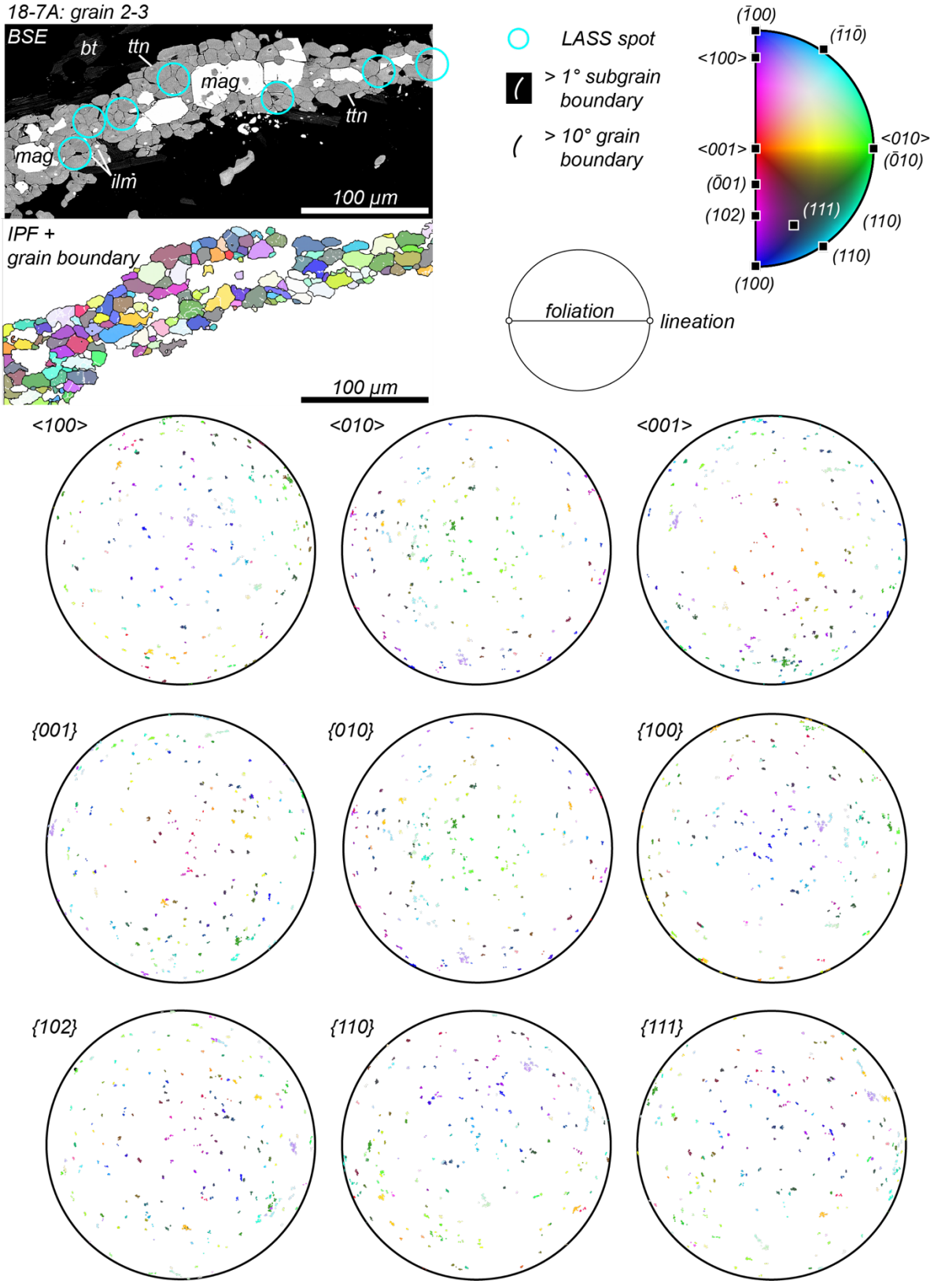
18-7A: grain 2-3
BSE
bt
ttn
mag
ttn
mag
ilm
100 µm
IPF +
grain boundary
100 µm
LASS spot
> 1° subgrain boundary
> 10° grain boundary
(1̄00)
(1̄1̄0)
<100>
<010>
(01̄0)
<001>
(001̄)
(102)
(111)
(110)
(110)
(100)
foliation
lineation
<100>
<010>
<001>
{001}
{010}
{100}
{102}
{110}
{111}

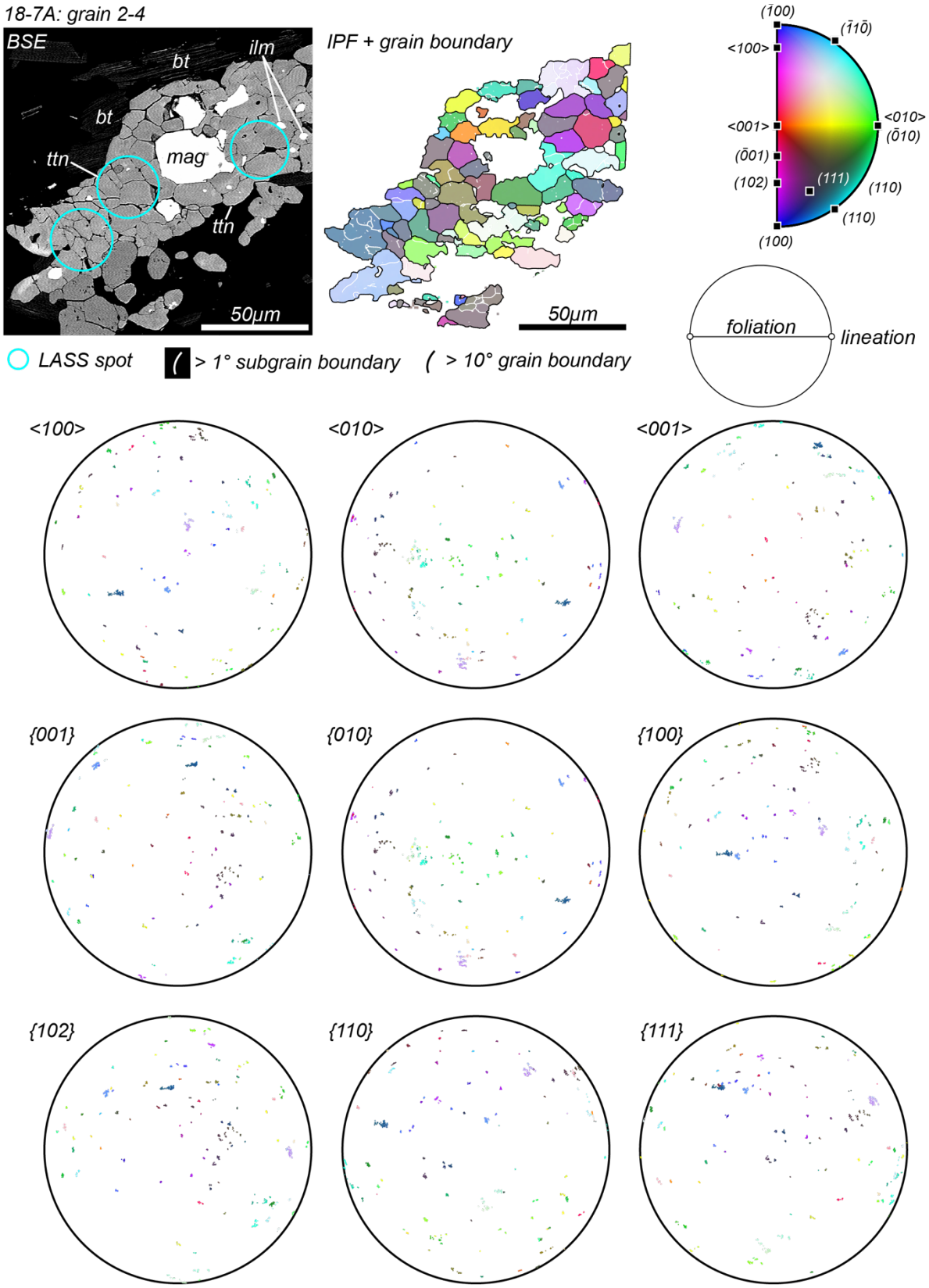
18-7A: grain 2-4
BSE
bt
ilm
bt
ttn
mag
ttn
50μm
IPF + grain boundary
50μm
(1̄00)
(1̄1̄0)
<100>
<001>
<010>
(0̄10)
(0̄01)
(102)
(111)
(110)
(110)
(100)
foliation
lineation
LASS spot
> 1° subgrain boundary
> 10° grain boundary
<100>
<010>
<001>
{001}
{010}
{100}
{102}
{110}
{111}

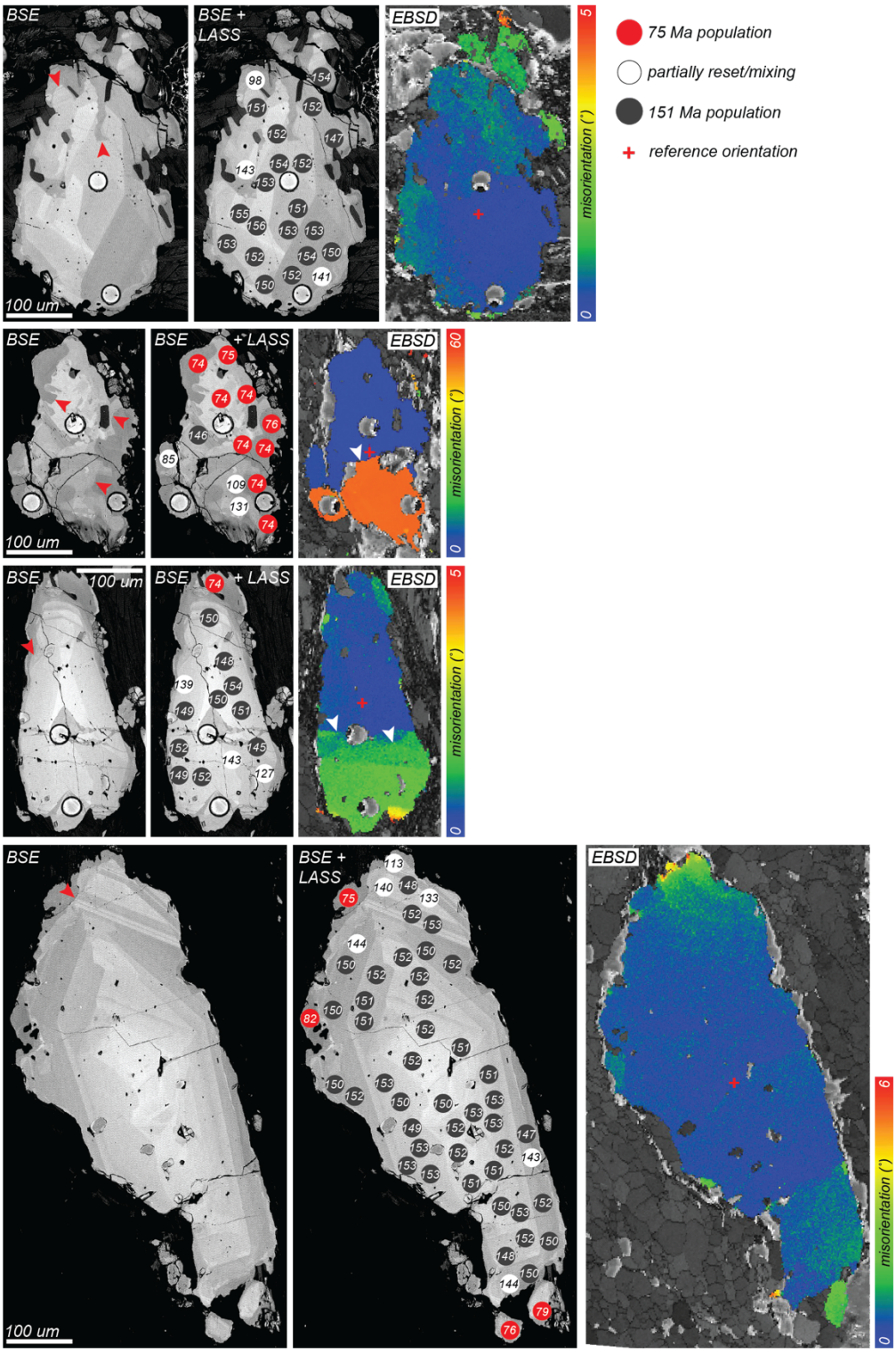

Figure S5. BSE maps (left) with overlain LASS spots and ^{207}Pb-corrected ^{206}Pb-^{238}U dates (center) and EBSD relative misorientation maps for unbent, euhedral titanite (right). Typical date uncertainties are ~3.5% (see also Table S2). Red arrows denote lobate–cuspate rims indicative of interface-coupled dissolution–reprecipitation. White arrows on EBSD maps denote misorientation changes across brittle fractures visible in BSE images.

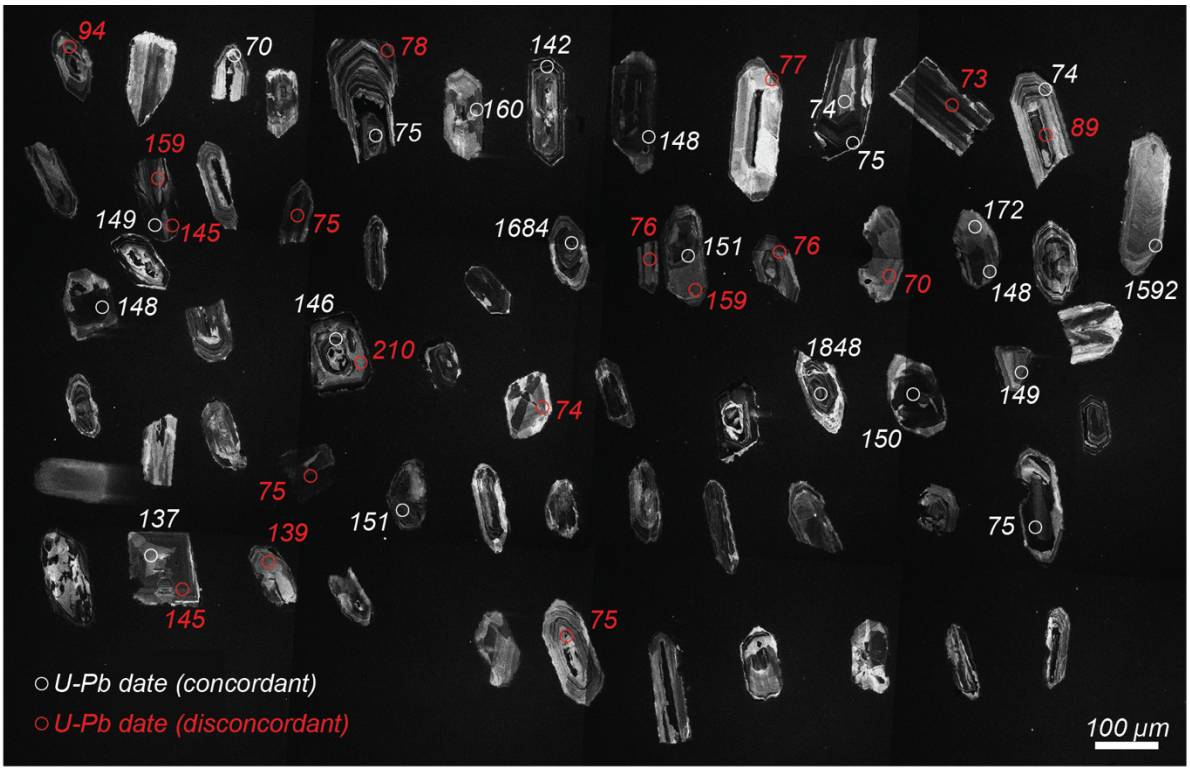

Figure S6A. Zircon CL images, laser-ablation spots, and U-Pb dates from zircons from aplite dike sample 18-7C. Dates older than 1000 Ma are ^{207}Pb-^{206}Pb dates. Dates younger than 1000 Ma are ^{206}Pb-^{238}U dates. See text S1 for discussion of discordance filter.

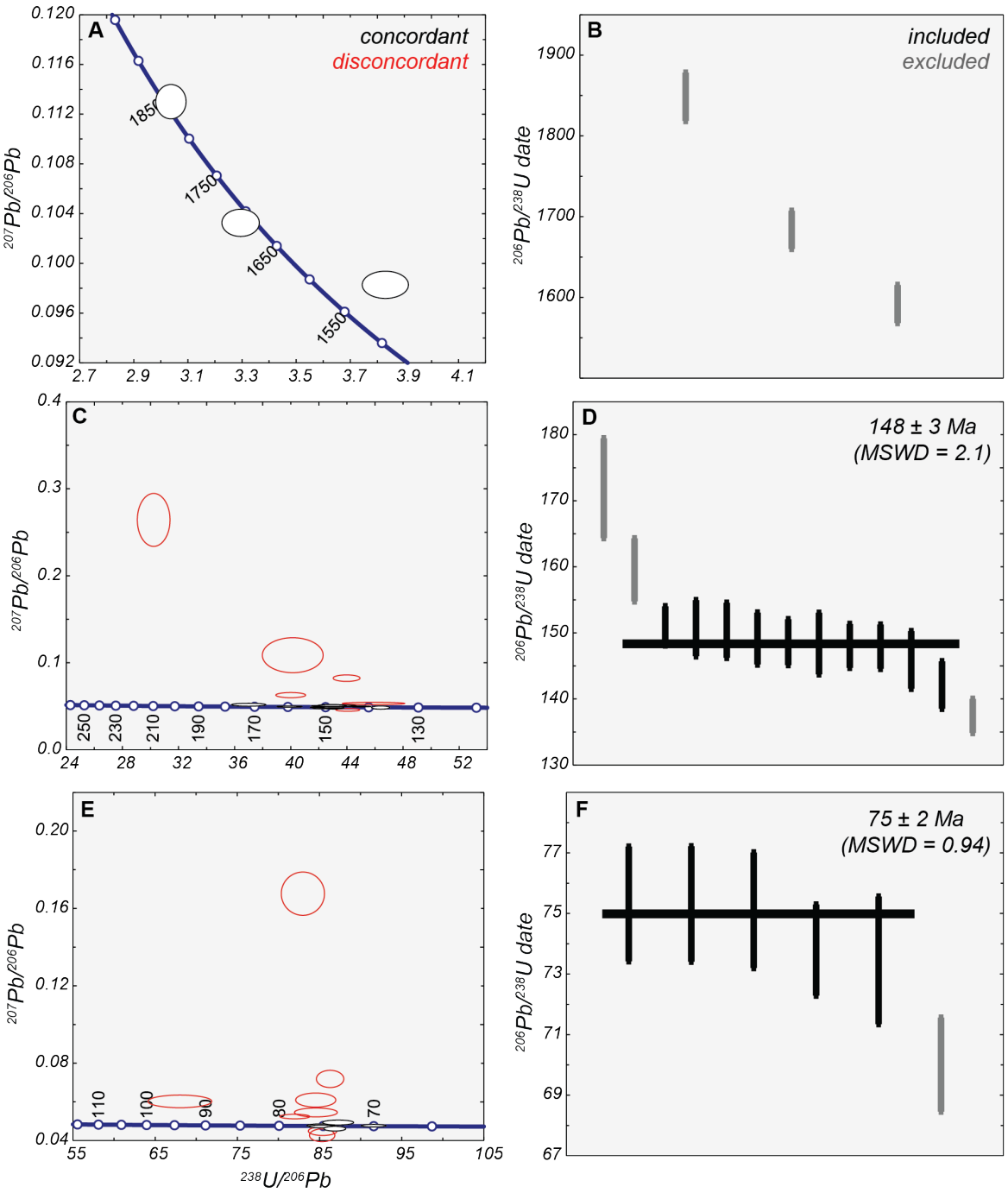

Figure S6B. Zircon U-Pb Tera-Wasserburg concordia diagrams (left) and rank-age plots (right) of zircon U-Pb data from aplite dike sample 18-7C. (A,B) Proterozoic dates, (C,D) Jurassic dates, (E,F) Cretaceous dates. Ages quoted in (D) and (F) are weighted means of the youngest coherent populations in each group. See text S1 for details on concordance filters.

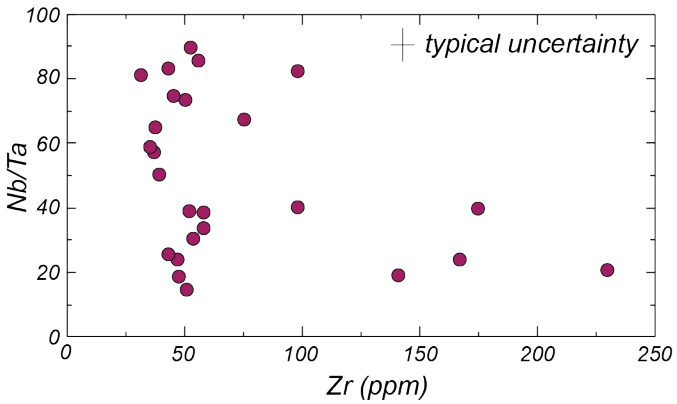

Figure S8. Zr vs. Nb/Ta for LASS analyses from BSE-dark, lobate–cuspate rims in sample 5-1A.

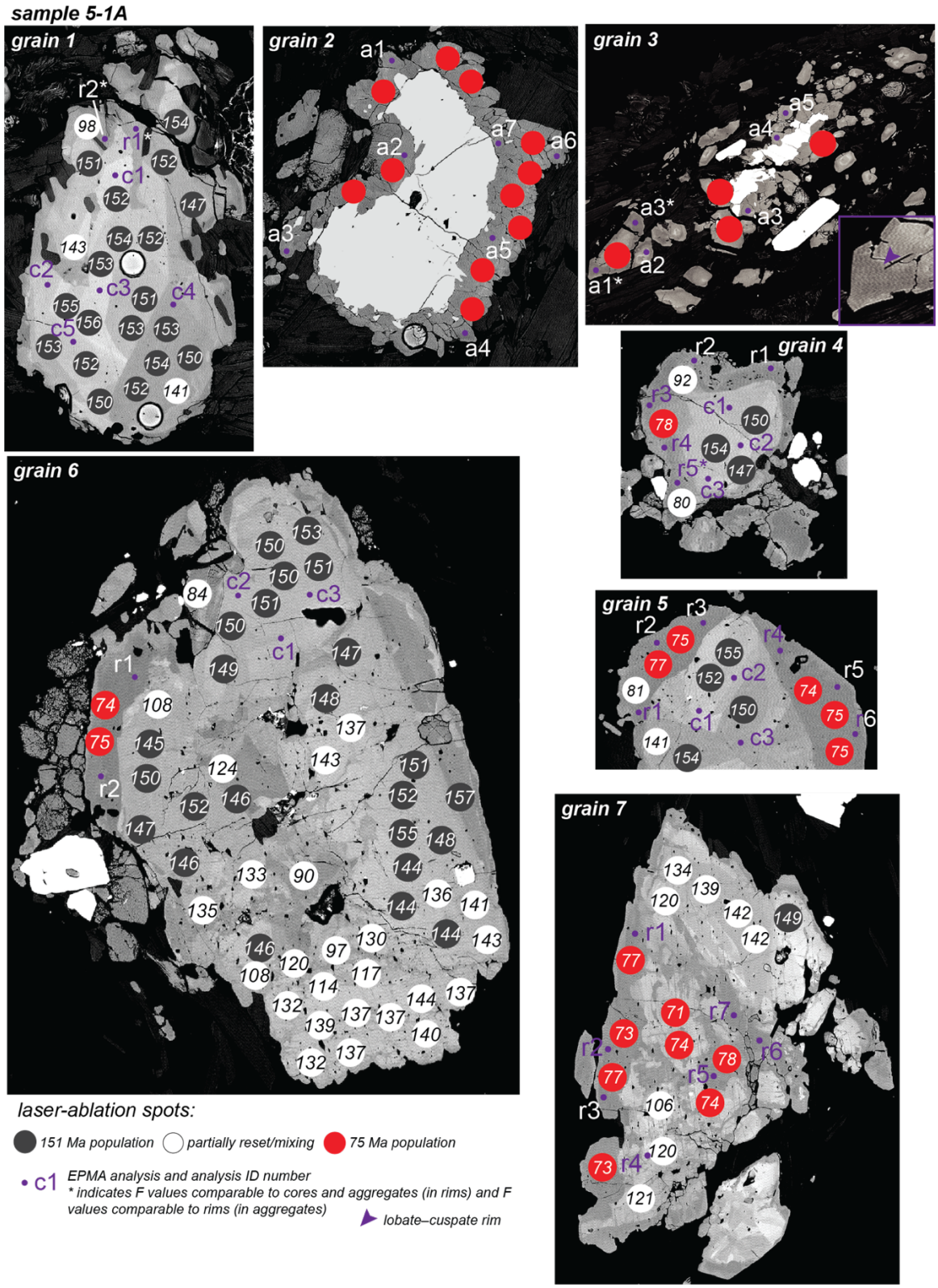

Figure S9. Locations of titanite EPMA analyses. Numbers in LASS spots are dates in Ma.

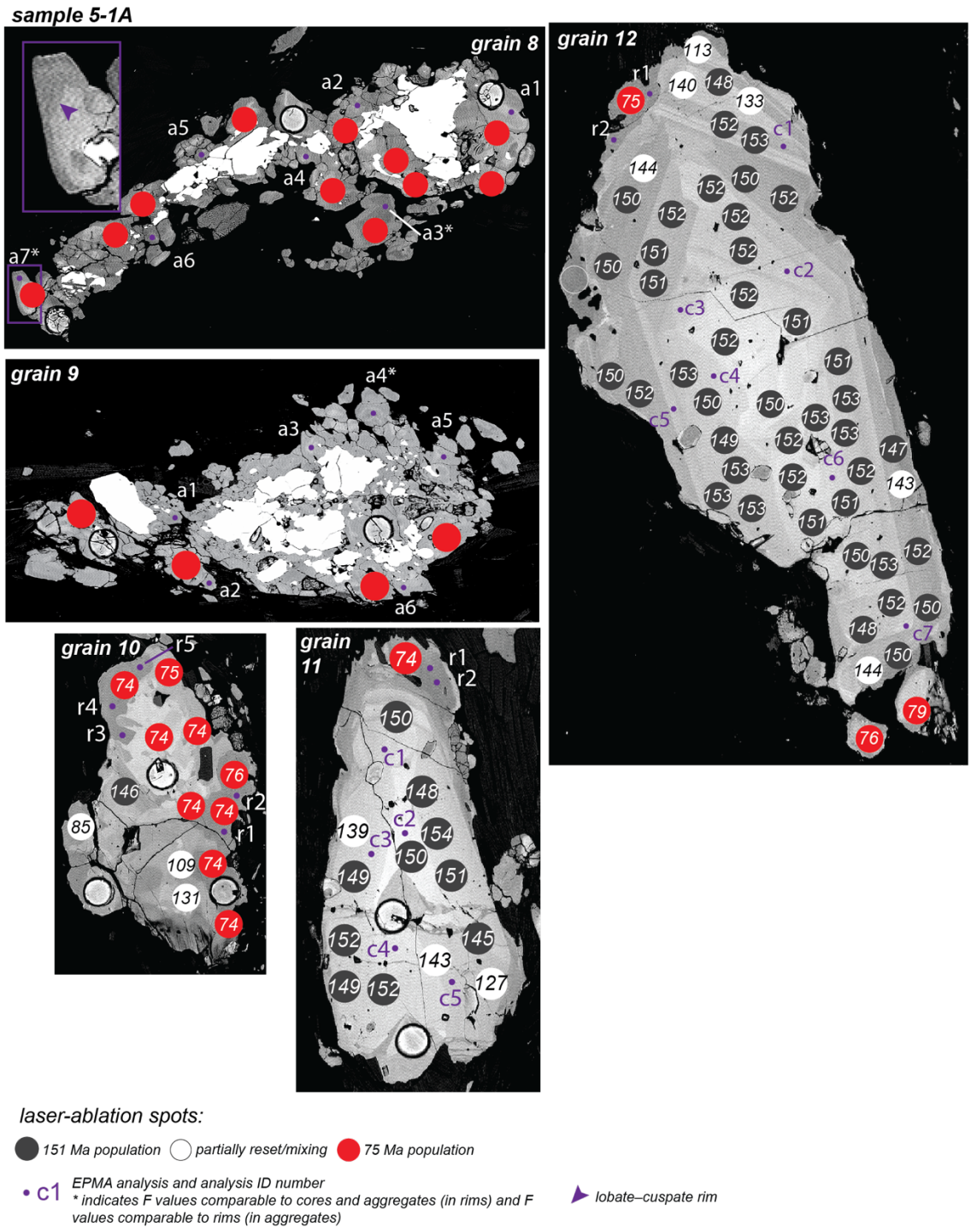

Figure S9, continued. Locations of titanite EPMA analyses. Numbers in LASS spots are dates in Ma.

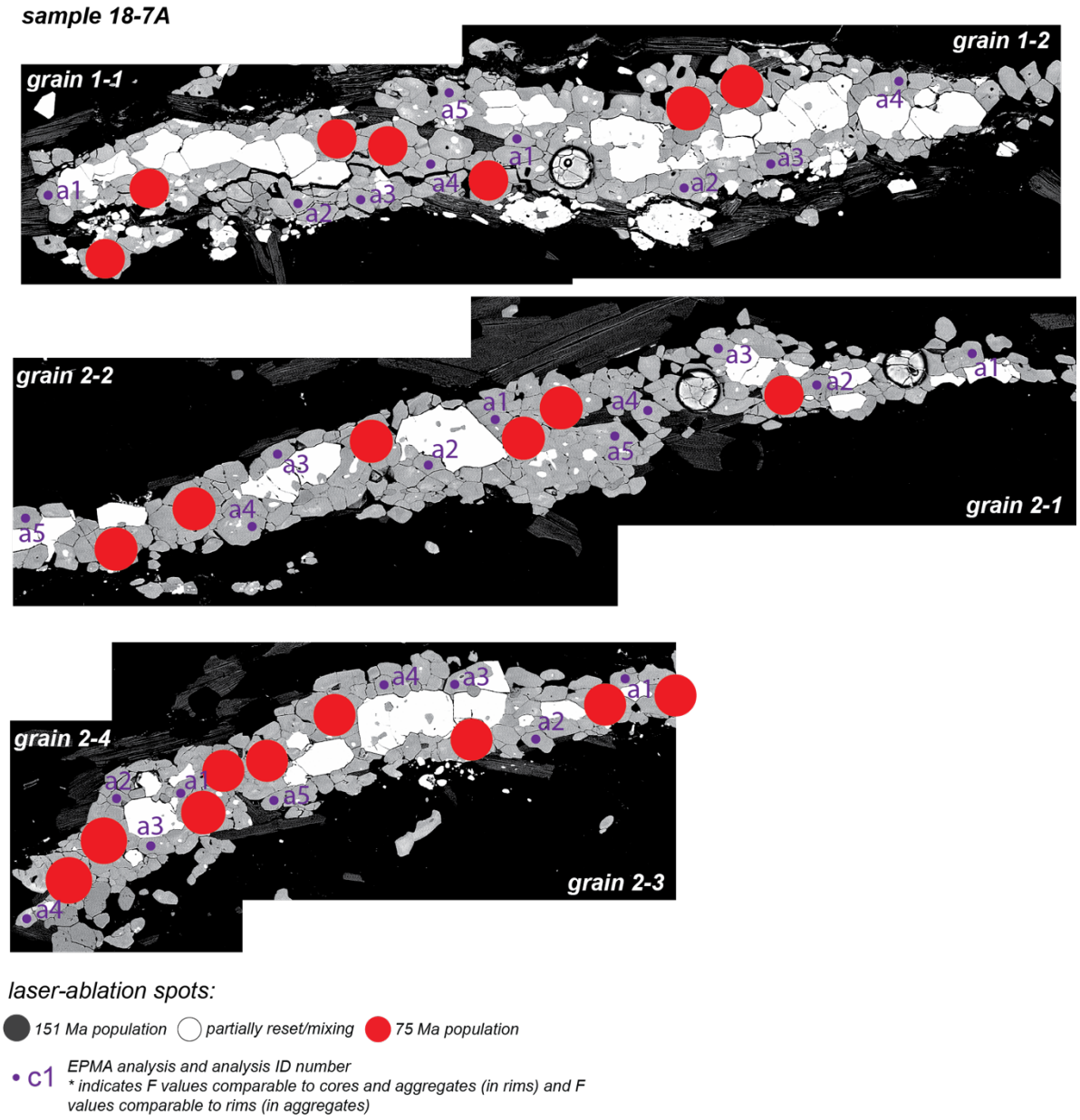

Figure S9, continued. Locations of titanite EPMA analyses.